Beatriz Macarena
Cobaleda Siles
2015

Modular Multimodal Iron Oxide-Based Nanocarriers for Image-Guided dsRNA Immunostimulation and Platinum Anticancer Drug Design

eman ta zabal zazu

Universidad del País Vasco
Euskal Herriko Unibertsitatea

eman ta zabal zazu

Universidad del País Vasco
Euskal Herriko Unibertsitatea

Modular Multimodal Iron Oxide-Based Nanocarriers for Image-Guided dsRNA Immunostimulation and Platinum Anticancer Drug Design

Beatriz Macarena Cobaleda Siles

2015

Table of contents

Acknowledgements 1
Abbreviations 3
Abstract 7
Resumen 9

Chapter 1: General Introduction

1.1 Nanotechnology in Medicine: Drug Delivery 16
1.2 Nanoconstructs for drug delivery applications 18
1.3 Nanomaterials in medical imaging technologies 20
1.4 Nanoparticles engineered to modulate immune responses 24
1.5 Nanoparticle-based vaccines for cancer immunotherapy 28
References 33

Justification and objectives of this thesis 39

Chapter 2 : Development of water soluble systems based on IONPs for multimodal imaging and drug delivery

2.1 *Introduction* 42
2.1.1 Magnetic properties of Iron Oxide Nanoparticles (IONPs) 42
2.1.2 Size, shape and chemical composition of IONPs 44
2.1.3 Surface coating 48
2.1.4 Application of IONPs for multimodal imaging 49
2.2 *Results and discussion* 54
2.2.1 Synthesis and characterization of hydrophobic MFe_2O_4 54
2.2.1.1 Synthetic procedures for size control of IONPs 54
2.2.1.2 Characterization of IONPs 58
2.2.1.3 Synthesis and size control of ZnSPIONs 62
2.2.1.4 Characterization of ZnSPIONs 65
2.2.2. Preparation and characterization of water soluble MFe_2O_4 69
2.2.2.1 Ligand exchange using 2,3-dimercaptosuccinic acid (DMSA) (DMSA-coated IONPs; IONP@DMSA) 69
2.2.2.2 Ligand exchange using polyethylenimine (PEI) (IONP@PEI) 72
2.2.2.3 Ligand addition using PEGylated phospholipids (PL-PEG) 75
2.2.3 Development of the multimodal imaging system 79
2.2.3.1 MR properties of IONP@PL-PEG micelles 79
2.2.3.2 Labeling IONP@PL-PEG micelles with Rhodamine-B dye 80

2.2.3.3 Labeling IONP@PL-PEG micelles with *fac*-$[M(OH_2)_3(CO)_3]^+$ complexes 82
2.3 *Conclusions* 88
References 90

Chapter 3: Development of IONP-filled PL-PEG micelles with immunostimulatory capacity

3.1 *Introduction* 100
3.1.1 General concepts of the immune system 100
3.1.2 Targeting pattern recognition receptors 103
3.1.3 Features of the vaccine adjuvant poly (I:C) 107
3.1.4 Interactions between NPs and the components of the immune system 109
3.2 *Results and discussion* 114
3.2.1 Attachment of poly (I:C) onto IONPs@PL-PEG amine micelles 114
3.2.1.1 Synthesis and characterisation 114
3.2.1.2 Immunostimulatory activity 118
3.2.2 Attachment of poly (I:C) onto IONP@PL-PEG methoxy micelles 120
3.2.2.1 Synthesis and characterisation 120
3.2.2.2 Immunostimulatory activity 124
3.2.2.3 Fluorescence microscopy: cellular uptake of the poly (I:C)-IONP@PL-PEG methoxy micelles 134
3.2.2.4 Bimodal detection of poly (I:C)-IONP@PL-PEG methoxy micelles 136
3.2.2.5 SPECT/CT and MR imaging: *in vivo* trafficking of the poly (I:C)-IONP@PL-PEG methoxy micelles 137
3.2.2.6 Studying the innate immune response 145
3.3 *Conclusions* 149
References 150

Chapter 4: Development of IONP-filled PL-PEG micelles for harnessing a platinum-based chemotherapy with an immune system attack on cancer cells

4.1 *Introduction* 160
4.1.1 Cancer therapies 160
4.1.2 Anti-tumor immune response 161
4.1.3 Cancer nanotechnology: targeting strategies 163
4.1.4 Development of cancer nanomedicine combining imaging and therapy 165
4.2 *Results and discussion* 169
4.2.1 Synthesis and Characterization of poly (I:C)-IONP@PL-PEG-Pt(IV) micelles 169
4.2.1.1 Synthesis and characterization of DSPE-PEG(2000)-Pt(IV) 169
4.2.1.2 Formation of poly (I:C)-IONP@PL-PEG-Pt(IV) micelles 175
4.2.2 *In vitro* and *in vivo* behavior of poly (I:C)-IONP@PL-PEG-Pt(IV) micelles 180

4.2.2.1 Cytotoxic activity of poly (I:C)-IONP@PL-PEG-Pt(IV) micelles in human cancer cell lines 180
4.2.2.2 Immunostimulatory activity of poly (I:C)-IONP@PL-PEG-Pt(IV) micelles in cells of the immune system 184
4.2.2.3 Immunostimulatory activity of poly (I:C)-IONP@PL-PEG-Pt(IV) micelles *in vivo* 190
4.2.2.4 *In vivo* trafficking of poly (I:C)-IONP@PL-PEG-Pt(IV) micelles 195
4.3 *Conclusions* 197
References 198

Summary of results 205
Experimental section 207
Appendix 235

Acknowledgements

First of all, I would like to thank Professor Juan C. Mareque-Rivas, my PhD director, for providing me the opportunity to develop this thesis under his supervision. Thanks for guiding and helping me when it was necessary. Thanks for teaching me that doing a job well doesn´t mean to do it fast but thoroughly, thinking and taking care of your work and maturing it somehow. I have learnt a lot during these years and I will always be grateful for it.

I would also like to thank all my colleagues in the lab during these years with special thanks to: Malou, Ane and Aintzane, thanks for your immunology classes and for letting this intruder fall in love a bit with biology. Luca, you are a great researcher, you have already demonstrated it and you will still showing it, thanks for teaching me that we must never give up and that hard work is your best cover letter. Javi, you are an important part of this work, thanks for your help and the good moments working together. Manu and Silvia, you both are great and your enthusiasm and happiness makes very easy being around you inside and outside the lab. Last chance of pizza pote!!!!!!Amaia, Anja and Abraha thanks for being part of this thesis and I wish you the best!!!!

Thanks to my "student room cuadrilla", I will always remember the laughters and the good moments we shared in this period (inside and outside the room) and the helps and efforts that we have made together. Aitor and Mikel G., I will miss you a lot!!!No more ELISA on Fridays Ane!!!!Especially thanks to Maria and Mikel, because these years would have been more difficult without your support and friendship.

I want to thank also to all the people in the centre that has worried for me or helped me at some point (Larraitz, Marta, Josune, Xabi, Carlos, David, Eunice, Ana Sánchez, Danijela, Zuriñe, Fernando, Paola, Juanjo, Eneko…..). Thank you!!

I lovingly thank Edu, who supported me each step of this long way. I know all your sacrifice for us and I could not have accomplished this without you. I cannot imagine a better partner. We have a long long way together in the future.

And last but not least because they come first to me, my family and my friends. Thank you for standing beside me, for supporting me with a call or visit and for making me see where are the important things in life. Thanks to my mom and dad for the values that they have transmitted me that are not taught in any school. Thanks to my brother, cousins and uncles because you were always there with positive energy. And in a very special way, thanks to my grandparents for the lessons of life and the love that I have always received from them.

And again…..THANK YOU SO MUCH TO EVERYONE!!!!!!

Abbreviations

acac	Acetylacetonate	**DOTA**	1,4,7,10-tetra-azacyclododecane-*N,N´,N´´,N´´´*-tetraacetic acid
AFM	Atomic Force Atomic Force Microscopy	**DOTAP**	1,2-dipalmitoyl-3-trimethylammonium-propane
APCs	Antigen presenting cells	**dsRNA**	Double-stranded ribonucleic acid
APTES	3-aminopropyltriethoxysilane	**DTPA**	Diethylenetriamine pentaacetic acid
AuNPs	Gold nanoparticles	**ECD**	Ectodomain
BFC	Bifunctional chelator	**EE**	Early endosomes
BMDCs	Primary bone marrow-derived dendritic cells	**e.g.**	Exempli gratia
°C	Celsius degrees	**ELISA**	Enzyme-Linked ImmunoSorbent Assay
ca.	Circa (around, about)	**emu**	Electromagnetic units
CCR7	Chemokine receptor type 7	**EPR**	Enhanced permeability and retention effect
CD	Circular Dichroism	**et al.**	Et alii (and others)
CD80/86	Cluster of differentiation 80/86	**FA**	Folic acid or folate
Cisplatin	*cis*-dichlorodiamminoplatinum (II)	**FDA**	Food and Drug Administration
COSY	Correlation spectroscopy	**Fig.**	Figure
CpG	Interaction cytosine-phosphate-guanine	**FT-IR**	Fourier transform infrared spectroscopy
CT	Computerized tomography	**g**	Gram
CTAB	Cetyltrimethylammonium bromide	**h**	Hour
D_H	Hydrodynamic diameter	**H_c**	Coercivity
DAMPs	Damage-associated molecular patterns	**IC_{50}**	Half maximal inhibitory concentration
DAPI	4',6-diamidino-2-phenylindole	**ICP-AES**	Inductively coupled plasma atomic emission spectroscopy
DCs	Dendritic cells	**ICP-MS**	Inductively coupled plasma mass spectrometry
DCC	Dicyclohexylcarbodiimide	**i.e.**	Id est (that is)
DLS	Dynamic light scattering	**IFNs**	Interferons
DMAP	4-(dimethylamino)pyridine	**IL-**	Interleukin-
DMEM	Dulbecco's Modified Eagle Medium	**i.m.**	Intramuscular
DMSA	2,3-dimercaptosuccinic acid	**IONPs**	Iron oxide nanoparticles
DNA	Deoxyribonucleic acid	**i.p.**	Intraperitoneal
DOSY	Diffusion ordered spectroscopy	**IR**	Infrared spectroscopy

ISCOMs	Immunostimulating complexes	**NLRs**	nucleotide oligomerization domain (NOD)-like receptors
i.v.	Intravenous	**NMR**	Nuclear magnetic resonance
i.t.	Intratumoral	**NOTA**	1,4,7-triazacyclononane-*N,N´,N´´,*-triacetic acid
k	Boltzmann´s constant	**NPs**	Nanoparticles
K	Particle anisotropy constant	**OAc**	Oleic acid
Kb	Kilobases	**OAm**	Oleylamine
KDa	Kilodalton	**Oe**	Oersted
keV	Kiloelectron volt	**O_h**	Octahedral sites
kT	Thermal energy	**PAMPs**	Pathogen-associated molecular patterns
KV	Magnetic anisotropy energy	**PBS**	Phosphate-buffered saline buffer
LC-ESI-MS	Liquid chromatography electrospray ionization mass spectrometry	**PC**	1-palmitoyl-2- oleoyl-*sn*-glycero-3-phosphocholine
		PL	Phospholipid
LNs	Lymph nodes	**PDT**	Photodynamic therapy
LRR	Leucine-rich repeats	**PEG**	Polyethylene glycol
M_s	Saturation magnetization	**PEI**	Polyethylenimine
mAb	Monoclonal antibody	**PET**	Positron emission tomography
MDA-5	Melanoma-differentiation-associated gene 5	**pg**	picogram
mg	Milligram	**poly (I:C)**	Polyinosinic:polycytidylic acid
MHC	Major histocompatibility complex molecules	**ppm**	Part per million
min	Minutes	**PRRs**	Pattern recognition receptors
mL	Milliliter	**PS**	Photosensitizer
mm	Millimeter	**QDs**	Quantum dots
mmol	Millimole	**RES**	Reticuloendothelial system
µg	Microgram	**Rhod**	Lissamine rhodamine B-modified phospholipid
µL	Microliter	**RIG-I**	Retinoic acid-inducible gene I
µm	Micrometer	**RLRs**	(RIG-I)-like receptors
mM	Millimolar	**ROS**	Reactive oxygen species
MPa	Megapascal	**s**	Second
MPS	Mononuclear phagocyte system	**s.c.**	Subcutaneous
MRI	Magnetic Resonance Imaging	**siRNA**	Small interfering RNA
MTT	3-(4,5-dimethylthiazol-2-yl)-2,5-diphenyltetrazolium bromide	**SPECT**	Single-photon emission computed tomography
mV	Millivolt	**SRB**	Sulforhodamine B colorimetric assay
MyD88	Myeloid differentiation primary-response protein 88	**t**	Time
NK cells	Natural killer cells	**$t_{1/2}$**	Half-life

Nm	Nanometer	**T**	Temperature
T_1	Longitudinal (or spin-lattice) relaxation time	**UCNPs**	Upconverting nanoparticles
T_2	Transverse (or spin-spin) relaxation time	**V**	Particle volume
T_d	Tetrahedral sites	**VLP**	Virus-like particles
TEM	Transmission electron microscopy	**VSM**	Vibrating sample magnetometry
TGA	Thermogravimetric analysis	**WHO**	World Health Organization
TLR	Toll-like receptor	**ζ**	Zeta-potential
TRIF	Toll/IL-1R domain-containing adaptor inducing IFN	**ZnSPIO**	Non-stoichiometric zinc ferrite
US	Ultrasound		

Abstract

The intrinsic properties of iron oxide nanoparticles (IONPs) make them attractive candidates for clinical applications that combine noninvasive imaging with therapy, which is an area of considerable current interest. In the area of infectious diseases and cancer, there is a growing interest in targeted activation of Toll like receptors (TLRs), which are key players in the innate immune system.

The increasingly important need for combining complementary imaging modalities (multimodal imaging) to overcome the intrinsic limitations of each single technique and of using molecular imaging in drug development has triggered our interest in developing multimodal imaging probes which could be applied for efficient stimulation of the immune system against infectious diseases and cancer. Besides the possibility of using nanoparticles (NPs) with multimodal imaging features for drug discovery and development, the possibility of incorporating different complementary drug payloads in nanosystems could potentially lead to enhanced efficacy of conventional therapies.

In this thesis we present an IONP-based self-assembled nanoconstruct (IONP-filled micelles prepared from hydrophobic IONPs and PEGylated phospholipids; IONP@PL-PEG) which combines multimodal imaging capabilities with immunological and anticancer activity. For fluorescence imaging *in vitro* the IONPs incorporated rhodamine-labeled PLs and for *in vivo* SPECT imaging they were radiolabeled with ^{99m}Tc tricarbonyl. Immunological activity is induced by decorating with polyinosinic:polycytidylic acid poly (I:C) the IONP@PL-PEG micelles; a synthetic mimic of viral double-stranded RNA (dsRNA) recognized by Toll like receptor 3 (TLR3) which has been recently shown to have both anticancer activity and adjuvant effects on mammalian immune responses.

The anticancer activity, however, is provided by the attachment of a Pt(IV) cisplatin prodrug as a chemotherapeutic agent. The succinic acid-derivatized Pt(IV) complex *cis, cis, trans*-[$Pt(NH_3)_2Cl_2(O_2CCH_2CH_2CO_2H)_2$] as cisplatin prodrug is conjugated to the amine end group of a commercially available phospholipid with a PEG2000 moiety (DSPE-PEG(2000)-NH_2) via DCC-mediated coupling reaction. The association of poly (I:C) with a Pt(IV)-functionalized water soluble micelles with encapsulated IONPs inside (poly (I:C)-Pt(IV)-IONP

micelles) provides a promising double functionalization with chemotherapy and immunostimulatory drugs in a single system.

The poly (I:C)-Pt(IV)-IONP nanoconstruct is capable of efficiently presenting and specifically delivering poly (I:C) to endosomal TLR3 in cells of the immune system to trigger potent immune responses and possesses the ability to induce cytotoxic activity against different human cancer cells via intracellular reduction of the Pt(IV) prodrug to cisplatin.

We also show that this pathogen-mimetic construct can be tracked *in vitro* and *in vivo* in real time using three complementary imaging modalities: fluorescence microscopy, SPECT and MRI. The combination of SPECT/MRI reveals effective lymphatic trafficking of the multifunctional nanoconstruct, which is a desirable feature for targeted chemoimmunotherapy.

Resumen

Las nanopartículas (NPs) llevan siendo consideradas como vehículos de transporte de fármacos desde hace más de 30 años. La estabilidad, la capacidad de mejorar las propiedades de la carga que transportan y el control sobre las propiedades físico-químicas, son entre otras, las principales ventajas del uso de la nanotecnología en la administración de fármacos. Sin embargo, actualmente la aplicación de la nanotecnología no se limita únicamente a la administración de fármacos y es una herramienta importante para aplicaciones biomédicas muy diversas. Actualmente existe gran interés en el desarrollo de nanomateriales multifuncionales que se puedan utilizar tanto para diagnóstico como para terapia. En concreto, el concepto de agente teragnóstico (terapia + diagnóstico) a través de nanomateriales se postula como sumamente eficaz en el tratamiento y diagnóstico simultáneo de patologías de elevada morbi-mortalidad como el cáncer.

La administración de fármacos mediado por nanopartículas ha emergido como una metodología potente para el tratamiento de diversas enfermedades, como el cáncer o enfermedades infecciosas. El índice terapéutico de los medicamentos tradicionales puede ser mejorado a través del aumento de especificidad debido a la focalización de medicamentos a un tejido, célula o compartimiento intracelular en particular, al control sobre la cinética de liberación, a la protección del agente activo o una combinación de todas ellas gracias al uso de nanopartículas.

La aplicación de la nanotecnología en la investigación sobre el cáncer centra el concepto terapéutico de la nanomedicina en la necesidad de encontrar tratamientos más eficaces que los actuales. Uno de los retos más importantes de la nanotecnología en el tratamiento del cáncer es la posibilidad de destruir las células cancerosas pero causando un daño mínimo a los tejidos y órganos sanos. El transporte de fármacos antitumorales se divide en dos estrategias: el aprovechamiento de las características fisiológicas de tumores sólidos que permite la acumulación pasiva de NPs en los tumores y/o la decoración de las NPs con moléculas con afinidad específica para las células cancerosas.

El destino de las nanopartículas dentro del cuerpo está determinado por sus propiedades físico-químicas, tales como el tamaño, la forma y la carga superficial. Estas propiedades controlan el tiempo de circulación en el interior de los vasos sanguíneos, la biodistribución y cómo de rápido las nanopartículas serán eliminadas por el organismo.

Las nanopartículas de óxido de hierro (IONPs) pertenecen a una clase de materiales inorgánicos que están compuestas por un núcleo magnético que puede estar recubierto por materiales inorgánicos u orgánicos. Las propiedades físicas únicas de las nanopartículas magnéticas como agentes de contraste en resonancia magnética molecular (RMI) les convierten en una nueva clase de sondas de diagnóstico. Además han mostrado un gran potencial para el transporte de fármacos y/o terapias controladas por la aplicación de campos magneticos. Las IONPs se pueden funcionalizar con moléculas que permitan el reconocimiento selectivo de células mediante la unión a los receptores que se expresan en las membranas de células diana, incluyendo grandes biomoléculas (ácidos nucleicos, proteínas, ...). En el caso de las células cancerosas que sobre expresan receptores específicos distintos de las células normales, el uso de estas moléculas diana es un método ampliamente utilizado.

A lo largo de esta tesis, las nanopartículas hidrofóbicas de óxido de hierro fueron utilizadas como núcleo del sistema. Sin embargo, es necesario cubrir la superficie de estas nanopartículas para hacerlas solubles en medios acuosos cuando se considera un potencial uso en el campo biomédico. Hay varias estrategias y ligandos para la estabilización de materiales hidrófobos en medio acuoso, pero probablemente los ligandos de recubrimiento de superficies más ampliamente utilizados son los polímeros anfifílicos como los fosfolípidos tipo PEG (contienen en su estructura un poliéter ampliamente utilizado llamado polietilenglicol). En este trabajo, las IONPs se encapsularon utilizando fosfolípidos PEGilados con diferentes grupos funcionales formando micelas que contienen IONP en su interior (micelas IONP@PL-PEG).

El desarrollo de un sistema de administración de fármacos con actividad inmunológica y anticancerígena con capacidad de proyección de imagen multimodal es el principal objetivo de esta tesis. El proceso de síntesis, caracterización y el éxito de este objetivo se discute a lo largo de cuatro capítulos.

El **capítulo uno** ofrece una visión general sobre los principales temas que luego se desarrollarán a lo largo de la tesis. Una introducción a los sistemas de administración de fármacos a escala nanométrica y su aplicación en el campo de la nanomedicina.

La tesis se divide a continuación en tres partes interrelacionadas. La primera parte se centra en la síntesis y diseño de nanopartículas de óxido de hierro solubles en agua (IONP) para crear un agente de contraste trimodal (MRI-SPECT-óptica) en un único sistema. El desarrollo y la caracterización de las nanopartículas hidrofóbicas e hidrofílicas se discuten en detalle en el **capítulo dos**.

La segunda parte se centra en el diseño, la preparación y el comportamiento de micelas de IONPs cargadas con una molécula inmunoestimuladora (poly (I:C)) para activar una respuesta inmune potente *in vitro* e *in vivo*. Los resultados de estos estudios se presentan en el **capítulo tres**.

La última parte se discute en el **capítulo cuatro**. Las micelas de IONP se cargan con un complejo de Pt (IV) inerte que actúa como profármaco de cisplatino y con el poly (I:C) como agente inmunoestimulador para combinar los efectos de dos terapias complementarias para matar células tumorales *in vitro* e *in vivo*.

Las nanopartículas magnéticas discutidas en esta tesis fueron preparadas de un tamaño adecuado para poder ser transportadas por los vasos linfáticos, el cual se describe en la literatura entre los 10 y los 80 nm. En este sentido, el nanosistema es capaz de migrar desde el sitio de la inyección a los ganglios linfáticos (LNs) a través del sistema de vasos linfáticos. El tráfico linfático eficiente es especialmente útil en tratamientos de inmunoterapia del cáncer de tumores metastásicos, no solo porque los LNs son centros de movilización y coordinación de la respuesta inmune ante una infección o un tumor, sino porque el cáncer metastático deriva en gran parte de la diseminación (metástasis) a los LNs.

Las micelas de IONPs se marcaron con un fosfolípido modificado con rodamina B disponible en el mercado para proporcionar al sistema con capacidades de formación de imágenes ópticas. A continuación, el poly (I:C) se incorporó a las micelas mediante interacciones no covalentes logrando el sistema denominado como micelas poly (I:C)-IONP@PL-PEG.

La incorporación de fluorescencia en el sistema nos permitió demostrar mediante imágenes de microscopía que el sistema es capaz de alcanzar los compartimentos endosomales diana *in vitro*, lo cual es necesario para desencadenar a través del receptor TLR3 las cascadas de señalización intracelulares que pueden inducir una respuesta inmune.

La capacidad de las micelas poly (I:C)-IONP@PL-PEG de activar las células del sistema inmune se investigó *in vitro* en macrófagos y en células dendríticas derivadas de médula ósea (BMDCs), dos de los tipos de células implicadas en la defensa del sistema inmune. En la segunda parte de la tesis se demuestra que la activación de las células y la posterior secreción de citoquinas son varios órdenes de magnitud mayor cuando la molécula inmunoestimulante poly (I: C) se conjuga con las micelas IONP que cuando el fármaco se incuba solo con las células.

En la tercera parte, un Pt(IV) profármaco se une covalentemente a la micela, las micelas IONP@PL-PEG-Pt(IV) inducen mayor aumento en la secreción de citoquinas en comparación con las micelas poly (I:C)-IONP@PL-PEG cuando ambos sistemas se incuban con células dendríticas. Debido a que el control de las micelas IONP y las drogas (profármaco de Pt (IV) y cisplatino) no producen ninguna actividad, el resultado sugiere que es debido al transporte del profármaco Pt (IV) a través de la micela de IONP.

Los resultados observados *in vivo* sugieren que las micelas poly (I:C)-IONP@PL-PEG-Pt(IV) pueden penetrar en el espacio intersticial alrededor del lugar de inyección y son absorbidos gradualmente por los capilares linfáticos al sistema linfático. La migración de las construcciones se confirmó *in vivo* utilizando MRI, SPECT y citometría de flujo. Mediante MRI fue posible realizar un seguimiento de la presencia de las micelas poly (I:C)-IONP@PL-PEG en los órganos linfoides por dos rutas diferentes de administración, aprovechando las propiedades magnéticas intrínsecas del núcleo de las micelas.

El uso de tomografía computarizada de emisión de fotón único (SPECT / CT) confirmó también el tráfico de las micelas a lo largo del sistema linfático *in vivo*. El agente radioactivo *fac*-$[^{99m}Tc(OH_2)_3(CO)_3]^+$ se usó para marcar las micelas poly (I:C)-IONP@PL-PEG con y sin el profármaco Pt (IV) y se inocularon por diversas vías de administración, incluidas la inyección intratumoral. La entrega eficiente y la acumulación dentro de los LNs de drenaje sugieren que el sistema podría actuar como actúan las vacunas para inducir una respuesta inmune

efectiva. Por otro lado, la acumulación que se observa en el tumor podría implicar que se podrían inyectar dosis más bajas de agente terapéutico, reduciendo así los efectos secundarios.

Mediante citometría de flujo se analiza la maduración de las BMDCs en los órganos linfáticos (ganglios linfáticos de drenaje y bazo). La maduración de la BMDCs se evaluó a través del aumento en la expresión de marcadores de superficie específicos, tales como CD80 y CD86 cuando las células se incubaron con las micelas poly (I:C)-IONP@PL-PEG con y sin el profármaco de Pt (IV) durante 24 h. La maduración de las células dendríticas es uno de los requisitos necesarios para promover la activación del sistema inmune para reconocer y destruir las células cancerosas. De esta forma se abriría otra puerta a una terapia contra el cáncer que está cada vez más reconocido en la medicina práctica, que consiste precisamente en ayudar a estimular las defensas naturales del cuerpo para combatir el cáncer y se conoce como inmunoterapia contra el cáncer.

1

General Introduction

This chapter briefly covers the increasing relevance of nanotechnology in the development of promising drug delivery systems, its use in molecular imaging and how nanoparticles can be used to modulate immune responses in the context of immunotherapy and developing vaccines.

1.1 Nanotechnology in Medicine: Drug Delivery

In 1959, six years before receiving the Nobel Prize, Richard Feynman gave a lecture with the now famous title "There is plenty of room at the bottom" which laid the foundations for what later became known as nanotechnology.[1] Since then, several definitions have been used to describe the term Nanotechnology and still nowadays, there is no universal definition for this field of science.[2] However, definitions of nanotechnology include two common criteria: the size scale (roughly in the 1-100 nm size range) and the unique properties that the nanoscale confers. In general terms, nanotechnology is about the design, characterization, production and application of structures, devices and systems by controlling shape and size at the nanoscale. This specific control of the size at the nanometer scale is the difference between nanotechnology and other areas of technology.

The area of nanotechnology has developed and expanded rapidly in the last thirty years and there are many different sectors benefiting from nanotechnology (communications, engineering, robotics, etc.). Among the multidisciplinary scientific fields where nanotechnology is involved with millions of dollars invested per year,[3] the application of nanotechnologies in medicine, known as nanomedicine, is a promising and rapidly growing field.[4] Areas such as disease diagnosis, targeted drug delivery, and molecular imaging are being intensively investigated and some nanotechnology-based products are already undergoing clinical trials.[5,6]

Some features of nanoscale materials that have contributed to their rapid expansion in the pharmaceutical and biomedical field as drug delivery vehicles are:

1. Improving the properties of the therapeutic payload. The absorption or encapsulation of drugs into these delivery vehicles can improve the solubility of poorly-water soluble drugs and the stability of drugs that may be degraded chemically or enzymatically.
2. Large surface area. This property underpins the possibility of functionalizing nanomaterials for different applications by attachment of both small molecules and large macromolecules, providing multivalent structures and the combination of multifunctional compounds in a single system, such as two or more therapeutic drugs.

3. Targeted delivery of drugs to specific cells, organs or tissues in the body. An advantage of using nanocarriers is in the ability of developing suitable drug delivery systems that take the therapeutically active drug molecule only to the site of action, without affecting healthy organs and tissues. [7]
4. Simultaneous integration of diagnosis and therapy. The possibility of combining therapeutic agents with molecular imaging modalities (due to the intrinsic properties of the nanomaterial or the addition of imaging agents) in a single system allows their visualization in the specific site of action.
5. Monitoring the real-time efficacy of a therapeutic agent. Nanoscale systems that can act like imaging agents provide information about the targeted site and the evolution of the tissue being treated.[8]

Nanotechnology can play an important role in the development of new drugs/therapies.[9,10] Nanocarriers can enhance the efficacy of the therapeutic drugs which as free agents are limited due to high cytotoxicity, degradation or rapid clearance by the body. Using nanocarries these drugs can therefore be administered at lower doses with improved accumulation at target sites and reduction of severe side effects.

The site-specific drug delivery can be developed either through **i)** active or **ii)** passive targeting approaches.[11–14] **i)** Nanocarriers can be modified with ligands which have selective affinity for specific receptors overexpressed in target organs, tissues or cells. A variety of molecules including peptides, antibodies, carbohydrates and nucleic acids can be used as targeting moieties. This specificity is one of the most promising features of nanocarriers over other drug delivery systems. **ii)** On the other hand, by passive targeting approaches, drug delivery systems accumulate at their target due to their physicochemical properties, such as size, morphology or surface charge. This effect was first reported by Matsumura and Maeda in 1986 and it is usually favored by the differences between normal tissue and the diseased tissue.[15] One of main paradigms of passive targeting is the accumulation of nanoparticle in tumors due to the enhanced and permeability retention (EPR) effect. The blood vessels in many tumor types are irregular in shape and present greater permeability compared with normal vessels, which means that nanocarriers can permeate through the leaky tumor vessels and be retained at the tumor site.

1.2 Nanoconstructs for drug delivery applications

A wide variety of nanocarriers including polymeric nanomaterials, liposomes, dendrimers, micelles, NPs based on biological molecules and inorganic nanomaterials have been developed for drug delivery applications due to their biocompatibility, controlled size and shape, high drug loading capacity **(Fig. 1.1)** and other intrinsic properties such as light harvesting, superparamagnetism etc.[16] Liposomes were the first NPs used as drug delivery systems in 1960,[17] but since then all of these platforms among other applications, have been tried for therapeutic purposes.[10]

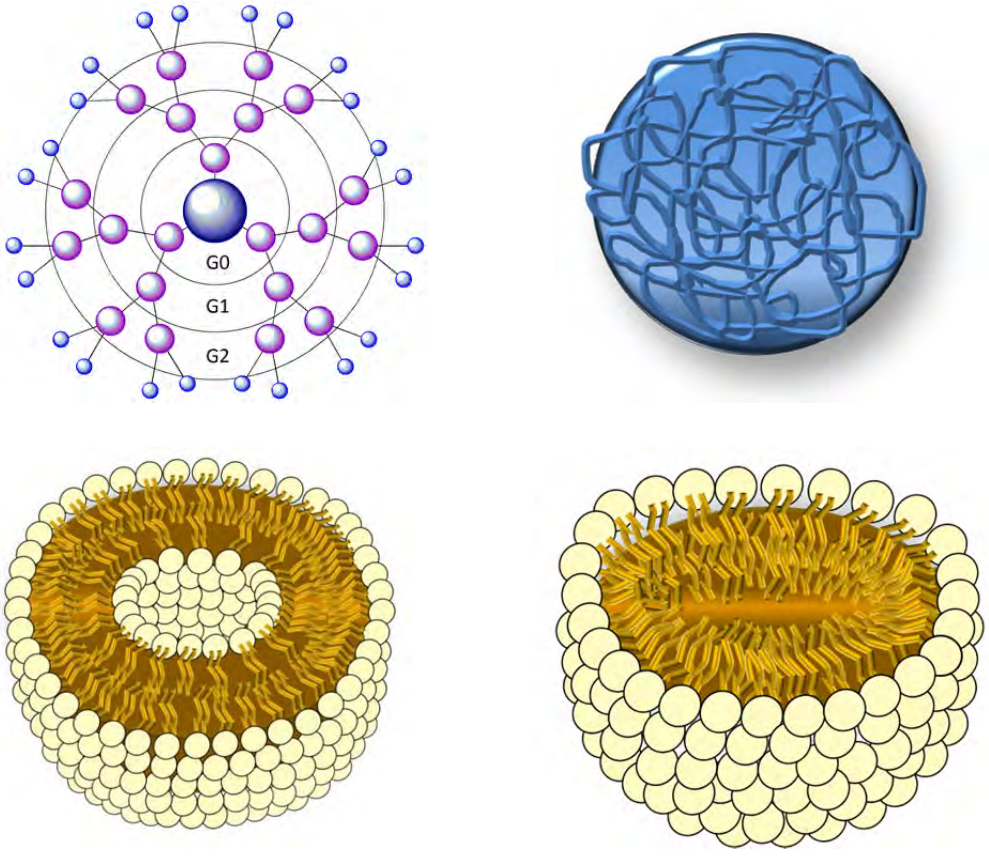

Fig. 1.1. Schematics of different nanotechnology based drug delivery systems. **a)** Typical architecture of a second generation dendrimer; **b)** Polymer nanoparticle; **c)** Liposome; **d)** Micelle.

These nanocarriers are usually structured in three main components: 1) a nanoparticle core which can encompass hydrophobic and/or hydrophilic material, 2) a

surface which can be modified with targeting moieties or certain functional groups and 3) a therapeutic payload. Nanoscale delivery systems can be based on organic or inorganic materials or hybrids structures and all of these components and materials are included in the term nanoparticle.[18]

Different synthetic or natural polymeric materials are used for preparing drug delivery materials. Polysaccharides (chitosan, dextran etc.), polyethylene glycol (PEG) or poly(vinylpyrrolidone) (PVP) are widely used.[19] A key requirement for clinical translation is to be non-toxic, biocompatible and biodegradable. Furthermore, inorganic NPs (iNPs) can be incorporated (or be transported) into these polymeric materials: gold nanoparticles (AuNPs), iron oxide nanoparticles (IONPs) or silica nanoparticles are some examples of the variety of materials available.[20] This hybrid materials have exhibited improved properties compared to typical NPs, such as biocompatibility, versatility, stability or an increase in the circulation time in the blood stream after injection.[21]

The case of the iron oxide-based materials is particularly attractive because of their unique features such as biocompatibility and superparamagnetism.[22] IONPs can be loaded within liposomes, micelles or dendrimers, among other types of delivery systems or can be coated with organic or inorganic materials, such as surfactants or polymers and silica.[23–26] Versatile IONPs can be prepared by surface modification and further functionalization with several types of biomolecules or drugs, such as nucleic acids, proteins or chemotherapeutics, which makes these inorganic materials very attractive in the therapeutic field. The choice of IONPs has the added advantage that the body can process iron naturally. Iron is stored in the protein ferritin (a bioinorganic hybrid nanoparticle) and can be metabolized to end up in hemoglobin/myoglobin where it can be used for oxygen transport in red blood cells/muscle tissue, in iron-dependent enzymes etc .[27]

The magnetic properties of IONPs make them ideal contrast agents for magnetic resonance imaging (MRI). Although there are other NPs available with similar or superior magnetic properties than IONPs,[28] they encompass many desirable characteristics, such as biocompatibility, stability, imaging capabilities and the possibility of modulating their surface according to the chemical needs that make them ideal nanocarriers for many biomedical applications.[22,29,30]

The use of IONPs in theranostics (combination of diagnostic and therapeutic capabilities into a single agent) applications has experienced a significant progress in recent years.[31] In diagnosis, their magnetic properties focused the use of IONPs as contrast agents for MRI, while on the therapeutic field, hyperthermia, photodynamic therapy (PDT) and drug delivery are some of the most widespread applications.

1. Hyperthermia is an attractive option and probably the most common therapeutic application of IONPs.[24] When the IONPs are heated by an external alternating magnetic field, the increase in the temperature above 42 °C promotes cell death. Hyperthermia has already been tested in cancer treatment with promising results, because cancer cells are more sensitive to high temperatures than normal cells and in the mentioned temperature normal cells are not injured.
2. The conjugation of IONPs with a photosensitizer (PS) has promoted their use for photodynamic therapy (PDT).[32] The activation of the PS with light at a specific wavelength, cause the drug reacts with molecular oxygen to generate singlet oxygen and other reactive oxygen species (ROS) leading to tumor cell death.
3. IONP-based delivery can play a significant role in biomedical applications such as gene therapy or cancer treatment.[33] The therapeutic drugs are coupled to IONP to enhance delivery or uptake by target cells and kill cancer cells, reducing the toxicity in non-target cells/organs.

1.3 Nanomaterials in medical imaging technologies

Inorganic nanoparticles are especially interesting for both imaging and therapeutic purposes, due to their intrinsic imaging capabilities which allow their monitorization and the delivery of therapeutic molecules simultaneously.[34–36] Gold nanoparticles (AuNPs),[37] iron oxide nanoparticles (IONPs)[38] and quantum dots (QDs) as semiconductor nanocrystals[39] are examples of iNPs with inherent imaging properties (plasmonics, superparamagnetism, size and composition dependent fluorescence emission) that are being investigated to explore their potential for use in molecular imaging applications **(Fig. 1.2)**.

In addition to these intrinsic imaging properties, it is possible to encapsulate, adsorb or conjugate additional imaging agents, like fluorophores or radionuclides, to achieve the desired imaging properties or to generate a system with multimodal imaging capabilities.

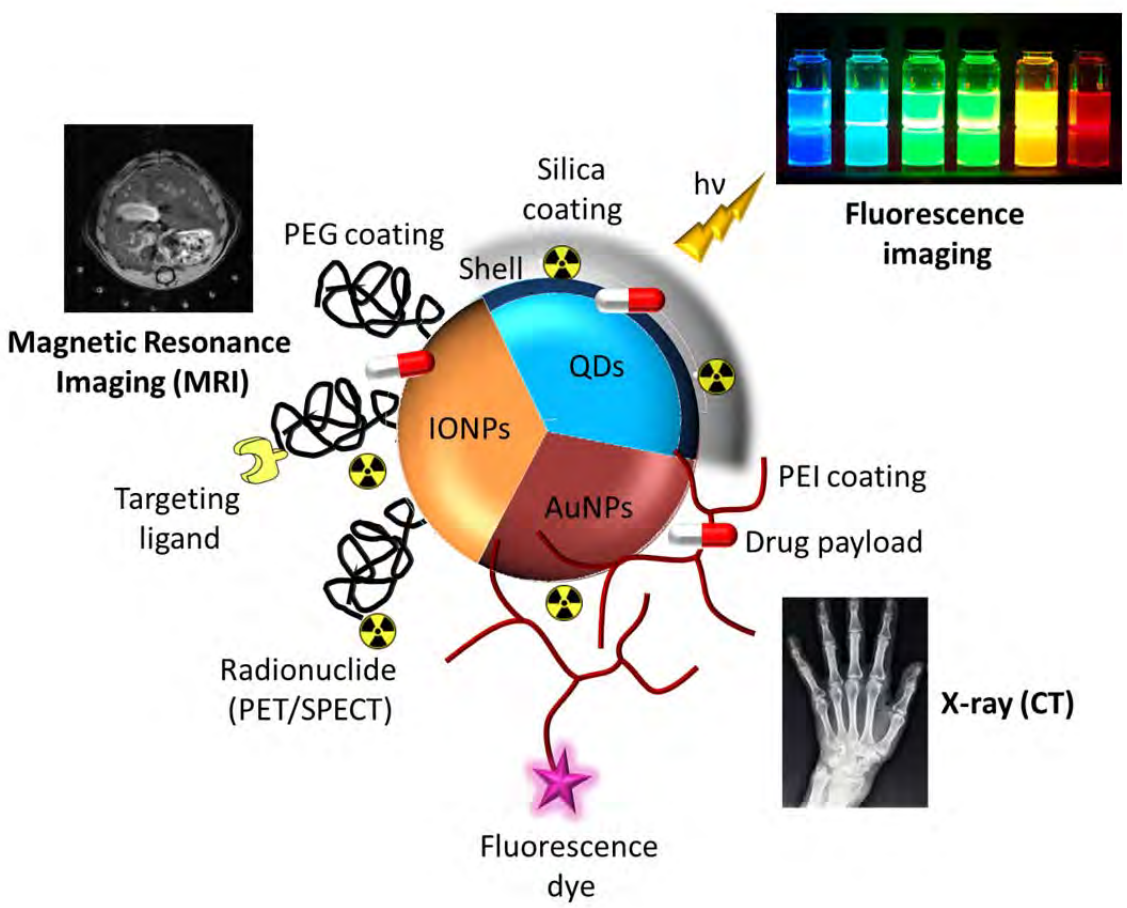

Fig. 1.2. Illustration of multifunctional nanoconstructs consisting of inorganic nanoparticles cores with their corresponding intrinsic imaging capabilities. Organic functional coatings and different biomolecules can be conjugated to the surface of the NPs, including fluorophores and radionuclides. The drug delivery function is represented with the therapeutic payload.

Imaging techniques play an important role in preclinical research, including stem cell-based therapies (e.g. for tracking of transplanted cells), cancer research (e.g. sequential analysis of metastasis) or investigation of vascular disorders (e.g. ischemia, infarction and atherosclerosis).[40] Preclinical imaging has an important role in drug development, for instance *in vitro* to elucidate the cellular target localization and *in vivo* in elucidating the

biodistribution and clearance of the drug or monitoring the therapeutic response of the new drug.[41]

Optical, magnetic resonance and radionuclide imaging are three complementary imaging technologies that can benefit from NPs in preclinical studies. The possibility of combining different molecular imaging techniques in a single construct leads to complementary information and synergistic advantages while allows to overcome the intrinsic limitations of each imaging modality.[36,42,43]

1. Optical Imaging

Optical imaging is a non-invasive technique that involves the detection of light photons transmitted through tissues. For some applications conventional fluorophores (fluorescent dyes or proteins) are being replaced by NP-based light emitters (QDs or upconverting nanoparticles, UCNPs) with unique photoluminescence properties.[44]

Additionally, the wide range of available organic dyes can be used to fluorescently label NPs which are not intrinsically fluorescent. The general strategies for generating fluorescent NPs in this way consist of encapsulation, covalent conjugation or application of non-covalent chemistry.[45] Whereas the versatile chemistry that can be used for incorporation of fluorescent dyes in NPs is an advantage, the fluorescence intensity and photobleaching are two problems often encountered for optical imaging of NPs using these labeling procedures.

2. Magnetic Resonance Imaging (MRI)

Magnetic resonance imaging is a non-invasive imaging technique used for visualizing soft tissues in the body.[46] MRI is a diagnostic technique based on interactions between the nuclei of hydrogen atoms (protons) in water molecules within the body and a powerful magnetic field. [47]

The body is able to be influenced by an external magnetic field due to the presence of protons in living tissue containing water molecules (approximately 80 % of our body). The inherent difference in relaxation times between biological tissues[48,49] (because the concentration of water in each tissue can be different or for instance, due to the presence of iron in the liver, which influences the contrast of MR images compared with other organs in

the body) or between normal and pathologic tissue not always is enough to obtain a desirable contrast in MRI.[50] For this reason, there is considerable need for developing exogenous MR contrast agents.

MRI contrast agents, as T_1 positive contrast agents or T_2 negative contrast agents, can improve the sensitivity of MRI by increasing the contrast of the target from the background. Contrast agents act selectively reducing T_1 or T_2 relaxation times of tissue water through the interaction between the electron spins of the contrast agent and the water protons present in the tissue. Superparamagnetic iron oxide nanoparticles (SPIONs) have been extensively investigated as T_2 contrast agents.[51] SPIONs provide darker MR images of target tissues and there are several products commercialized and used already in clinics based on SPIONs. On the other hand, T_1 imaging typically uses as contrast agents paramagnetic materials which provide bright contrast where they are localized. Although ultrasmall iron oxide nanoparticles (around 3 nm of diameter) can be used as T_1 contrast agents, gadolinium-based species are the prevailing T_1 contrast agents in clinical use.

3. Radionuclide Imaging

Nuclear imaging is a branch of medical imaging that uses radioactive isotopes (also known as tracers) to provide diagnostic information about the functionality of organs within the body, or to treat them. The two main techniques are PET (Positron Emission Tomography) and SPECT (Single Photon Emission Computed Tomography). Compared with other imaging modalities, SPECT and PET possess better sensitivity and have no tissue penetration limits.[52]

The tracers used in SPECT emit gamma radiation that is measured directly, whereas the radionuclides used in PET are positron emitters and their gamma rays emission is not direct. The decay of a positron emitter produces a positron (electron´s antiparticle), which travels depending on its energy a certain distance. When this positron interacts with an electron of a surrounding atom, two gamma photons are emitted with 511 keV each and emitted at 180 ° to each other ($e^- + e^+ \rightarrow \Upsilon + \Upsilon$). The collision between positron and electron is known as annihilation. PET measures the resulting two gamma photons emitted.

It is important to remark that radionuclides are always administered at doses free of pharmacological side effects.[53] Various positron-emitting isotopes are commonly used as PET isotopes, including ^{18}F, ^{15}O, ^{13}N, ^{11}C, ^{14}O, ^{124}I, and ^{68}Ga, and most isotopes are produced in a cyclotron. The short half-live of many of these isotopes (^{18}F = 109.74 min., ^{15}O = 122.24 seconds, ^{13}N = 9.97 min., ^{11}C = 20.38 min.) requires a cyclotron source close to the imaging facility of the hospitals or research institutes.[54]

For SPECT imaging, there is also a wide range of isotopes available, including ^{99m}Tc, ^{131}I, ^{123}I or ^{111}In, usually with higher half-lives than PET radiotracers.

The option of incorporating radioactive isotopes into nanoconstructs opens up the possibility of combining complementary imaging techniques in a single system, such as MRI/SPECT for radiolabeled IONPs or PET/NIR imaging for radiolabeled inorganic fluorescence nanocrystals. Development of new nano-systems with multimodal imaging capability is one of the objectives of this thesis.

1.4 Nanoparticles engineered to modulate immune responses

The immune system protects the body from those agents that can cause disease, so-called pathogens (including viruses, bacteria, fungi, protozoa etc.). The immune system´s function is fine-tuned to maintain host integrity against internal or external challenges and can be inhibited (immunosuppression) or stimulated (immunostimulation) when needed. Vaccines and cancer immunotherapies attempt to stimulate the immune system to fight infections or destroy tumors, whereas a desirable immunosuppression is beneficial for the treatment of autoimmune diseases, transplantations or prevention of allergic reactions, among others.

Nanoparticles can be engineered either to avoid immune recognition or to specifically interact and work with the immune system. An interaction between a nanoparticle and the immune system can be considered desirable when it may lead to beneficial medical applications, such as vaccines or immunotherapeutics for cancer treatment.

Vaccines mimic pathogens (but do not cause the disease) and to be effective they must evoke the appropriate immune response. The substances used to trigger these specific immune responses are the antigens present on the surface of pathogens. The goal of vaccination is the generation of a strong immune response against the administered antigen able to provide long-term protection against infection.

At cellular level, when the body is infected by a pathogen, it responds by activating a variety of immune cells **(Fig. 1.3)**.[55] Initially, the antigen is processed and digested by antigen presenting cells (APCs) into small pieces (peptides), which bind to the major histocompatibility complex (MHC) proteins on the surface of the APCs. Then, this complex formed by a foreign peptide and MHC protein, binds to a T cell receptor present on the surface of other type of immune cell, the CD8 cytotoxic T cell or CD4 helper T cell. The cytotoxic T cells travel throughout the body and when they detect a cell bearing their target antigen, cytotoxic T cells lyse that cell and hence, kill the cells infected by the foreign substance. The helper T cells can activate antigen-specific B cells to produce antibodies, which can neutralize and help to eliminate pathogens from the body. Some of the T and B cells in charge of fighting against infectious organisms become long-lived "memory" cells. The memory capacity allows the confrontation with the same infectious organism at posterior times.

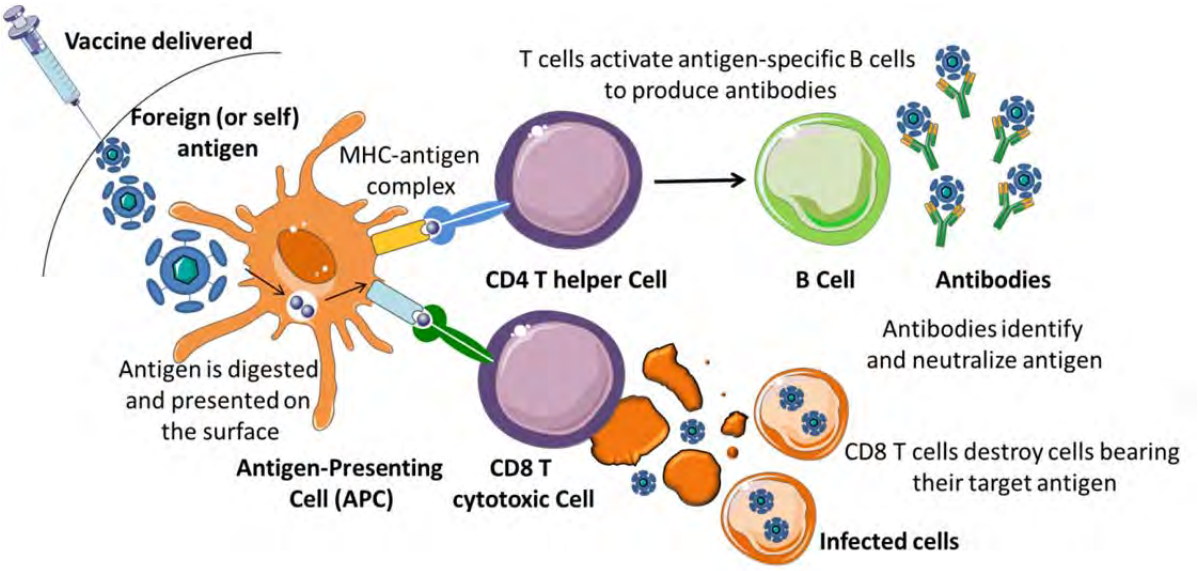

Fig. 1.3. Response to a vaccine. When the APCs find the vaccine antigen, engulf and digest it, displaying a piece of the antigen on its surface. APCs migrate to lymph nodes where specific CD4 T helper cells recognize the antigen as foreign and become activated. Some T cells activate B cells to transform in plasma B cells, which produce antibodies specific to the vaccine antigen. Each antibody attaches to one specific target antigen (like a lock and a key). That process prevents the antigen from entering a cell and developing the disease. If CD8 T cytotoxic cells are activated, they will traffic through the body looking for infected cells with their target antigen and they will destroy them.

A vaccine can be prophylactic to prevent the risk of future infection by a pathogen, or therapeutic such is the case of cancer vaccines. But to achieve these objectives it is often required the addition of compounds that enhance the specific immune response against the inoculated antigens, known as adjuvants.[56,57] Thus, an immunologic adjuvant is defined as any substance that acts to accelerate, prolong or enhance antigen-specific immune responses, but is not immunogenic itself. The two main purposes of adjuvants are: to enhance the immunogenicity of antigens and reduce the amount or the number of immunizations of antigen needed for obtaining protective immunity. In summary, adjuvants are intended to improve the efficacy of vaccines.

A number of mechanisms through which adjuvants mediate their activity have been postulated.[58,59] **(1)** Depot effect. The formation of a depot at the site of injection provides a prolonged and slow release of antigen/adjuvant at the site of injection, which increase

recruitment and activation of APCs. **(2)** Up-regulation of cytokines and chemokines. Particulate adjuvants can create a local pro-inflammatory environment to recruit immune cells. Furthermore, chemokines play a critical role in tissue specific migration of immune cells and have been shown to be up-regulated by adjuvants at the injection site. **(3)** Activation through targeted ligands for pattern recognition receptors (PRRs), for instance through toll-like receptors (TLR) ligands (MPL binds to TLR4, dsRNA binds to TLR3,…) the immune response is induced. **(4)** Maturation and activation of immune cells. Increasing the expression on MHC class II, or cell maturation markers leads to enhance ability of APCs to induce T lymphocyte activation and differentiation.

The traditional vaccines are based on live viruses that have been attenuated (that is, weakened or altered so that they do not to cause illness), killed organisms or viruses, inactivated toxins or simply components of the pathogens. Conventional vaccines are undoubtedly the most effective tools for infectious diseases prevention and eradication nowadays. However, there are many diseases for which effective vaccines are yet to be developed and other diseases where the effectiveness of current vaccines needs to be improved (e.g. to overcome the dangers associated with live attenuated pathogens).

The use of NPs as vaccine delivery vehicles has received much attention in recent years as promising candidates for improving vaccine formulation, mainly their efficacy, safety and stability.[60] NPs have demonstrated to be promising platforms in both prophylactic[60,61] and therapeutic[62–64] approaches.

Nanomaterials including liposomes, virus-like particles (VLP), polymeric nanoparticles or immunostimulating complexes (ISCOMs) have been studied as delivery vehicles for different vaccine components.[56] The possibility to act by themselves as adjuvants or to encapsulate or decorate the NP with an antigen and an adjuvant in a single system is also attractive to facilitate the engulfment of both components by the same cell.[65–68] Furthermore, NPs can avoid the degradation of the biomolecules upon injection and induce a long-lived immune response.

It has been reported that the use of nanomaterials can increase the uptake by cells compared with free molecules.[69] However, there are several NP properties such as the particle size, surface functional groups or surface charge, that can affect the uptake by the

APCs (an other types of cells involves in the immune response) and affect the subsequent immune response induced.[70] Lymph nodes (LNs) are one of the target organs for vaccine delivery, because T and B cells among other important cells of the immune system, reside in LNs. The size is a crucial parameter related with the biodistribution of antigen delivery systems and with their ability to target APCs.[71] The adequate control of the size together with the site of injection are considered key parameters controlling the efficacy of vaccine delivery carriers.[72,73]

Furthermore, dimension and structure of vessels in the body establish size limitations on carrier design. After subcutaneous or intramuscular administration, particles with size of 20-100 nm can penetrate the extracellular matrix and enter directly into the lymphatic vessels. Then, the particles can travel to the LNs, where NPs are taken up by the resident dendritic cells (among the APCs, dendritic cells (DCs) are considered the professional APCs) and generate the effective immune response. If NPs are smaller than 20 nm, they will be eliminated directly from the body through the blood capillaries, although some fraction can reach LNs as well. And finally, if the size of the particles is larger than 100 nm, they cannot cross the extracellular matrix and reach LNs directly. However, the peripheral DCs can capture the NPs, migrate to the LNs and initiate the immune response. [74] Several studies have shown that immunization with NPs in the range of 20-200 nm elicits stronger immune responses than larger-sized NPs.[70,75] Development of new size-selected nano-systems with lymphatic trafficking capability for delivery of immunostimulatory molecules is one of the objectives of this thesis.

1.5 Nanoparticle-based vaccines for cancer immunotherapy

One of the main therapeutic uses of nanomaterials is focused in cancer therapy.[66] The main goal of cancer treatment is to either kill or arrest cancer cell division without affecting surrounding healthy cells and tissue. Cancer is a disease of unregulated cell growth, where cells divide and grow uncontrollably, resulting in the formation of tumours. One of the traditional cancer treatments involves the administration of chemotherapeutic drugs into the bloodstream. Chemotherapy-based treatment started in 1946, when Gilman and coworkers administered a derived from mustard gas (tris(β-chloroethyl) amine

hydrochloride) which resulted in the regression of the cancer.[76] Since then, very potent chemotherapeutic agents, including camptothecin, taxenes, doxorubicin or platinating agents have been used against several tumor types.[77]

Nanoparticles can encapsulate and deliver one or more chemotherapeutic agents to improve the therapy provided by the free agents.[78] Although the recent advent of nanoparticle-based drug delivery systems has improved the efficacy of chemotherapeutics, one of the fundamental paradigms in their design and use is evading surveillance by the immune system to enhance anticancer efficacy. However, the possibility of harnessing the immune system by targeting its stimulation to fight against cancer offers a new strategy in the development of cancer vaccines. Over the last 15 years, studies based on the activation of the immune system cells to eliminate malignant cells have increased significantly.

In cancer immunotherapy, NPs can increase the uptake of antigens and adjuvants by DCs which results in enhanced immune responses against tumor growth **(Fig. 1.4)**.[75,79] Activating DCs is particularly important because they are the most potent and efficient APCs and the key regulators of the immune response. The stimulation of DCs and successfully migration to lymphatic organs trigger the activation and maturation of T-cells and natural killer (NK) cells to kill the cancer cells. The possibility of incorporating antigens and adjuvants into a single system or the combination of several adjuvants and delivery to the targeted site of action make NPs ideal platforms for developing a cancer vaccine based on immunotherapy.

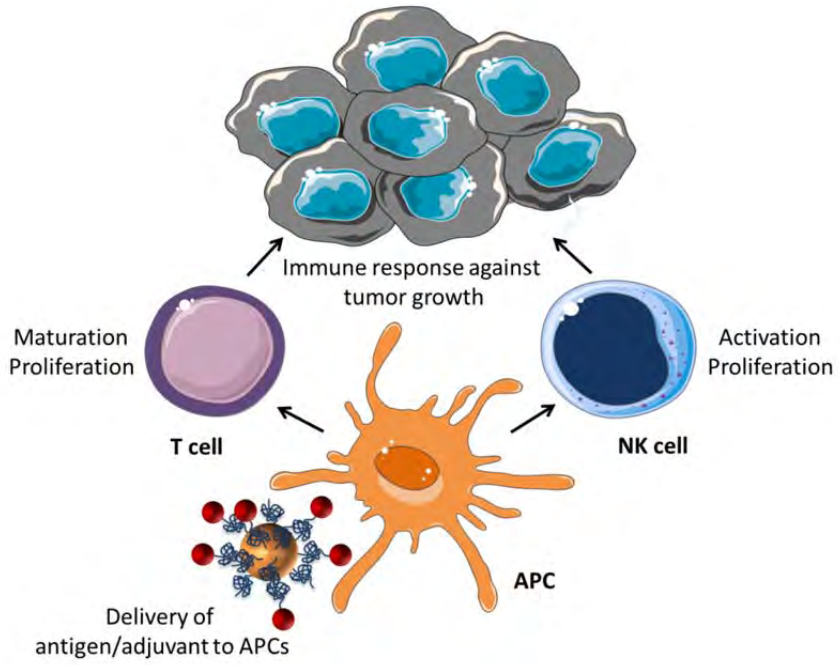

Fig. 1.4. Nanoparticles loaded with antigen and/or adjuvants to target APCs, promote the activation and maturation of immune system cells, such as T-cells and NK (natural killers) cells, initiating immune response against cancer cells.

Several TLR ligands have been tested as adjuvants of cancer vaccines in clinical trials with promising results, including CpG (TLR 9 ligand)[80] and poly (I:C) (TLR 3 ligand).[81] These synthetic ligands (mimicking natural pathogen-associated molecular patterns (PAMPs) found in viruses) allow the immune system to recognize the pathogen as a threat. One of the multiple approaches to overcome the immunosuppressive tumor environment is mediated by the activation of DCs by the TLRs, which results in secretion of cytokines and costimulatory molecules that stimulate certain cells of the immune system including T cells and NK cells.

Compared to chemotherapy, harnessing the body's own immune system to recognize and destroy cancer cells has major advantages, including tumor cell specificity, reduction of off-target side effects and the potential for a durable treatment effect in the absence of repeated drug administration due to adaptive immunity, creating immunological memory for the cancer cells.[82] In this sense, the use of NPs as targeted agents should be far more effective than nonspecific immunomodulatory agents.

Cancer immunotherapy represents one of the most promising new cancer treatment approaches since the development of the first chemotherapeutic drugs, and the use of nanotechnology can enhance the delivery and efficacy of immunotherapeutic agents as it has been mentioned in this introduction. Furthermore, the large surface area of NPs should facilitate the incorporation of multiple chemo and/or immunotherapeutic agents in a single system with the goal of obtaining synergistic effects between drugs and between chemotherapy and immunotherapy. This aspect has not been pursued so far and represents the other objective of this thesis work; development of nanoconstructs simultaneously loaded with chemo and immunotherapy drugs.

References

1. R. Feynman. There´s plenty of room at the bottom. *Eng. Sci.* **23,** 22-36 (1960).

2. Shatkin, J. A. *Nanotechnology. Health and Environmental Risks*. (2013).

3. Sahoo, S. K., Parveen, S. & Panda, J. J. The present and future of nanotechnology in human health care. *Nanomedicine* **3,** 20–31 (2007).

4. Zhang, L. *et al.* Nanoparticles in Medicine : Therapeutic Applications and Developments. *Clin. Pharmacol. Ther.* **83,** 761–769 (2008).

5. Kawasaki, E. S. & Player, A. Nanotechnology, nanomedicine, and the development of new, effective therapies for cancer. *Nanomedicine* **1,** 101–9 (2005).

6. Lü, J.-M. *et al.* Current advances in research and clinical applications of PLGA-based nanotechnology. *Expert Rev. Mol. Diagn.* **9,** 325–41 (2009).

7. Manolova, V. *et al.* Nanoparticles target distinct dendritic cell populations according to their size. *Eur. J. Immunol.* **38,** 1404–13 (2008).

8. Ferrari, M. Cancer nanotechnology: opportunities and challenges. *Nat. Rev. Cancer* **5,** 161–71 (2005).

9. De Jong, W. H. & Borm, P. J. A. Drug delivery and nanoparticles:applications and hazards. *Int. J. Nanomedicine* **3,** 133–49 (2008).

10. Farokhzad, O. C. & Langer, R. Impact of nanotechnology on drug delivery. *ACS Nano* **3,** 16–20 (2009).

11. Sudimack, J. & Lee, R. J. Targeted drug delivery via the folate receptor. *Adv. Drug Deliv. Rev.* **41,** 147–62 (2000).

12. Brannon-Peppas, L. & Blanchette, J. O. Nanoparticle and targeted systems for cancer therapy. *Adv. Drug Deliv. Rev.* **56,** 1649–59 (2004).

13. Ojea-Jiménez, I. *et al.* Engineered inorganic nanoparticles for drug delivery applications. *Curr. Drug Metab.* **14,** 518–30 (2013).

14. Maeda, H., Wu, J., Sawa, T., Matsumura, Y. & Hori, K. Tumor vascular permeability and the EPR effect in macromolecular therapeutics: a review. *J. Control. Release* **65,** 271–284 (2000).

15. Matsumura, Y. & Maeda, H. A new concept for macromolecular therapeutics in cancer chemotherapy: mechanism of tumoritropic accumulation of proteins and the antitumor agent smancs. *Cancer Res.* **46,** 6387–92 (1986).

16. Muthu, M. S., Leong, D. T., Mei, L. & Feng, S.-S. Nanotheranostics - application and further development of nanomedicine strategies for advanced theranostics. *Theranostics* **4,** 660–77 (2014).

17. Petros, R. A. & DeSimone, J. M. Strategies in the design of nanoparticles for therapeutic applications. *Nat. Rev. Drug Discov.* **9,** 615–27 (2010).

18. Wicki, A., Witzigmann, D., Balasubramanian, V. & Huwyler, J. Nanomedicine in Cancer Therapy: Challenges, Opportunities, and Clinical Applications. *J. Control. Release* **200,** 138–157 (2014).

19. Liechty, W. B., Kryscio, D. R., Slaughter, B. V & Peppas, N. A. Polymers for drug delivery systems. *Annu. Rev. Chem. Biomol. Eng.* **1,** 149–73 (2010).

20. Vivero-Escoto, J. L. & Huang, Y.-T. Inorganic-organic hybrid nanomaterials for therapeutic and diagnostic imaging applications. *Int. J. Mol. Sci.* **12,** 3888–927 (2011).

21. Kango, S. *et al.* Surface modification of inorganic nanoparticles for development of organic–inorganic nanocomposites—A review. *Prog. Polym. Sci.* **38,** 1232–1261 (2013).

22. Mahmoudi, M., Sant, S., Wang, B., Laurent, S. & Sen, T. Superparamagnetic iron oxide nanoparticles (SPIONs): development, surface modification and applications in chemotherapy. *Adv. Drug Deliv. Rev.* **63,** 24–46 (2011).

23. Lu, A.-H., Salabas, E. L. & Schüth, F. Magnetic nanoparticles: synthesis, protection, functionalization, and application. *Angew. Chem. Int. Ed. Engl.* **46,** 1222–44 (2007).

24. Laurent, S., Dutz, S., Häfeli, U. O. & Mahmoudi, M. Magnetic fluid hyperthermia: focus on superparamagnetic iron oxide nanoparticles. *Adv. Colloid Interface Sci.* **166,** 8–23 (2011).

25. Khodadust, R., Unsoy, G., Yalcın, S., Gunduz, G. & Gunduz, U. PAMAM dendrimer-coated iron oxide nanoparticles: synthesis and characterization of different generations. *J. Nanoparticle Res.* **15,** 1488 (2013).

26. Mok, H. & Zhang, M. Superparamagnetic iron oxide nanoparticle-based delivery systems for biotherapeutics. *Expert Opin. Drug Deliv.* **10,** 73–87 (2013).

27. Thorek, D. L. J., Chen, A. K., Czupryna, J. & Tsourkas, A. Superparamagnetic iron oxide nanoparticle probes for molecular imaging. *Ann. Biomed. Eng.* **34,** 23–38 (2006).

28. Dousset, V. *et al.* Comparison of ultrasmall particles of iron oxide (USPIO)-enhanced T2-weighted, conventional T2-weighted, and gadolinium-enhanced T1-weighted MR images in rats with experimental autoimmune encephalomyelitis. *AJNR. Am. J. Neuroradiol.* **20,** 223–7 (1999).

29. Shin, T.-H., Choi, Y., Kim, S. & Cheon, J. Recent advances in magnetic nanoparticle-based multi-modal imaging. *Chem. Soc. Rev.* (2015). doi:10.1039/c4cs00345d

30. Santhosh, P. B. & Ulrih, N. P. Multifunctional superparamagnetic iron oxide nanoparticles: promising tools in cancer theranostics. *Cancer Lett.* **336,** 8–17 (2013).

31. Xie, J., Lee, S. & Chen, X. Nanoparticle-based theranostic agents. *Adv. Drug Deliv. Rev.* **62,** 1064–79 (2010).

32. Wang, D. *et al.* Targeted iron-oxide nanoparticle for photodynamic therapy and imaging of head and neck cancer. *ACS Nano* **8,** 6620–32 (2014).

33. Jurgons, R. *et al.* Drug loaded magnetic nanoparticles for cancer therapy. *J. Phys. Condens. Matter* **18,** S2893–S2902 (2006).

34. Koo, H. *et al.* In vivo targeted delivery of nanoparticles for theranosis. *Acc. Chem. Res.* **44,** 1018–28 (2011).

35. Cheon, J. & Lee, J.-H. Synergistically integrated nanoparticles as multimodal probes for nanobiotechnology. *Acc. Chem. Res.* **41,** 1630–40 (2008).

36. Kelkar, S. S. & Reineke, T. M. Theranostics: combining imaging and therapy. *Bioconjug. Chem.* **22,** 1879–903 (2011).

37. Mieszawska, A. J., Mulder, W. J. M., Fayad, Z. A. & Cormode, D. P. Multifunctional gold nanoparticles for diagnosis and therapy of disease. *Mol. Pharm.* **10,** 831–47 (2013).

38. Bonnemain, B. Superparamagnetic agents in magnetic resonance imaging: physicochemical characteristics and clinical applications. A review. *J. Drug Target.* **6,** 167–74 (1998).

39. Chan, W. C. . *et al.* Luminescent quantum dots for multiplexed biological detection and imaging. *Curr. Opin. Biotechnol.* **13,** 40–46 (2002).

40. Khalil, M. M., Tremoleda, J. L., Bayomy, T. B. & Gsell, W. Molecular SPECT Imaging: An Overview. *Int. J. Mol. Imaging* **2011,** 796025 (2011).

41. Agdeppa, E. D. & Spilker, M. E. A Review of Imaging Agent Development. *AAPS J.* **11,** 286–299 (2009).

42. Phillips, M. A., Gran, M. L. & Peppas, N. A. Targeted Nanodelivery of Drugs and Diagnostics. *Nano Today* **5,** 143–159 (2010).

43. Lee, D.-E. *et al.* Multifunctional nanoparticles for multimodal imaging and theragnosis. *Chem. Soc. Rev.* **41,** 2656–72 (2012).

44. Jiang, S., Gnanasammandhan, M. K. & Zhang, Y. Optical imaging-guided cancer therapy with fluorescent nanoparticles. *J. R. Soc. Interface* **7,** 3–18 (2010).

45. Li, K. & Liu, B. Polymer-encapsulated organic nanoparticles for fluorescence and photoacoustic imaging. *Chem. Soc. Rev.* **43,** 6570–97 (2014).

46. Jones, Chris J. and Thornback, J. R. in *Med. Appl. Coord. Chem.* (2007).

47. Sun, C., Lee, J. S. H. & Zhang, M. Magnetic nanoparticles in MR imaging and drug delivery. *Adv. Drug Deliv. Rev.* **60,** 1252–65 (2008).

48. Bottomley, P. A., Foster, T. H., Argersinger, R. E. & Pfeifer, L. M. A review of normal tissue hydrogen NMR relaxation times and relaxation mechanisms from 1-100 MHz: dependence on tissue type, NMR frequency, temperature, species, excision, and age. *Med. Phys.* **11,** 425–48 (1984).

49. Stanisz, G. J. *et al.* T1, T2 relaxation and magnetization transfer in tissue at 3T. *Magn. Reson. Med.* **54,** 507–12 (2005).

50. Bottomley, P. A., Hardy, C. J., Argersinger, R. E. & Allen-Moore, G. A review of 1H nuclear magnetic resonance relaxation in pathology: are T1 and T2 diagnostic? *Med. Phys.* **14,** 1–37 (1987).

51. Weissleder, R., Bogdanov, A., Neuwelt, E. A. & Papisov, M. Long-circulating iron oxides for MR imaging. *Adv. Drug Deliv. Rev.* **16,** 321–334 (1995).

52. Vallabhajosula, S. *Molecular Imaging. Radiopharmaceuticals for PET and SPECT*. (2009). doi:10.1007/978-3-540-76735-0

53. Blankenberg, F. G. & Strauss, H. W. Nuclear medicine applications in molecular imaging. *J. Magn. Reson. Imaging* **16,** 352–61 (2002).

54. Key, J. & Leary, J. F. Nanoparticles for multimodal in vivo imaging in nanomedicine. *Int. J. Nanomedicine* **9,** 711–26 (2014).

55. Banchereau, J. & Steinman, R. M. Dendritic cells and the control of immunity. *Nature* **392,** 245–52 (1998).

56. Aguilar, J. C. & Rodríguez, E. G. Vaccine adjuvants revisited. *Vaccine* **25,** 3752–62 (2007).

57. Reed, S. G., Orr, M. T. & Fox, C. B. Key roles of adjuvants in modern vaccines. *Nat. Med.* **19,** 1597–608 (2013).

58. Awate, S., Babiuk, L. A. & Mutwiri, G. Mechanisms of action of adjuvants. *Front. Immunol.* **4,** 114 (2013).

59. Cox, J. C. & Coulter, A. R. Adjuvants--a classification and review of their modes of action. *Vaccine* **15,** 248–56 (1997).

60. Correia-Pinto, J. F., Csaba, N. & Alonso, M. J. Vaccine delivery carriers: insights and future perspectives. *Int. J. Pharm.* **440,** 27–38 (2013).

61. Kushnir, N., Streatfield, S. J. & Yusibov, V. Virus-like particles as a highly efficient vaccine platform: diversity of targets and production systems and advances in clinical development. *Vaccine* **31,** 58–83 (2012).

62. Krishnamachari, Y., Geary, S. M., Lemke, C. D. & Salem, A. K. Nanoparticle delivery systems in cancer vaccines. *Pharm. Res.* **28,** 215–36 (2011).

63. Bolhassani, A., Safaiyan, S. & Rafati, S. Improvement of different vaccine delivery systems for cancer therapy. *Mol. Cancer* **10,** 3 (2011).

64. Hamdy, S., Haddadi, A., Hung, R. W. & Lavasanifar, A. Targeting dendritic cells with nano-particulate PLGA cancer vaccine formulations. *Adv. Drug Deliv. Rev.* **63,** 943–55 (2011).

65. Petrovsky, N. & Aguilar, J. C. Vaccine adjuvants: current state and future trends. *Immunol. Cell Biol.* **82,** 488–96 (2004).

66. Zhao, L. *et al.* Nanoparticle vaccines. *Vaccine* **32,** 327–37 (2014).

67. Fox, C. B., Kramer, R. M., Barnes V, L., Dowling, Q. M. & Vedvick, T. S. Working together: interactions between vaccine antigens and adjuvants. *Ther. Adv. vaccines* **1,** 7–20 (2013).

68. Gregory, A. E., Titball, R. & Williamson, D. Vaccine delivery using nanoparticles. *Front. Cell. Infect. Microbiol.* **3,** 13 (2013).

69. Takami Akagi, Masanori Baba, and M. A. in *Polym. Nanomedicine* 31–64 (2012). doi:10.1007/12_2011_150

70. Oyewumi, M. O., Kumar, A. & Cui, Z. Nano-microparticles as immune adjuvants: correlating particle sizes and the resultant immune responses. *Expert Rev. Vaccines* **9,** 1095–107 (2010).

71. Smith, D. M., Simon, J. K. & Baker, J. R. Applications of nanotechnology for immunology. *Nat. Rev. Immunol.* **13,** 592–605 (2013).

72. Reddy, S. T. *et al.* Exploiting lymphatic transport and complement activation in nanoparticle vaccines. *Nat. Biotechnol.* **25,** 1159–64 (2007).

73. Pérez-Campaña, C. *et al.* Biodistribution of different sized nanoparticles assessed by positron emission tomography: a general strategy for direct activation of metal oxide particles. *ACS Nano* **7,** 3498–505 (2013).

74. Moghimi, S. M., Hunter, A. C. & Murray, J. C. Long-Circulating and Target-Specific Nanoparticles : Theory to Practice. **53,** 283–318 (2001).

75. Park, Y.-M. *et al.* Nanoparticle-based vaccine delivery for cancer immunotherapy. *Immune Netw.* **13,** 177–83 (2013).

76. DeVita, V. T. & Chu, E. A history of cancer chemotherapy. *Cancer Res.* **68,** 8643–53 (2008).

77. Díaz, M. R. & Vivas-Mejia, P. E. Nanoparticles as Drug Delivery Systems in Cancer Medicine: Emphasis on RNAi-Containing Nanoliposomes. *Pharmaceuticals (Basel).* **6,** 1361–80 (2013).

78. Goldberg, M. S. Immunoengineering: How Nanotechnology Can Enhance Cancer Immunotherapy. *Cell* **161,** 201–204 (2015).

79. Silva, J. M., Videira, M., Gaspar, R., Préat, V. & Florindo, H. F. Immune system targeting by biodegradable nanoparticles for cancer vaccines. *J. Control. Release* **168,** 179–99 (2013).

80. Jahrsdörfer, B. & Weiner, G. J. CpG oligodeoxynucleotides as immunotherapy in cancer. *Update Cancer Ther.* **3,** 27–32 (2008).

81. Steinhagen, F., Kinjo, T., Bode, C. & Klinman, D. M. TLR-based immune adjuvants. *Vaccine* **29,** 3341–55 (2011).

82. Couzin-Frankel, J. Breakthrough of the year 2013. Cancer immunotherapy. *Science* **342,** 1432–3 (2013).

Justification and objectives of this thesis

The role of the immune system consists of protecting the body against infectious organisms and other potential threats. The treatment of diseases modulating (inducing, enhancing or suppressing) an immune response is the basis of immunotherapy, either fighting against infectious diseases or being able to trigger responses against tumors. The specificity of the immune system in defending us against cancer and the possibility of providing a more effective and less harmful therapy compared with conventional treatments has made immunotherapy a promising treatment for people living with cancer and the unwanted effects of current treatments.

The possibility of developing therapeutic vaccines with NPs has shown a great potential in the last decade and has already led to some nanomedicines to be approved for clinical or pre-clinical trials (e.g. Gardasil, a virus-like particle (VLP)-based vaccine against human papilloma virus (HPV)).

Significant advances in medicine have been made possible by the use of imaging technologies, and it is now widely accepted that molecular imaging will play an increasingly important role in drug discovery and development, and in facilitating and speeding up clinical translation of nanomedicines. Compared to other areas, however, molecular imaging has been applied much less for guiding the development of synthetic vaccines. In molecular imaging there is great interest in multimodal imaging probes as new tools to overcome the limitations of each type of imaging modality and obtain complementary information. The development of nanomaterials which allow the combination of molecular imaging and therapy in a single construct is nowadays a major trend in nanomedicine. All these aspects have provided impetus for this thesis work and guided the choices made with regards to research targets, molecular building blocks and nanomaterials used. In particular the utility of IONPs as MRI contrast agents for tumor imaging, of poly (I:C) for immunotherapy and of cisplatin for chemotherapy has been proven in clinical applications

This PhD thesis is focused on the development of multifunctional IONPs which are engineered to trigger potent immune responses in cells of the immune system and

controlled delivery of cisplatin for cancer cell killing whilst acting as multimodal imaging agent. When this thesis work was started in 2011 very few systems combined even two of these three features, thus the possibility of integrating for the first time the three features in a single agent was an important aim of this thesis work. Towards this "final" goal the specific objectives set out for this thesis work were:

- The synthesis of different types of IONPs coated with different ligands and functional groups for developing water soluble systems with suitable properties for acting as an effective MRI contrast agent and multi-drug delivery vehicle.

- The incorporation of multimodal imaging features in the IONPs to monitor the trafficking of the nanoconstructs *in vitro* and *in vivo* using complementary imaging modalities.

- The development of a IONP-based system capable of mimicking a pathogen (e.g. bacteria and viruses) by decorating it with poly (I:C); a synthetic analogue of viral double-stranded RNA (dsRNA) widely used as an adjuvant for vaccines in clinical trials.

- The use of the IONP-based system for the transport and delivery of different therapeutic drugs. Specifically, we wished to combine in a single nanoconstruct an inert form of cisplatin which could be activated inside cancer cells for chemotherapy and poly (I:C) which could promote immunostimulation for immunotherapy.

- The study of the immunostimulatory properties of the newly developed nanoconstructs *in vitro* and *in vivo* compared with the free drugs.

- The development of nanoconstructs capable of killing different human cancer cells as effectively as cisplatin but using intert Pt(IV) prodrugs.

- The development of a system able to reach secondary lymphatic organs, such as lymph nodes (LNs) to activate immune responses against infectious diseases or tumors. Therefore, the system has to be capable of migrating from the site of injection to LNs through the lymphatics.

2

Development of water soluble systems based on IONPs for multimodal imaging and drug delivery

In this chapter, the synthesis and characterization of hydrophobic iron oxide nanoparticles with a size range between 4-10 nm is described and discussed. Hydrophobic nanoparticles are subsequently encapsulated in PEGylated phospholid (PL-PEG) micelles to achieve water soluble systems. These IONP@PL-PEG micelles are prepared and extensively characterized for their posterior application as MRI contrast agents and delivery vehicle of immunostimulatory double stranded RNA.[1–3] *With the incorporation of a fluorophore and a radiotracer in the system, a stable multimodal imaging agent was developed which can be followed in vitro and in vivo by different complementary imaging techniques.*

2.1 Introduction

2.1.1 Magnetic properties of Iron Oxide Nanoparticles (IONPs)

Magnetic materials are classified by their susceptibility to a magnetic field into diamagnetic, paramagnetic or ferromagnetic materials. In the first two, the magnetic properties do not persist after the external magnetic field is removed, whilst for ferromagnetic materials, these properties are stable after the removal of the external field. The magnetic properties of the nanoparticles (NPs) are size-dependent. The smaller is their size, the stronger is the influence of the thermal energy on the NPs. When the size of a ferromagnetic material is small enough the thermal energy (kT) is comparable to the magnetic anisotropy energy (KV) **(Fig. 2.1a)**, where k is Boltzmann´s constant, T is the temperature, K is the particle anisotropy constant and V is the particle volume. If the thermal energy is much higher than the anisotropy energy then the material is defined as superparamagnetic.[4,5]

Superparamagnetic NPs display paramagnetism and large magnetic susceptibility, that is, a behavior between paramagnetic and ferromagnetic material, which is very useful for biomedical applications, because once the external field is removed, the magnetization disappears (net magnetization of zero). The superparamagnetic behavior of IONPs appears at sizes less than 25 nm; that is because when the particle size decreases to this size the formation of domain walls or multi domains begins to be unfavorable and each particle comprise a single domain where all magnetic spins are aligned unidirectionally **(Fig. 2.1b)**.[6]

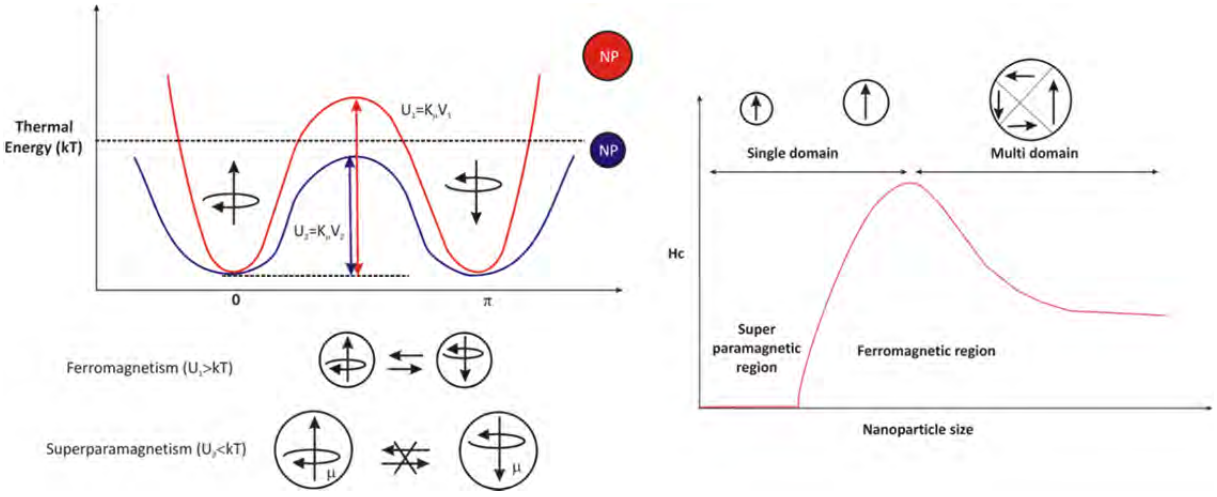

Fig. 2.1. Diagram of magnetic nanoparticles from ferromagnetism to superparamagnetism (left) and plot of nanoparticle magnetic domain size-dependency (right). Adapted from *Acc. Chem. Res.,* **2008,** 41, 179.

The most widely used materials with superparamagnetic behavior are iron oxides, for which the two main forms are magnetite Fe_3O_4 and maghemite γ-Fe_2O_3. Both magnetite and maghemite exhibit a spinel crystal structure (AB_2O_4) with the difference that magnetite contains both Fe^{2+} and Fe^{3+}cations, whereas in maghemite all the cations are in the trivalent state. Both iron oxides crystallize in the inverse spinel type structure, that is the tetrahedral sites (A indicates T_d sites) are occupied by Fe^{3+} and the octahedral sites (O_h) are occupied by Fe^{2+} and Fe^{3+} ions (B-sites). In contrast to inverse spinel, in the normal spinel, the tetrahedral sites (T_d) are occupied by Fe^{2+} cations.

As a result of their superparamagnetism, iron oxides are commonly used as T_2 contrast agents in Magnetic Resonance Imaging (MRI). An effective magnetic resonance (MR) contrast agent must have a strong effect to accelerate spin-lattice relaxation (T_1), which produces bright contrast images or to shorten spin-spin relaxation (T_2), which produces dark contrast images. They are most commonly known, as longitudinal (T_1) and transversal (T_2) relaxations. Both relaxation process are represented by the corresponding relaxation rates, r_1 and r_2 ($r = 1/T$ (s^{-1})) and the relaxivity values ($R = r/\text{concentration}$ (mM^{-1} s^{-1})). Contrast agents are classified in T_1 or T_2 types depending on their relaxation processes and consequently to their positive or negative enhancement.[7] T_1 contrast agents are commonly paramagnetic materials and gadolinium (Gd^{3+}) based contrast agents are the

most widely used T_1 contrast agents.[8] T_2 contrast agents are usually superparamagnetic materials such as iron oxides. However, the application of IONPs with a core size less than 4 nm as T_1 contrast agents has also been explored. Frascione *et al.* [9] reported that at lower concentrations of these IONPs appears an intense T_1 effect because the T_1 and T_2 relaxation times are reduced at nanomolar level. However, Kim *et al.*[10] discussed that their large surface area and the 5 unpaired electrons enhance T_1 effect (increasing the r_1 value), while the small magnetic moment suppresses the T_2 effect due also to their small size.

2.1.2 Size, shape and chemical composition of IONPs

Several synthesis of IONPs have been reported in the last decades by numerous research groups with excellent narrow size distributions and even shape-control.[11] Literature data shows that the particle size can be tuned from 4 to 12 nm by changing the reaction parameters, that is, controlling the nucleation and growth steps during the synthesis. This control is based on the work published by LaMer and Dinegar in 1950 for sulfur hydrosols.[12] The diagram in **Fig. 2.2** illustrates the development of the nanoparticle growth, with the saturation of the reagents and the short step of self-nucleation and the growth of stable nanoparticle seeds (nuclei). For a non-specific amount of mass, when the saturation occurs there are a larger amount of starting points generating more nuclei and obtaining the smaller NPs. According to Johnston,[13] the nucleation is possible if the thermal energy is lower than the binding energy of the molecule formed. This process is not straightforward and the reaction conditions should be carefully controlled during the synthesis for obtaining NPs of the desired size. Reaction temperature and heating rate between the different temperature steps (commonly called temperature ramp), purity of the reagents and the solvents choice are the most common factors to take into account.

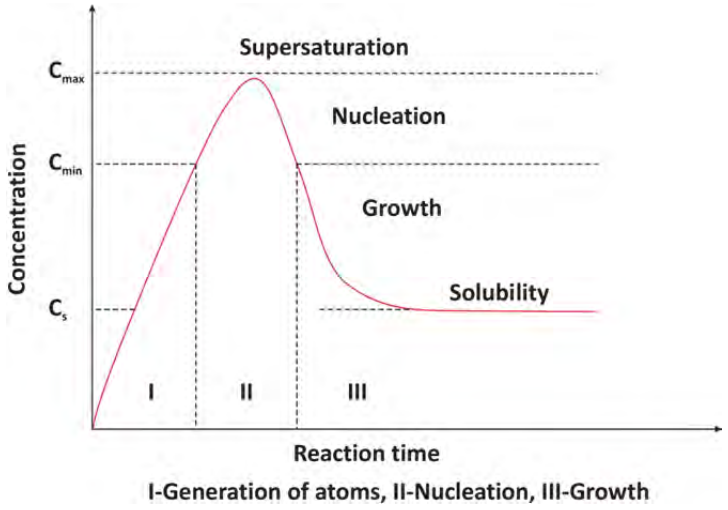

Fig. 2.2. Plot of La Mer and Dinegar model for the generation of atoms, nucleation, and subsequent growth of colloidal synthesis (LaMer and Dinegar 1950)

The ability to control the particle size starts with the choice of the synthetic method. One of the most common synthetic methods used so far is the thermal decomposition of metallic compounds. It is a widely used method applied for the synthesis of IONPs, due to the highly monodisperse distributions achieved, the crystallinity of the obtained NPs and because the reaction is carried out in one step with high yields. The main drawback of this method is obtaining hydrophobic NPs, which implies a second step to convert them into hydrophilic systems for their application in the biomedical field. The protocol described by *Sun et al.*[14] based on the thermal decomposition of metallic precursors in organic solvents, was adopted during this work as the basis in the synthesis of the different NPs.

However, there are others methods of synthesis used in the production of magnetic NPs, which deserve to be briefly mentioned.

Coprecipitation method.[15,16] This procedure is the classical method to achieve magnetic NPs in aqueous media. Fe(II) and Fe(III) salts (usually $FeCl_2$ and $FeCl_3$) are precipitated in a basic solution (NH_4OH or NaOH) in the presence of coating materials (e.g. dextran). The iron hydroxide precipitate is treated by centrifugation, then the mixture is treated with acic or base to control the pH and the Fe_3O_4 is collected as the final product. The main advantage of this method is the possibility to synthesize NPs in large scale, but the difficulty in controlling their size is the major disadvantage.

Hydrothermal synthesis.[17,18] This method uses water as a solvent and is carried out under critical water conditions (374 °C and 22.1 MPa). The high pressures and temperatures of this method, requires the use of an autoclave for the preparation of the NPs.

Sol-Gel reactions.[19,20] The method is based on a stable dispersion of colloids in a solvent (sol). When these particles in sol are polymerized, a gel state is produced where both liquid and solid are dispersed in each other and with a subsequent heat treatment NPs of desired size are obtained. The principal advantage of this method is the control of the nanoparticle morphology and the homogeneity of the materials.

In this group it is also included the polyol method,[21,22] which differs in the use of polyalcohols as solvents (polyethyleneglycol or propylene glycol) instead of water.

After the synthesis method has been defined, the resulting NPs can be classified in two main groups depending on their overall diameter, including the iron oxide core and the hydrated coating. Thus, the IONPs are classified into two types:

SPIOs (SuperParamagnetic Iron Oxides). The core of these type of NPs is around 6 nm with a hydrodynamic diameter usually above 50 nm.[23] In this group are included some commercial contrast agents[24] typically used today in clinical medicine such as Lumirem (silicon-coated iron oxide nanoparticles) and Endorem (coated with dextran), which have average sizes of 300 nm and 150 nm respectively. The former is specially manufactured for gastrointestinal tract images and the later is well known because was approved in 1996 for the detection of liver lesions.

USPIOs (Ultrasmall SuperParamagnetic Iron Oxides). The magnetic core of these NPs approaches 3 nm with a hydrodynamic diameter smaller than 50 nm. There are also commercial agents included in this group such as Sinerem (IONPs coated with dextran with an average diameter size of 30 nm), which is used for the detection of human brain tumors,[25] or Combirex, developed for the detection of vessel abnormalities.

There are not specific advantages and drawbacks in the use of one type over the other, the choice is made depending on the specific biomedical application. The smaller size of USPIOs makes them more suitable to enhance the plasma half-life, because they do not accumulate in the mononuclear phagocyte system (MPS) (formerly called reticuloendothelial

system (RES)) as fast as larger NPs. Furthermore, they can travel through small organs or tissues in the body such as the lymphatic system, being this characteristic very useful for the detection of sentinel lymph nodes or metastatic nodes. After intravenous injection, NPs systems larger than 200 nm are removed by mechanical filtration by the spleen and NPs with a hydrodynamic diameter of 5-10 nm are eliminated by renal excretion. However sizes between 10 and 100 nm prevent both elimination routes, control the MPS uptake and even control the tumor penetration.[26,27]

The size and shape of the NPs are two critical parameters involved in their subsequent applications. The biodistribution, the targeting to reach the desirable cells, blood circulation half-time and cell uptake are controlled by these two factors.

Although spherical NPs have been traditionally employed for biomedical applications, many research groups in the field are involved in the development of nonspherical NPs for hyperthermia, cancer treatment or magnetic resonance. Different morphologies are possible varying the experimental conditions during the synthesis, obtaining rods, discs, triangles or squares. It is reported that NPs shape directly influences uptake into cells. For instance, Gratton *et al.* determined that rods show the highest uptake, followed by spheres, cylinders and cubes.[28] But, the matter is still controversial since there are evidences shown by Qiu *et al.*, that spheres present better uptake than rods.[29,30] Although several groups have focused on the study of the cellular uptake depending on the NPs shape, these studies are very complex due to the interactions between rods and cells depending of their orientation.

The possibility of doping the iron oxide structure with different M^{2+} cations, such as Co, Mn or Zn, confers the opportunity of obtaining different magnetic properties.[31–33] The synthesis of $(Zn_xMn_{1-x})Fe_2O_4$ NPs and nano-alloy of FeCo NPs has been reported in the literature with longitudinal (r_1) and transverse (r_2) relaxivity values superior to conventional iron oxide nanoparticles.[34]

This chapter is focused on two types of IONPs: Fe_3O_4 and $(Zn_xFe_{1-x})(Fe_2O_4)$.

2.1.3 Surface coating

Other key parameter for biomedical applications and their behavior *in vitro* and *in vivo* is the surface chemistry of the magnetic NPs. This factor is especially important to avoid the aggregation of the system, to control the charge, to enhance the circulation half-time in the blood stream or to avoid the action of the MPS (that means to retard the uptake by macrophages of the MPS and the rapid clearance to the liver, spleen and bone marrow). So, for biomedical applications it is necessary a system able to stay in the body long enough to reach the target and deliver drugs, in a sufficiently high concentration to be efficient and also, give enough time to capture images by imaging techniques.

The coating on the NP surface plays an important role in the quality of the magnetic material, preserving and modulating the magnetic properties of IONPs.[35,36] The coating of IONPs often results in large hydrodynamic diameters and the formation of aggregates or clusters, which in turn enable these systems to present an increase in r_2 relaxivity values. In this chapter a modified PEGylation method based on IONPs filled micelles is described.[37] Through this protocol, it is possible to modulate the desirable magnetic behavior depending on their size.

Usually the choice of the coating is determined by the posterior needs, hence by the nature of the functional molecules that are attached on the outer sphere of the nanoparticle. Notably, it is key to find a balance for a multimodal agent that preserves its magnetic properties as well as its biofunctionalization capability. To achieve such a goal, several organic and inorganic coatings have been used to decorate IONPs and make them hydrophilic. Three coating strategies have typically been adopted to cover iron-based nanoparticle:

1. **Ligand addition method.** This method refers to the addition of a molecular layer bound by hydrophobic interactions with the original ligand. The most widely used coating for such purpose is polyethylene glycol (PEG), usually called PEGylation method. PEG polymers with sizes below 100 KDa are amphiphilic, allowing their handling in several organic solvents, such as toluene, chloroform or hexane as well as water. This characteristic allows their use in a broad number of reactions which require either aqueous or organic solvents. Several

advantages have been reported for PEGylation method apart from conferring water solubility:[38–41]

- Minimizes the aggregation due to the hydrophilicity and steric repulsion of their chains.
- Shows low toxicity and immunogenicity.
- Avoids non-specific cellular uptake interactions.
- Enhances the plasma half-life on IONPs in the blood stream.

2. Ligand exchange method. Ligand exchange refers to replacing the original hydrophobic surfactants with new hydrophilic ones. The new ligands must have higher affinity to the particle surface than the original surfactants. Polyethylenimine (PEI)[42,43] and 2,3-dimercaptosuccinic acid (DMSA)[44,45] are two of the most common ligands used following this strategy.

3. Inorganic coating method. The objective of this method is to cover completely the surface of the NPs with new ligands, for example in the case of potentially toxic particles, such as CdSe@ZnS Quantum Dots (QDs), is the best strategy to follow. Normally this coating is non-biodegradable, which is the main obstacle for making them biocompatible. Silica coating is one of the most popular in this surface modification.[46,47]

2.1.4 Application of IONPs for multimodal imaging

In recent years, it has been extensively reported that inorganic nanoparticles (iNPs) are promising platforms to develop multimodal contrasts agents combining their intrinsic magnetic properties with complementary imaging motifs, such as fluorophores or radiotracers.[48,49]

The most common imaging techniques used today in clinical medicine are optical imaging, ultrasound (US), computed tomography (CT), magnetic resonance imaging (MRI), positron emission tomography (PET) and single photon emission computed tomography (SPECT). Their principal advantages and drawbacks are summarized in **Fig. 2.3**.

Each imaging technique has its own strengths and limitations but the combination of different modalities in a single probe will help to overcome the limitations of the currently employed clinical agents. Based on recent developments, the combination of more than one imaging modality using these iNPs (all-in-one imaging) to improve medical diagnosis can be expected to become a clinical reality in the not too distant future. The main obstacle, however, will be to optimize the multimodal system(s) to each disease and each patient (i.e. for personalized medicine).

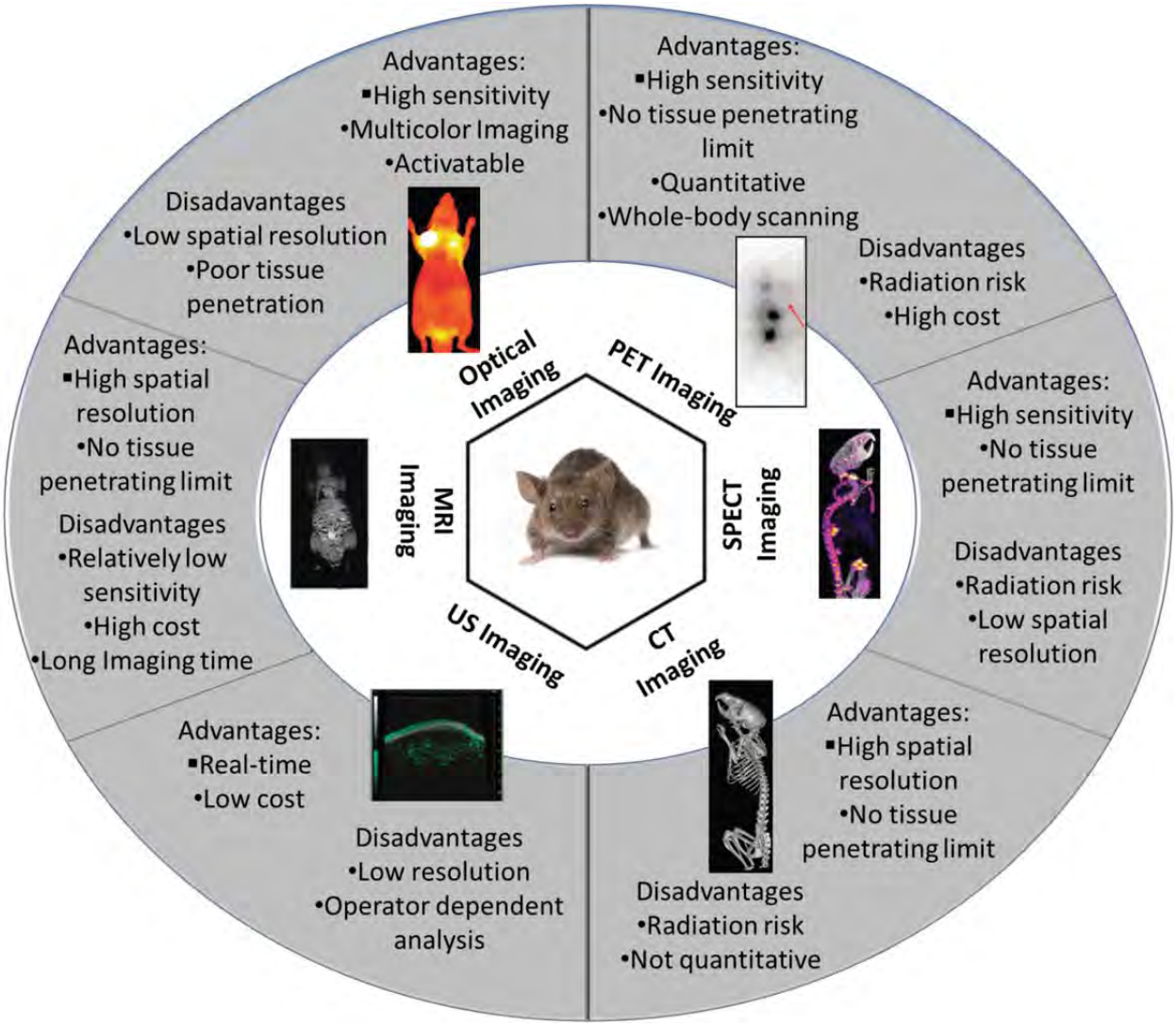

Fig. 2.3. Advantages and drawbacks of imaging techniques currently used in biomedical applications. Adapted from *Chem. Soc. Rev.,* 2012, **41,** 2656.

The combination of more than one technique in one only instrument is available nowadays with, for instance, the PET/CT system. PET provides the functional information and CT the anatomical information of the radioactivity distribution within the organism.

The iNPs described in this chapter can be labeled with a variety of radioisotopes for PET/MRI or SPECT/MRI imaging studies, integrating in one only system the high resolution of MRI and the high sensitivity of PET/SPECT.

MRI is a non-invasive imaging diagnostic technique capable of providing anatomical images with high resolution (10-100 μm). It is a relatively new technique (the first MRI image *in vivo* is reported to be take by Paul C. Lauterbur in 1974).[50] Only a few years later, himself reported also the first study *in vivo* with IONPs.[51] Nowadays, MRI is one of the most routinely used imaging modalities in both clinical and research settings. The use of non-ionizing energy and the high spatial resolution are the two main advantages of MRI, whereas the low sensitivity is its major limitation. Moreover, the dark signal produced in the body can be often confused with signals from bleedings, blood clots or magnetic susceptibility artifacts of iron oxide, which can distort the image.[52,53] The use of contrast agents such as iNPs can improve this drawback, enhancing the contrast of body organs or tissues compared with the background. Thus this chapter is focused in the synthesis and characterization of this type of iNPs which also allow the integration of other imaging modalities in the same system.

PET and SPECT are non-invasive techniques introduced during the 1970s by David E. Kuhl and Roy Q. Edwards[54] with the ability to detect biological and physiological processes using radioactive materials at doses free of pharmacologic side effects.[55] PET and SPECT are highly sensitive, quantitative, and show good tissue penetration depth, however they are limited by their low spatial resolution (1-2 mm).[56]

In 1989 Bligh *et al.*[57] reported the first magnetite radiolabelling with ^{99m}Tc and ^{111}In. Since then, other radiolabelling approaches with PET and SPECT isotopes have been reported in the literature.[58–62] The half-life of the radionuclide is an important consideration in the radionuclide attachment to the IONPs because it determines the acquisition imaging time and the study length. Typical isotopes used as radionuclides in PET imaging are ^{64}Cu with $t_{1/2}$ =12.7 h, ^{18}F with $t_{1/2}$=109.8 min and ^{68}Ga with $t_{1/2}$= 68.1 min. Whereas, ^{99m}Tc with

$t_{1/2}$= 6 h and ^{111}In with $t_{1/2}$=2.8 days are the most common for SPECT imaging. The radionuclides can be introduced or attached in the IONPs following three strategies:

- **Using chelating agents able to incorporate radionuclides into the IONPs system.** These chelating molecules are usually called bifunctional chelating agents (BFCs).[63] They are covalently attached to the NP surface and possess a terminal group capable of reacting with the radionuclide. The NP-radionuclide complex prevents the release of the radioisotope during the *in vivo* studies due to the ability of the radionuclides to form stable complexes with the chelating agents. 1,4,7,10-tetra-azacyclododecane-*N,N´,N´´ ,N´´´*-tetraacetic acid (DOTA), 1,4,7-triazacyclononane- *N,N´,N´´,*-triacetic acid (NOTA) or diethylenetriamine pentaacetic acid (DTPA) are some representative examples of the most commonly used chelating agents. Two strategies have been reported for this radiolabeling process. Adding the radionuclide into the NP-BFC pre-formed system[64] or forming firstly the radionuclide-BFC system and in a second step the NP is added.[65] Both methods have pros and cons. The main disadvantage of the former is the presence of non-specific interactions of the radionuclide with the NP surface. This is related with the advantage of the second method, because it is possible to purify the radionuclide free from the BFC achieving cleaner reactions. In both strategies the use of linkers as a conjugation strategy has the main disadvantages that the BFC increase the length or the overall diameter of the nanoparticle and can alter the biological properties of the radiolabeled-system.

- **Through direct radiolabelling on the nanoparticle surface.**[66,67] The affinity of the inorganic material for the radionuclide is the key point of this strategy. The surface coating ligand plays an important role in this strategy, because the NP surface has to be sufficiently accessible for the entry of the radioisotope. The NP system is incubated directly with the radionuclide and usually a purification step by centrifugation is necessary to eliminate the free radioactivity. Working under mild conditions during the radiolabeling to avoid damage in the decorated biomolecules or significant changes on the NP surface is the main disadvantage of this method. However, the minimum manipulation of the radionuclide avoiding the unnecessary exposure to radioactivity is the most important advantage. Furthermore, the possibility of not using more ligands attached onto the NP surface leaving enough space for the decorating biomolecules or fluorophores is the principal factor to select this strategy for the thesis purpose.

- **Incorporation of the radionuclide during the NP synthesis.**[68,69] In this method the radioactive isotope is considered another reaction reagent. There are two major obstacles to the ordinarily use of this strategy, the access to a proper and expensive equipment and the use of radionuclides with a half-life long enough to support the reaction times. In this strategy it is included the possibility to active NPs by direct irradiation of the material. Pérez-Campaña *et al.*[70] have recently reported by the activation of titanium dioxide nanoparticles enriched in ^{18}O as a method for ^{18}F labeling.

Optical imaging is another non-invasive technique used in diagnosis and treatment of diseases that involves the detection of light photons transmitted through tissues. The traditional visible light dyes and the recently developed near-IR dyes (600-1000 nm region) are the most common fluorescent moieties. The latter ones offer the advantage that cellular and tissue components present an insignificant autofluorescence in the near-IR spectral region and furthermore the wavelength in the near-IR region has strong tissue penetration, which make them perfect for *in vivo* fluorescence imaging.

The choice of semiconductor NPs (QDs) for optical applications is particularly significant due to their intrinsic fluorescence properties. These NPs are very attractive because their emission spectra can be tuned varying their size or composition and due to their photochemical stability prevent/less likely the typical photobleaching of the conventional dyes.[71] Even the combination of IONPs with QDs has been a method reported in the literature to obtain this bimodal magnetic-fluorescent system applied for cell labeling or intracellular tracking.[72–75]

2.2 Results and discussion

2.2.1 Synthesis and characterization of hydrophobic MFe_2O_4

The most suitable synthesis of MFe_2O_4 for the specific research objectives of this thesis is the thermal decomposition method due to the good size control and high crystallinity of the obtained materials. Monodisperse nanocrystals were produced by thermal decomposition of a metallic precursor in high boiling solvent.

This synthetic approach was selected to prepare two different types of nanoparticles based on the spinel structure (AB_2O_4):

- IONPs with a magnetite Fe_3O_4 structure.
- ZnSPIONs with a general structure $(Zn_xFe_{1-x})(Fe_2O_4)$.

2.2.1.1 Synthetic procedures for size control of IONPs

The synthesis of the different sizes of IONPs were performed starting from the same metallic precursor, $Fe(acac)_3$. This compound is one of the most widely used iron precursors in thermal decomposition reactions and is commercially available and less toxic than the other precursor commonly utilized such as $Fe(CO)_5$. Oleylamine (OAm) and oleic acid (OAc) are used as surfactants in high boiling solvents, while 1,2-hexadecanediol is employed as reducing agent (general scheme represented in **Fig. 2.4**).

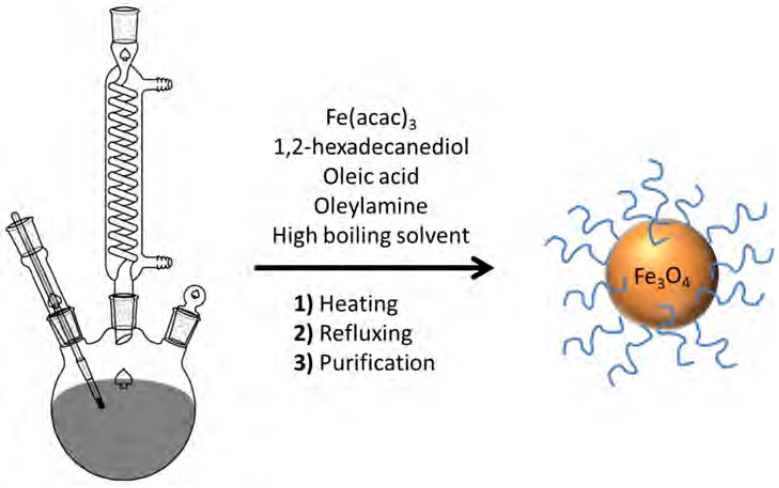

Fig. 2.4. General synthesis of hydrophobic IONPs.

The use of OAm as surfactant, solvent or reducing agent is one of the reaction settings to control the size and shape of IONPs.[76] OAm is commonly used when strong heating conditions are needed, due to its high boiling point of 350 °C, and the presence of a double bond in its structure promotes their use instead other primary alkylamines such as octadecylamine or hexadecylamine.

Despite the amount of research carried out over these materials, there are still considerable unsolved issues related with their synthesis and the factors relying on the reaction progression. For example, in 2004 Sun and co-workers[14] discussed that the use of OAm and OAc together is necessary to obtain the desirable NPs size. If OAc is utilized alone in the reaction, a viscous product difficult to purify and characterize will be obtained. Nevertheless, the choice of OAm as a single surfactant causes a much lower yield product. Although, later in 2009, the same author[77] pointed out that using only OAm with $Fe(acac)_3$ as a precursor and benzyl ether as solvent, it is possible to control the nanoparticle size, obtaining good crystalinity and size distribution. In this case, the OAm acts as a reducing agent and a stabilizer. Varying the ratio between the OAm and the solvent the authors could tune the sizes from 7 to 10 nm. They discuss that the excess of OAm in the synthesis provides a reductive environment comparable with the one given by the 1,2-hexadecanediol.

The stoichiometry between both reagents is a factor able to control the shape of the NPs. Sun and co-workers,[78] discuss that they obtain NPs with truncated octahedron shape, instead of spheres, using a 1:1 volume ratio of OAm:OAc. Whereas for obtaining spherical NPs, they increase the ratio to 1.5:1 of OAm:OAc respectively.

In addition to OAm, the choice of the solvent affects the size of the NPs. The most common solvents used are phenyl ether, benzyl ether or 1-octadecene. If phenyl ether is used as solvent, with a boiling point of 259 °C, the nanoparticle size will be around 4 nm, however if we choose benzyl ether, with 295 °C, the size increases to 6 nm.[14] The choice of 1-octadecene with a boiling point of 310 °C, is the best option for NPs higher than 10 nm. Although the polarity of the solvents can influence the nanoparticle growth, the reaction temperature and the temperature rates are the key factors to obtain a monodisperse size distribution. The volume of the solvent, is also important as it can affect the reaction

mechanism, because during the nucleation process, the nuclei have to be saturated in the reaction mixture to form the NPs. In larger volumes of solvent, more nuclei are needed to reach saturation step, resulting in smaller NPs than with the same amount of precursor in less volume of solvent.

The typical preparation employed in this thesis to obtain IONPs of 4 nm consists in mixing $Fe(acac)_3$, 1,2-hexadecanediol, OAm and OAc and phenyl ether under magnetic stirring and a flow of nitrogen. The mixture then was heated to 200 °C for 30 min and brought to reflux for another 30 min. The heat source was removed and the mixture was cooled down to room temperature. Finally, hydrophobic IONPs were obtained after several purification/centrifugation steps with ethanol as precipitant.

The conditions to obtain IONPs of 6 nm are rather similar. Using the same molar ratios, the solvent is changed to benzyl ether. The mixture was firstly heated to 200 °C for 2 h. At this stage, the precursor begins to decompose and form the NP nuclei. The formation of larger NP sizes is based on the increase of the reaction time at this point and it is called Ostwald ripening process.[79,80] Large particles grow larger while small particles become even smaller helping to reach the desirable size. It is a spontaneous phenomenon that occurs because larger crystals are energetically favored over smaller crystals. After this first heating step, the mixture was brought to reflux for 1 h. The treatment after the heat source is removed is exactly the same as the previous synthesis.

The 6 nm IONPs were used as seeds to synthesize larger NP, increasing the size in 2-3 nm each reaction. The seeds were dissolved in hexane before mixing them with the rest of reagents: $Fe(acac)_3$, 1,2-hexadecanediol, OAm and OAc in benzyl ether. In this case the mixture is firstly heated at 100 °C for 1 h to eliminate the hexane. Then, it is heated to 200 °C for 1 h and finally it is brought to reflux for 30 min. This protocol afforded the IONPs of 9 nm shown in **Fig. 2.5**.

Significantly, the reaction procedure can be extended to prepare other metal ferrite nanoparticles such as $MnFe_2O_4$ or $CoFe_2O_4$, which are also used as MRI contrast agents due to their highest magnetization values.[81]

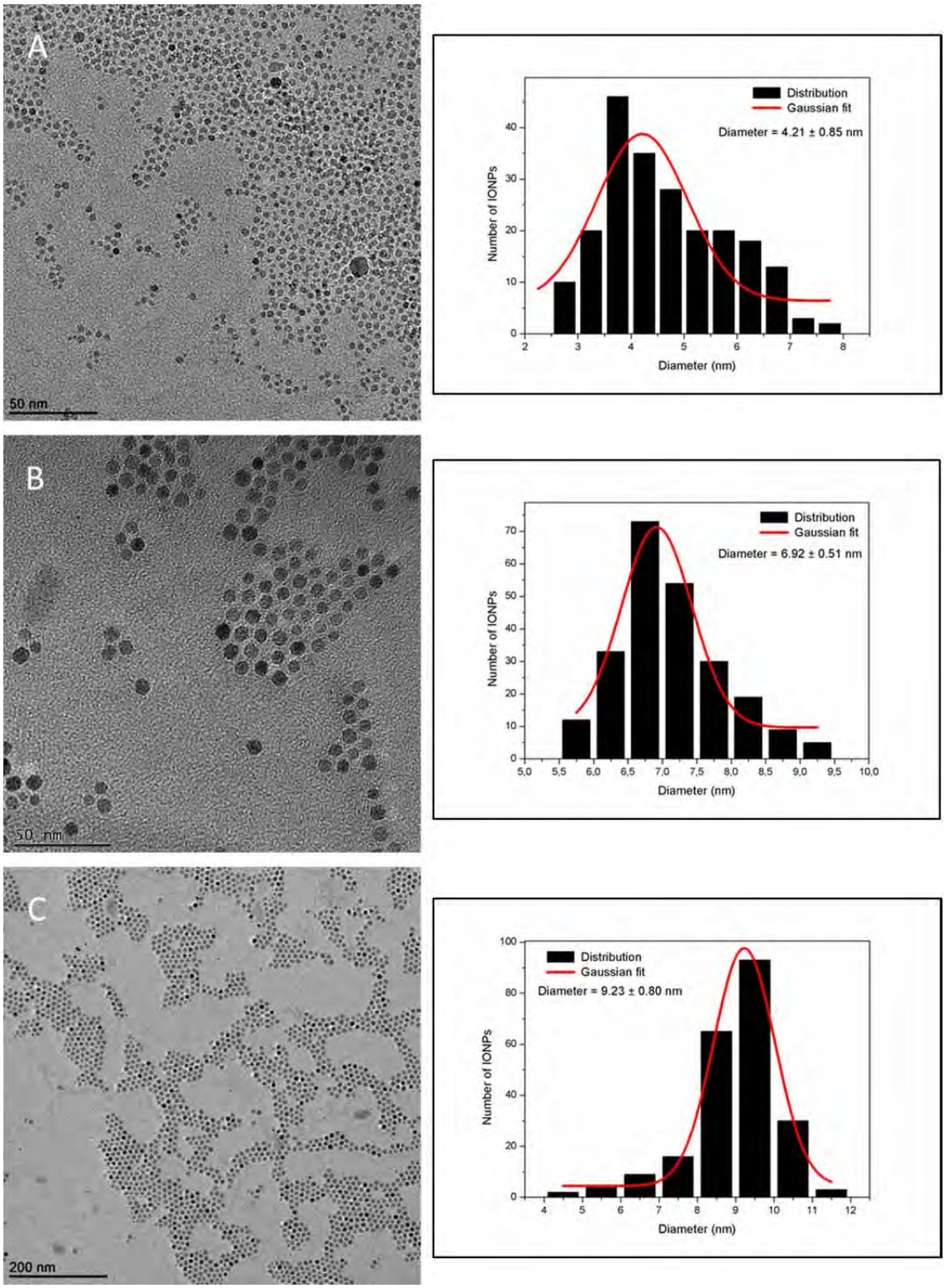

Fig. 2.5. Representative TEM images and size-histograms of IONPs.

2.2.1.2 Characterization of IONPs

For the complete characterization of these IONPs the following techniques were used: TEM, XPS, ICP-AES, FT-IR, TGA and magnetization studies. TEM is the first and the most informative method to characterize the size and shape of hydrophobic NPs. The sizes obtained for the hydrophobic materials shown in **Fig. 2.5** were consistent with the expected sizes. Furthermore, each one was obtained with a narrow size distribution. The images show icosahedral shaped NPs with a diameter of 4.21 ± 0.85, 6.92 ± 0.51 and 9.23 ± 0.80 nm, respectively (images **(a)** to **(c)**).

Because IONPs can be oxidized and then transformed into other metal ferrite structures (α-Fe_2O_3 or ϒ-Fe_2O_3), the XPS method can help to confirm the formation of Fe_3O_4 in the IONPs syntheses. **Fig. 2.6a** shows the XPS Fe 2p spectra of three different IONPs measured to confirm that the syntheses are reproducible. The names NP7, NP8 and NP9 correspond to the preparation of three representative hydrophobic IONPs of 6.75 ± 1.19, 5.05 ± 0.40 and 8.33 ± 0.81 nm respectively. The absence of satellites peaks around 716, 730 and 719 and 733 eV corresponding to FeO and Fe_2O_3, respectively, indicates that the samples are in fact Fe_3O_4. **Fig. 2.6b** shows XPS Fe 3p spectra, confirming that the presence of Fe^{3+} over Fe^{2+} is significantly higher. The ratio Fe^{3+}/ Fe^{2+} obtained is around 1.9 in all the samples measured, which is in good agreement with the theoretical ratio for pure Fe_3O_4 of 2/1.

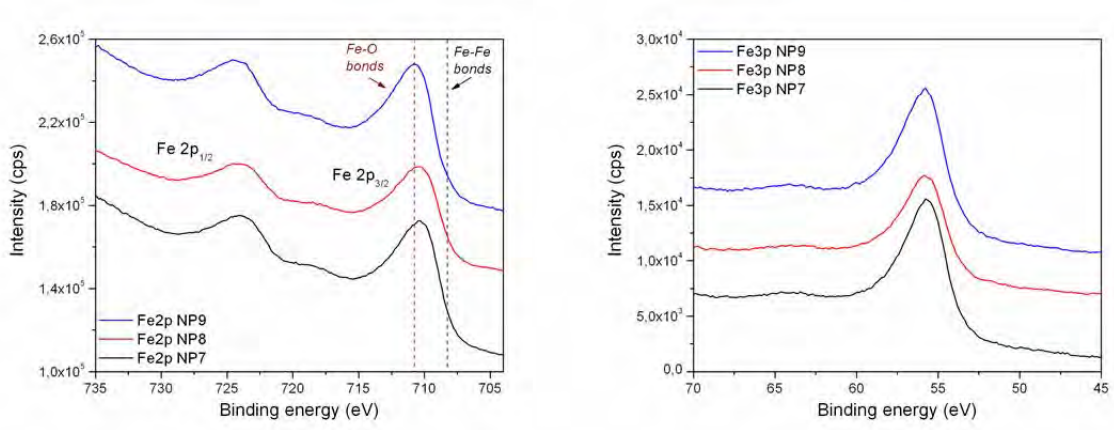

Fig. 2.6. XPS spectra of hydrophobic IONPs. **a)** Fe2p and **b)** Fe 3p spectra.

Based on the Fourier Transform Infrared (FTIR) spectra we can confirm the chemical structure and the surface composition of the IONPs synthesized **(Fig. 2.7)**. The band at 592 cm^{-1} is assigned to the vibration of the Fe–O bond and indicates the presence of Fe_3O_4. The position and separation of carboxylate bands (Δ) in the 1300-1700 cm^{-1} region can be used to deduce the metal carboxylate coordination mode.[82,83] For Δ > 200 cm^{-1} a monodentate ligand is expected, Δ < 110 cm^{-1} confirms the formation of a bidentate ligand and if Δ is between 140 cm^{-1} and 200 cm^{-1} a bridging ligand exists. The differences between the characteristic carboxylate bands reveal the presence of two coordination modes: bidentate and bridging coordination, with a Δ of 104, 133, 160 and 189 cm^{-1}, corresponding with the differences between the peaks at 1610, 1554, 1525, 1450 and 1421 cm^{-1}. The presence of the very weak carbonyl peak at 1707 cm^{-1} suggests that most of oleic acid is attached to the surface of the nanoparticle. The broad band at 3448 cm^{-1} is due to OH stretching corresponding to hydroxyl groups attached to the iron oxide surface and ν(NH_2) due to the presence of oleylamine. The characteristic modes of oleyl groups present in pure oleic acid and oleylamine are detected in the FTIR spectrum of IONPs.[83] The peaks at 3013 cm^{-1} are assigned to ν(=CH), 2922 cm^{-1} for ν_{as}(CH), 2851 cm^{-1} for ν_s(CH), as they are clearly defined in both pure oleic acid and oleylamine spectra. A broad band at 1576 cm^{-1} for δ(NH_2), and a very weak peak at 1073 cm^{-1} for ν(CN) confirm the presence of oleylamine. In the broad band at 1430 cm^{-1} $\delta_{as}(CH_3)$ and $\delta_s(CH_3)$ are included and together with the broad band at 1544 cm^{-1} are attributed to the oleate ion immobilized on the magnetite surface.[84] Thereby, the FTIR spectrum concludes that the IONPs synthesized following the thermal decomposition method are coated by oleylamine and oleic acid coordinated with the iron atoms on their surface.

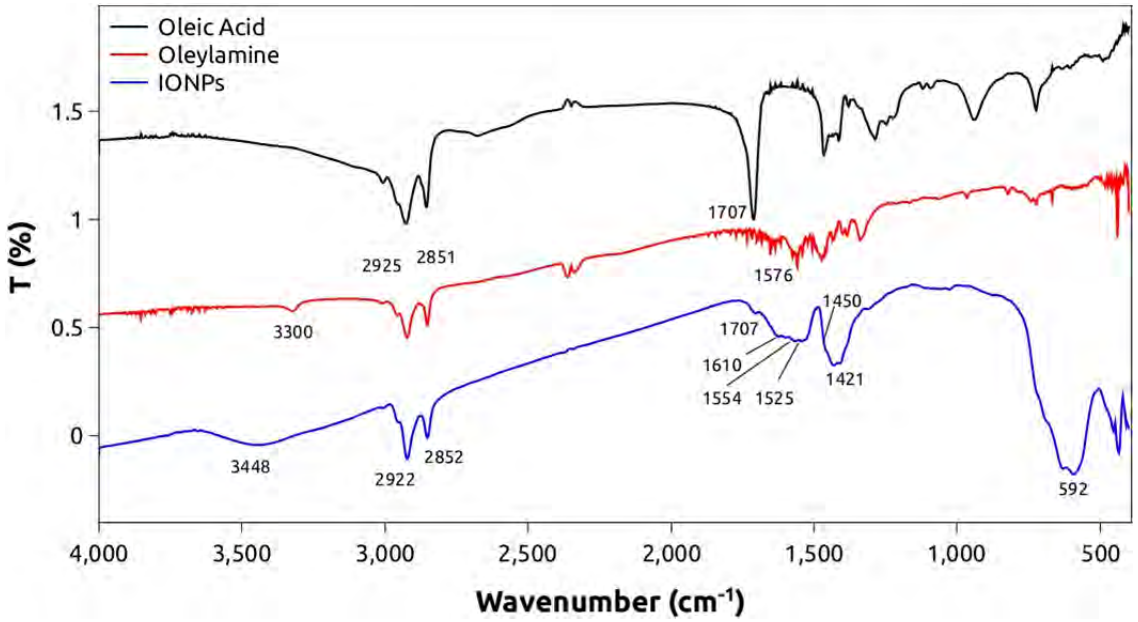

Fig. 2.7. FT-IR spectra of pure oleic acid, pure oleylamine and hydrophobic IONPs.

Thermogravimetric analysis (TGA) was performed to analyze the presence of oleic acid on the IONPs surface. This study is usually performed under inert atmosphere and is based on the measurement of weight gain/loss as the temperature is increased. Each change in weight corresponds to a physical or chemical process (vaporization, crystallization, oxidation,..), due to the increasing temperature. **Fig. 2.8** shows the complete decomposition of oleic acid when the temperature reaches 400 °C (dotted line), in contrast to the behavior of the hydrophobic material, which showed three weight loss steps (solid line). The first weight loss step falls in the range between 40 and 160 °C a short step due to the water lost. The second weight loss step from 250 to 450 °C, is probably due to the loss of free oleic acid on the surface of the IONPs.[84] Finally, the third weight loss step is from 600 to 800 °C and it corresponds to the lost of oleic acid directly bonded onto the IONPs surface. This shift in the temperature could be due to chemisorption of the oleic acid on the IONPs surface, requiring higher temperature for the vaporization of the oleic acid coated on the IONPs than for the oleic acid alone. These studies revealed that the composition of the hydrophobic material consists in 58% of magnetite mass percent and 42% of organic fraction. The sample was studied by the analytical technique ICP-AES to confirm the composition, obtaining 57% and 43%, respectively. Due to the agreement between both techniques and the better

accessibility to the last one, it was decided to use ICP-AES technique from now on to analyze the amount of iron, zinc or another elemental composition of the nanomaterials prepared.

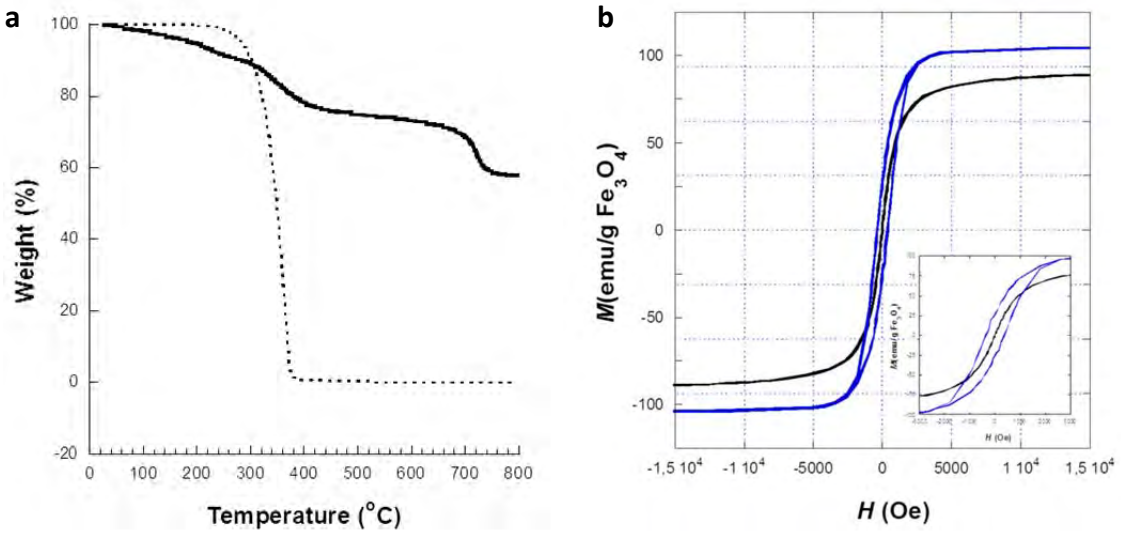

Fig. 2.8. (a) TGA analysis curves for 7 nm hydrophobic IONPs (solid line) and oleic acid (dotted line). **(b)** Magnetization loops for the 7 nm hydrophobic IONPs measured at 2 K (blue) and 293 K (black). Expanded view insets.

To confirm the superparamagnetic behavior of the hydrophobic IONPs, magnetization measurements as a function of the temperature and applied fields were performed. Magnetic measurements were carried out for 6.92 nm hydrophobic IONPs using the Vibrating Sample Magnetometry (VSM) technique. The **Fig. 2.9** shows the hysteresis loops of 6.92 nm hydrophobic IONPs at 2 K and 293 K. The ferromagnetic properties appear with decreasing temperature with the coercivity (H_c) at 360 Oe. However, the hydrophobic IONPs exhibit superparamagnetic behavior at room temperature without presence of hysteresis or remanence. The magnetization value (M_s) of 91 emu g^{-1} is among the highest reported so far.[85–87] With decreasing the temperature, the magnetization of the sample increases, indicating the transition from superparamagnetic to ferromagnetic behavior.

2.2.1.3 Synthesis and size control of ZnSPIONs

The standard structure of magnetite (AB_2O_4) can be modified with several divalent metal cations M^{2+}, such as Mn^{2+}, Ni^{2+} or Zn^{2+} which affects the magnetic properties of spinel ferrites.[31] Gao and Cheon[32,33] described two different procedures to achieve ZnSPIONs based on the metal dopant substitution strategy of iron oxide nanoparticles. These procedures achieve that Zn^{2+} occupy T_d sites (A position) into an inverse spinel structure, that is, Zn^{2+} cations displace the Fe^{3+} changing the net magnetization and the resulting relaxivity values. The replacement of Fe^{3+} with Zn^{2+} ions leads to the transfer of Fe^{3+} ions from T_d to O_h site which produces incremental changes in the magnetization value (M_s).[32,88,89] These changes explain the magnetic behavior of ZnSPIONs with one of the highest relaxivity values among the contrast agents available. $MnFe_2O_4$ nanoparticles are also included in the list of the best magnetic resonance contrast agents, because they also exhibit higher relaxivity values,[81] but the reduced toxicity of Zn over Mn for humans,[90] seems to tip the balance in favor of the ZnSPIONs.

Gao and Cheon procedures were followed to prepare different hydrophobic ZnSPIONs controlling the size and the stoichiometry of the syntheses. In both cases, they remark the importance to find the right stoichiometry in the general formula of $(Zn_xFe_{1-x})Fe_2O_4$, because if the doping level of Zn^{2+} ions is higher than $x > 0.4$, the net magnetization moment will decrease instead to increase (because the interactions between Fe^{3+} ions in O_h sites are dominant), obtaining the opposite of the desirable effect.

The protocol reported by Gao and co-workers was used to prepare the ZnSPIONs shown in **Fig. 2.9a**. The smallest size of 3.55 ± 0.30 nm was prepared using $Fe(acac)_3$ as precursor and $ZnEt_2$ as zinc source. This source is used over $Zn(acac)_2$ because the authors of this protocol discussed that the resulting ZnSPIONs are more monodisperse and the stoichiometry can be better controlled. It is important to take special care with this protocol because $ZnEt_2$ is a pyrophoric reagent, thus, the reaction must be kept under inert atmosphere avoiding as much as possible any contact with water. OAc is used as surfactant and 1,2-hexadecanediol as reducing agent. Hexadecylamine (instead OAm) is used to facilitate the incorporation of the zinc into the mixture when the $ZnEt_2$ is incorporated in the reaction. $ZnEt_2$ is added in a second stage when the temperature is raised to 150 °C. The

stoichiometry is controlled by the amount of the reagent added in this step and it is calculated by the molar ratio of Zn and Fe, represented as "x" in the general formula. After 30 min at 275 °C, the mixture was cooled down to room temperature and several washes and precipitation steps were carried out to isolate the final product.

To obtain bigger ZnSPIONs, the procedure is similar to the previous synthesis with the only difference that in the first step the mixture was heated at 200 °C for 1 h. Then the $ZnEt_2$ was added precisely to carefully control the stoichiometry of the reaction and finally the temperature is raised to 300 °C for 1 h. The hydrophobic NPs represented in **Fig. 9b** with 5.65 ± 0.43 nm were synthesized following this procedure.

These 5.65 nm ZnSPIONs were used as seeds to synthesize larger NP. The seeds were dissolved in hexane before mixing them with the rest of reagents: $Fe(acac)_3$, 1,2-hexadecanediol, hexadecylamine and oleic acid in benzyl ether. The mixture is heated firstly at 100 °C for 30 min to eliminate the hexane. Then, the mixture is heated at 200 °C for 1h. After this stage and before the reflux, the $ZnEt_2$ was added into the mixture. Finally, the mixture is brought to reflux for 30 min. The protocol afforded 9.02 ± 0.53 nm hydrophobic NPs represented in **Fig. 2.9c.**

In the syntheses of 3.55, 5.65 and 9.02 nm ZnSPIONs quite narrow size distributions were obtained as the authors mentioned.

We also tested a second procedure based on Cheon protocol, in this procedure, the metallic precursor used was $Fe(acac)_3$ and the zinc source was $ZnCl_2$. The procedure consists in mixing all the reaction reagents ($Fe(acac)_3$, $ZnCl_2$, OAc and OAm in octyl ether) under magnetic stirring and inert atmosphere and increasing the temperature to 300 °C for 1h. After removing the heating source, a precipitation stage is carried out. Bigger NPs, around 15 nm should be synthesized following this protocol.

The results were not very encouraging, although the synthesis was performed several times following the published protocol we could not achieve the desired NPs.

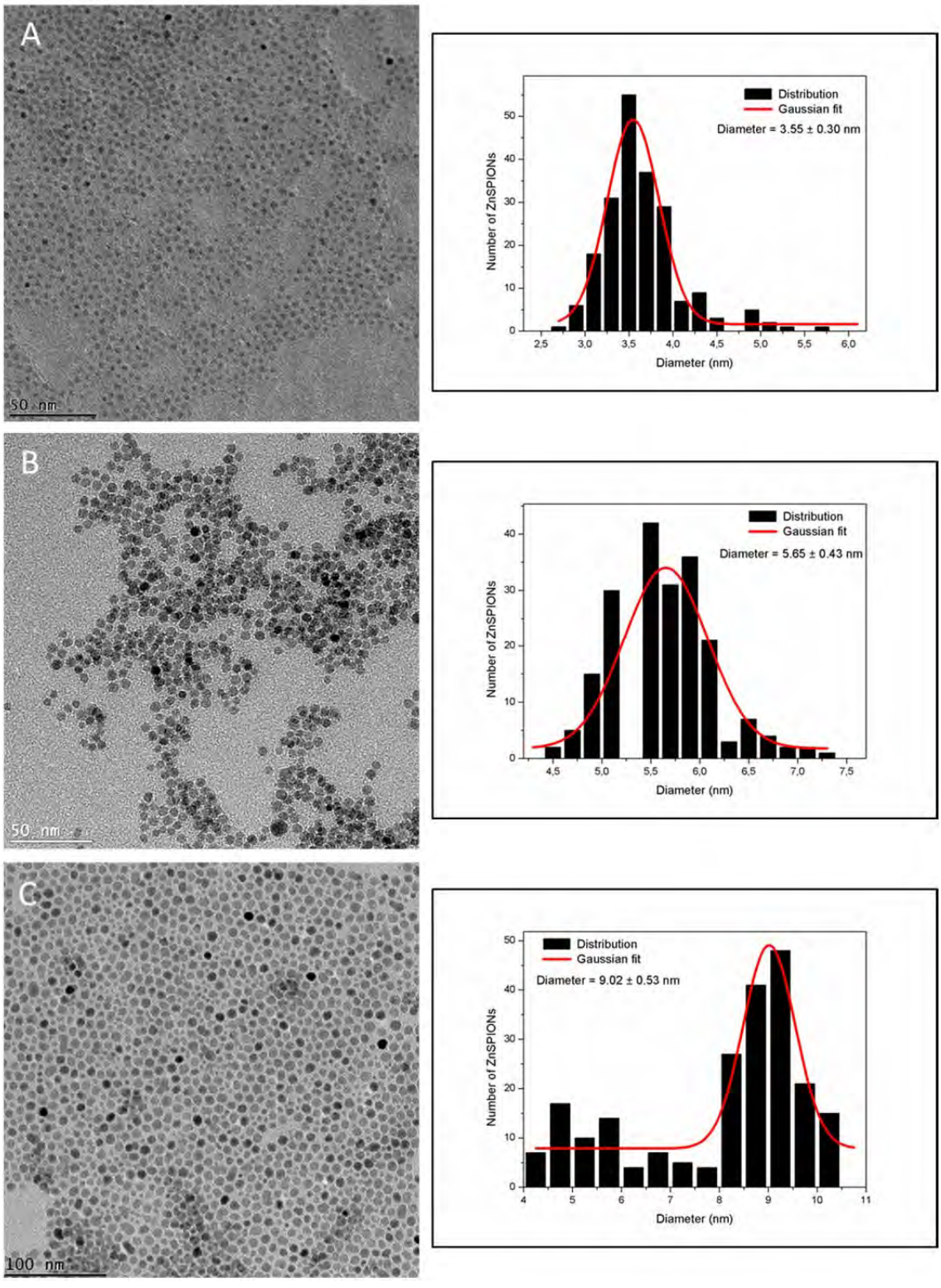

Fig. 2.9. Representative TEM images and size-histograms of ZnSPIONs.

2.2.1.4 Characterization of ZnSPIONs

A key step in the preparation and characterization of ZnSPIONs for the development of improved MRI constrast agents is to achieve the proper zinc doping level in the spinel structure. Thus, it is necessary to find the balance between the suitable size and suitable doping level for obtaining a magnetic behaviour which translates in better T_2 relaxivity values than with the un-doped materials. For this reason this section focuses the discussion on the results of the studies carried out to study the changes, elemental makeup and the oxidation states brought about by zinc doping in the as prepared hydrophobic ZnSPIONs. The first experiments performed were to verify the zinc presence by XPS analyses.

Fig. 2.10a shows the XPS Zn 2p spectra of the 3.55 nm ZnSPIONs. The peak around 1021 eV is associated with Zn^{2+} in ZnO binding and it matches well with the literature values. Moreover, the Zn 2p binding energy and the binding energy difference values between the two peaks (around 24 eV) reveal that Zn atoms are in +2 oxidation state in ZnO.[91] Also we can confirm this oxidation state using the XPS O 1s spectrum, because it is reported than ZnO has an spectrum with two peaks as we have seen in the measurements. The broad asymmetric curve can be deconvoluted into two well-defined peaks at binding energy of 532.1 and 530.1 eV. The peak at 530.1 eV is characteristic of the metal–oxygen–metal (M–O–M) lattice, whilst the peak at 532.1 eV has been reported to indicate the presence of other oxygen species (i.e. carboxylate species) and/or defect sites with low oxygen co-ordination in $Zn_xFe_{3-x}O_4$ systems. The peak at 534 eV is associated with the bending energy of the OH in the carboxylic acid group.[92]

In the three sizes synthesized (3.55, 5.65 and 9.02 nm) a reproducible pattern of XPS Zn 2p spectra was obtained, confirming that in all the reactions the iron oxide nanoparticles were successfully doped with zinc. The Zn/Fe ratio was calculated using the ICP-AES technique, obtaining consistent values with the expected ones (the ratio of Zn/Fe precursors used in the syntheses was 0.21) as they are shown in **Table 2.1**. Although XPS is a surface chemical analysis technique, the experiments suggests that there is a structural homogeneity on the NPs because when defects are generated on the structure, these are easily detected on the surface of the material. Furthermore, the presence of three types of

oxygen sites on the surface is in agreement with the creation of oxygen vacancies due to Zn doping into the structure.

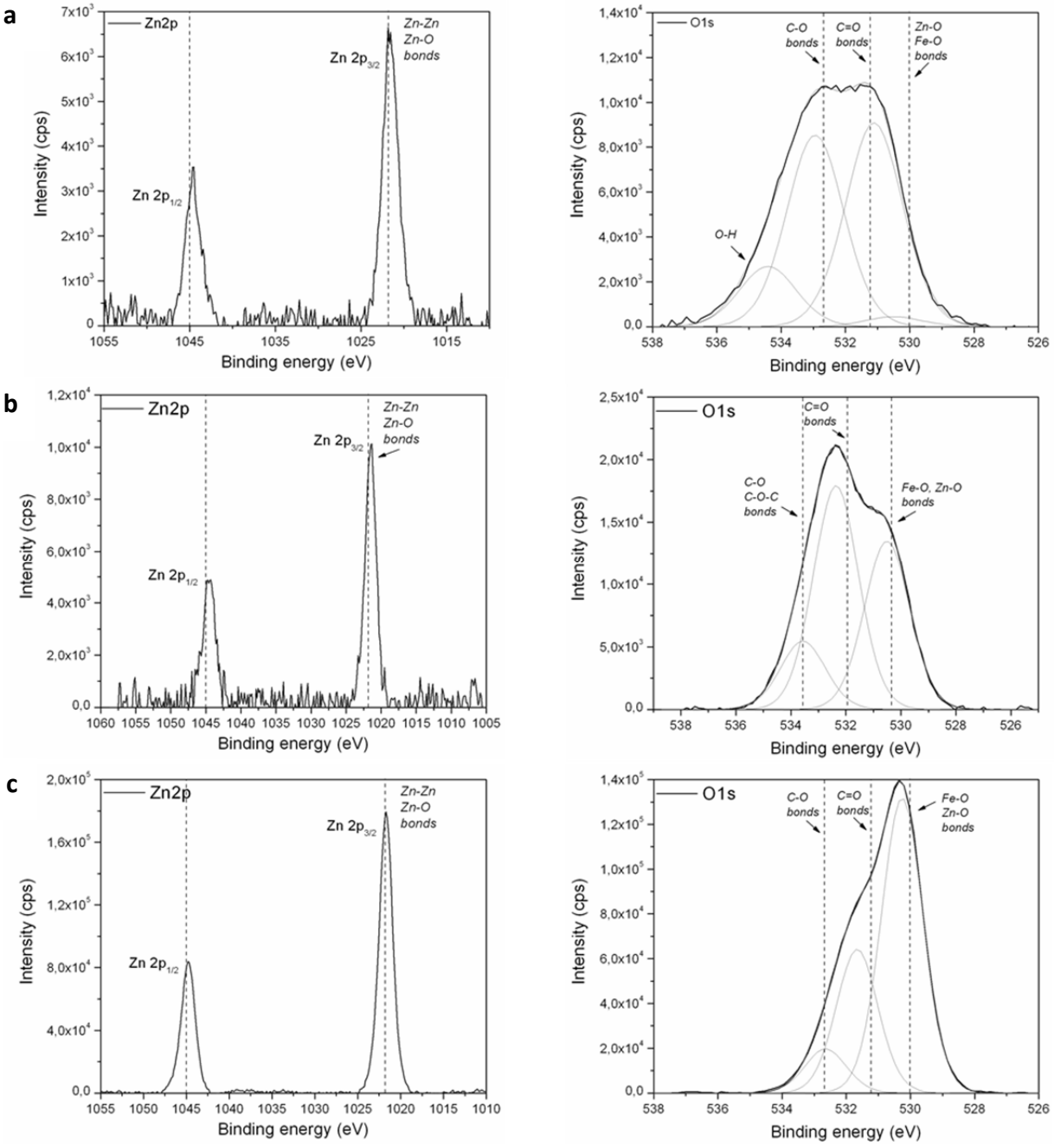

Fig. 2.10. XPS spectra of Zn 2p and O 1s of ZnSPIONs **(a)** 3.55 nm, **(b)** 5.65 nm and **(c)** 9.02 nm.

Size (nm)	Zn (mg/L)	Fe (mg/L)	Zn (μmols)	Fe (μmols)	Zn/Fe	Zn_x doped
3.55	0.51	2.93	0.779	5.246	0.15	0.39
5.65	1.00	3.42	1.528	6.123	0.25	0.60
9.02	1.09	5.86	1.676	10.492	0.16	0.41

Table 2.1. Values of Zn/Fe ratio corresponding to the 3.55, 5.65 and 9.02 nm ZnSPIONs obtained by ICP-AES.

TGA analysis was used to characterize the amount and interaction of the oleic acid/oleate capping ligands bound to the ZnSPIONs **(Fig. 2.11a)**. Controlled heating of the as prepared hydrophobic NPs yielded two distinct weight loss peaks. The mass loss between 300 and 450 °C corresponds to the desorption of an outer layer of these organic capping ligands. A second inflection point occurs between 650 and 800 °C as it was aforementioned from the loss of the more tightly bound oleate. This inner layer of oleate capping ligands is thought to be stabilized via metal carboxylate coordination bonds. As a result, it can only be removed from the surface at higher temperatures. The higher temperature required to remove the oleate ligands from the ZnSPIONs agrees well with what would be expected on the basis of the Irving Williams series, which establishes the relative stabilities of complexes formed by metal ions and in which Zn^{2+} ions form stronger complexes than Fe^{2+} ions. TGA showed that metal oxide content was 58 % and 72 % for the IONPs and ZnSPIONs, respectively.

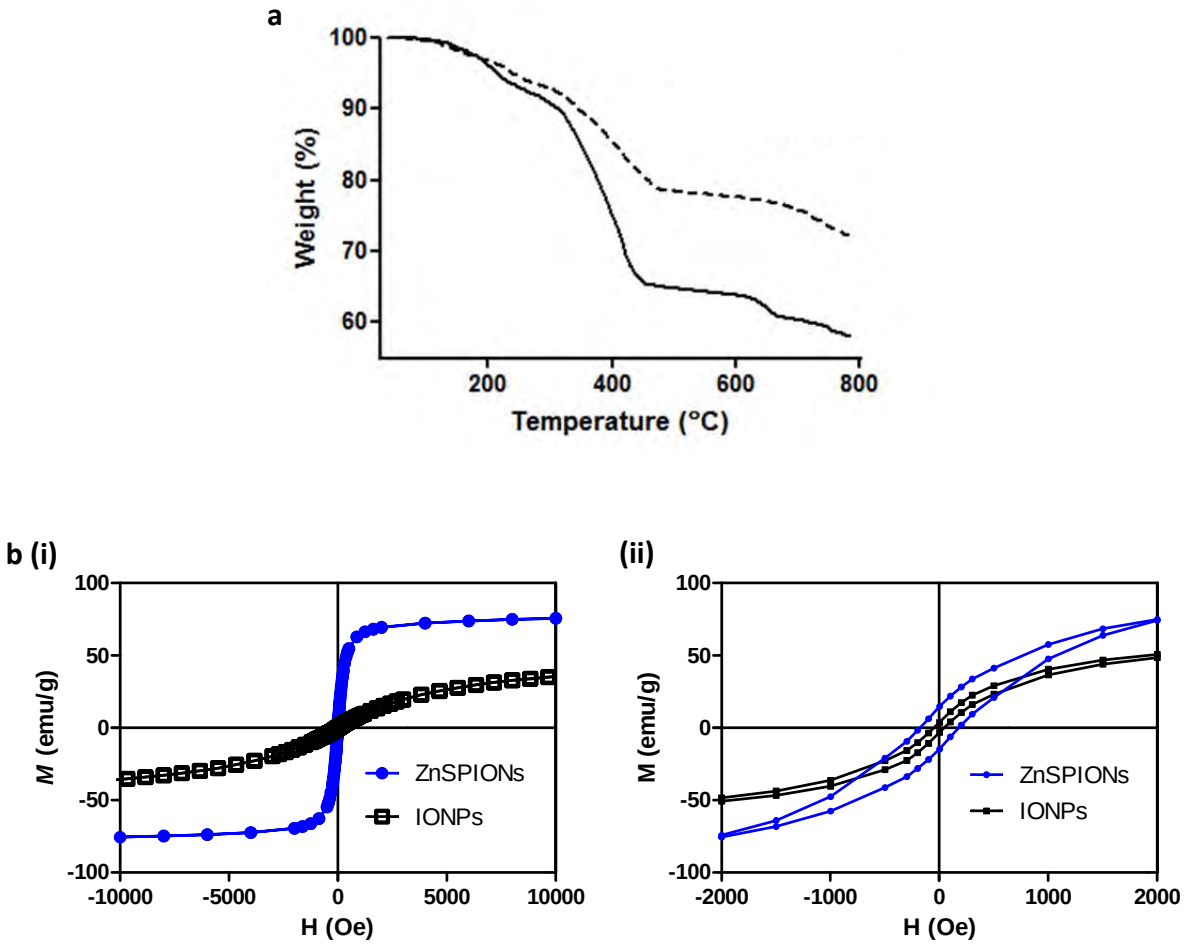

Fig. 2.11. (a) TGA analysis curves of the oleic acid–capped ZnSPIONs 5.65 nm (dotted line) and IONPs 5.05 nm (solid line). **(b)** Magnetization curves of IONPs and ZnSPIONs at **(i)** 293 K and **(ii)** 5 K (magnified view).

One of the motivations for doping magnetite NPs with Zn^{2+} ions is to improve the magnetic properties of IONPs for biomedical applications. The magnetization (*M*) versus applied magnetic field (H) of the IONPs and ZnSPIONs used for the above assay was measured at 5 K and 293 K **(Fig. 2.11b)**. These 5-6 nm NPs exhibit superparamagnetic behavior without hysteresis and remanence at 293 K and ferromagnetic behavior with a coercivity (H_c) of 51 Oe (IONPs) and 178 Oe (ZnSPIONs) at 5 K. The M_s of the IONPs and ZnSPIONs is 55 emu g^{-1} and 76 emu g^{-1} respectively at 293 K. The higher magnetization of the ZnSPIONs arises from the partial substitution of Fe^{3+} cations at A sites by non-magnetic atoms such as Zn^{2+}, which results in an enhancement of the net moment due to the reduced antiferromagnetic interaction between the Fe^{3+} ions at A and B sites. Since this effect is seen to increase only up to a certain percentage of zinc (< 20% of the total transition metal total),

the prepared $Zn_{0.5}Fe_{2.5}O_4$ NPs can be considered optimum for enhanced MR imaging, where a high mass magnetization value typically leads to enhanced MRI sensitivity (*vide infra*).

2.2.2 Preparation and characterization of water soluble MFe_2O_4

The main drawback of the synthesis of IONPs by the thermal decomposition method is that the surface of the NPs has to be modified to achieve a water soluble system. This surface modification will affect the surface charge, the biocompatibility and the magnetic properties of the water soluble system.

The methods applied during this work to obtain water soluble systems are ligand exchange using DMSA and PEI as ligands and ligand addition using PEGylated phospholipids (PL-PEG).

2.2.2.1 Ligand exchange using 2,3-dimercaptosuccinic acid (DMSA) (DMSA-coated IONPs; IONP@DMSA)

DMSA is a small molecule, but it has excellent capacity to complex with metallic ions by its carboxylic groups. The remaining free carboxylate groups provide negative surface charge and the ability to conjugate with biomolecules. The high stability in aqueous solution comes also from the intermolecular disulfide cross-linking between DMSA molecules.[93] In fact, due to their chelating role, DMSA is actually used in humans in the treatment of arsenic and mercury poisoning.[94]

The surface modification using DMSA takes place by ligand exchange with the oleic acid present on the surface of the hydrophobic IONPs **(Fig. 2.12a)**. The critical factor of this synthesis, after the stirring overnight and the purification steps, is the addition of an alkaline solution to dissolve the final pellet. Then, the mixture is adjusted at pH 7 with an acidic solution. This final treatment instead of redispersing the mixture directly in an aqueous solution at pH 7, seems to be essential for the longer stability of the sample. This method afforded stable water soluble systems even three months after their preparation with no significant alteration in their size or charge.

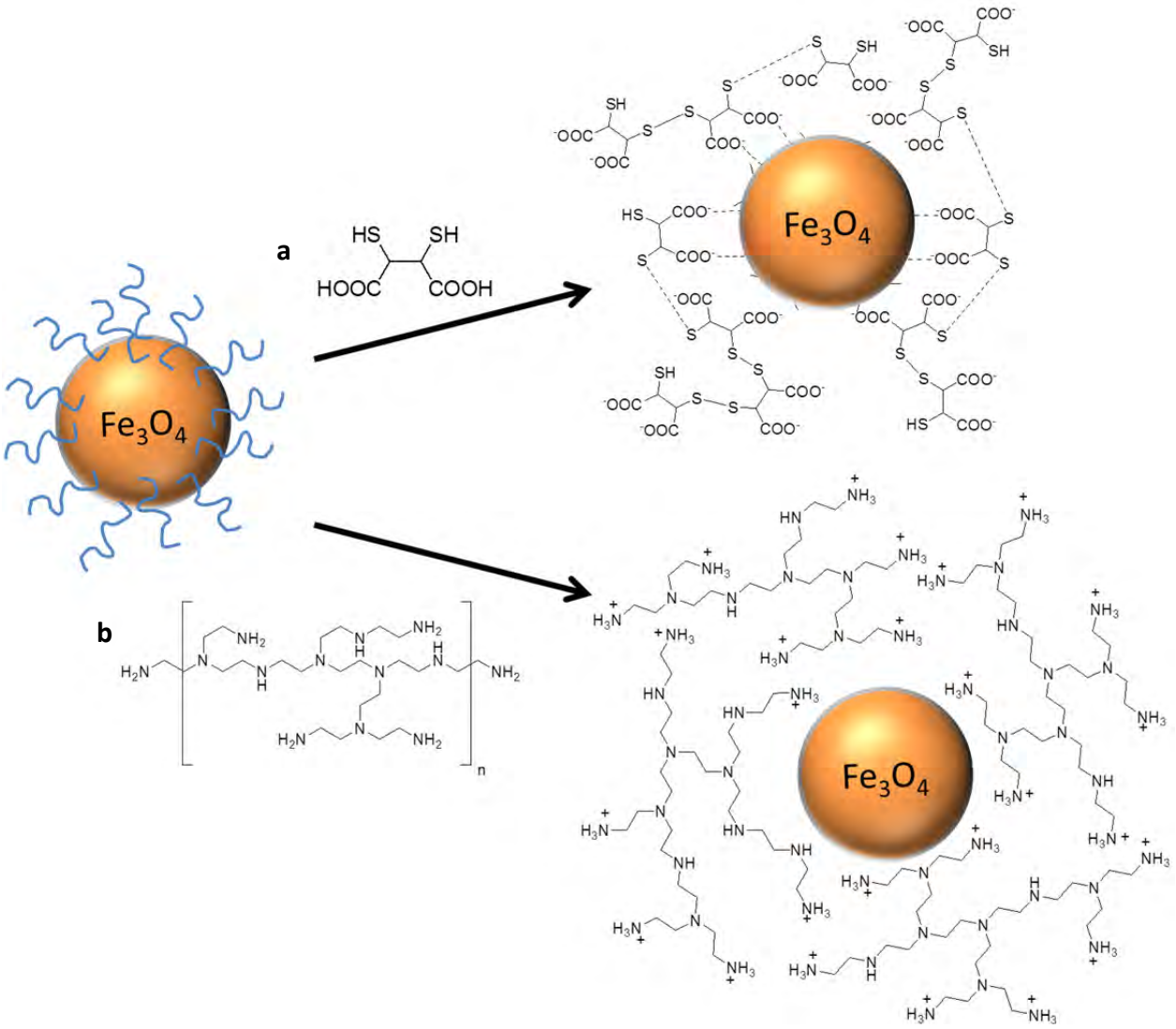

Fig. 2.12. Schematic illustration of the ligand exchange method using two different coatings **(a)** DMSA or **(b)** PEI.

Roca *et al.*[45] suggested that the suspension of DMSA-coated IONPs at pH 7 is unstable because both carboxylic groups are bonding to the NP surface and the thiol groups can form disulfur bonds between particles triggering instability. On the contrary, in alkaline solution the relative orientation of carboxylic groups changes and only some bind to the IONP. In this way the deprotonation of the metal-freee carboxylic groups provide enough strong negative charge on the surface of the particles to minimize their association via disulphide cross linking. In the presence of acidic pH, the protonation of carboxylate groups leads to

aggregation.[95] However, Huh et al.[44] explain that these disulfide cross-linking can promote stability of the solution, presumably by promoting linking of DMSA molecules around the IONP.

Ligand exchange was successfully performed on the 6.92 and 9.23 nm IONPs previously presented in **Fig. 2.5**. The DMSA-coated IONPs were characterized by TEM and by DLS to determine the hydrodynamic diameter (D_H) of the micelles. The D_H values obtained by DLS are 58.77 and 21.04 nm respectively, however the presence of aggregates of around 100 nm is also visible by TEM, probably due to the mentioned interparticle cross-linking between disulfide bonds. The likely disulfide cross-linking appears to generate worm-like structures as it is clearly visible in the TEM images shown in **Fig. 2.13a**.

Zeta potential measurements (ζ) demonstrate that the DMSA was successfully incorporated with values around -40 mV at pH 7 in the NPs tested, **Fig. 2.13c.** These values are comparable with the systems reported so far.[45,93]

The relaxivity measurements were carried out at 1.5 T and these studies showed that the r_2 values increase from 100 to 170 $mM^{-1}s^{-1}$ with the increase of the nanoparticle size from ca. 6 nm to 9 nm. These r_2 values are in good agreement with the values obtained by Roca et al. if one takes into consideration that both the IONP size and aggregate size contribute to the overall enhancement of r_2.[96,97]

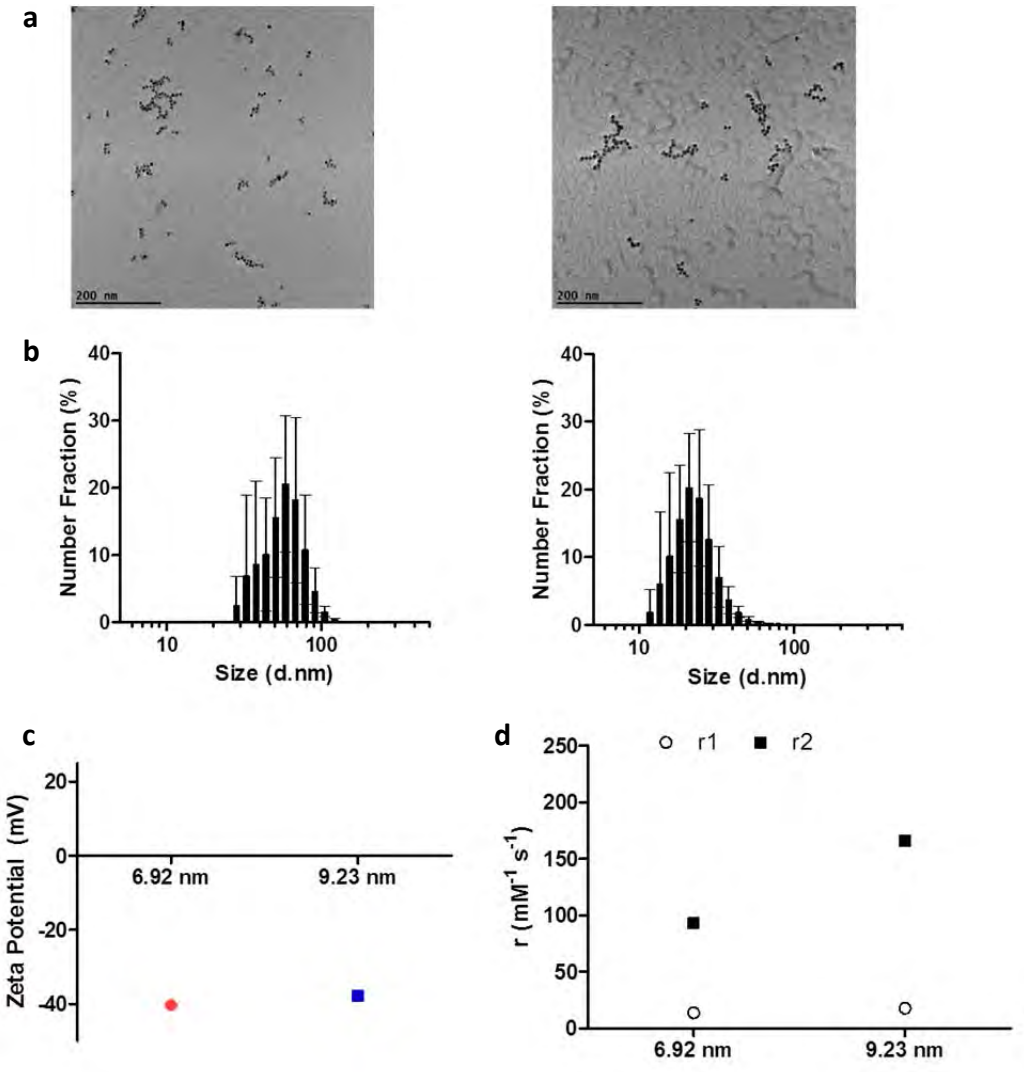

Fig. 2.13. Characterization of DMSA-coated IONPs. **(a)** TEM images. **(b)** DLS measurements. **(c)** Zeta potential values. **(d)** Relaxivity measurements of the micelles prepared with 6.92 and 9.23 nm hydrophobic IONPs.

2.2.2.2 Ligand exchange using polyethylenimine (PEI) (IONP@PEI)

The ligand exchange method was applied to coat 6.92 and 9.23 nm IONPs with polyethyleneimine (PEI) to make them water soluble and suitable for biomedical applications **(Fig. 2.12b)**.

PEI is a water-soluble cationic polymer whose properties have attracted the attention of many research groups for different applications, including in adsorption separation fields

of heavy-metal ions[98] and uses in biology and medicine as non-viral vectors for plasmid and oligonucleotide delivery.[99] Several types of NPs, including IONPs, have been capped with this polymer coating; mainly to develop efficient delivery systems for nucleic acids.[100,101]

PEI is available in a wide range of molecular weights with branched or linear structures.[102] It is reported, for instance, a discrepancy between the behavior of the different molecular weight of PEI during the studies *in vitro* and *in vivo* of PEI/DNA complexes.[100,103] The experimental studies reported indicate that the low molecular weight PEIs show a greater transfection efficiency and lower toxicity compared to high molecular weight PEIs,[102,104] and that linear PEIs are relatively nontoxic compared with the branched PEIs. However linear PEIs are less water soluble and exhibit poor transfection efficiency.[105] Levereging all these factors two molecular weights of branched PEIs were chosen, 1.8 and 25 kDa, in order to find a balance between low toxicity in cells and an efficient delivery of drugs or biomolecules.

In the case of PEI polymer of 25 kDa, the procedure followed to functionalized the IONPs consists of exchanging the hydrophobic layer with PEI in chloroform under stirring. After the complete evaporation of the chloroform and the addition of water, the sample was centrifuged and dialyzed for 24 h to eliminate the excess of PEI free, generating a very stable system and soluble system in water.

As it is shown in **Fig. 2.14a**, DLS measurements showed that the IONPs coated with PEI (IONP@PEI systems) present larger hydrodynamic diameters than the IONP@DMSA systems with 68.06 and 91.28 nm for 6.92 and 9.23 nm IONPs respectively. The TEM images of the IONP@PEI formed are shown as a representative of the results obtained. The shape of the aggregates seems to be different, DMSA coated IONPs are grouped in a straight line, whilst PEI-coated IONPs are grouped as spherical structures, suggesting that the multidentate polymeric coating contributes significantly towards regulating the shape and size of these nanostructures.

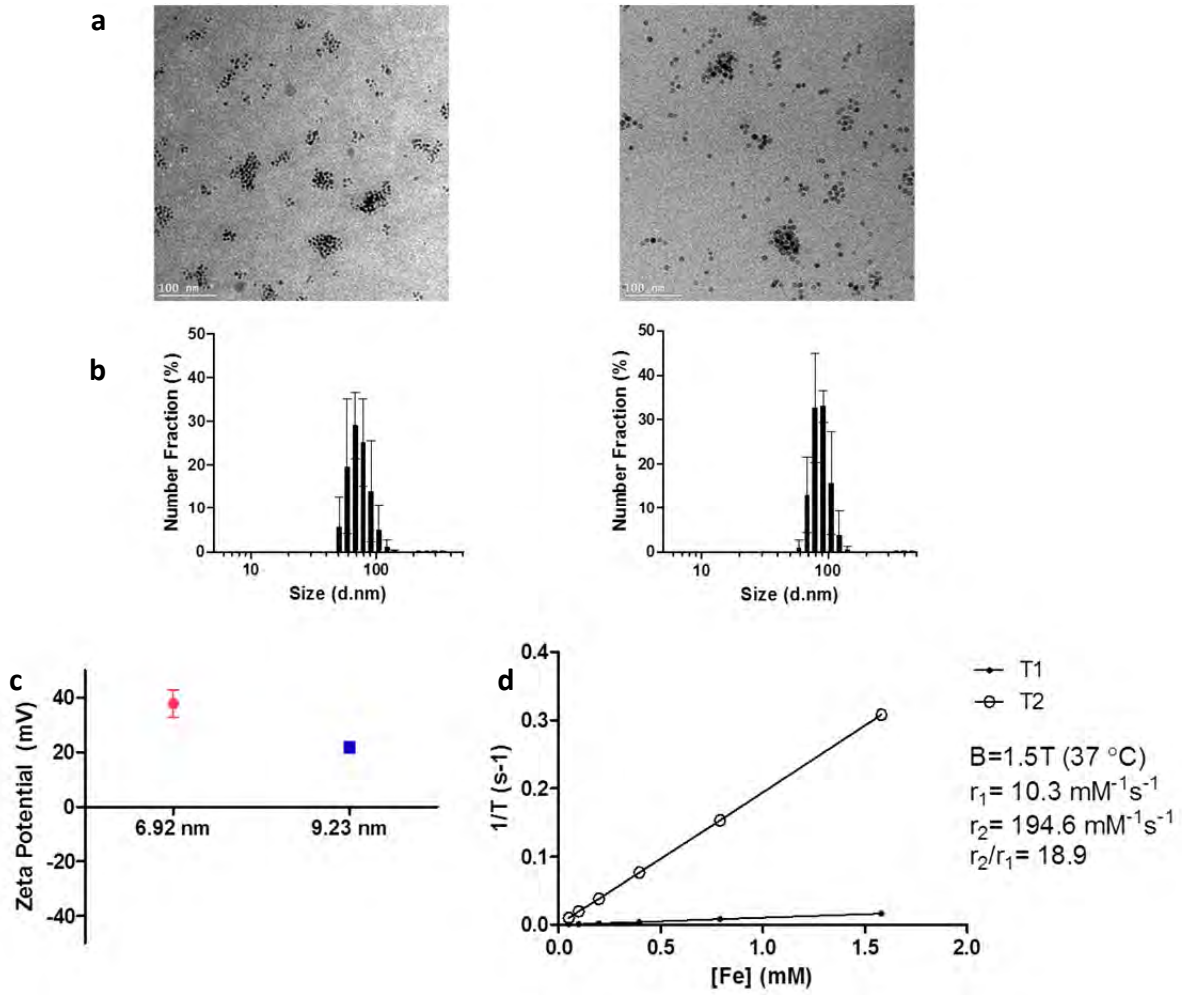

Fig. 2.14. Characterization of PEI-coated IONPs. **(a)** TEM images. **(b)** DLS measurements. **(c)** Zeta potential values of the micelles prepared with 6.92 and 9.23 nm hydrophobic IONPs. **(d)** Relaxivity measurements of the IONP@PEI-6.92 nm.

The ζ-potential measurements reflect that the exchange of ligand occurred successfully due to the positive values obtained for 6.92 and 9.23 nm IONPs of + 38 and + 22 mV, respectively **(Fig. 2.14c)**.

The relaxivity measurements of the system formed with the IONPs of 6.92 nm are reported in the **Fig. 2.14d.** The r_2 value of 194 $mM^{-1}s^{-1}$ suggests that it could be a good MRI contrast agent.

The above procedure and others methods involving sonication were used to perform ligand exchange with PEI polymer of 1.8 kDa, but water-soluble and stable samples could not

be achieved with any of the hydrophobic NPs used before. Based on the experiments carried out by Steitz *et al.*[106] it is possible that the minimum ratio PEI:Fe to avoid the flocculation of the NPs and to cover completely the surface of the IONPs is not achievable with such low MW PEI polymer.

2.2.2.3 Ligand addition using PEGylated phospholipids (PL-PEG)

a) IONP-filled PL-PEG micelles (IONP@PL-PEG)

Among all the polymers and ligands suitable for improving the solubility and the biocompatibility of hydrophobic NPs, PEG and its derivatives have been widely used. PEG polymers have low toxicity and no immunogenicity and there are several PEGylated products approved by the FDA (Food and Drug Administration) for clinical use.[107]

In this work, PEGylated phospholipids (with PEG of molecular weight 2000 (PEG2000)) were used for the functionalization of the IONPs containing. The use of PL-PEG micelles to encapsulate NPs or other kinds of hydrophobic molecules for biomedical applications has been widely reported in the literature.[72,108–110] In the specific case of the IONPs prepared in this thesis, the stability of the resulting IONP@PL-PEG micelles arises from the hydrophobic interaction between the layer oleic acid/oleyamine coating the hydrophobic IONP and the hydrocarbon part of the PL-PEG **(Fig. 2.15)**.

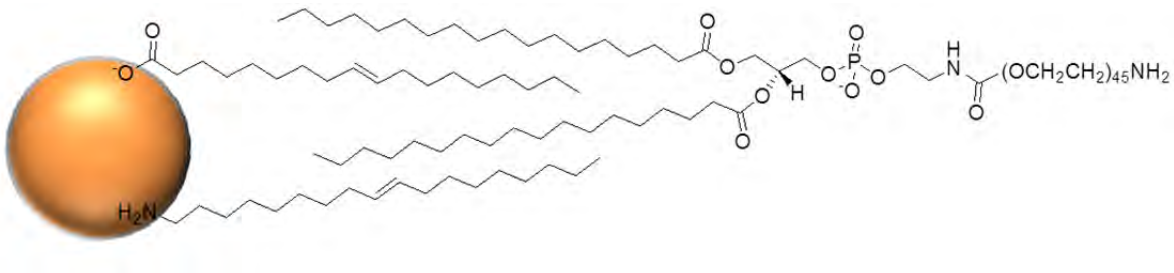

Fig. 2.15. Bilayer structure around the IONP core in IONP@PL-PEG micelles.

The general preparation of the IONP@PL-PEG micelles is based on the self-assembly of the PL-PEG molecules around the hydrophobic IONP(s).[108] To prepare micelles filled with a single or small number of IONPs the hydrophobic IONPs (1 mg) and PEG-phospholipid(s) (2 mg) were dissolved in chloroform. The solvent was allowed to evaporate slowly overnight. After complete evaporation of the solvent under vacuum, the residue was heated at 80 °C and then it was rehydrated in 1 mL of water. The solution was centrifuged. The supernatant containing individual micelles was passed through a filter and ultracentrifuged to remove the empty micelles. Finally the pellet was dissolved in PBS, obtaining micelles with one or a few IONPs inside.

To prepare IONP@PL-PEG micelles decorated with amine or carboxylic acid groups a mixture of DPPE-PEG(2000)-OMe and DSPE-PEG(2000)-NH_2 or DSPE-PEG(2000)-COOH in 50-50 percentage was used keeping the IONP:PL-PEG mass ratio also 1:2.

The results from a representative synthesis are shown in **Fig. 2.16** with hydrophobic IONPs of 4.21 nm encapsulated inside of three different type of micelles performed with: **(i)** DPPE-PEG(2000)-OMe, **(ii)** DPPE-PEG(2000)-OMe and DSPE-PEG(2000)-COOH and **(iii)** DPPE-PEG(2000)-OMe and DSPE-PEG(2000)-NH_2**.** The values of D_H obtaining by DLS are very similar in the three cases, ca. 24, 21 and 24 nm for micelles, respectively.

The presence of amine and carboxylic groups in the micelles were confirmed by ζ-potential measurements as it shown in **Fig. 2.16**. It was demonstrated by the ζ-potential measurements that the charge of the micelles had changed, which implies that the surface of the NPs was modified successfully.

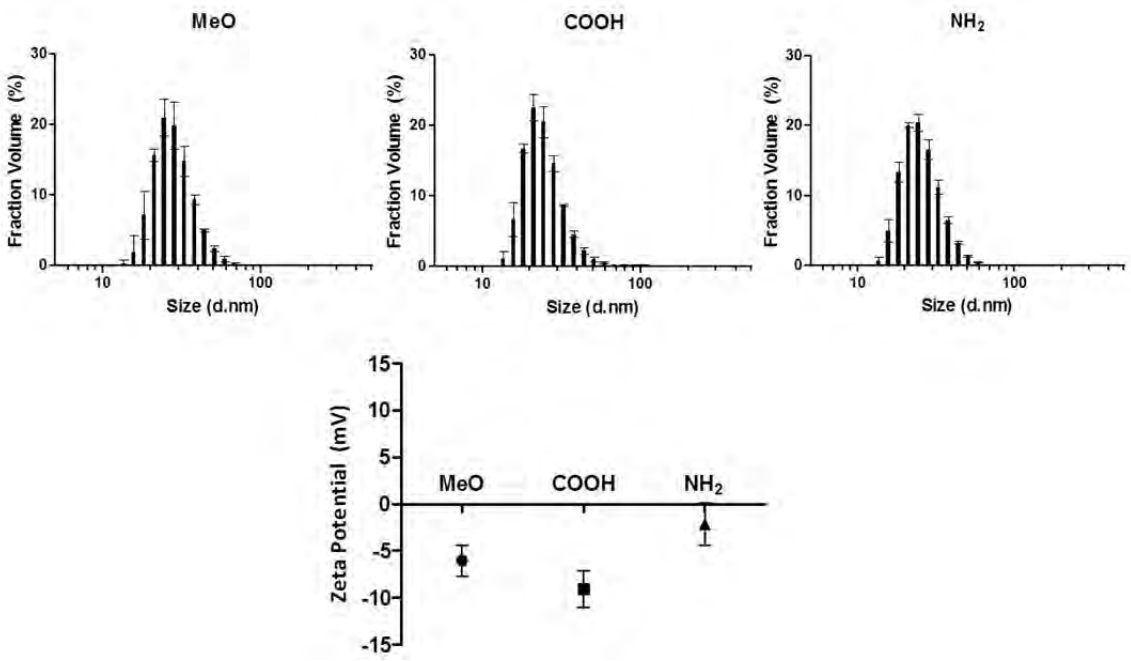

Fig. 2.16. Size and ζ-potential measurements of IONP-PL-PEG-X micelles (X = OMe, COOH, NH_2).

Next we attempted to tune the size of the micelles seeking the formation of micelles loaded with much larger numbers of IONPs to compare the different relaxivity properties as a result IONP clustering **(Table 2.2).**

The size of the IONP@PL-PEG micelles can be adjusted by changing the mass ratio of hydrophobic IONPs and PL-PEG during the synthesis. Large IONP@PL-PEG micelles could be obtained for instance in the following way. 1 mg of hydrophobic IONPs and 1 mg of PEG-phospholipid(s) were dissolved in chloroform. After the evaporation and rehydration steps, the solution was centrifuged. The supernatant solution was discarded and the pellet was resuspended in water and centrifuged. The supernatant contains the large micelles.

The comparison of relaxivity values obtained for small and large IONP@PL-PEG micelles was studied at 1.5 T only with DPPE-PEG(2000)-OMe on their surface to simplify (i.e. IONP@PL-PEG methoxy micelles) the experiment but with the three hydrophobic IONPs previously shown in **Fig. 2.5** of 4.21, 6.92 and 9.23 nm.

IONP core (nm)	D_H	r_2 ($mM^{-1}s^{-1}$)	r_1 ($mM^{-1}s^{-1}$)	r_2/r_1
4.21 ± 0.85	20.8	30.5	2.9	10.5
6.92 ± 0.51	25.6	44.2	4.9	9.0
	283.0	134.6	3.7	36.4
	483.0	150.0	3.6	41.7
9.23 ± 0.80	22.3	90.0	6.1	14.7
	86.0	165.1	6.4	25.8

Table 2.2. Relaxivities, core and hydrodynamic diameters of different IONP@PL-PEG methoxy micelles.

For all the IONP@PL-PEG methoxy micelles prepared the longitudinal relaxivity r_1 stayed in 3-7 $mM^{-1}s^{-1}$, increasing progressively with the size of the hydrophobic IONPs, and decreasing slightly as the D_H of the micelle increased. The effect in the transverse relaxivities r_2 values is more significant, obtaining values ranging from 31 to 90 $mM^{-1}s^{-1}$ for single micelles to 65 to 160 $mM^{-1}s^{-1}$ for micelles with large IONP clusters. As an example of the large effect of IONP clustering on r_2, going from single/small micelles (D_H ca. 20 nm) to larger systems (D_H ca. 480 nm) with the 6.92 nm IONPs, the r_2 values change from 44 $mM^{-1}s^{-1}$ to 150 $mM^{-1}s^{-1}$ respectively.

b) ZnSPION@PL-PEG micelles

Initially the protocol described by Bárcena *et al.*[33] was followed for the preparation of the encapsulated ZnSPIONs into PL-PEG micelles. We found, however, that we could not only reduce the amount of PL-PEG four times using chloroform as solvent but also that it was possible to carry out the rehydration without heating for 3 h at 70 °C. ZnSPIONs (1 mg) and DPPE-PEG(2000)-OMe (5 mg) are dissolved in chloroform. The organic solvent was allowed to evaporate using an argon flow. After 20 min., a final evaporation with 30 s in a water bath at 70 °C was carried out and then it was rehydrated in 1 mL of water. Then, the samples are treated in the same way as in the case of IONPs.

The micelle sizes and r_1 and r_2 values measured at 1.5 T are represented in **Table 2.3.** The r_2 values decreased from ca. 117 to 75 mM^{-1} s^{-1} going from 9.02 to 3.55 nm core sizes with a similar D_H of around 20 nm. The effect of Zn(II) doping is also evident by comparing

with the results shown in **Table 2.2** for IONP@PL-PEG methoxy micelles. These results are also in agreement with the magnetization results.

Core size (nm)	Size (nm)	r_2 ($mM^{-1}s^{-1}$)	r_1 ($mM^{-1}s^{-1}$)	r2/r1
3.55 ± 0.30	18.30	74.5	3.8	19.6
5.65 ± 0.43	25.00	94.9	6.8	13.9
9.02 ± 0.53	25.80	117.3	10.3	11.4

Table 2.3. Relaxivities, core and hydrodynamic diameters of different ZnSPION@PL-PEG methoxy micelles.

2.2.3 Development of the multimodal imaging system

2.2.3.1 MR properties of IONP@PL-PEG micelles

Two of the systems described on **Table 2.2** were selected for a more detailed study of IONP@PL-PEG micelles as MRI contrast agents: the micelles with D_H=25 nm and with D_H= 283 nm obtained with the hydrophobic IONPs of 6.92 nm.

The MRI signal intensity of these two micelles was evaluated through the preparation of phantoms at the same iron concentrations. As **Fig. 2.17a** shows, for a given iron concentration larger micelles exhibited a darker image (T_2-weighted) comparing with the smaller micelles, that is, the aggregates increase the image contrast. Comparing with other research groups focused in the same single and aggregate contrast agents analysis,[85,111] this work is one of the few examples where the coating used to tune the size of the IONP-based contrast agent was not changed.

The images are also consistent with the relaxivity values obtained at 11.7 T as **Fig. 2.17b** shows. Single micelles present a r_2 value of 68.8 $mM^{-1}s^{-1}$ compared with the 86.9 $mM^{-1}s^{-1}$ achieved for the aggregates. Both the T_2-weighted MR images and the relaxivity values show the powerful enhancement of single and aggregate IONP micelles (performed with PEG phospholipids) even at high fields.

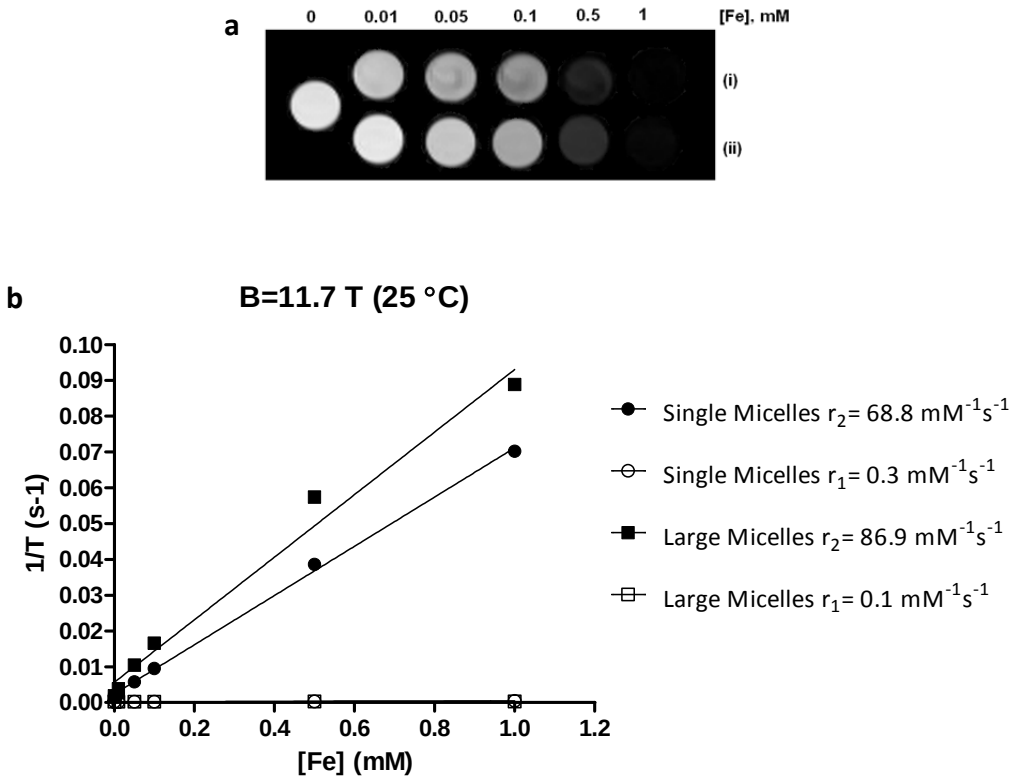

Fig. 2.17. (a) T_2-weighed MR images of aqueous solutions of micelles with large (i) and single/small (ii) IONP@PEG micelles (11.7 T, 25 °C).**(b)** Plot of $1/T_1$ and $1/T_2$ over Fe concentration of single/small and clusters of IONP@PEG micelles.

2.2.3.2 Labeling IONP@PL-PEG micelles with Rhodamine-B dye

The addition of a commercially available rhodamine B-modified phospholipid (DPPE-Rho) during the micelle formation confers fluorescent properties to IONP-filled micelles.

By incorporation of 1-5% of the total amount of lipid of DPPE-Rho to the initial lipid mixture in chloroform during micelle preparation, stable fluorescent micelles were obtained. UV-Vis studies demonstrated around 64 % of the fluorophore added is incorporated in the IONP@PL-PEG micelles and DLS studies demonstrated that the addition of the fluorophore into the micelle structure at this low percentage does not generate significant changes into the overall size of the system **(Fig. 2.18)**.

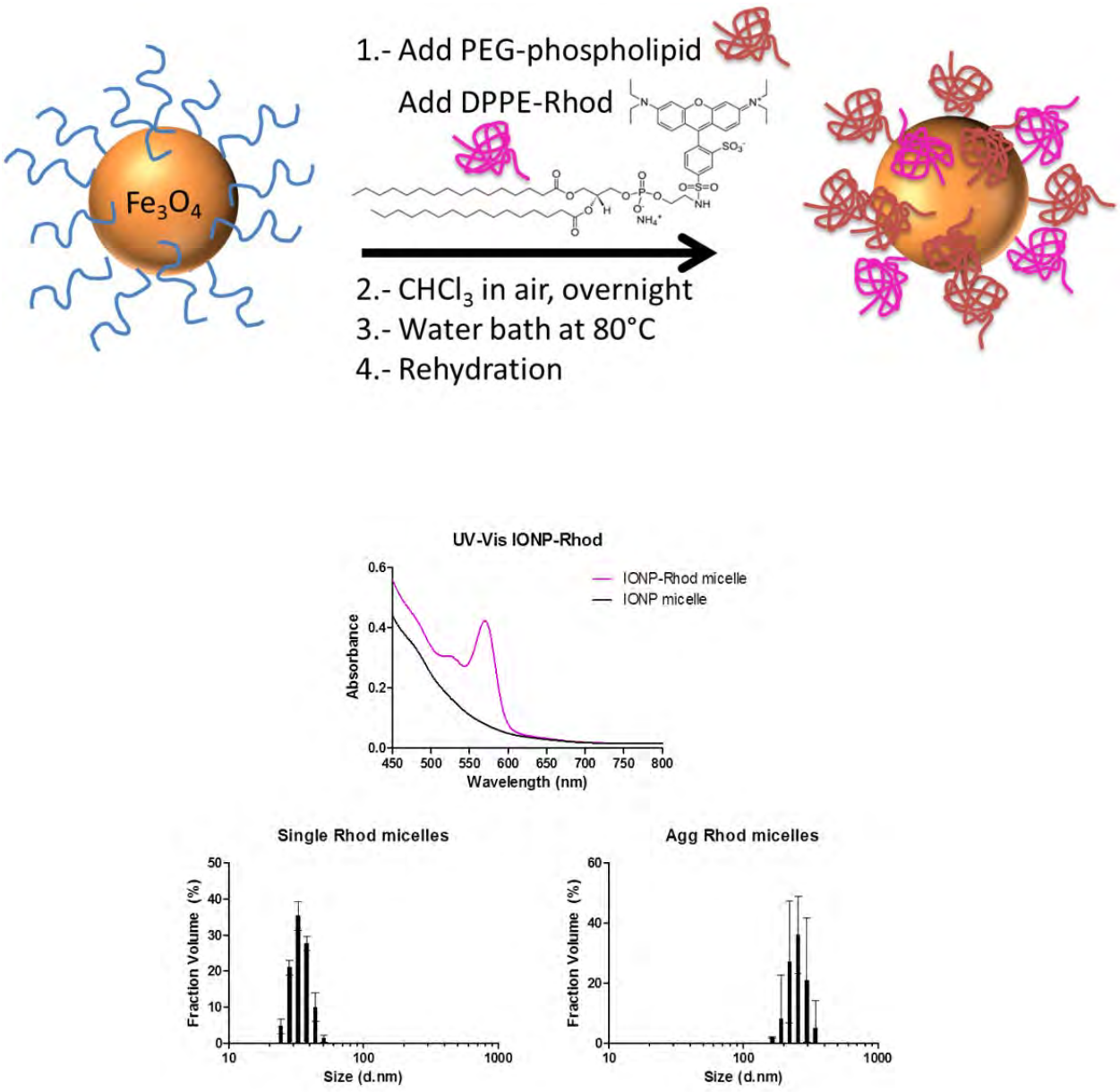

Fig. 2.18. Synthesis scheme and characterization of rhodamine-labeled IONP@PL-PEG micelles.

The samples were visualized *in vitro* after incubation with J774 macrophages. The cells were plated in microslides at a concentration of $1x10^6$ cells/mL and left to adhere overnight. Cell nuclei were stained with DAPI and after three washes the rhodamine-labeled IONP@PL-PEG micelles were added to cells at [Fe]= 10 µg/mL. The samples were incubated for 30 min and then the cells were cleaned with two washes to eliminate the micelles floating outside the cells. The protocol afforded the images shown in **Fig. 2.19.**

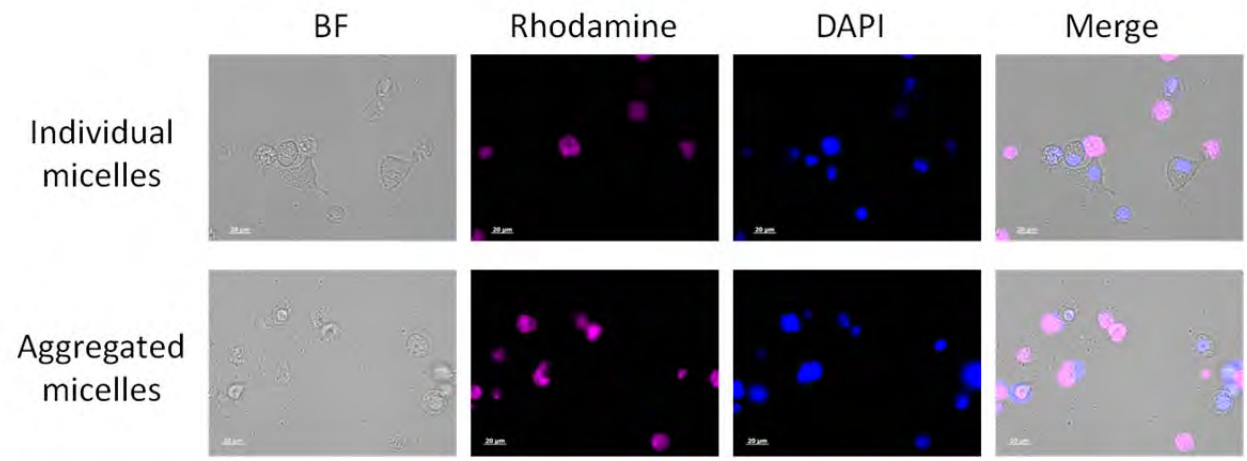

Fig. 2.19. Representative fluorescence microscope images of DAPI stained J774 macrophages after incubation with rhodamine-labeled IONP@PL-PEG micelles for 30 min. Fluorescent single and larger micelles were performed with a hydrophobic core size of 6.92 nm with D_H of 25 and 285 nm, respectively.

2.2.3.3 Labeling IONP@PL-PEG micelles with *fac*-$[M(OH_2)_3(CO)_3]^+$ complexes

To complete the trimodal MRI-Optical-SPECT contrast agent, it was decided to incorporate a radionuclide to induce SPECT imaging capabilities on IONP-filled micelles. The selected radionuclide was ^{99m}Tc, because ^{99m}Tc-based imaging agents can be visualized by SPECT and they are commonly used in medical facilities.[112,113]

Among the compounds currently available for the development of ^{99m}Tc SPECT imaging agents, *fac*-$[^{99m}Tc(OH_2)_3(CO)_3]^+$ is a promising new precursor[114–116] likely to become increasingly popular because it can now be formed in clinical and pre-clinical settings by conversion of generator elutes using new commercially available aqueous-based kit preparations.[117,118] To investigate the feasibility of radiolabeling the IONP@PL-PEG micelles with *fac*-$[^{99m}Tc(OH_2)_3(CO)_3]^+$, we carried out preliminary studies with the cold congener for *fac*-$[Re(OH_2)_3(CO)_3]^+$. By using *fac*-$[Re(OH_2)_3(CO)_3]^+$ it was possible to estimate the efficacy of the binding to the IONP@PL-PEG micelles and characterize the products by UV-Vis and FTIR techniques.

In a typical experiment a solution of IONP@PL-PEG micelles in water (at concentrations ranging from 6 mM to 16 mM Fe, 250 μL) was added to aqueous solutions of

fac-$[Re(OH_2)_3(CO)_3]^+$ (400 μL, 2.8 mM). The mixture was vortexed for 30 s and then heated at 90 °C for 20 min. The reaction mixture was allowed to cool down to RT and then centrifuged at 1000 g for 3 min. The supernatant was transferred to a NanoSep 100k *centrifugal device* and centrifuged at 8200 g for 10 min. The retentate was washed with water twice and after the final centrifugation the IONP@PL-PEG micelles were recovered from the membrane surface by adding and rinsing with a pipette tip (with a total volume of around 500 μL). This purification process was repeated using a new NanoSep 100k *centrifugal device.* Retentates and filtrates were lyophilised and analyzed by FT-IR.

As **Fig. 2.20a** shows in the FTIR spectrum, the micelles are transparent in the 1800-2200 cm^{-1} range, while the typical ν(CO) stretching bands corresponding to the $[Re(CO)_3]^+$ moiety are clearly distinguished at 2020 and 1909 cm^{-1}. The UV-Vis spectrum also show the efficient labeling of the IONP@PL-PEG micelles with *fac*-$[Re(OH_2)_3(CO)_3]^+$ complexes.

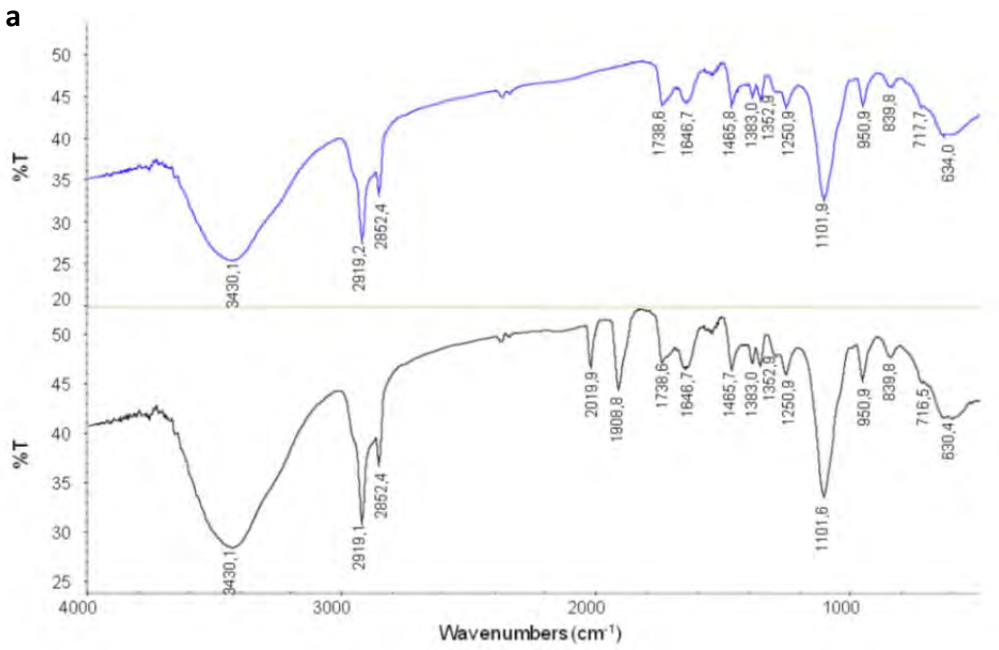

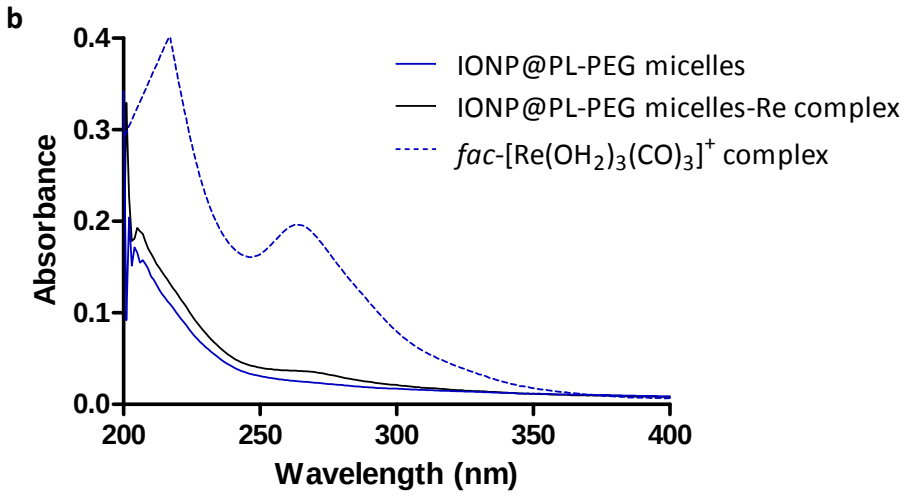

Fig. 2.20. (a) FT-IR and **(b)** UV-Vis spectra of IONP@PL-PEG methoxy micelles before (blue) and after (black) reaction with *fac*-$[Re(OH_2)_3(CO)_3]^+$

Successful attachment of $[Re(CO)_3]^+$ to the micelles allowed us to move to radiolabeling with the radioactive ^{99m}Tc compound. The *fac*-$[^{99m}Tc(OH_2)_3(CO)_3]^+$ complex is generated from $^{99m}TcO_4^-$ by the commercially available *IsoLink* kit following the manufacturer instructions. The labeling is carried out following a similar procedure of heating and centrifugation steps. 400 µL of *fac*-$[^{99m}Tc(OH_2)_3(CO)_3]^+$ are added to 400 µL of micelle solution. The mixture is heated at 90 °C for 25 min and then is allowed to cool down to room temperature. The mixture is purified/centrifuged using an ultrafiltration centrifugal device to eliminate the non-binding ^{99m}Tc complex. The radiolabeling binding (%) is measured by the difference between the total activity and the activity retained in the filter. The radiolabeling yield of the IONP-filled micelles was around 80%.

The labeling and stability of Re(I)- and Tc(I)-tricarbonyl complexes with IONPs micelles can be explained based on the nature of *fac*-$[M(OH_2)_3(CO)_3]^+$ complex. The chemistry of this complex is dominated by the fact it has three available coordination sites resulting from water substitution. Regardless of whether the hard–soft condition for ligand and metal centre matches, in this case for Tc(I)/Re(I) almost any donating molecules can be used as ligands. Moreover mono-, bi- and tri-dentate chelation with ligands at the IONP surface combined with O-H---O hydrogen bonding and hydrophobic interactions between the tricarbonyl fragment and the hydrocarbon chains are therefore possible for promoting

binding and stabilizing the M(I) tricarbonyl complexes at the IONP surface. On the one hand, the behavior of *fac*-$[M(OH_2)_3(CO)_3]^+$ as a weak acid provides the deprotonation of coordinated water ligands which might lead to terminal hydroxo complexes (hard base). This deprotonation allows the formation of hydroxo bridges for instance with Fe^{3+} (hard acid).[114] However, there is a second proposal based on the hydroxyl groups always present on the iron oxide nanoparticle surface, as it was shown in the FT-IR spectra of hydrophobic IONPs.[119,120] The high stability of $[M(CO)_3]^+$ moiety in water and the exchanging potential of the labile ligands by *fac*-$[M(OH_2)_3(CO)_3]^+$ like H_2O promote the addition of other incoming chelators.[114] In the case of the labeling with IONPs, the most likely ligands are the OH^- groups from the nanoparticle surface. In both cases, the attachment implies the formation of metal-hydroxo-iron bridge (M(I)-OH-Fe) and an additional stability due to the hydrogen bonding OH·····O and the hydrophobic interactions between the micelle and the complex.[121,122]

The stability of the IONP@PL-PEG micelles-$^{99m}Tc(CO)_3$ interaction was assessed through the different biodistribution of the radiolabeled micelles compared with the *fac*-$[^{99m}Tc(OH_2)_3(CO)_3]^+$ complex when they are injected in mice. Both systems were administered via tail vein injection and as the **Fig. 2.21** shows, after 30 min the differences are observable. The radiolabeled micelles are accumulated in the liver and the spleen, while the complex was already found in the bladder and kidneys via urine. The images after 24 h and the posterior *ex vivo* analysis **(Fig. 2.21d)** suggest firstly, that the *fac*-$^{99m}Tc\ (CO)_3$ moiety remains bound to the micelles and that the interaction is sufficiently stable under *in vivo* conditions even 24 h post injection. Secondly, at 3 h or even less, it is possible to observe the biodistribution of the system which makes it a promising SPECT imaging device for medical imaging application.

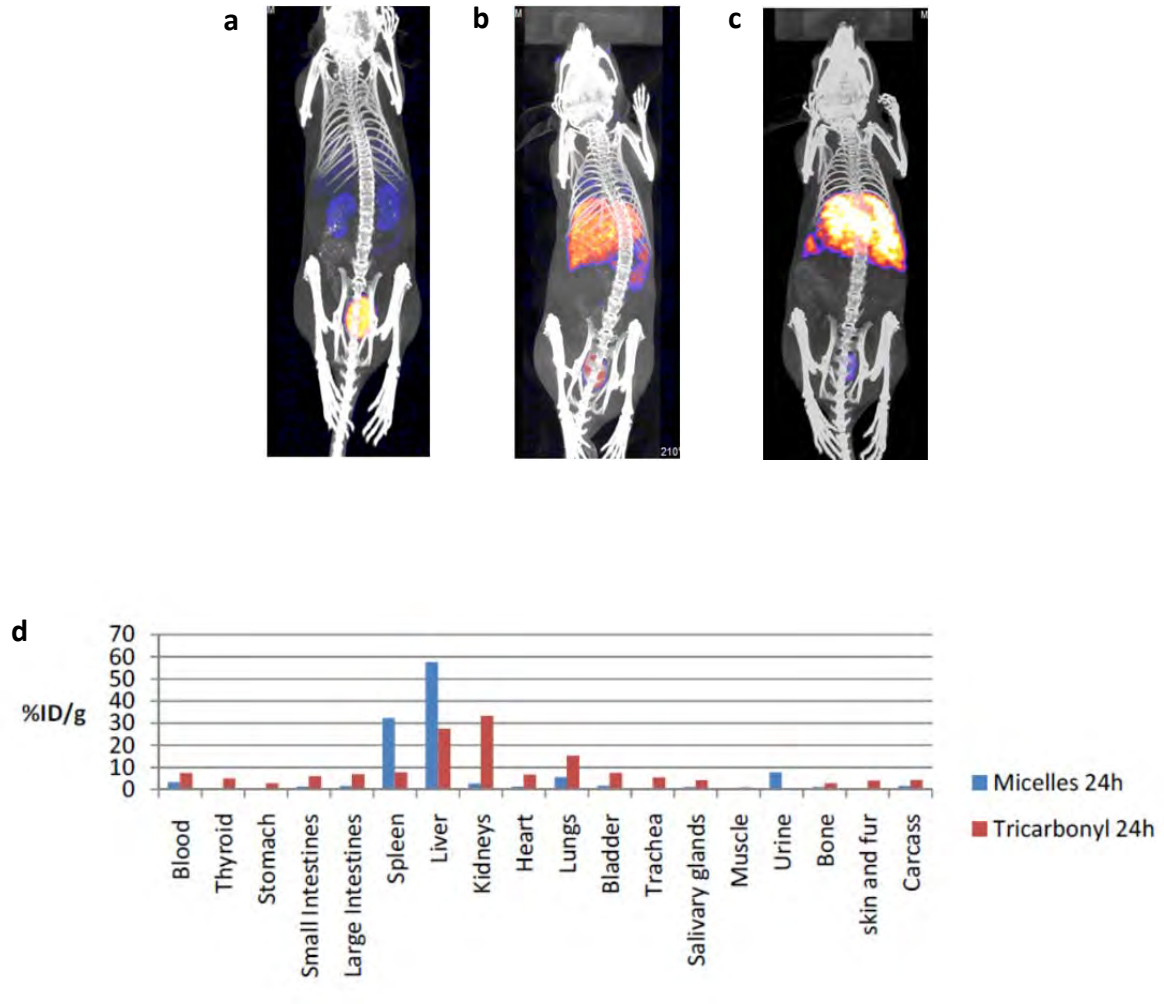

Fig.2.21. *In vivo* SPECT/CT images of mice injected with **(a)** *fac*-[^{99m}Tc(OH$_2$)$_3$(CO)$_3$]$^+$ after 30 min **(b)** small IONP@PL-PEG methoxy micelles-^{99m}Tc(CO)$_3$ after 3 h or **(c)** 24 h. **(d)** Ex vivo biodistribution represented by the injected dose remaining after 24 h.

In a second experiment the biodistribution of the single/small (D_H = 13 nm) and large micelles (D_H = 460 nm) were compared via tail vein injection. The larger micelles show a behavior comparable with that of large aluminum NPs studied by J. Llop and co-workers.[123] After 30 min, the vast majority of the large micelles were found in the liver and the spleen with presence in the lungs (**Fig. 2.22**). The radiolabeling was also as efficient as with the single micelles, however the iron concentration was different due to the different yield in the synthesis. [Fe]= 8 mM for larger micelles and [Fe]= 16 mM for single micelles. That result

suggests that the amount of iron can be reduced for the following experiments because the quality of the labeling and the images were good enough.

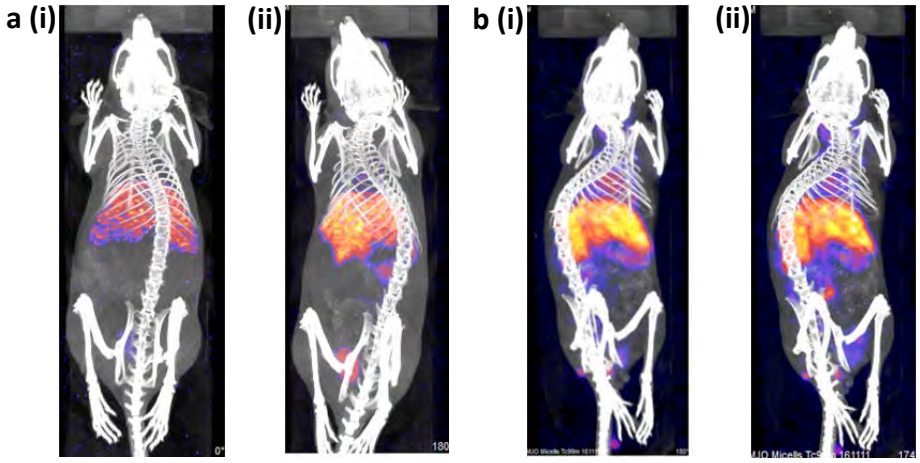

Fig.2.22. *In vivo* SPECT/CT images of mice injected with **(a)** small (D_H = 13 nm) and **(b)** large (D_H = 460 nm) IONP@PL-PEG methoxy micelles-$^{99m}Tc(CO)_3$after **(i)** 30 and **(ii)** 150 min.

2.3 Conclusions

Two types of IONPs have been synthesized and characterized. The hydrophobic Fe_3O_4 and ZnSPIONs were prepared with different sizes with narrow and homogeneous size distribution. The composition and magnetic properties were characterized and consistent with high quality IONPs and optimum zinc(II) doping for biomedical applications as MRI contrast agents.

Different strategies and ligands were used to make the hydrophobic IONPs and ZnSPIONs water soluble. Ligand exchange reactions with DMSA afforded worm-like structures, whereas ligand exchange with PEI led to spherical structures; in both cases these nanosystems had a size < 100 nm, which is considered ideal for drug delivery purposes. In the case of IONPs encapsulated into water soluble micelles prepared with PEGylated phospholipids (IONP@PL-PEG micelles), it was demonstrated that the D_H can be modulated changing the mass ratio between IONPs and PL-PEG to obtain systems ranging from 10-500 nm. The relaxivity values obtained and the strong signal provided on MR images with IONP-filled micelles suggest that they could be used as potent contrast agents similar or even better than the clinically used IONPs. The DMSA and PEI coated IONPs also showed excellent relaxivity values and could afford useful drug delivery systems.

In the case of the IONP@PL-PEG micelles, fluorescence imaging properties could be added by the incorporation of a rhodamine B-modified PL, allowing visualization of the cellular uptake by cells of the immune system by *in vitro* fluorescence imaging studies.

The multimodal imaging features of the IONP@PL-PEG micelles were completed by the successful binding of ^{99m}Tc-tricarbonyl complex (an emerging new precursor for the development of SPECT imaging agents) as radionuclide to allow *in vivo* imaging studies using SPECT.

References

1. Hennessy, E. J., Parker, A. E. & O'Neill, L. A. J. Targeting Toll-like receptors: emerging therapeutics? *Nat. Rev. Drug Discov.* **9,** 293–307 (2010).

2. Kanzler, H., Barrat, F. J., Hessel, E. M. & Coffman, R. L. Therapeutic targeting of innate immunity with Toll-like receptor agonists and antagonists. *Nat. Med.* **13,** 552–9 (2007).

3. Rakoff-Nahoum, S. & Medzhitov, R. Toll-like receptors and cancer. *Nat. Rev. Cancer* **9,** 57–63 (2009).

4. Xu, C. & Sun, S. Monodisperse magnetic nanoparticles for biomedical applications. *Polym. Int.* **56,** 821–826 (2007).

5. Jun, Y.-W., Seo, J.-W. & Cheon, J. Nanoscaling laws of magnetic nanoparticles and their applicabilities in biomedical sciences. *Acc. Chem. Res.* **41,** 179–89 (2008).

6. Colombo, M. *et al.* Biological applications of magnetic nanoparticles. *Chem. Soc. Rev.* **41,** 4306–34 (2012).

7. Okuhata, Y. Delivery of diagnostic agents for magnetic resonance imaging. *Adv. Drug Deliv. Rev.* **37,** 121–137 (1999).

8. Caravan, P. Strategies for increasing the sensitivity of gadolinium based MRI contrast agents. *Chem. Soc. Rev.* **35,** 512–23 (2006).

9. Frascione, D. *et al.* Ultrasmall superparamagnetic iron oxide (USPIO)-based liposomes as magnetic resonance imaging probes. *Int. J. Nanomedicine* **7,** 2349–59 (2012).

10. Kim, B. H. *et al.* Large-scale synthesis of uniform and extremely small-sized iron oxide nanoparticles for high-resolution T1 magnetic resonance imaging contrast agents. *J. Am. Chem. Soc.* **133,** 12624–31 (2011).

11. Reddy, L. H., Arias, J. L., Nicolas, J. & Couvreur, P. Magnetic nanoparticles: design and characterization, toxicity and biocompatibility, pharmaceutical and biomedical applications. *Chem. Rev.* **112,** 5818–78 (2012).

12. LaMer, V. K. & Dinegar, R. H. Theory, Production and Mechanism of Formation of Monodispersed Hydrosols. *J. Am. Chem. Soc.* **72,** 4847–4854 (1950).

13. Johnston, R. L. *Atomic and Molecular Clusters*. (Taylor & Francis Ltd., London 2002, 2002).

14. Sun, S. *et al.* Monodisperse MFe_2O_4 (M = Fe, Co, Mn) nanoparticles. *J. Am. Chem. Soc.* **126,** 273–9 (2004).

15. Laurent, S. *et al.* Magnetic iron oxide nanoparticles: synthesis, stabilization, vectorization, physicochemical characterizations, and biological applications. *Chem. Rev.* **108,** 2064–110 (2008).

16. Jolivet, J.-P. *et al.* Size tailoring of oxide nanoparticles by precipitation in aqueous medium. A semi-quantitative modelling. *J. Mater. Chem.* **14,** 3281 (2004).

17. Daou, T. J. *et al.* Hydrothermal Synthesis of Monodisperse Magnetite Nanoparticles. *Chem. Mater.* **18,** 4399–4404 (2006).

18. Yan, J. *et al.* Hydrothermal synthesis of monodisperse Fe_3O_4 nanoparticles based on modulation of tartaric acid. *Colloids Surfaces A Physicochem. Eng. Asp.* **340,** 109–114 (2009).

19. Hench, L. L. & West, J. K. The sol-gel process. *Chem. Rev.* **90,** 33–72 (1990).

20. Lu, Y., Yin, Y., Mayers, B. T. & Xia, Y. Modifying the Surface Properties of Superparamagnetic Iron Oxide Nanoparticles through A Sol − Gel Approach. *Nano Lett.* (2002).

21. Fievet, F., Lagier, J., Blin, B., Beaudoin, B. & Figlarz, M. Homogeneous and heterogeneous nucleations in the polyol process for the preparation of micron and submicron size metal particles. *Solid State Ionics* **32-33,** 198–205 (1989).

22. Viau, G. Nucleation and growth of bimetallic CoNi and FeNi monodisperse particles prepared in polyols. *Solid State Ionics* **84,** 259–270 (1996).

23. Zhang, Z. *et al.* Comparison of superparamagnetic and ultrasmall superparamagnetic iron oxide cell labeling for tracking green fluorescent protein gene marker with negative and positive contrast magnetic resonance imaging. *Mol. Imaging* **8,** 148–55

24. Bonnemain, B. Superparamagnetic agents in magnetic resonance imaging: physicochemical characteristics and clinical applications. A review. *J. Drug Target.* **6,** 167–74 (1998).

25. Enochs, W. S., Harsh, G., Hochberg, F. & Weissleder, R. Improved delineation of human brain tumors on MR images using a long-circulating, superparamagnetic iron oxide agent. *J. Magn. Reson. Imaging* **9,** 228–32 (1999).

26. Nishiyama, N. & Kataoka, K. Current state, achievements, and future prospects of polymeric micelles as nanocarriers for drug and gene delivery. *Pharmacol. Ther.* **112,** 630–48 (2006).

27. Moghimi, S. M., Hunter, A. C. & Murray, J. C. Long-Circulating and Target-Specific Nanoparticles : Theory to Practice. **53,** 283–318 (2001).

28. Gratton, S. E. A. *et al.* The effect of particle design on cellular internalization pathways. *Proc. Natl. Acad. Sci. U. S. A.* **105,** 11613–8 (2008).

29. Qiu, Y. *et al.* Surface chemistry and aspect ratio mediated cellular uptake of Au nanorods. *Biomaterials* **31,** 7606–19 (2010).

30. Chithrani, B. D., Ghazani, A. A. & Chan, W. C. W. Determining the size and shape dependence of gold nanoparticle uptake into mammalian cells. *Nano Lett.* **6,** 662–8 (2006).

31. Bateer, B. *et al.* Synthesis, size and magnetic properties of controllable $MnFe_2O_4$ nanoparticles with versatile surface functionalities. *Dalton Trans.* (2014). doi:10.1039/c4dt00089g

32. Jang, J. *et al.* Critical enhancements of MRI contrast and hyperthermic effects by dopant-controlled magnetic nanoparticles. *Angew. Chem. Int. Ed. Engl.* **48,** 1234–8 (2009).

33. Bárcena, C. *et al.* Zinc ferrite nanoparticles as MRI contrast agents. *Chem. Commun.* 2224–6 (2008). doi:10.1039/b801041b

34. Seo, W. S. *et al.* FeCo/graphitic-shell nanocrystals as advanced magnetic-resonance-imaging and near-infrared agents. *Nat. Mater.* **5,** 971–6 (2006).

35. LaConte, L. E. W. *et al.* Coating thickness of magnetic iron oxide nanoparticles affects R2 relaxivity. *J. Magn. Reson. Imaging* **26,** 1634–1641 (2007).

36. Tromsdorf, U. I. *et al.* Size and Surface Effects on the MRI Relaxivity of Manganese Ferrite Nanoparticle Contrast Agents. *Nano Lett.* **7,** 2422–2427 (2007).

37. Blanco, N. G. *et al.* Iron oxide-filled micelles as ligands for fac-$[M(CO)_3]^+$ (M = ^{99m}Tc, Re). *Chem. Commun.* **48,** 4211 (2012).

38. Amstad, E. *et al.* Surface functionalization of single superparamagnetic iron oxide nanoparticles for targeted magnetic resonance imaging. *Small* **5,** 1334–42 (2009).

39. Tromsdorf, U. I., Bruns, O. T., Salmen, S. C., Beisiegel, U. & Weller, H. A highly effective, nontoxic T1 MR contrast agent based on ultrasmall PEGylated iron oxide nanoparticles. *Nano Lett.* **9,** 4434–40 (2009).

40. Gupta, A. K. & Curtis, A. S. G. Surface modified superparamagnetic nanoparticles for drug delivery: interaction studies with human fibroblasts in culture. *J. Mater. Sci. Mater. Med.* **15,** 493–6 (2004).

41. Lee, H. *et al.* Antibiofouling polymer-coated superparamagnetic iron oxide nanoparticles as potential magnetic resonance contrast agents for in vivo cancer imaging. *J. Am. Chem. Soc.* **128,** 7383–9 (2006).

42. Goon, I. Y. *et al.* Fabrication and Dispersion of Gold-Shell-Protected Magnetite Nanoparticles: Systematic Control Using Polyethyleneimine. *Chem. Mater.* **21,** 673–681 (2009).

43. McBain, S. C., Yiu, H. H. P., El Haj, A. & Dobson, J. Polyethyleneimine functionalized iron oxide nanoparticles as agents for DNA delivery and transfection. *J. Mater. Chem.* **17,** 2561 (2007).

44. Huh, Y.-M. *et al.* In vivo magnetic resonance detection of cancer by using multifunctional magnetic nanocrystals. *J. Am. Chem. Soc.* **127,** 12387–91 (2005).

45. Roca, A. G. *et al.* Effect of nanoparticle and aggregate size on the relaxometric properties of MR contrast agents based on high quality magnetite nanoparticles. *J. Phys. Chem. B* **113,** 7033–9 (2009).

46. Jana, N. R., Earhart, C. & Ying, J. Y. Synthesis of Water-Soluble and Functionalized Nanoparticles by Silica Coating. *Chem. Mater.* **19,** 5074–5082 (2007).

47. Liz-Marzán, L. M., Giersig, M. & Mulvaney, P. Synthesis of Nanosized Gold−Silica Core−Shell Particles. *Langmuir* **12,** 4329–4335 (1996).

48. Kim, J., Piao, Y. & Hyeon, T. Multifunctional nanostructured materials for multimodal imaging, and simultaneous imaging and therapy. *Chem. Soc. Rev.* **38,** 372–90 (2009).

49. Cheon, J. & Lee, J.-H. Synergistically integrated nanoparticles as multimodal probes for nanobiotechnology. *Acc. Chem. Res.* **41,** 1630–40 (2008).

50. Lauterbur, P. C. Magnetic resonance zeugmatography. *Pure Appl. Chem.* **40,** 149–157 (1974).

51. Mendonca Dias, M. H. & Lauterbur, P. C. Ferromagnetic particles as contrast agents for magnetic resonance imaging of liver and spleen. *Magn. Reson. Med.* **3,** 328–30 (1986).

52. Kim, T. *et al.* Mesoporous silica-coated hollow manganese oxide nanoparticles as positive T1 contrast agents for labeling and MRI tracking of adipose-derived mesenchymal stem cells. *J. Am. Chem. Soc.* **133,** 2955–61 (2011).

53. Na, H. Bin *et al.* Development of a T1 contrast agent for magnetic resonance imaging using MnO nanoparticles. *Angew. Chem. Int. Ed. Engl.* **46,** 5397–401 (2007).

54. Carlsson, S. A Glance at the history of Nuclear Imaging. *Acta Oncol. (Madr).* **34,** 1095 (1995).

55. Blankenberg, F. G. & Strauss, H. W. Nuclear medicine applications in molecular imaging. *J. Magn. Reson. Imaging* **16,** 352–61 (2002).

56. Mahmoudi, M., Serpooshan, V. & Laurent, S. Engineered nanoparticles for biomolecular imaging. *Nanoscale* **3,** 3007–26 (2011).

57. Bligh, S. W. A., Sadler, P. J., Marriott, J. A., Latham, I. A. & Kelly, J. D. Characterization and in vivo distribution of ^{99m}Tc- and ^{111}In-labelled magnetite. *Int. J. Radiat. Appl. Instrumentation. Part A. Appl. Radiat. Isot.* **40,** 751–757 (1989).

58. Lewin, M. *et al.* Tat peptide-derivatized magnetic nanoparticles allow in vivo tracking and recovery of progenitor cells. *Nat. Biotechnol.* **18,** 410–4 (2000).

59. Jarrett, B. R., Gustafsson, B., Kukis, D. L. & Louie, A. Y. Synthesis of ^{64}Cu-labeled magnetic nanoparticles for multimodal imaging. *Bioconjug. Chem.* **19,** 1496–504 (2008).

60. Glaus, C., Rossin, R., Welch, M. J. & Bao, G. In vivo evaluation of ^{64}Cu-labeled magnetic nanoparticles as a dual-modality PET/MR imaging agent. *Bioconjug. Chem.* **21,** 715–22 (2010).

61. Bouziotis, P., Psimadas, D., Tsotakos, T. & Stamopoulos, D. Radiolabeled Iron Oxide Nanoparticles As Dual-Modality SPECT / MRI and PET / MRI Agents. 1–9 (2012).

62. Sandiford, L. *et al.* Bisphosphonate-anchored PEGylation and radiolabeling of superparamagnetic iron oxide: long-circulating nanoparticles for in vivo multimodal (T1 MRI-SPECT) imaging. *ACS Nano* **7,** 500–12 (2013).

63. Brechbiel, M. W. Bifunctional chelates for metal nuclides. *Q. J. Nucl. Med. Mol. imaging Off. Publ. Ital. Assoc. Nucl. Med. [and] Int. Assoc. Radiopharmacol. (IAR), [and] Sect. Soc. Radiopharm.* **52,** 166–73 (2008).

64. Liu, S. Bifunctional coupling agents for radiolabeling of biomolecules and target-specific delivery of metallic radionuclides. *Adv. Drug Deliv. Rev.* **60,** 1347–70 (2008).

65. Torres Martin de Rosales, R. *et al.* ^{99m}Tc-bisphosphonate-iron oxide nanoparticle conjugates for dual-modality biomedical imaging. *Bioconjug. Chem.* **22,** 455–65 (2011).

66. Madru, R. *et al.* ^{99m}Tc-labeled superparamagnetic iron oxide nanoparticles for multimodality SPECT/MRI of sentinel lymph nodes. *J. Nucl. Med.* **53,** 459–63 (2012).

67. Jauregui-Osoro, M. *et al.* Biocompatible inorganic nanoparticles for [18F]-fluoride binding with applications in PET imaging. *Dalton Trans.* **40,** 6226–37 (2011).

68. Cydzik, I. *et al.* A novel method for synthesis of ^{56}Co-radiolabelled silica nanoparticles. *J. Nanoparticle Res.* **14,** 1185 (2012).

69. Dybowska, A. D. *et al.* Synthesis of isotopically modified ZnO nanoparticles and their potential as nanotoxicity tracers. *Environ. Pollut.* **159,** 266–73 (2011).

70. Pérez-Campaña, C. *et al.* Production of ^{18}F-Labeled Titanium Dioxide Nanoparticles by Proton Irradiation for Biodistribution and Biological Fate Studies in Rats. *Part. Part. Syst. Charact.* **31,** 134–142 (2014).

71. Bruchez Jr., M. Semiconductor Nanocrystals as Fluorescent Biological Labels. *Science (80-.).* **281,** 2013–2016 (1998).

72. Park, J.-H., von Maltzahn, G., Ruoslahti, E., Bhatia, S. N. & Sailor, M. J. Micellar hybrid nanoparticles for simultaneous magnetofluorescent imaging and drug delivery. *Angew. Chem. Int. Ed. Engl.* **47,** 7284–8 (2008).

73. Erogbogbo, F. *et al.* Biocompatible magnetofluorescent probes: luminescent silicon quantum dots coupled with superparamagnetic iron(III) oxide. *ACS Nano* **4,** 5131–8 (2010).

74. Wang, D., He, J., Rosenzweig, N. & Rosenzweig, Z. Superparamagnetic Fe_2O_3 Beads−CdSe/ZnS Quantum Dots Core−Shell Nanocomposite Particles for Cell Separation. *Nano Lett.* **4,** 409–413 (2004).

75. Selvan, S. T., Patra, P. K., Ang, C. Y. & Ying, J. Y. Synthesis of silica-coated semiconductor and magnetic quantum dots and their use in the imaging of live cells. *Angew. Chem. Int. Ed. Engl.* **46,** 2448–52 (2007).

76. Mourdikoudis, S. & Liz-Marzán, L. M. Oleylamine in Nanoparticle Synthesis. *Chem. Mater.* **25,** 1465–1476 (2013).

77. Xu, Z., Shen, C., Hou, Y., Gao, H. & Sun, S. Oleylamine as Both Reducing Agent and Stabilizer in a Facile Synthesis of Magnetite Nanoparticles. *Chem. Mater.* **21,** 1778–1780 (2009).

78. Hou, Y., Xu, Z. & Sun, S. Controlled synthesis and chemical conversions of FeO nanoparticles. *Angew. Chem. Int. Ed. Engl.* **46,** 6329–32 (2007).

79. Peng, X., Wickham, J. & Alivisatos, A. P. Kinetics of II-VI and III-V Colloidal Semiconductor Nanocrystal Growth: "Focusing" of Size Distributions. *J. Am. Chem. Soc.* **120,** 5343–5344 (1998).

80. Park, J., Joo, J., Kwon, S. G., Jang, Y. & Hyeon, T. Synthesis of monodisperse spherical nanocrystals. *Angew. Chem. Int. Ed. Engl.* **46,** 4630–60 (2007).

81. Lee, J.-H. *et al.* Artificially engineered magnetic nanoparticles for ultra-sensitive molecular imaging. *Nat. Med.* **13,** 95–9 (2007).

82. Bronstein, L. M. *et al.* Influence of Iron Oleate Complex Structure on Iron Oxide Nanoparticle Formation. *Chem. Mater.* **19,** 3624–3632 (2007).

83. Perez De Berti, I. O. *et al.* Alternative low-cost approach to the synthesis of magnetic iron oxide nanoparticles by thermal decomposition of organic precursors. *Nanotechnology* **24,** 175601 (2013).

84. Mahdavi, M. *et al.* Synthesis, surface modification and characterisation of biocompatible magnetic iron oxide nanoparticles for biomedical applications. *Molecules* **18,** 7533–48 (2013).

85. Ai, H. *et al.* Magnetite-Loaded Polymeric Micelles as Ultrasensitive Magnetic-Resonance Probes. *Adv. Mater.* **17,** 1949–1952 (2005).

86. Hu, F. *et al.* Ultrasmall, Water-Soluble Magnetite Nanoparticles with High Relaxivity for Magnetic Resonance Imaging. *J. Phys. Chem. C. Nanomater. Interfaces* **113,** 20855–20860 (2009).

87. Frey, N. A., Peng, S., Cheng, K. & Sun, S. Magnetic nanoparticles: synthesis, functionalization, and applications in bioimaging and magnetic energy storage. *Chem. Soc. Rev.* **38,** 2532–42 (2009).

88. Bercoff, P. G. & Bertorello, H. R. Exchange constants and transfer integrals of spinel ferrites. *J. Magn. Magn. Mater.* **169,** 314–322 (1997).

89. Verma, K., Kumar, A. & Varshney, D. Effect of Zn and Mg doping on structural, dielectric and magnetic properties of tetragonal $CuFe_2O_4$. *Curr. Appl. Phys.* **13,** 467–473 (2013).

90. Goldhaber, S. B. Trace element risk assessment: essentiality vs. toxicity. *Regul. Toxicol. Pharmacol.* **38,** 232–242 (2003).

91. Stickle, W. F., Sobol, P. E., Bomben, K. D., Chastain, J. & King, R. C. Handbook of X-ray Photoelectron Spectroscopy.

92. Sepúlveda-Guzmán, S. *et al.* Synthesis and characterization of an iron oxide poly(styrene-co-carboxybutylmaleimide) ferrimagnetic composite. *Polymer (Guildf).* **48,** 720–727 (2007).

93. Chen, Z. P. *et al.* Preparation and characterization of water-soluble monodisperse magnetic iron oxide nanoparticles via surface double-exchange with DMSA. *Colloids Surfaces A Physicochem. Eng. Asp.* **316,** 210–216 (2008).

94. Flora, S. J. S. & Pachauri, V. Chelation in metal intoxication. *Int. J. Environ. Res. Public Health* **7,** 2745–88 (2010).

95. Fauconnier, N., Pons, J. N., Roger, J. & Bee, A. Thiolation of Maghemite Nanoparticles by Dimercaptosuccinic Acid. *J. Colloid Interface Sci.* **194,** 427–433 (1997).

96. Roch, A., Muller, R. N. & Gillis, P. Theory of proton relaxation induced by superparamagnetic particles. *J. Chem. Phys.* **110,** 5403 (1999).

97. Bjørnerud, A. & Johansson, L. The utility of superparamagnetic contrast agents in MRI: theoretical consideration and applications in the cardiovascular system. *NMR Biomed.* **17,** 465–77 (2004).

98. An, F. & Gao, B. Chelating adsorption properties of PEI/SiO_2 for plumbum ion. *J. Hazard. Mater.* **145,** 495–500 (2007).

99. Boussif, O. *et al.* A versatile vector for gene and oligonucleotide transfer into cells in culture and in vivo: polyethylenimine. *Proc. Natl. Acad. Sci.* **92,** 7297–7301 (1995).

100. Von Harpe, A., Petersen, H., Li, Y. & Kissel, T. Characterization of commercially available and synthesized polyethylenimines for gene delivery. *J. Control. Release* **69,** 309–322 (2000).

101. Lou, L. *et al.* Functionalized magnetic-fluorescent hybrid nanoparticles for cell labelling. *Nanoscale* **3,** 2315–23 (2011).

102. Kircheis, R., Wightman, L. & Wagner, E. Design and gene delivery activity of modified polyethylenimines. *Adv. Drug Deliv. Rev.* **53,** 341–358 (2001).

103. Godbey, W. T., Wu, K. K. & Mikos, A. G. Size matters: molecular weight affects the efficiency of poly(ethylenimine) as a gene delivery vehicle. *J. Biomed. Mater. Res.* **45,** 268–75 (1999).

104. Neamnark, A. *et al.* Aliphatic lipid substitution on 2 kDa polyethylenimine improves plasmid delivery and transgene expression. *Mol. Pharm.* **6,** 1798–815 (2009).

105. Seib, F. P., Jones, A. T. & Duncan, R. Comparison of the endocytic properties of linear and branched PEIs, and cationic PAMAM dendrimers in B16f10 melanoma cells. *J. Control. Release* **117,** 291–300 (2007).

106. Steitz, B. *et al.* Characterization of PEI-coated superparamagnetic iron oxide nanoparticles for transfection: Size distribution, colloidal properties and DNA interaction. *J. Magn. Magn. Mater.* **311,** 300–305 (2007).

107. Knop, K., Hoogenboom, R., Fischer, D. & Schubert, U. S. Poly(ethylene glycol) in drug delivery: pros and cons as well as potential alternatives. *Angew. Chem. Int. Ed. Engl.* **49,** 6288–308 (2010).

108. Dubertret, B. *et al.* In vivo imaging of quantum dots encapsulated in phospholipid micelles. *Science* **298,** 1759–62 (2002).

109. Jokerst, J. V, Lobovkina, T., Zare, R. N. & Gambhir, S. S. Nanoparticle PEGylation for imaging and therapy. *Nanomedicine (Lond).* **6,** 715–28 (2011).

110. Hu, R. *et al.* PEGylated Phospholipid Micelle-Encapsulated Near-Infrared PbS Quantum Dots for in vitro and in vivo Bioimaging. *Theranostics* **2,** 723–33 (2012).

111. Lu, J. *et al.* Manganese ferrite nanoparticle micellar nanocomposites as MRI contrast agent for liver imaging. *Biomaterials* **30,** 2919–28 (2009).

112. R.Weissleder, B.D.Ross, A. R. and S. S. G. *Molecular Imaging: Principles and Practice*. (2010).

113. Kobayashi, H., Longmire, M. R., Ogawa, M. & Choyke, P. L. Rational chemical design of the next generation of molecular imaging probes based on physics and biology: mixing modalities, colors and signals. *Chem. Soc. Rev.* **40,** 4626–48 (2011).

114. Alberto, R., Schibli, R., Waibel, R., Abram, U. & Schubiger, A. P. Basic aqueous chemistry of $[M(OH_2)_3(CO)_3]^+$ (M=Re, Tc) directed towards radiopharmaceutical application. *Coord. Chem. Rev.* **190-192,** 901–919 (1999).

115. Schibli, R. *et al.* Steps toward High Specific Activity Labeling of Biomolecules for Therapeutic Application: Preparation of Precursor $[^{188}Re(H_2O)_3(CO)_3]^+$ and Synthesis of Tailor-Made Bifunctional Ligand Systems. *Bioconjug. Chem.* **13,** 750–756 (2002).

116. Banerjee, S. R. *et al.* New directions in the coordination chemistry of ^{99m}Tc: a reflection on technetium core structures and a strategy for new chelate design. *Nucl. Med. Biol.* **32,** 1–20 (2005).

117. Schibli, R. & Schubiger, P. A. Current use and future potential of organometallic radiopharmaceuticals. *Eur. J. Nucl. Med. Mol. Imaging* **29,** 1529–42 (2002).

118. Koźmiński, P., Gniazdowska, E., Fuks, L. & Kowalska, S. "2+1" Tricarbonyltechnetium(I)/tricarbonylrhenium(I) mixed-ligand complexes with methyl thiosalicylate and isocyanide ligands as potential precursors of radiopharmaceuticals. *Appl. Radiat. Isot.* **69,** 436–442 (2011).

119. Wu, W., He, Q. & Jiang, C. Magnetic iron oxide nanoparticles: synthesis and surface functionalization strategies. *Nanoscale Res. Lett.* **3,** 397–415 (2008).

120. Huang, X. *et al.* Magnetic nanoparticles with functional silanes: evolution of well-defined shells from anhydride containing silane. *J. Mater. Chem.* **19,** 4231–4239 (2009).

121. Alberto, R. *et al.* Synthesis and reactivity of $[NEt_4]_2[ReBr_3(CO)_3]$. Formation and structural characterization of the clusters $[NEt_4][Re_3(\mu_3\text{-}OH)(\mu\text{-}OH)_3(CO)_9]$ and $[NEt_4][Re_2(\mu\text{-}OH)_3(CO)_6]$ by alkaline titration. *J. Chem. Soc. Dalt. Trans.* 2815 (1994). doi:10.1039/dt9940002815

122. Egli, A. *et al.* Hydrolysis of the Organometallic Aqua Ion fac-Triaquatricarbonylrhenium(I). Mechanism, p K a , and Formation Constants of the Polynuclear Hydrolysis Products. *Organometallics* **16,** 1833–1840 (1997).

123. Pe, C. *et al.* Biodistribution of different sized nanoparticles assessed by Positron Emission Tomography : a general strategy for direct activation of metal. 3498–3505 (2013).

3

Development of IONP-filled PL-PEG micelles with immunostimulatory capacity

The aim of this chapter is to study the immunological activity of the previously described IONP@PL-PEG micelles after their functionalization with the immunotherapeutic agent poly (I:C). The stimulatory activity of this synthetic dsRNA coupled to the micelles by covalent and non-covalent binding is studied first in vitro in different APCs, and then in vivo by characterizing the innate immune responses generated following its administration by different routes in mice. The cellular uptake and biodistribution of the poly (I:C)-IONP@PL-PEG micelles is investigated by fluorescence microscopy, MRI and SPECT.

3.1 Introduction

3.1.1 General concepts of the immune system

The immune system is constituted by a network of cellular and humoral (mediated by macromolecules, such as antibodies) components that work together to protect the body from infection. The immune system defends and prevents the host from diseases caused by a range of microbes, such as viruses, bacteria, fungi and parasites. Hence, the immune system is fundamental for life and without it death from infection would be inevitable.

There are two branches of the immune system by which the body identifies and protects against foreign material: the innate and the adaptive immune system **(Fig. 3.1)**. The first line of defense is the innate immune system; considered to be natural and non-specific because it provides the host the ability to recognize and immediately destroy certain microbes upon the first encounter. The cellular components of innate immunity include antigen-presenting dendritic cells (DCs), phagocytic macrophages and granulocytes, cytotoxic natural killer cells (NK cells play essential roles in eliminating virally infected cells and tumor cells) and T lymphocytes.[1,2]

The adaptive immune system, also known as acquired or specific system, provides a specific response against an infectious agent, but also possesses specific immunological memory, which prevents the infectious agent causing disease during a future infection. Adaptive immunity is mediated by B and T lymphocytes. Whilst B cells differentiate into plasma cells whose primary function is the production of antibodies, T cells can differentiate into either T cytotoxic or T helper cells. The two main types of T helper cells are Th1 and Th2 cells, but there are also Th17 cells –a new subset of T helper cells which have been discovered and characterized in the last decade.[3–5] Each cell subset eliminates different types of pathogens: intracellular bacteria and viruses are removed by Th1 cells, helminth parasites by Th2 cells and extracellular bacteria and fungi by Th17 cells.

The innate response is an immediate or short term response occurring within minutes or hours after infection. In contrast, the adaptive response requires days or weeks to take form.

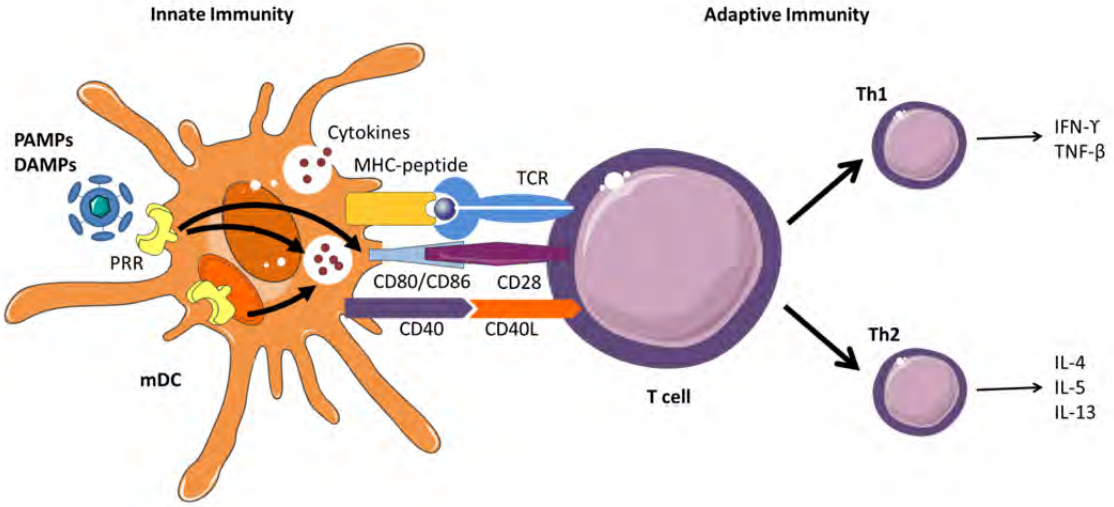

Fig. 3.1. Interface between innate and adaptive immunity**.** Pathogen promotes maturation of DCs to provide pathogen-specific T cells. Naïve T cells then differentiate into Th1 or Th2 cells.

An antigen is a substance able to induce a specific immune response and show immunological properties. Through antigen presenting cells (APCs) antigens are presented to the adaptive immune system, thereby, acting as a bridge between innate and adaptive immunity. Among the APCs, dendritic cells (DCs) are considered the professional APCs due to the constitutive expression of co-receptors required to allow APC-T cell signaling and activate the antigen presentation process.[6,7]

When the body is challenged by an injury or an infection, DCs travel to the site of infection to capture foreign microbes which are then digested into smaller protein fragments or peptides and displayed on their cell surface Major Histocompatibility Complex (MHC) molecules. The DCs then travel to lymphoid tissues, regions rich in T and B cells, of which DCs are efficient stimulators.[8,9] Whilst B cells recognize native antigen through their B-cell receptors, T lymphocytes by themselves are not able to do so and must be presented antigen by antigen-MHC complexes on the surface of DCs.

There are two types of MHC molecules, MHC class I and MHC class II, which are involved in the stimulation of cytotoxic T cells and helper T cells, respectively.[8] The main role of cytotoxic T cells is to directly kill the target cell, whereas helper T cells have

immune-regulatory effects such as activation of immune cells by releasing cytokines or induction of memory responses. Intracellular antigens are loaded onto MHC class I molecules and are recognized by cytotoxic T cells, whilst extracellular antigens that have entered a cell by endocytosis, are presented by MHC class II to helper T cells. APCs capable of cross-presentation (also known as cross-priming) are primarily DCs, but macrophages, B lymphocytes and sinusoidal endothelial cells have also been shown to be able to do so.[10] The underlying intracellular mechanism is still unclear but it is based on an exchange of presentation pathway, in which antigenic fragments that enter the cytoplasm via the endocytotic pathway are presented through the MHC class I molecules.

In most tissues, DCs are presented in an "immature state". When they encounter an infectious agent they begin to phagocytose (eat) the pathogen and immature DCs transform into mature DCs and their mobilization or migration to lymphoid organs starts **(Fig. 3.2)**. Mature DCs express high levels of co-stimulatory molecules (CD80, CD86) and the lymph node homing receptor CCR7,[8,11] as well as receptors of the tumor necrosis factor (TNF) family and they produce inflammatory cytokines such as IL-6, IL-12 and IFNs.[12] These co-stimulatory molecules, receptors and cytokines can be promoted by the triggering of Toll-like receptors (TLRs) on APCs, which have an essential function in the innate immune system to activate antimicrobial responses.[13–15]

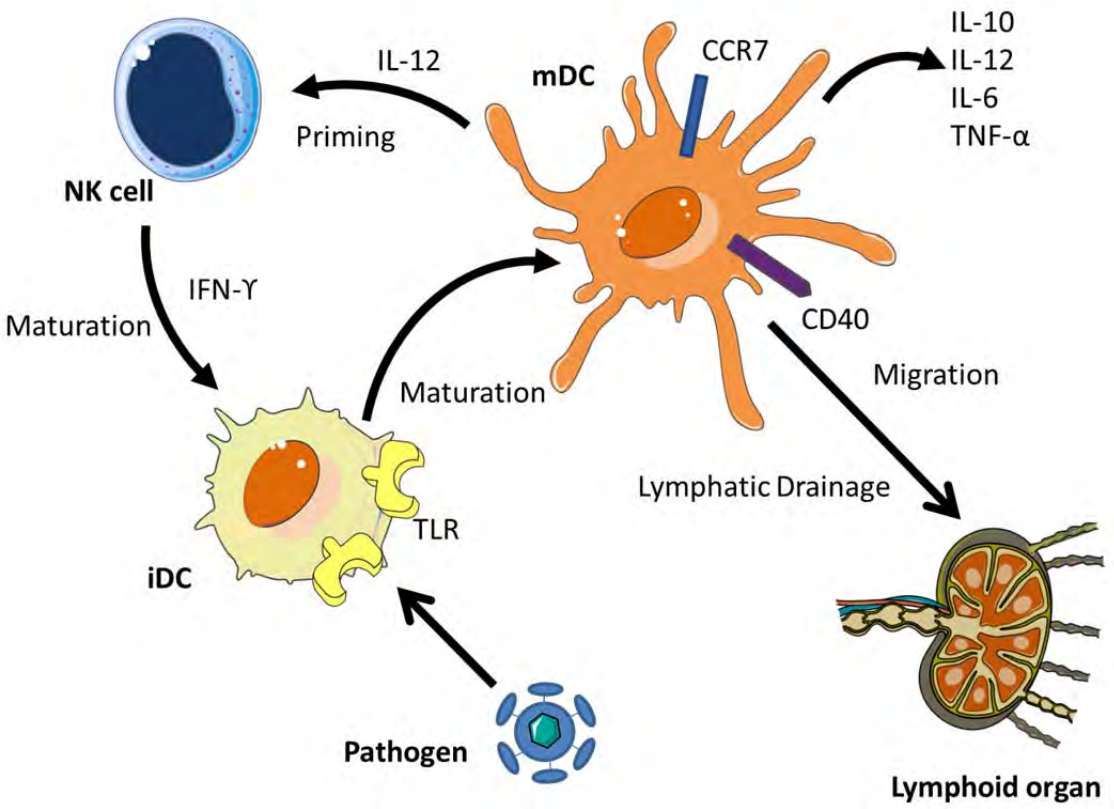

Fig. 3.2. DC activation by pathogens promotes the migration process to the draining lymphoid organs by triggering a maturation stage, which implies secretion of cytokines, chemokines or high levels of antigen presenting molecules.

3.1.2 Targeting pattern recognition receptors

The innate immune system plays a crucial role in the early recognition and subsequent triggering of a proinflammatory response.[16] This recognition is mediated by a class of protein receptors called “pattern recognition receptors” (PRRs) expressed by cells of the innate immune system. There are three types of PRRs involved in the recognition of pathogens: retinoic acid-inducible gene I (RIG-I)-like receptors (RLRs), nucleotide oligomerization domain (NOD)-like receptors (NLRs) and the aforementioned TLRs. There is another family called C-type lectin receptors (CLRs), involved in fungal recognition and the modulation of immune system. TLRs and RLRs both play essential roles in the detection and recognition of viral invasion and are involved in the production of type I interferons (IFNs) and proinflammatory cytokines.

RLRs include the dsRNA sensors RIG-I (retinoic-acid-inducible protein 1) and MDA-5 (melanoma-differentiation-associated gene 5), which upon ligand binding results in the production of IFNs in infected cells.[17]

NLRs are known to regulate a specific cytokine named interleukin-1 β (IL-1β) through activation of caspase-1, which is activated independently of TLR signalling. The maturation of IL-1 β is necessary in the process of dsRNA stimulation.[18] This cytokine plays an important role as mediator of the inflammatory response, and it is involved in a variety of cellular activities, including cell proliferation, differentiation, and apoptosis.

TLRs were the first and are the best characterized subclass of trans-membrane PRRs. They were discovered over a decade ago and so far, 10 human and 13 murine TLRs have been characterized.[19] TLRs can be divided according to their cellular location; TLR1,-2,-4,-5,-6, and -10 are expressed on the cell surface, whereas TLR3,-7,-8 and -9 are expressed in intracellular compartment membranes including endosomes and the endoplasmic reticulum.

TLRs are capable of recognizing specific molecules including lipids, nucleic acids or proteins associated with pathogenic microorganisms known as PAMPs (pathogen-associated molecular patterns) and endogenous molecules created upon tissue injury called DAMPs (damage-associated molecular patterns). The detection and connection TLR-PAMPs/DAMPs have been thoroughly studied.[20–22] It has been shown that TLRs bind to a variety of different ligands; for example lipopolysaccharide (LPS) binds to TLR4, CpG DNA from bacteria and viruses are detected by TLR9, and single-stranded viral RNA or imidazoquinolines are detected by TLR7. The most relevant receptor for the work developed in this thesis is TLR3 which recognizes viral dsRNA and its synthetic analog poly (I:C).[23]

TLR signaling pathways can be classified as MyD88 (myeloid differentiation primary-response protein 88)-dependent or TRIF (Toll/IL-1R domain-containing adaptor inducing IFN)-dependent pathways but TLR3 is unique among reported TLRs because its signaling activity depends exclusively on the TRIF pathway. The activation of MyD88 and TRIF drives the induction of inflammatory cytokines or type I IFNs and inflammatory

cytokines, respectively.[24] The orchestration of signaling from TRIF activation to cytokines production is mediated by the activation of several receptors as is represented in **Fig. 3.3**.

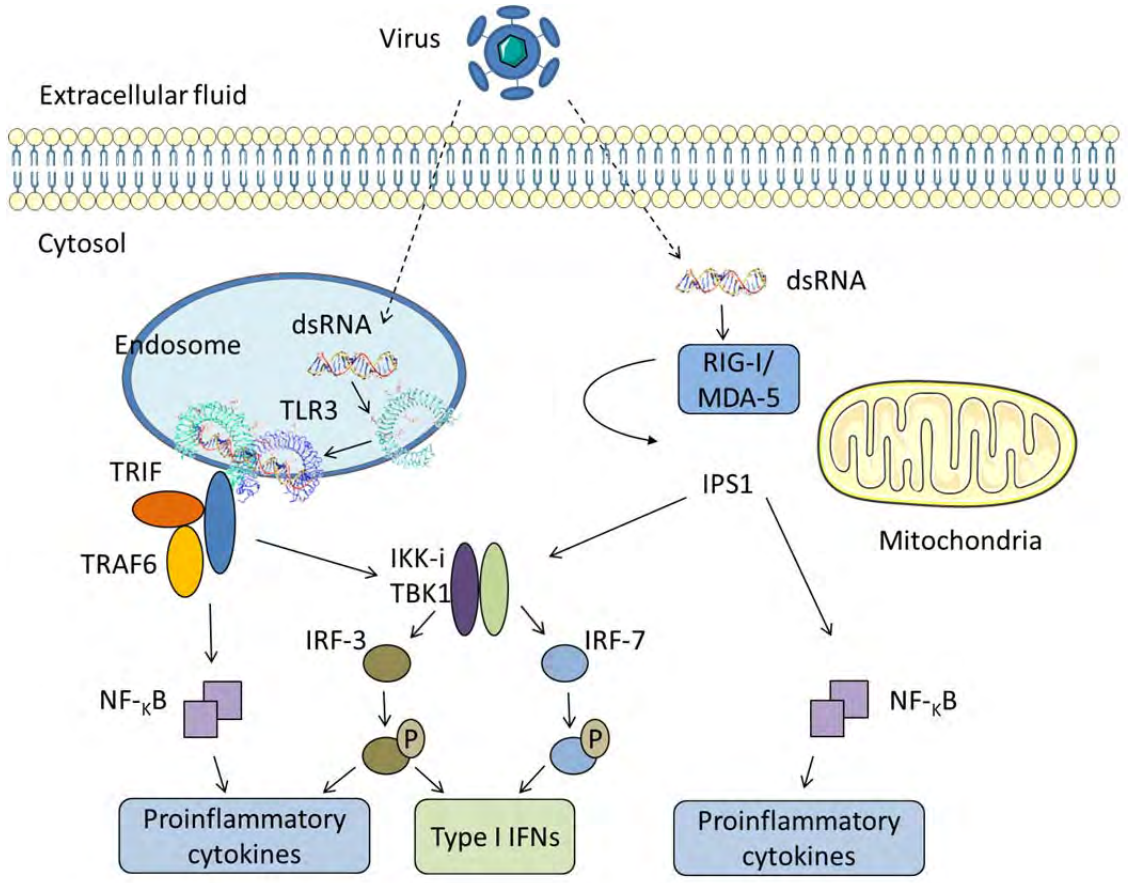

Fig. 3.3. Intracellular TLR3 signaling pathway which induces production of inflammatory cytokines and type I IFNs. Adapted from *Cell*, **2006,** 124,783.

TLR3 is located predominantly within early endosomes but its expression on the cell surface is reported in some cell types.[25,26] Its crystal structure was published initially by the research groups led by Davies[27] and Wilson[28] (2005) and later in 2008, the crystal structure was completed with the dsRNA binding site by Davies and collegues.[29]

TLR3 has a defined binding site called ectodomain (ECD) where the interaction between TLR3 and dsRNA occurs. The interaction of dsRNA with TLR3-ECD promotes the dimerization of the receptor and leads to the activation of downstream signaling starting with the TRIF factor. Human and mouse TLR3-ECDs share 78 % of their sequence identity and their structures are highly homologous.[29] The ligand binding site ECD consists of leucine-rich repeats (LRR, which are amino acid sections rich in the hydrophobic amino

acid leucine) forming a protein structural domain with a horseshoe-shape. The TLR3-ECD horseshoe consists of 23 LRR repeats capped at each end by specialized N- (LRR-NT) and C- (LRR-CT) terminal domains.[29,30]

The TLR3-dsRNA binding is guided by several requirements. The presence of carbohydrates along one side of the structure blocks the access of ligands to this surface sites, but the opposite surface lacks glycosylation and allows the interaction. The acidic pH present in endosomal compartments (≈ pH 6.5) regulates TLR3-dsRNA binding. In fact, Botos *et al.* have reported that at neutral pH TLR3 does not bind dsRNA.[30] Another key factor in the TLR3-dsRNA binding is the length of the nucleic acid. An oligonucleotide with at least 40-50 bp (base pairs) is needed to form a dimer structure. The interaction of dsRNA with TLR3 takes place between the sugar-phosphate backbone of the dsRNA and the N— and C— terminal site on the glycan-free surface of each monomer, as highlighted in **Fig. 3.4** where the crystal structure is represented.

a

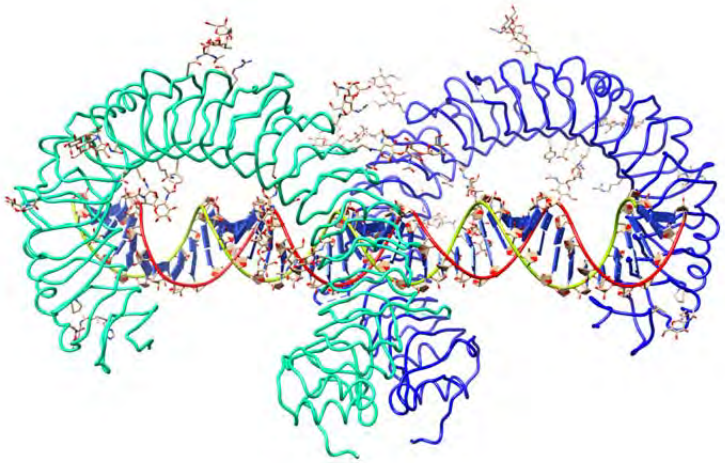

Fig. 3.4. Crystal structure of dsRNA-TLR3 binding. **(a)** Side view of TLR3 dimer bound to dsRNA. **(b)** Top view of the TLR3-dsRNA complex. Adapted from RCSD Protein Data Bank (PDB).

3.1.3 Features of the vaccine adjuvant poly (I:C)

The objective of a vaccine is to induce immunity by administering an antigen against which antibodies will be produced. A common problem which can happen is that no immune response is activated, simply because the vaccine is too "clean" and the body does not see the antigen. Over the past two decades considerable attempts have been made to increase the immunogenicity of vaccines by including substances known as adjuvants (from Latin "adiuvare" meaning to help).[31,32]

Adjuvants improve vaccine efficacy either by enhancing the magnitude or the duration of the antigen specific immune response. They exist in a wide variety of forms, including nanoparticle delivery systems, soluble ligands, metal salts or emulsions. Among the various methods in which adjuvants can function, soluble ones are capable of interacting with the previously mentioned TLRs.[33] There are few adjuvants available for human use, and poly (I:C) is one of the few nucleic acids used as therapeutic agent approved for advanced cancer treatments in humans.[34,35] Currently, one company, Hemispherx Biopharma Inc.,[36] is involved in clinical trials using a specifically configured dsRNA, called Ampligen (poly I:poly $C_{12}U$). On its own or in combination with other drugs, poly (I:C) is being developed for the potential treatment of viral diseases and diseases of

the immune system including HPV, HIV, chronic fatigue syndrome (CFS), hepatitis and influenza.

Poly (I:C) is a synthetic analog of viral dsRNA, a molecule associated with viral infection because most viruses produce dsRNA during their intracellular replication cycle.[37] Its structure consists of two helical strands, one strand based on a polymer of inosinic acid and the other of cytidylic acid, connected via hydrogen bonds and the stacking between base pairs **(Fig. 3.5)**. *In vitro* poly (I:C) induces a very potent IFN production and maturation of DCs.[38] Furthermore, recent studies have highlighted the potential of using poly (I:C) to induce cancer cell apoptosis and has been shown to activate NK cells via innate immune cells.[39–42]

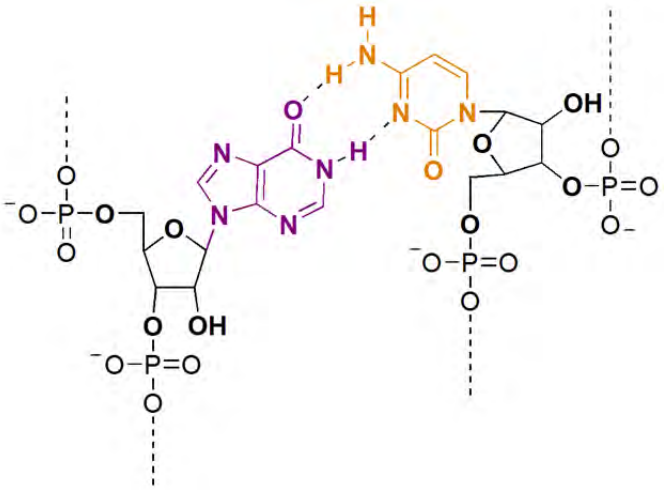

Fig. 3.5. Schematic structure of poly (I:C). The polymer is comprised of one strand each of polyinosinic acid (purple colour) and polycytidylic acid (orange colour).

Poly (I:C) is sensed by both TLR3 (located on the cell surface or in the endosomes) and MDA-5 (located in the cytoplasm) **(Fig. 3.3)**. The recognition of dsRNA by RIG-I/MDA-5 or TLR3 is cell-type dependent.[24,43] Both sensors initiate a cascade of signalling pathways that lead to the activation and expression of a complex system of regulatory factors and cytokines. However, the mechanisms by which both sensors recognize the dsRNA are still not completely clear. Cells infected by virus can produce Type I IFNs in a TLR3-independent manner.[44–46]

3.1.4 Interactions between NPs and the components of the immune system

NPs can be specifically designed to either target or avoid interactions with the immune system.[47,48] NPs can modulate the immune system by achieving either its suppression or its stimulation. NPs can be covered with a polymer, such as poly(ethylenglycol) (PEG) to avoid the recognition by the immune system, suppressing recognition by macrophages and the subsequent clearance by the MPS.[49] However, NPs can also be designed to promote an immune response either by direct immunostimulation of APCs or by delivering molecules to specific cellular compartments.[50]

Within the immunostimulatory potential of NPs, the effects of NPs-based vaccines on the immune system and the ability to stimulate innate or adaptive immune responses are attracting great interest.[48,51] It has been published that depending on the administration route vaccine efficacy can be improved by the use of NPs.[52] Furthermore, the use of NPs as vaccine delivery vehicles offers several advantages, such as the ability to deliver the drug to a specific site, the possibility of enhancing drug stability and the opportunity of decreasing the risk of causing side-effects.

A common problem with NPs-based systems is the adsorption of serum proteins after administration, regardless of the route of injection. The main factor that controls NP-protein interaction is the physico-chemical characteristics of the NP shell. As proteins are charged macromolecules with both hydrophobic and hydrophilic domains, the charge, size and structure of NP shell can have an important impact on promoting protein-NP interactions. The physico-chemical properties of NPs can change considerably upon exposure to serum proteins, consequently affecting the recognition and uptake process which is involved in both the immune response and the systemic clearance **(Fig. 3.6)**. So, the physical and chemical features of NPs regulate the interaction with the immune system.

It is reported that the amount of plasma proteins absorbed is lower for smaller NPs, resulting in a faster systemic clearance for bigger NPs.[53,54] Ready *et al.* have reported

that the protein absorption can oscillate between 6 and 34 % on NPs with sizes of 80 and 240 nm respectively. Protein absorption can also have an influence on the circulating time in the body, biodistribution behavior and clearance of the NPs by macrophages.[55]

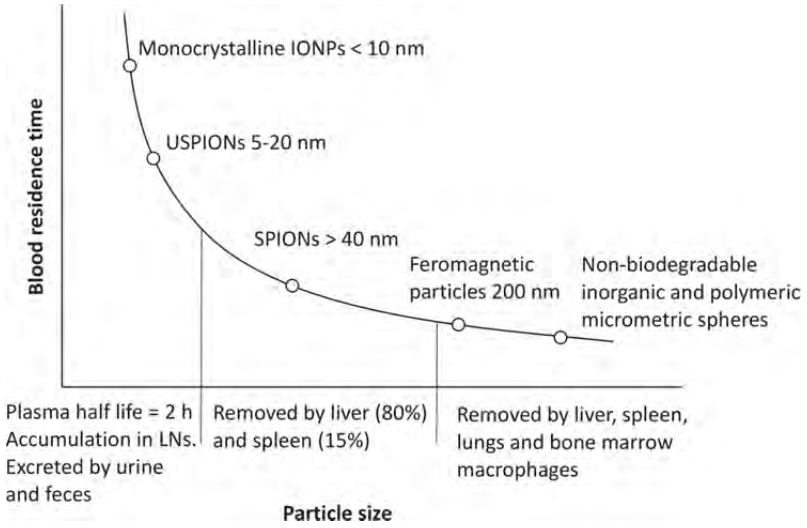

Fig. 3.6. Evolution of blood residence time with particle size. IONPs: iron oxide nanoparticles; USPIONs: ultrasmall superparamagnetic IONPs; SPIONs: large superparamagnetic IONPs. Adapted from *Nanotoday*, **2007**, 2,22.

The design and characterization of an optimal coating for the drug delivery carrier (as it was discussed in Chapter 2) is also essential to define and modulate immune responses.[56] Engineered nanoparticles with positive surface charge are often more cytotoxic than anionic or neutral ones.[57] The negatively charged plasma membrane of the cells binds more efficiently cationic NPs than anionic or neutral NPs, and the internalization of anionic NPs is typically faster than neutral ones due to the lower number of electrostatic interactions. For instance, it has been reported that *in vitro* and *in vivo* a high number of primary amine groups present on the surface of NPs increase the cytotoxicity of the nanocarrier. In the specific case of poly(amidoamine) (PAMAM) dendrimers (one of the most widely used dendrimers in biomedical applications) their cytotoxicity decreased when amine groups are neutralized with acetyl groups.[58]

It is important to highlight the role of NP size in both migration to lymph nodes and phagocytosis by immune cells. In terms of trying to mimic natural pathogens for synthetic vaccine development, it is appealing to make particles of similar sizes to the targeted pathogens, which ranges from 20-100 nm in the case of viruses to 100 nm-1 µm for bacteria. There are two main types of phagocytes in the immune system: macrophages and dendritic cells. Both types of cells can phagocytose NPs up to 10 µm but the optimal size for uptake by APCs is still a matter of debate. In the literature it is reported that 500 nm seems to be very efficient for both cell types, DCs[59] and macrophages.[60] However, NPs larger than 200 nm do not enter the lymphatic system unless they are transported there by DCs.[61] NPs less than 200 nm can effectively enter in the lymphatic system and reach the lymphoid organs through the lymph drainage. In fact, it is reported in the literature that the optimal NP size for this purpose is ca. 40 nm.[62]

The internalization of the NPs by phagocytes occurs through diverse processes depending on the engulfment of the foreign particles.[63] This uptake process is known as endocytosis and deserves to be explained in more detail.

The four categories of endocytosis are: phagocytosis, macropinocytosis and endocytosis mediate by caveolae and clathrin receptors. Phagocytosis occurs when the internalization is mediated by specific receptors. This process involves the uptake of larger particles and larger membrane areas than the other three mechanisms. In this type of internalization the vesicles formed are denominated phagosomes and they directly fuse with late endosomes or lysosomes. Macropinocytosis consists on the invagination of the membrane which form a vesicle that travels into the cytosol and finally, it fuses with other vesicles such as endosomes and lysosomes. Caveolin-dependent endocytosis occurs at regions of the membrane rich in cholesterol and sphingolipids and clathrin-dependent is characterized by a complex of proteins that are mainly associated with the cytosolic protein clathrin. The mechanism of internalization of nanomaterials is still a matter of debate, because the same nanomaterial can show more than one mechanism of internalization.[64]

The general endocytic pathway consists of different membrane compartments of which three are crucial. Firstly the particle is internalized by vesicles formed at the

membrane by the mechanisms described above. Then, the vesicles formed are fused with early endosomes (EE),[65] which are considered also recycling endosomes because at this stage, most of the ligands are separated from the receptors , allowing the receptors to come back to the cell surface. The EE possesses a mildly acidic pH. Late endosomes[66] receive the endocytic particles from the EE and from the phagosomes in the phagocytic mechanism. Late endosomes have acidic pH (around 5.5) which, as it was mentioned in a previous section is crucial for the recognition of TLR3 and dsRNA. Late endosomes are the bridge to deliver the material to the lysosomes[67] (with a more acidic pH of around 4.8) through another fusion mechanism of both intracellular compartments. In the lysosomes the molecules will finally be degraded by the presence of hydrolytic enzymes, thereby promoting the intracellular signaling pathway.

Another parameter that plays an important role in the immune response elicited by a particulate-delivered system is the administration route.[68] There are two major routes of drug administration, enteral and parenteral. Enteral administration involves any part of the gastrointestinal tract and the oral, sublingual, buccal and rectal administrations are included in this type. Parenteral administration, which does not involve the gastrointestinal tract include intravenous (i.v.), intramuscular (i.m.) or subcutaneous (s.c.) among others. The topical route, including transdermal or inhalation is usually considered parenteral administration route. Each route of administration has advantages and disadvantages that should be considered depending on the therapeutic objective to achieve or the organ to reach, and it is also determined by the properties of the drug, such as water or lipid solubility.[69]

The toxicity of the NP system associated with each specific route of administration is still a matter of debate.[69,70] Overall, i.p. route of administration is generally preferred when i.v. administration is not feasible, such as when tumor is located in the peritoneal cavity.[71] However other routes of administration for drug delivery vehicles based on NPs like oral or inhalation routes have been extensively reported with success and low toxicology results in some cases.[72]

Subcutaneous injection has been widely used as administration route when the drug has low oral bioavailability. If the main goal is to reach lymphatic organs, lymphatic

uptake is an important parameter, and in this case, s.c. administration has been reported as a promising option to target therapeutic nanoparticle-drugs to the lymphatics.[73] In fact, the immunization efficacy of "pathogen-mimicking" NPs is based on the capability to reach the lymphoid organs and activate APCs for the development of an immune response. The NP administration route can affect the strength of this immune response.[74]

The NP-based delivery system may therefore be designed to modulate the interactions with immune cells and migration to the lymph nodes. This work is focused on the development of NPs capable of promoting migration to the lymph nodes, where resident APCs will be responsible for the activation of antigen specific immune responses.

The development of a NP-based system with an average size below 100 nm is one of the goals of this work. This nanomaterial size is considered ideal for effective lymphatic delivery.[75–77]

In this work, by the analysis of cytokine levels and the use of imaging techniques, we will demonstrate the ability of the construct poly (I:C)-IONPs@PL-PEG micelles, to migrate from the site of injection through the lymphatic system as well as their accumulation in the lymphoid organs, the spleen and the lymph nodes, where they initiate the orchestration of signals required for the development of a powerful immune response.

3.2 Results and discussion

3.2.1 Attachment of poly (I:C) onto IONPs@PL-PEG amine micelles

3.2.1.1 Synthesis and characterisation

The micelles produced as described in Chapter 2 containing IONPs in their inside, are constituted by a PEGylated phospholipid (PL) micelle coat which are composed of PLs with a variety of terminal end-groups. By altering these end-groups different overall changes such as the surface charge, can be conferred to the NP and thus, different biomolecules including proteins or nucleic acids can be attached.

Attachment of nucleic acids to magnetic NPs has been reported by means of covalent and non-covalent interactions.[78,79] More recently and related with this work, Tremel and coworkers investigated the attachment of poly (I:C) to amino-functionalized iron oxide NPs by amide bond formation and showed that the biological activity of poly (I:C) was retained in a human renal cell line (kidney cancer cells Caki-1).[80,81]

The electrostatic interaction strategy has also been widely used to attach nucleic acids, such as poly (I:C), to different nanomaterials. Parker-Esquivel *et al.*[82] have reported the possibility of binding poly (I:C) onto MnO nanorods decorated with cationic polyamidoamine (PAMAM) dendrimers. Positively charged gold NPs have also been used to attach nucleic acids via electrostatic interactions.[83] The “lipoplexes” or “polyplexes” structures (depending on whether the scaffold is a liposome or a polymer respectively) are arguably the most widely used cationic vehicles for the delivery of nucleic acids, and probably one of the most studied systems to characterize the electrostatic interactions between the nanocarrier and nucleic acid.[84]

There are several studies comparing covalent and non-covalent strategies for the same purpose and evaluating the possible different behavior for a particular application.[85] M. de la Fuente and colleagues[86] recently published the gene delivery efficiency of gold NPs when a siRNA (small interfering RNA) is bound by covalent or ionic interactions. Both nanosystems are able to deliver siRNA without remarkable differences in toxicity or efficiency between them. In the same field, Bhatia and coworkers[87] have reported the

effect of NP-siRNA conjugation in gene silencing, and how the chemical modification of the 5´ end can limit the silencing activity.

Based on the diversity of studies and discrepancies of the results reported in the literature assessing both strategies, it was decided to investigate both covalent and non-covalent binding of poly (I:C) to the IONP@PL-PEG micelles. In the covalent strategy, primary terminal amine groups on the PEGylated PLs of the micelles are bound to the 5´-end phosphate group present in the poly (I:C) structure using 1-ethyl-3-(-3-dimethylaminopropyl) carbodiimide hydrochloride (EDC) as is shown in **Scheme 3.1**.[79]

In a typical reaction, 100 µL of poly (I:C) solution (1 mg/mL) was mixed with EDC (1.25 mg, 6.5 mmol) in MeIm (0.1 M, pH = 7.5) buffer. The activated poly (I:C) was added to 20 µL of IONP-filled micelles composed of DSPE-PEG(2000)-NH_2 ([Fe] ca. 17 mM). The volume was adjusted to 200 µL with MeIm buffer and the sample was left overnight stirring at room temperature. The sample was purified by washing several times with 1 mM PBS using centrifugation devices and ultracentrifugation.

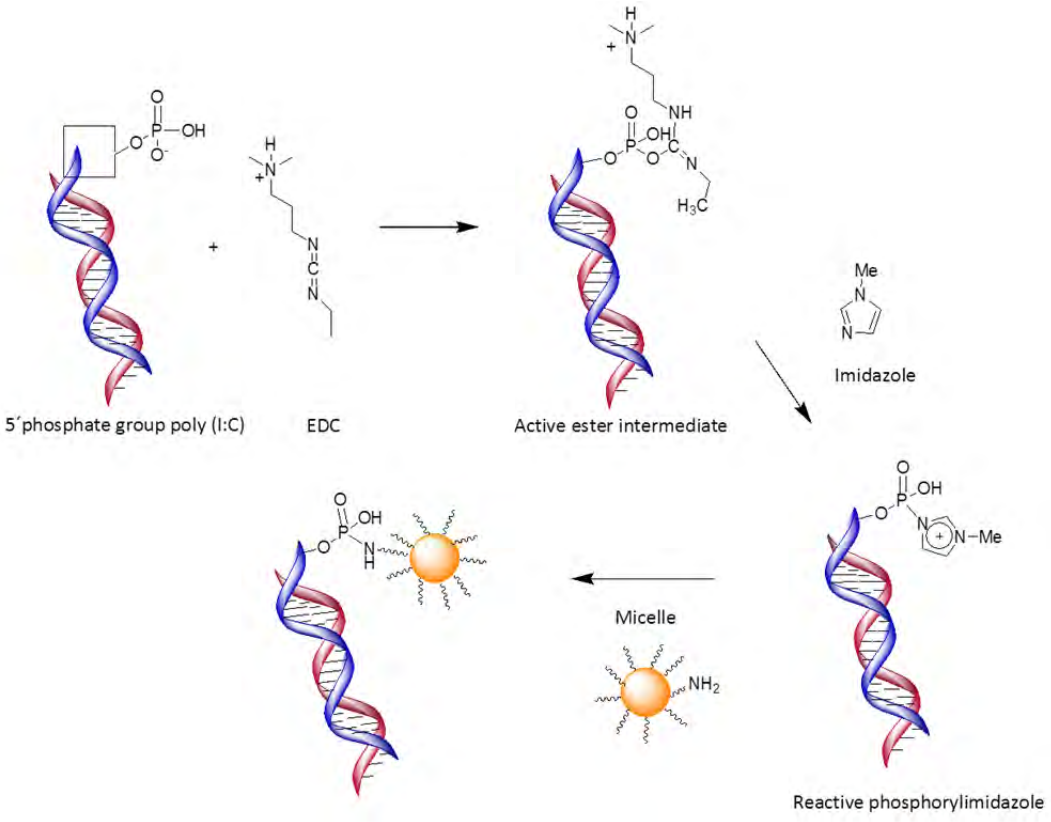

Scheme 3.1. Representative illustration of covalent strategy.

In the non-covalent strategy, 20 µL of IONP@PL-PEG amine micelles ([Fe] ca. 17 mM), was directly mixed with 100 µL of poly (I:C) solution (1 mg/mL). The volume was adjusted to 200 µL with MeIm buffer and the mixture was left stirring overnight at room temperature. Then the mixture was purified washing with 1 mM PBS several times using centrifugation devices as in the case of the covalent sample.

The covalently and non-covalently formed poly (I:C)-IONP@PL-PEG micelles were characterized by UV absorption. Nucleic acids absorb in the ultraviolet region of the spectrum due to the conjugated double bonds and aromatic rings. **Fig. 3.7** shows an example of the covalent and non-covalent attachment of poly (I:C) onto the samples. The peaks at 245 and 267 nm are characteristic of poly (I:C) and are present in all samples, control poly (I:C) alone and the poly (I:C)-IONP micelle systems, demonstrating the successful binding/attachment of poly (I:C) to the IONP@PL-PEG amine micelles.

The amount of poly (I:C) interacting with the IONP@PL-PEG amine micelles was quantified by hydrolyzing overnight a known IONP concentration in 0.2 M NaOH and then recording the UV-Vis absorbance at 251 nm **(Fig. 3.7b),** which was converted to concentration by comparison to a standard curve of hydrolyzed poly (I:C). The alkaline condition causes the breaking of interactions of the double helix. Thus, the amount of poly (I:C) attached to the micelle is determined, since the DNA/RNA bases absorb light in the 260 nm wavelength region. The binding efficiency seems to be similar in both strategies, ca. 83 % of the initial amount of poly (I:C) added.

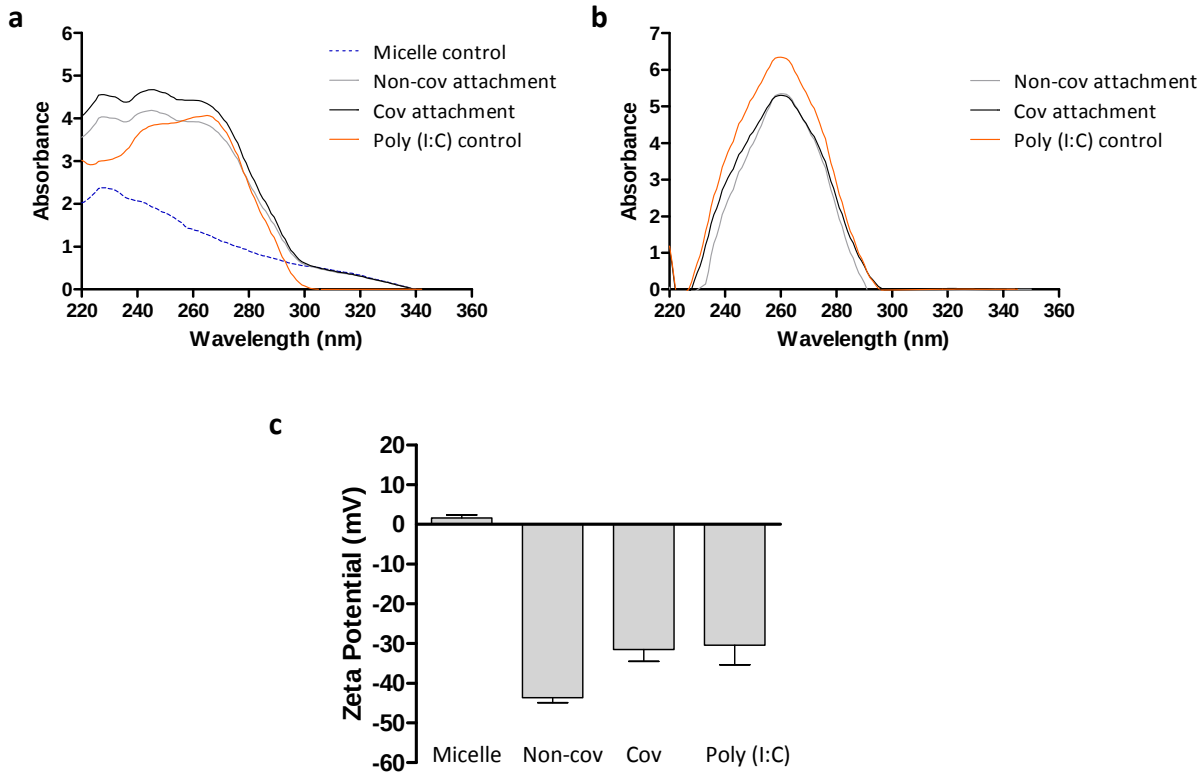

Fig. 3.7. (a) UV absorbance spectra of non-covalently and covalently formed poly (I:C)-IONP@PL-PEG micelles. **(b)** UV spectra of the hydrolyzed samples. **(c)** Zeta potential measurements.

Successful association, whether it be covalent or non-covalent, is expected to significantly shift the zeta potential of the micelle system due to association of the large negatively charged poly (I:C) polymer. The analysis reveals a significant shift in zeta potential from +2 mV to -43 mV in the case of non-covalent association, or -31 mV in the case of covalent association **(Fig. 3.7)**, which suggests that there has been a successful attachment of poly (I:C) by both methods. These zeta-potential values are in concordance with the results derived from analyzing the UV spectra and show that there is no significant difference in the amount of poly (I:C) that is loaded to the micelles using the two methods.

3.2.1.2 Immunostimulatory activity

It is reported that the attachment method of the nucleic acid in the delivery vehicle is very important for its appropriate release once inside the cells.[87] In this case, the dsRNA-NP interactions have to be robust enough to cross biological barriers and preserve the biomolecule, but may need to weak enough for the NP release the poly (I:C) upon binding with the TLR3. Hence, it is investigated if there are any significant differences in the stimulatory activity between non-covalent and covalent association of poly (I:C) to IONP@PL-PEG amine micelles. The samples were incubated with the murine macrophages cell line J774 which produce the proinflammatory IL-6 cytokine upon immunostimulation.

For these experiments, the cells were seeded in a 96-well plate and allowed to adhere overnight. Then the media was removed from each well and 100 µL of NP formulations were added, diluted accordingly in media. Cells were incubated for 24 h at 37 °C in 5 % CO_2. The supernatants were harvested and frozen for subsequent cytokine analysis, whereas the adherent cells in the bottom of the well were incubated for 1 h with MTT reagent to analyze the cell viability. A sandwich ELISA assay was used to quantify IL-6 cytokine production in cell supernatants. The results of both assays are shown in **Fig. 3.8.**

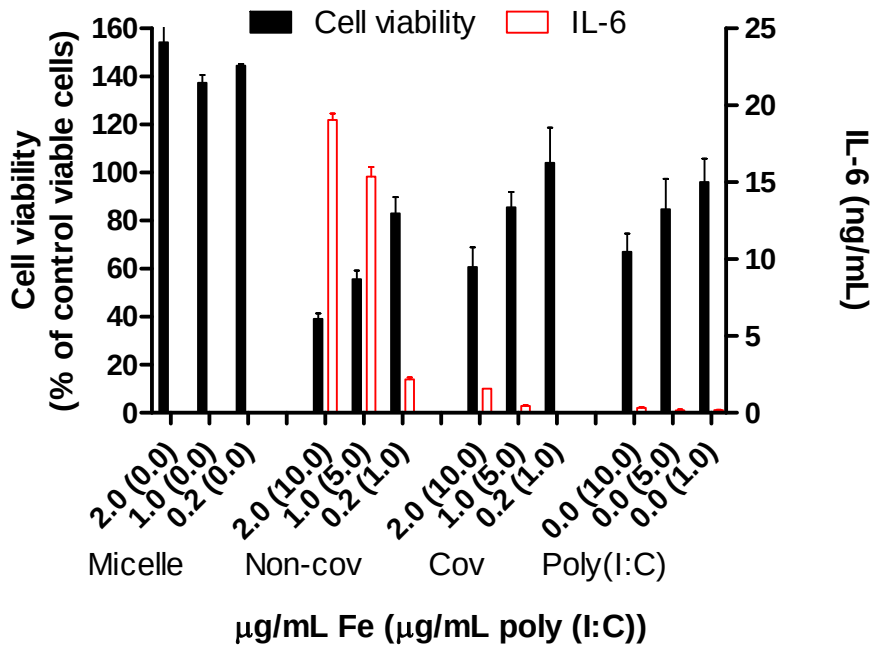

Fig. 3.8. Comparison of covalently (Cov) attaching poly (I:C) to IONP@PL-PEG amine micelles versus non-covalent (Non-cov) binding. Cell viability and IL-6 release in J774 macrophages. Data are presented as mean ± SEM of three replicates and representative of three independent experiments.

The first finding to comment is that the amine-decorated IONP@PL-PEG micelles are not toxic in the range of concentrations used and secondly, that the toxicity associated with the poly (I:C)-IONP@PL-PEG micelles systems is due to the presence of poly (I:C). The level of toxicity noted is also comparable to the poly (I:C) alone. In the same graph the level of cytokine IL-6 produced by cells upon exposure to the NPs systems or free poly (I:C) alone is shown on the right y-axis. The study shows significant differences in terms of biological activity due to the different ways by which the poly (I:C) was conjugated to the IONP micelles.

When cells are exposed to IONP@PL-PEG amine micelles with covalently attached poly (I:C) at 10 μg/mL the amount of IL-6 produced is relatively low (ca. 1.5 ng/mL), but still somewhat higher than with free poly (I:C) (< 0.5 ng/mL). Remarkably, when cells are exposed to the non-covalent system, a 10-fold increase in IL-6 production by cells is noted, obtaining the highest value of IL-6 ca. 19 ng/mL. The same trend is followed in all

the other concentrations tested with a concentration-dependent effect in the IL-6 cytokine production. Overall, although both covalent and non-covalent attachment of poly (I:C) resulted in effective delivery systems because their stimulatory capacity is greater than poly (I:C) alone, the non-covalent system was easier to prepare and provided much higher capacity to trigger IL-6 release **(Fig. 3.8).**

3.2.2 Attachment of poly (I:C) onto IONP@PL-PEG methoxy micelles

3.2.2.1 Synthesis and characterisation

The high levels of IL-6 produced using the non-covalent method prompted us to test this strategy using other PEGylated PLs. Specifically, the DPPE-PEG(2000)-OMe was used to prepare the micelles and to attach poly (I:C) by non-covalent interactions. The PEG-RNA interaction was recently studied in depth by Froehlich *et al.*.[88] In this publication, the multiple hydrophobic and hydrophilic interactions through the RNA bases and the backbone phosphate group with different PEG derivatives were analyzed by Fourier Transform Infrared Spectroscopy (FTIR), Circular Dichroism (CD) and Atomic Force Microscopy (AFM). The results showed that RNA can interact with all these different PEG derivatives by non-covalent interactions.

Initially, IONP@PL-PEG micelles functionalized with amine groups were expected to bind electrostatically to dsRNA. However, taking into consideration the results of Froehlich and colleagues and other publications where large DNA molecules can wrap around the curved surfaces of NPs[89–91], it is reasonable that poly (I:C) is capable of binding by non-covalent interactions to IONP@PL-PEG micelles independently of the terminal end-groups.

The PEGylated PLs functionalized with methoxy groups allowed the attachment of poly (I:C) to the micelles by the same general procedure followed for non-covalent attachment to the amine-decorated micelles. In this case, however, 20 µL of IONP@PL-PEG methoxy micelles ([Fe] ca. 17 mM), were directly mixed with different amounts of poly (I:C), covering a wide range of concentrations from 900 to 62.5 µg/mL, in a final

volume of 200 µL PBS (1 mM). After overnight stirring incubation with poly (I:C) at room temperature, centrifugation steps were used to remove poly (I:C) free molecules.

The IONP@PL-PEG methoxy micelles decorated with the lowest amount of poly (I:C) at 62.5 µg/mL were thoroughly characterized by UV absorption, DLS, TEM and by AFM to confirm that the behavior of poly (I:C) in the methoxy micelles is the same compared to the amine micelles **(Fig. 3.9)**. The size of the delivery system was also characterized to ensure that the system is below 100 nm (as it was previously mentioned, this is the optimal size for lymphatic uptake). AFM is a useful technique to visualize the morphology of the dsRNA before and after the addition to IONP@PL-PEG methoxy micelles. The relatively large size (1.5-8 kb) of the poly (I:C) allows its visualization by AFM, whereas with TEM only the IONP can be seen, regardless of the presence of poly (I:C).

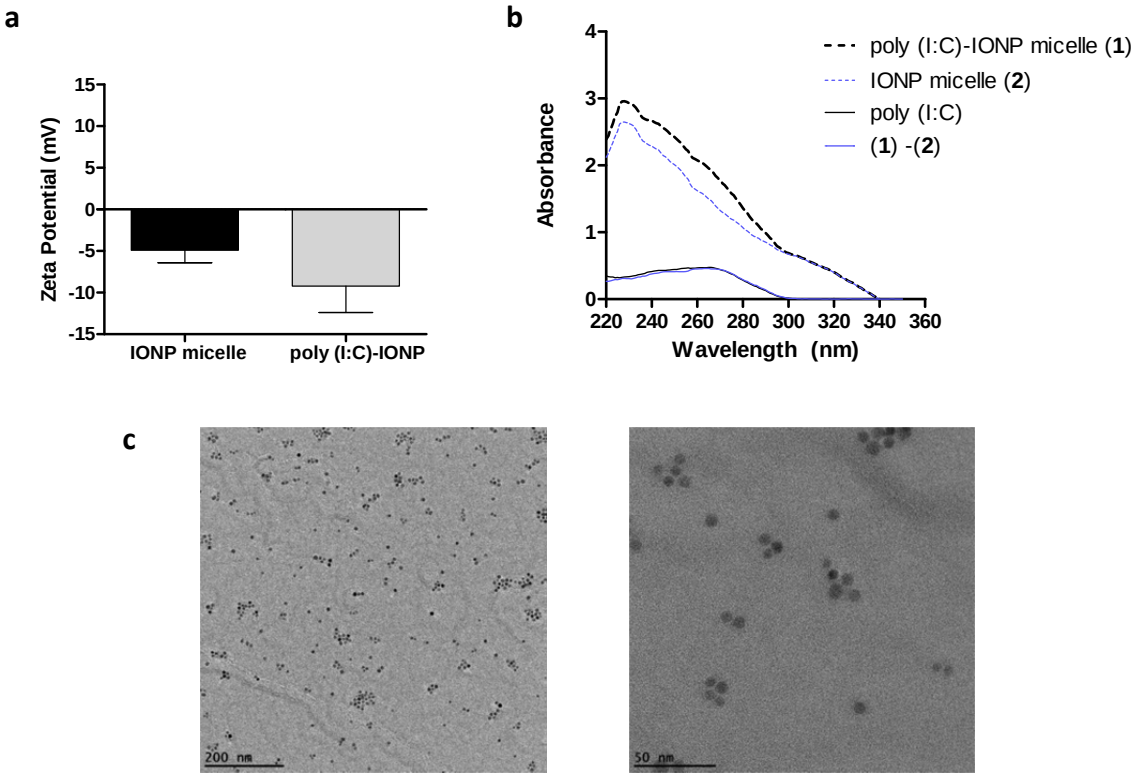

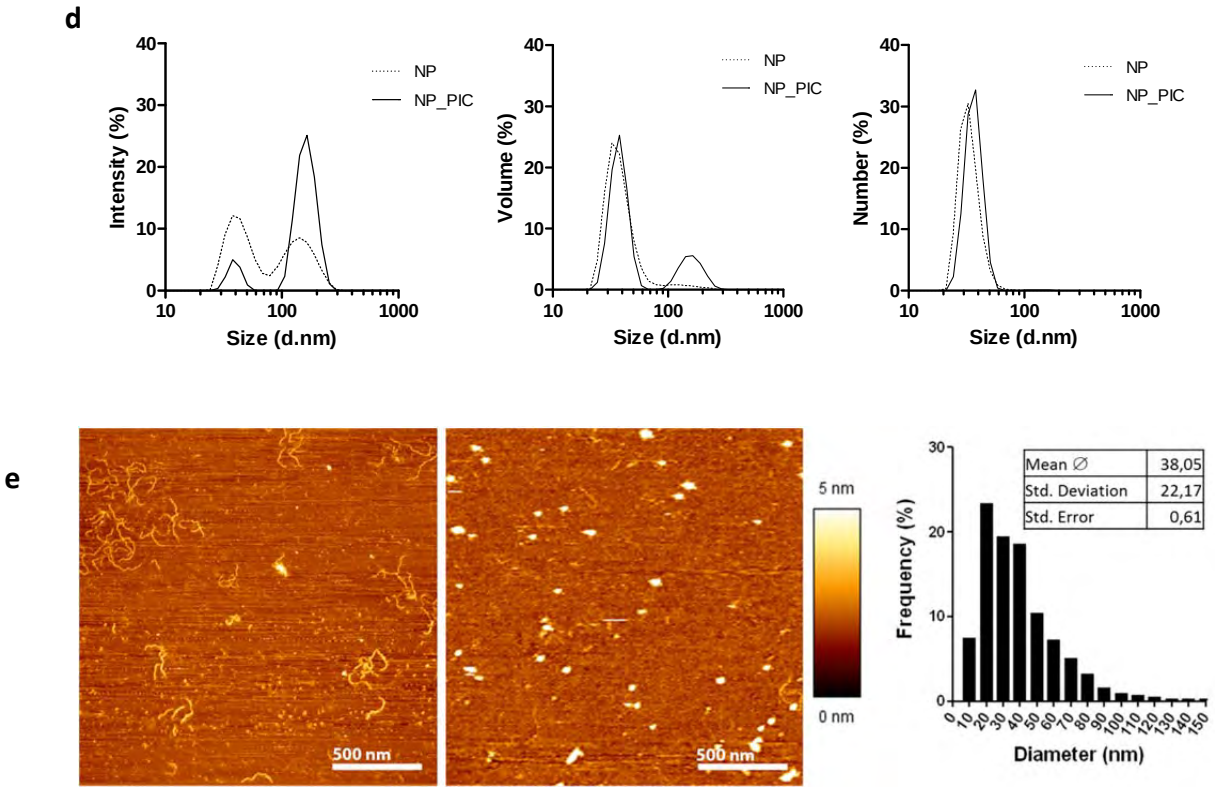

Fig. 3.9. Characterization of the poly (I:C)-IONP@PL-PEG methoxy micelles. **(a)** Zeta potential of IONP@PL-PEG methoxy micelles and poly (I:C)-IONP@PL-PEG methoxy micelles. **(b)** UV absorbance spectra recorded on a ND-1000 UV/Vis spectrophotometer of poly (I:C), IONP@PL-PEG methoxy micelles, poly (I:C)-IONP@PL-PEG methoxy micelles and poly (I:C)-IONP@PL-PEG methoxy micelles after removing the contribution of the IONP@PL-PEG methoxy micelles. **(c)** Representative TEM images of poly (I:C)-IONP micelles. Hydrophobic core: 6.75 ± 0.10 nm **(d)** Size distribution of IONP@PL-PEG methoxy micelles (NP) and poly (I:C)-IONP@PL-PEG methoxy micelles (NP_PIC) obtained by DLS. **(e)** AFM images of poly (I:C) alone (*left*) and poly (I:C)-IONP@PL-PEG methoxy micelles (*right*) with the size distribution histogram of more than 1000 micelles obtained using AFM.

As it is shown in **Fig. 3.9,** the zeta potential histogram and UV spectra confirm the success of the poly (I:C) attachment onto the methoxy-terminated micelles. It was found that the amount of poly (I:C) attached to the micelles was comparable with the non-covalent attachment to amine-terminated micelles. The surface of the NP presents a negative charge due to the net anionic charge on the oxygen phosphate moiety of the phospholipid[92] and as expected, the surface charge changes to a more negative value upon addition of poly (I:C). However, in this case the addition of poly (I:C) has only a small

effect on the zeta potential of the micelles (-5 mV to -9 mV) because in this system we wished to have a much higher IONP:poly (I:C) ratio (i.e. each micelle has much less poly (I:C)). It will be shown in the following sections this system has the best immunostimulatory capacity.

Even at high IONP:poly (I:C) ratio poly (I:C) retains the dsRNA structure after its conjugation with methoxy micelles. Thus, the UV spectrum of the poly (I:C)-IONP micelles is identical to that of poly (I:C) when the contribution of the IONP@PL-PEG methoxy micelle is removed from the poly (I:C)-IONP@PL-PEG methoxy micelle absorbance. DLS and TEM were used to determine the size of the poly (I:C)-IONP micelles. As **Fig. 3.9** shows, there is not a large increase in the size of the system, again this is because the thin layer formed by the small amount poly (I:C) around the IONP@PL-PEG methoxy micelle nanocarrier is guided by the width of the nucleic acid. The length between complementary nucleotide bases on opposite strands in the general double strand structure of nucleic acids is 2.2-2.6 nm.[93,94] Considering the size of poly (I:C) (1.5-8 kb), a single poly (I:C) molecule is sufficient to cover the micelle circumference, so the size difference observed by DLS measurements is in accordance with the proposed arrangement of poly (I:C) over the IONP@PL-PEG methoxy micelles.

However, it is important to highlight the differences between the three representative examples of DLS graphs for poly (I:C)-IONP@PL-PEG methoxy micelles and IONP@PL-PEG methoxy micelles, shown in **Fig. 3.9d.** The correlation function displays two intensity peaks for both systems. This is because DLS experiments are extremely sensitive to the presence of even traces of larger particles.[95] When light hits small particles, the light scatters in all directions (Rayleigh scattering) as long as the particles are smaller compared to the wavelength. It occurs when light travels through transparent solids and liquids. The Rayleigh approximation tells us that $I \alpha d^6$, where *I* is the intensity of light scattered and *d* is the particle diameter. As a result, a 50 nm particle will scatter one million times as much light as a 5 nm particle. So, if the number distribution of a system consisting of two different particle sizes in equal proportion (e.g. the spherical particles of diameter 5 and 50 nm) is plotted, two peaks of similar intensity are obtained. However, when this number distribution is converted into the intensity distribution, then the intensity of two peaks changes to a 1:1 000 000 ratio because the scattering intensity of a

sphere is proportional to d^6. In our case, to elucidate the importance of the second peak in the intensity distribution, which corresponds to the larger population, Mie theory was applied to convert the intensity distribution into a number distribution (a complex function performed by the software of the equipment which describes how spherical particles scatter light). Then, the second peak nearly disappeared on plotting the number distribution, assuming that the origin of this second peak is due to very small impurities of the sample, like small amount of aggregates, not detectable by other techniques.

The poly (I:C)-IONP@PL-PEG methoxy micelles were also studied by AFM using the tapping mode which can gather information on the morphology of the NPs **(Fig. 3.9e)**. The samples were taken onto a 3-aminopropyltriethoxysilane (APTES) modified mica surface in water. Imaging poly (I:C) alone displays the elongated coil state of the nucleic acid of few nm height. However, the morphology of the dsRNA changes upon addition of IONP micelles to compact globular structures with an average size of 40 nm. Imaging the sample after addition of IONP@PL-PEG methoxy micelles clearly shows the binding with the dsRNA. The diameter less than 50 nm obtained by DLS studies correlates nicely with the particle size determined by this AFM analysis. Correlating the results obtained from DLS, this strongly suggests that poly (I:C) has wrapped itself around the IONP@PL-PEG methoxy micelles, a hypothesis which is also supported by the TEM and zeta potential data.

3.2.2.2 Immunostimulatory activity

a) Effect of the IONP-to-poly (I:C) ratio

The ability of IONP@PL-PEG methoxy micelles decorated with different amounts of poly (I:C) to activate the immune system was investigated *in vitro* in the aforementioned murine macrophage cell line J774. The cell viability was also analyzed after 24 h of incubation with a range of IONP@PL-PEG methoxy micelles carrying different poly (I:C) concentrations.

Fig. 3.10a shows the cell viability of macrophages upon exposure to the NP systems and poly (I:C) alone. The percentage of alive cells obtained in the NP systems is

comparable to the alive cells in the presence of poly (I:C) alone at the same concentration. Comparing the samples at a fixed amount of 5 μg/mL of poly (I:C) it is observed that cell viability is ca. 60 % or greater for poly (I:C) alone in samples with iron concentrations of 1.0 and 2.0 μg/mL Fe. It is necessary to increase the amount of iron up to 4 μg/mL Fe to observe a decrease in cell viability below to 50 % (red colour points in **Fig. 3.10a**).

It can also be observed that cell viability decreases as the amount of added poly (I:C) is increased, getting to a lowest value of 40 % of survival when the cells are incubated with higher ratios of IONP-to-poly (I:C) (2.0 μg/mL Fe with 15 or 18 μg/mL poly (I:C)).

The IONP-to-poly (I:C) ratio affects the activity of the poly (I:C)-IONP micelles in the cytokine production as it is shown in **Fig. 3.10b.** Taking 5 μg/mL of poly (I:C) as a fixed amount of dsRNA, it can be noted that increasing the amount of NP increases significantly the immunostimulatory efficiency of the nanosystem. The importance of the NP-to-dsRNA ratio is highlighted in the systems with 1.0 and 2.0 μg/mL Fe, whose cytokine release value increase more than three times from 6 ng/mL to 21 ng/mL of IL-6, respectively. However, the production of IL-6 does not increase notably when the amount of NP is increased up to 4 μg/mL Fe.

Due to the toxicity of the latter sample (4 μg/mL Fe-5 μg/mL poly (I:C)) another comparison can be done with two samples with a 60 % of cell viability. When the sample incubated during 24 h with macrophages contains 4 μg/mL Fe-1.25 μg/mL poly (I:C), the cytokine release is similar to the sample with 2 μg/mL Fe-1.25 μg/mL poly (I:C) incubated under the same conditions (16 ng/mL compared to 19 ng/mL of cytokine respectively). This result emphasizes that increasing the amount of NPs does not always lead to increased release of cytokines by the J744 macrophages.

When the micelle concentration is fixed and combined with increasing amounts of poly (I:C), the cytokine production does not seem proportional to the amount of the poly (I:C) attached to the IONP micelles. For instance, when cells are incubated with 2.0 μg/mL Fe and 7.5 μg/mL poly (I:C), the IL-6 value is approximately 26 ng/mL IL-6, whilst the cells are incubated with 2.0 μg/mL Fe and 15 μg/mL poly (I:C) the values obtained are

approximately 28 ng/mL IL-6 (instead of the double quantity expected as the amount of poly (I:C) is double).

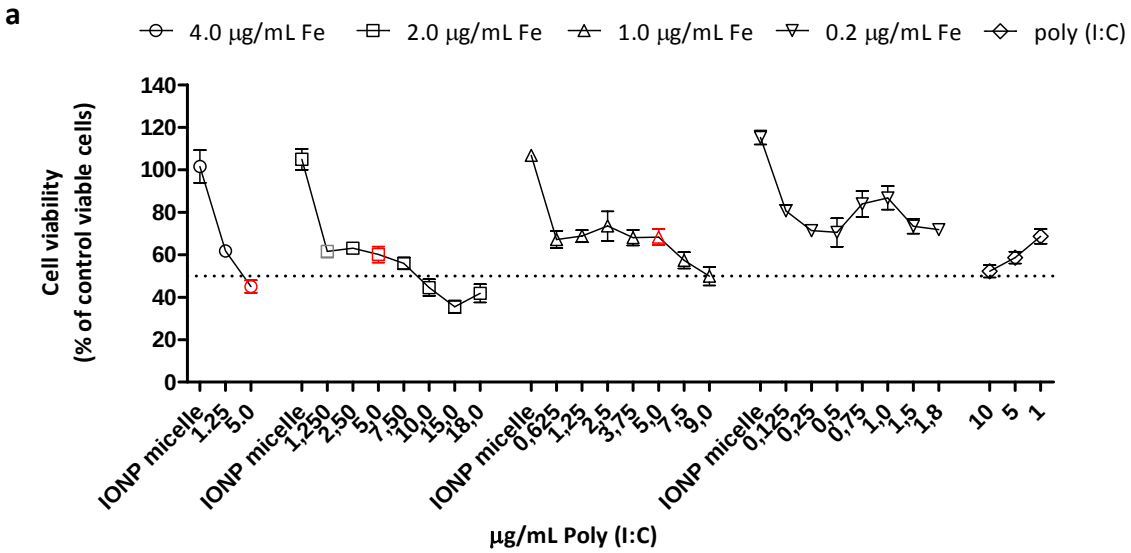

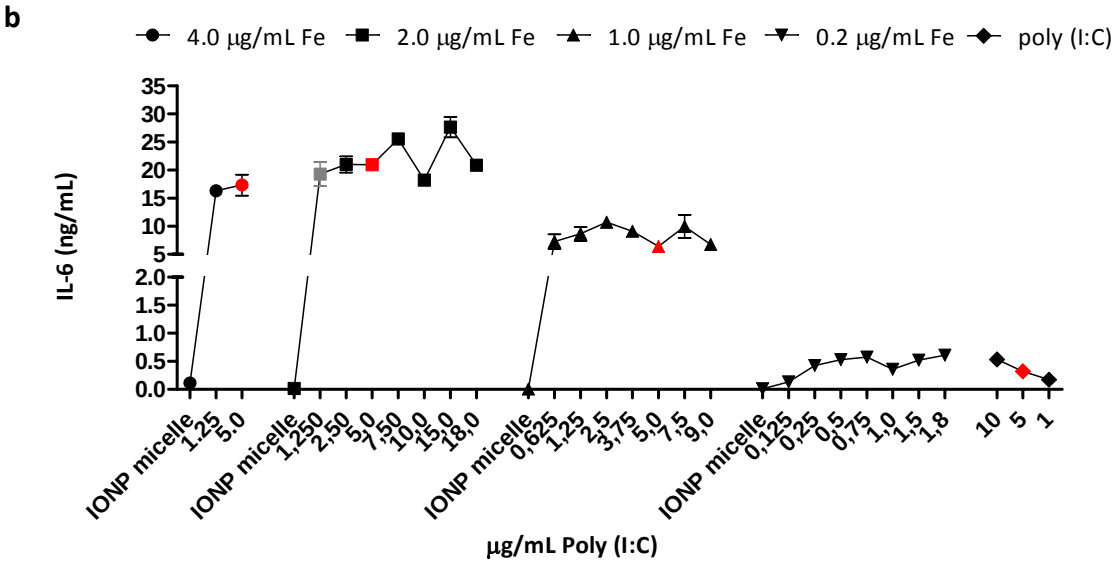

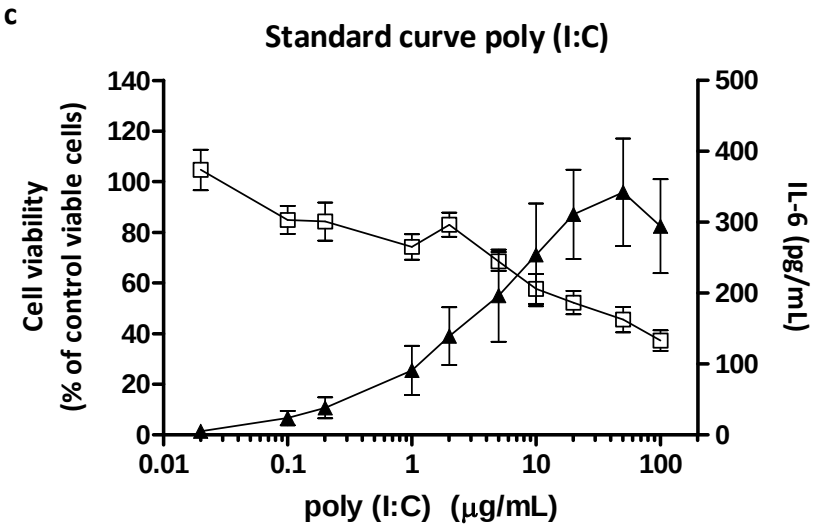

Fig. 3.10. Cytotoxicity **(a)** and IL-6 production **(b)** of IONP@PL-PEG micelles loaded with several concentrations of poly (I:C) (900 to 62.5 μg/mL) with IONP@PL-PEG micelles and free poly (I:C) as controls. **(c)** Cytotoxicity and IL-6 production of free poly (I:C) at different concentrations. The incubation is performed in J774 macrophages incubated for 24 h at 37 °C. Data are presented as mean ± SEM of three replicates and representative of three independent experiments.

As noted in the IONP formulations performed with PEGylated amine phospholipids, cytokine production when the poly (I:C) is attached onto the micelles by non-covalent approach is several orders of magnitude higher than with the poly (I:C) alone. **Fig. 3.10c** shows on the left y-axis the cell viability by cells upon exposure to the poly (I:C) alone and on the right y-axis the values corresponding to the cytokine release.

It is concluded that the highest activity considering the IONP-to-poly (I:C) ratio is obtained with the lowest amount of poly (I:C) attached onto the micelle, because with 2.0 μg/mL Fe and 1.25 μg/mL poly (I:C) the IL-6 value obtained is approximately 19 ng/mL IL-6 (grey colour point in **Fig. 3.10)**. It is probable that in this case the poly (I:C) is more shielded by the delivery system compared with higher amounts of poly (I:C) and it is able to reach the endosomes without degradation. Based on the cytotoxicity and stimulation assays it is concluded that an "excess" in the amount of poly (I:C) does not increase proportionally the production of cytokines.

b) Comparison of IONP-filled micelles with liposomes

The strong immunostimulatory ability of poly (I:C)-IONP micelles, prompted us to compare the system with a liposomal transfection agent widely used to facilitate the delivery of negatively charged biomolecules such as DNA or RNA into cells. The cationic lipid 1,2-dipalmitoyl-3-trimethylammonium-propane (chloride salt) (DOTAP) in combination with 1-palmitoyl-2- oleoyl-*sn*-glycero-3-phosphocholine (PC) were used to prepare DOTAP-containing liposomes using a method previously described in the literature.[96] In this method, DOTAP and PC are dissolved in $CHCl_3$ and mixed at 1:1 molar ratio in a total amount of lipid of 1.5 mM. The solvent is evaporated using a rotary evaporator for 30 min at 60 °C and the thin film formed is completely dried with a N_2 flow. The film is rehydrated using Tris buffer (10 mM, pH 7.4) and vortexed to encourage the liposome formation. The most common working ratio is 5-10 μg DOTAP/μg nucleic acid, although the efficacy of the complexes depends on several parameters, including the cell line, type of nucleic acid or incubation time. It has been reported that DOTAP and poly (I:C) can form complexes able to induce immune response in macrophages[97] and bone marrow dendritic cells[98] within these concentrations.

Following a similar protocol to that used with IONP micelles, 50 μL of DOTAP-containing liposomes and poly (I:C) (62.5 μg/mL) were mixed at room temperature and left stirring overnight. The sample and the corresponding control of DOTAP liposomes without poly (I:C) were incubated with macrophages during 24 h, following which the supernatants were collected and the cytokine production was tested by ELISA assay.

As **Fig. 3.11** shows the presence of DOTAP increases the production of IL-6 cytokine comparing with the poly (I:C) control, however, the values obtained are not as high as those seen when IONP@PL-PEG methoxy micelles are used as nanocarriers. For instance, at the highest concentration of poly (I:C) loaded, the cytokine production of IONP@PEG methoxy micelles is 10-fold higher than those obtained when liposomes are used as delivery system, ca. 16 ng/mL compared with 1.3 ng/mL of IL-6 respectively.

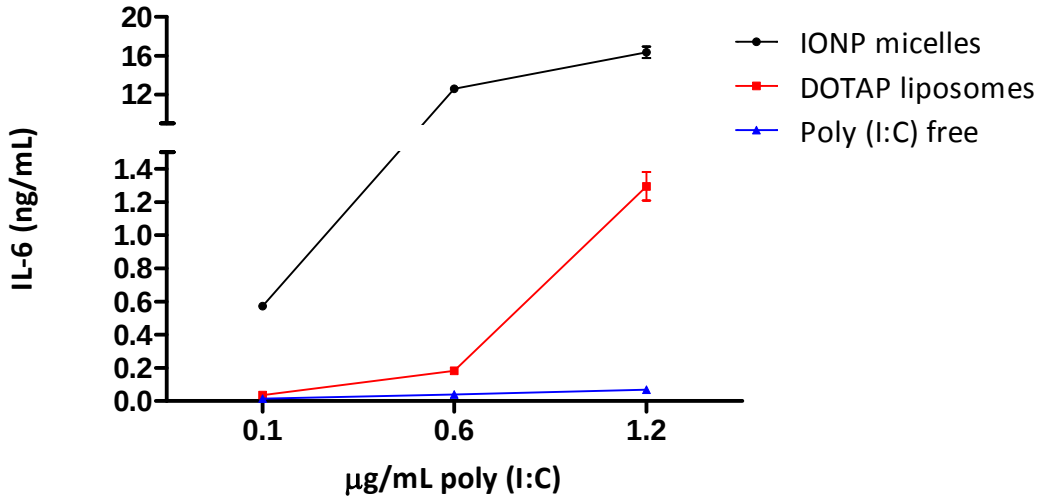

Fig. 3.11. Cytokine release of macrophages incubated for 24 h with poly (I:C)-IONP@PL-PEG micelles, poly (I:C) complexed to DOTAP liposomes and free poly (I:C). Data are presented as mean ± SEM of three replicates.

c) Effect of serum proteins on the association of poly (I.C)

The effect of serum proteins on the non-covalent interactions of the IONP@PL-PEG methoxy micelles with poly (I:C) was also investigated. For this, the micelles are formed in DMEM cell culture media. **Fig. 3.12** shows the IL-6 release at three different concentrations of poly (I:C). In all cases, the systems are more active than free poly (I:C), however, the reference system of 2 μg/mL Fe-1.0 μg/mL poly (I:C) is around 10-fold less active than the poly (I:C)-IONP@PL-PEG methoxy micelles performed in an aqueous solution (0.7 ng/mL compared to 16 ng/mL previously observed).

The results may reflect the ability of the proteins to compete and be adsorbed at the surface of the IONP@PL-PEG methoxy micelles thereby, decreasing the interaction with the poly (I:C). However, it is important to highlight that the interaction between poly (I:C) and IONP-filled micelles appears to be robust enough to take place even in the presence of other biomolecules and salts and trigger significantly higher IL-6 release than free poly (I:C) at the same concentration.

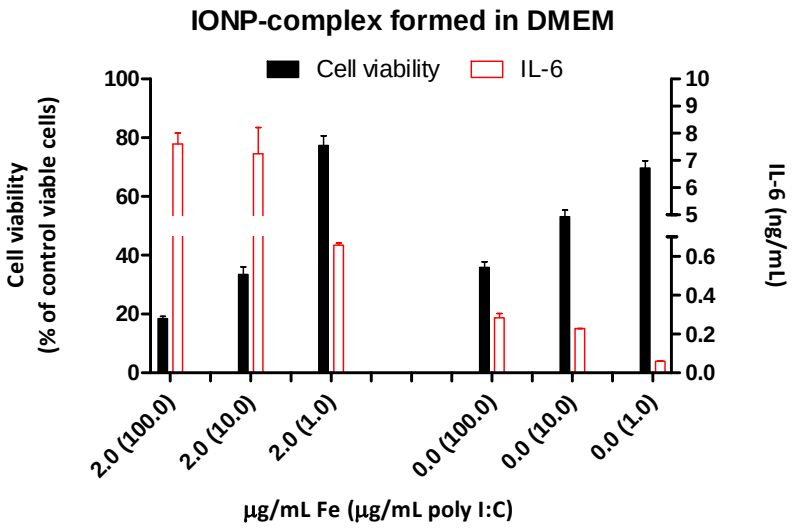

Fig. 3.12. Cytotoxicity and IL-6 production of poly (I:C)-IONP@PL-PEG micelles formed in DMEM and free poly (I:C). The incubation is performed in J774 macrophages incubated for 24 h at 37 °C. Data are presented as mean ± SEM of five replicates.

d) Effect of temperature and incubation time

In this section the IL-6 release at shorter incubation times is assessed. The objective is to elucidate if forming poly (I:C)-IONP micelle complexes is beneficial to substantially reduce the cell contact time required to produce an immunostimulatory effect. **Fig. 3.13** shows the kinetics of IL-6 release when macrophages are exposed to 0.7 µg/mL of free poly (I:C) and the same concentration associated with IONP-filled micelles.

In this study, macrophages are incubated at the indicated time periods with poly (I:C)-IONP micelles and poly (I:C) control. Then the supernatants are removed, cells are washed twice with sterile PBS (10 mM) to remove residual material which was not internalized during these time periods and fresh media is added. After 24 h, the IL-6 cytokine production of new supernatants is quantified by ELISA.

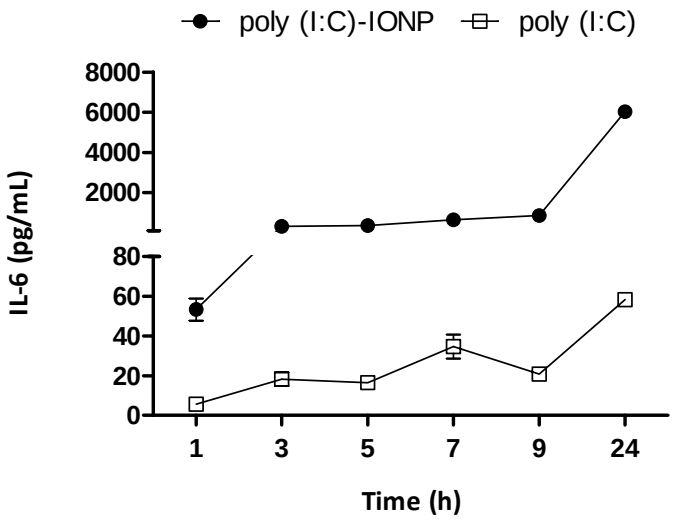

Fig. 3.13. IL-6 release from macrophages incubation with poly (I:C)-IONP@PL-PEG micelles and free poly (I:C) at various time periods at the same concentration of 0.7 μg/mL of poly (I:C). Data are presented as mean ± SEM of five replicates.

A couple of conclusions can be drawn from **Fig. 3.13.** At each time point, the poly (I:C)-IONP micelles are able to produce more IL-6 cytokine than the poly (I:C) alone, which is consistent with the previous results, due to the delivery role of the IONP micelles. So the vehicle is effective at short time periods. After 1 h of incubation of poly (I:C)-IONP micelles with macrophages, the amount of cytokine released is as high as poly (I:C) alone incubated for 24 h (55 pg/mL of IL-6). After 3 h, the amount of cytokines secreted by the sample (IONP@PL-PEG micelles loaded with 0.7 μg/mL of poly (I:C)) is even higher than the incubation during 24 h of 100 μg/mL of poly (I:C) alone (320 pg/mL compared to 294 pg/mL respectively) as it was shown in **Fig. 3.10.** It is clear, that the incubation with macrophages during 24 h is required for the production of the highest amount of cytokines, increasing notably between 9 and 24 h. This gradual release, is in agreement with a similar experiment carried out recently by Smole *et al.*,[99] with poly (I:C). Nucleic acids are rapidly degraded by nucleases and the nanocarrier probably, provides protection for poly (I:C) resulting in faster and more efficient cellular uptake and TLR3 delivery.

To confirm the intracellular entry of poly (I:C)-IONP micelles via endocytosis for subsequent binding of dsRNA with TLR3 receptor inside the endosomes, an experiment varying the incubation temperature with macrophages is performed **(Fig. 3.14)**.

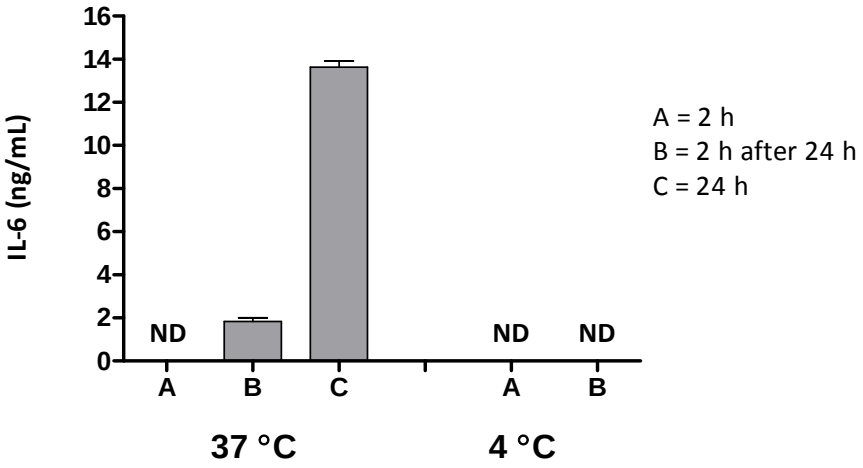

Fig. 3.14. Histogram of IL-6 cytokine production of poly (I:C)-IONP@PL-PEG micelles incubated at 4 °C and 37 °C during (A) 2 h and then supernatants were tested for IL-6; (B) 2 h pulse and then supernatants were removed and replaced with fresh media which after a further 22 h were tested or (C) 24 h and then supernatants were tested for IL-6. Sample incubated [Fe] = 2 μg/mL and [poly] = 1.25 μg/mL. ND = not detected.

Endocytosis is dependent on physical properties of the membrane. Dunn *et al.*[100] were the first researchers who reported that reduced temperature prevents the delivery of endocytosed particles to lysosomes. In mammalian cells, it is reported that at 16 °C this transfer is blocked and further reducing the temperature to 10°C completely inhibits the internalization. Membrane lipids at low temperatures present a highly ordered structure which confers low fluidity to the membrane, whereas at physiological temperatures is expected to be fluid which allows the formation of vesicles which bud off from the membrane, and consequently allow the internalization of the contents. To confirm the endocytic pathway, macrophages were incubated with poly (I:C)-IONP@PL-PEG methoxy micelles at 37 °C and at 4 °C. The samples were incubated during 2 h, then the supernatants were removed and new fresh media was added. After a further 22 h the

new supernatants were collected, corresponding with letter A and B in **Fig. 3.14** respectively. As a control, macrophages were incubated during 24 h at 37 °C (because at 4 °C without CO_2 source the macrophages would die) and then the supernatants were removed as usual to verify the success of the assay, corresponding with letter C. The production of IL-6 cytokine of the three supernatants were tested and quantified by ELISA assay. **Fig. 3.14** shows that in the incubation carried out at 4 °C, the IL-6 release was completely suppressed, which corroborates that endocytosis of poly (I:C)-IONP@PL-PEG methoxy micelles is required to deliver poly (I:C) within the endosomal compartments.

e) Dendritic cells stimulation with poly (I:C)-IONP@PL-PEG methoxy micelles

The ability of poly (I:C)-IONP@PL-PEG methoxy micelles to activate cells of the immune system was also investigated in DCs. Primary bone marrow-derived dendritic cells (BMDCs) were obtained from bone marrow of BALC/c mice (6-12 weeks) and used after maturation of extracted cells during 9 days by the method explained in the experimental section. Maturation to produce DCs was confirmed using flow cytometry with DC-specific antibody markers.

After seeding DCs in a 96-well plate, DCs were incubated with poly (I:C)-IONP@PL-PEG methoxy micelles and their corresponding controls under the same conditions that macrophages, at 37 °C for 24 h. Then, cell viability and IL-6 production were tested by MTT and ELISA assays respectively.

Fig. 3.15 shows the cytotoxicity and IL-6 production of the nanoconstruct containing 2 µg/mL Fe-1.25 µg/mL poly (I:C). Cytokine production in DCs treated with the poly (I:C)-IONP@PL-PEG methoxy micelles was several orders of magnitude higher compared with the cells treated with free poly (I:C). Similar effects were found in macrophages **(Fig. 3.10)**, however it is worth noting that the poly (I:C)-IONP@PL-PEG methoxy micelles are non-toxic in the range studied unlike what occurs in macrophages.

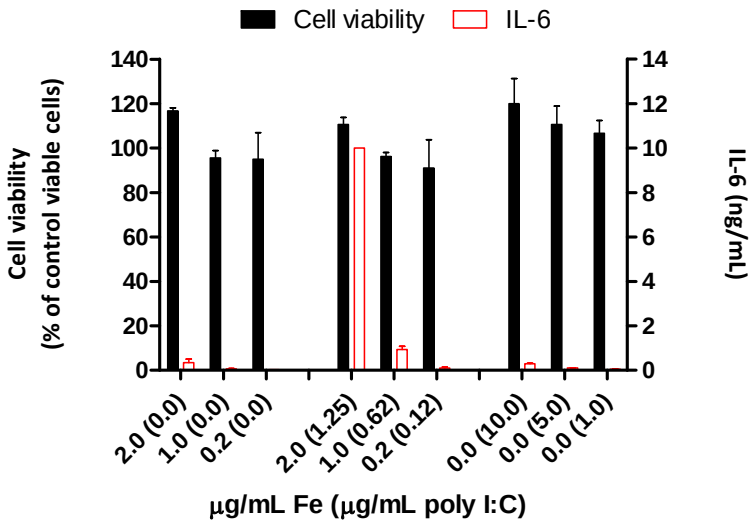

Fig. 3.15. Cytotoxicity and IL-6 production of poly (I:C)-IONP@PL-PEG micelles in BMDCs. Data are presented as mean ± SEM of three replicates.

3.2.2.3 Fluorescence microscopy: cellular uptake of the poly (I:C)-IONP@PL-PEG methoxy micelles

Microscopy studies were carried out to analyze the cell uptake and fate of the poly (I:C)-IONP@PL-PEG methoxy micelles and to investigate in detail the delivery of poly (I:C) to the target TLR3. The subcellular localization of poly (I:C)-IONP@PL-PEG methoxy micelles labeled with rhodamine B (Rhod) in J774 macrophages was performed using live and fixed cell microscopy as **Fig. 3.16** represents. After the incubation with the fluorescent micelles, cells were co-stained in green with specific markers of endosomal compartments and TLR3.

The colocalization of lysosomes with the rhodamine micelles was assessed using a late endosome and lysosome marker commercially available called LysoTracker.[101] First of all, nuclei are stained with DAPI (10 μg/mL). After washing with sterile PBS 10 mM, the system is incubated for 1 h at 37°C. The medium is removed and fresh medium containing Lystrotracker (1 μM) is added. After 1h, cells are washed and the mounting solution is added to preserve the cells. **Fig. 3.16a** shows that the poly (I:C)-IONP@PL-PEG methoxy micelles were found colocalized with lysosomes demonstrating their capability to reach the organelles where the signaling downstream starts and also to corroborate that the

internalization of the poly (I:C)-IONP@PL-PEG methoxy micelles occurs via endocytic mechanism.

To ensure that the system can reach the target TLR3, it is required to stain the receptors and analyze the colocalization with the samples by fluorescence microscopy. The fluorescence study was performed using an anti-TLR3 mAb and the Alexa 488-labeled secondary antibody. Cells were incubated with poly (I:C)-IONP@PL-PEG methoxy micelles for 1 h at 37 °C. Medium was removed and the adherent cells were fixed and permeabilized with 4 % formaldehyde and 0.1 % Triton X-100 in PBS 10 mM, respectively. After washing, the blocking buffer was added to avoid non-specific interactions (1 % BSA in PBS 10 mM) and then, cells were incubated overnight at 4 °C with the primary antibody (10 µg/mL). Then, after washing, the secondary antibody was added (10 µg/mL) and incubated for 1 h at room temperature. Nuclei were stained with DAPI (10 µg/mL) for 15 min. The colocalization of poly (I:C)-IONP@PL-PEG methoxy micelles with TLR3 as it is shown in **Fig. 3.16b** demonstrates that poly (I:C) is successfully delivered to TLR3.

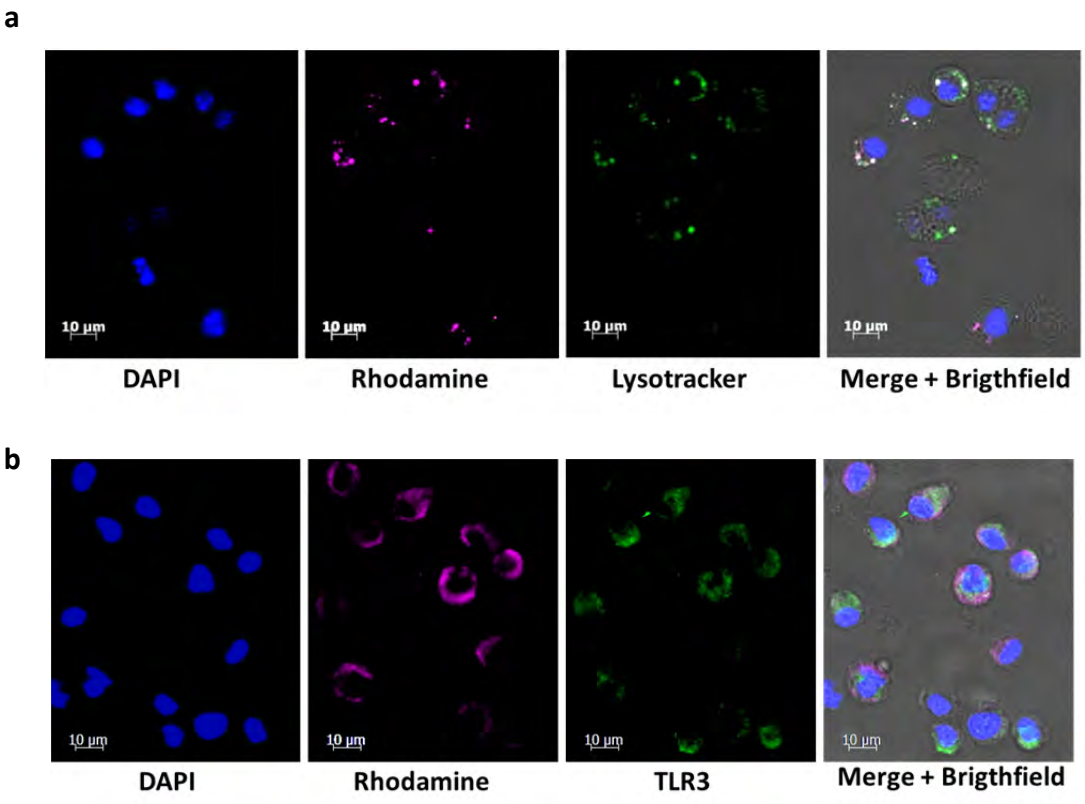

Fig. 3.16. Trafficking of poly (I:C)-IONP@PL-PEG micelles labeled with rhodamine B in J774 macrophages after 1 h of incubation.

3.2.2.4 Bimodal detection of poly (I:C)-IONP@PL-PEG methoxy micelles

Before investigating the biodistribution poly (I:C)-IONP@PL-PEG methoxy micelles *in vivo* two phantom studies were performed to find the *in vitro* detection limits of the nanoconstruct by MRI and SPECT imaging after radiolabelling with ^{99m}Tc tricarbonyl (radiolabelling was carried out as described in Chapter 2 and experimental section).The phantom study is the simplest way to know what resolution and image contrast is attainable by the biomodal imaging system using each technique. The phantom studies shown in **Fig. 3.17** demonstrate that poly (I:C)-IONP@PL-PEG methoxy micelles can be detected by MRI (7T) and SPECT with comparable detection limits. Despite the presence of poly (I:C) around the surface of the IONP micelles, there is no interference in the magnetic properties and it is possible to incorporate ^{99m}Tc tricarbonyl radionuclide to monitor the nanoconstructs. This result confirms the possibility of injecting poly (I:C)-IONP@PL-PEG methoxy micelles in mice and to gain insights into the *in vivo* trafficking using two complementary imaging modalities.

The longitudinal (r_1) and traverse (r_2) relaxivities are determined by measuring the T_1 and T_2 relaxation times at 7T. Poly (I:C)-IONP@PL-PEG methoxy micelles with a r_2= 129 mM^{-1} s^{-1} is a more potent T_2 contrast agent than the system with a comparable size based on ferumoxytol reported by Thorek *et al.* with a r_2= 89 mM^{-1} s^{-1}, a US Food and Drug Administration approved agent. It can be concluded that poly (I:C) does not interfere in the magnetic properties of the micelles due to the equivalence with **Fig. 2.17** in **Chapter 2** where relaxivity values and concentration detection limits are similar to those shown below.

a

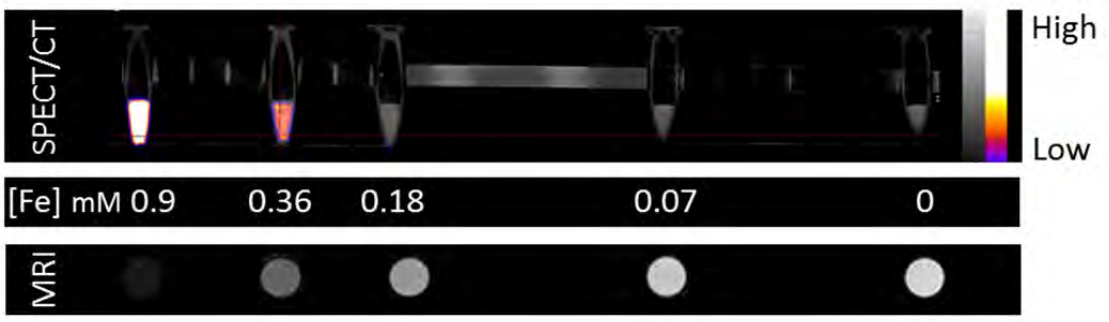

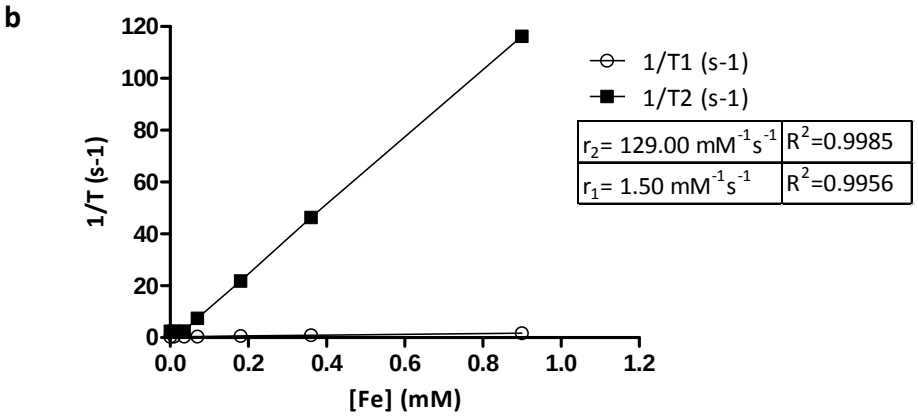

Fig. 3.17. (a) NanoSPECT/CT and T_2-weighted MR phantoms and **(b)** Plots of $1/T_1$ and $1/T_2$ vs concentration of poly (I:C)-IONP@PL-PEG methoxy micelles. Images and relaxation rates measured at 7 T at 25°C.

3.2.2.5 SPECT/CT and MR imaging: *in vivo* trafficking of the poly (I:C)-IONP@PL-PEG methoxy micelles

a) SPECT imaging of poly (I:C)-IONP@PL-PEG methoxy micelles

Due to the higher sensitivity of SPECT compared with MRI, this technique is capable of detecting small amounts of the radiolabeled system and thus, it is a good method to determine how important the administration route is for targeted drug delivery to the lymph nodes. The ability to detect poly (I:C)-IONP@PL-PEG methoxy micelles labeled with ^{99m}Tc tricarbonyl *in vivo* was studied through subcutaneous (s.c.) and intraperitoneal (i.p.) injection, which are two of the most relevant routes for administering TLR ligands and commonly used in vaccine development studies. Subcutaneous injections were administered in the dorsal-flank and abdominal region and the biodistribution of the nanoconstruct by these routes of administration was compared with i.p. injection.

Balb/c mice were injected with 100 µL of poly (I:C)-IONP@PL-PEG methoxy micelles labeled with with ^{99m}Tc tricarbonyl ([Fe]= 6 mM, within the recommended dose

for similar IONPs, 20 µmol Fe/kg)[106] via the s.c. and i.p. routes. Mice are imaged at various time points after injection: 10 min, 3 h and 24 h.

Fig. 3.18 shows the SPECT/CT studies performed via s.c. injection in the flank. The images show that at 3 h post injection, poly (I:C)-IONP@PL-PEG methoxy micelles remained almost completely at the site of injection, suggesting a possible depot effect due to the route of administration selected. After 24 h the depot effect at the injection site is still visible and the radiolabelled system is not located in any other organs.

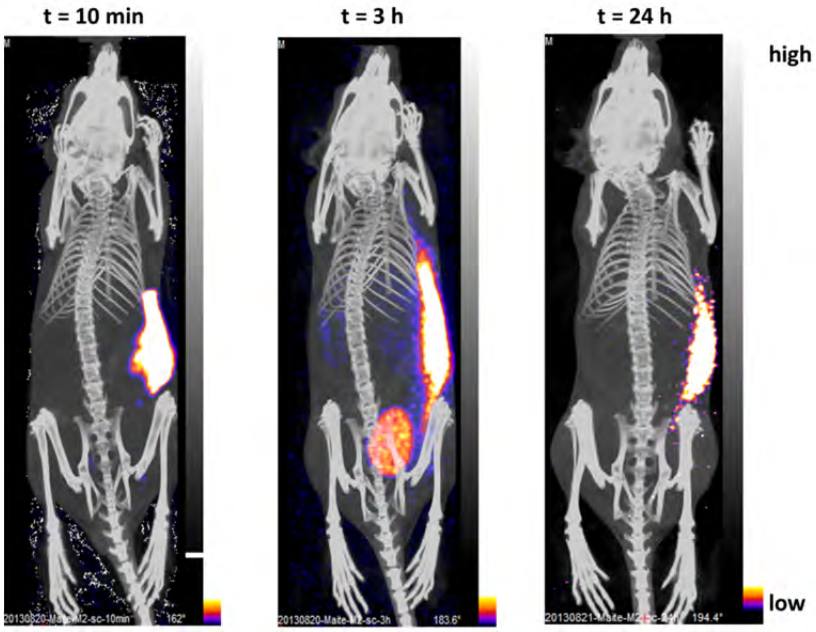

Fig. 3.18. SPECT/CT images of mice at different time points after s.c. administration of ^{99m}Tc tricarbonyl-poly (I:C)-IONP@PL-PEG methoxy micelles in the flank.

Whilst the depot effect can be helpful in obtaining a strong immune response after injection of vaccines or immunstimulatory substances, we were interested to see whether using another anatomical site our route of injection would allow us to visualise the movement of the IONP to the lymphatic system. Poly (I:C)-IONP@PL-PEG methoxy micelles were administrated via s.c. in the abdominal region and via i.p. route **(Fig. 3.19)**. The SPECT/CT studies reveal that after 24 h, a considerable amount of the poly (I:C)-IONP system remains at the site of injection. However, it is important to highlight that by both

administration routes the micelles diffuse from the site of injection to their relevant draining lymph nodes through the lymphatic system.

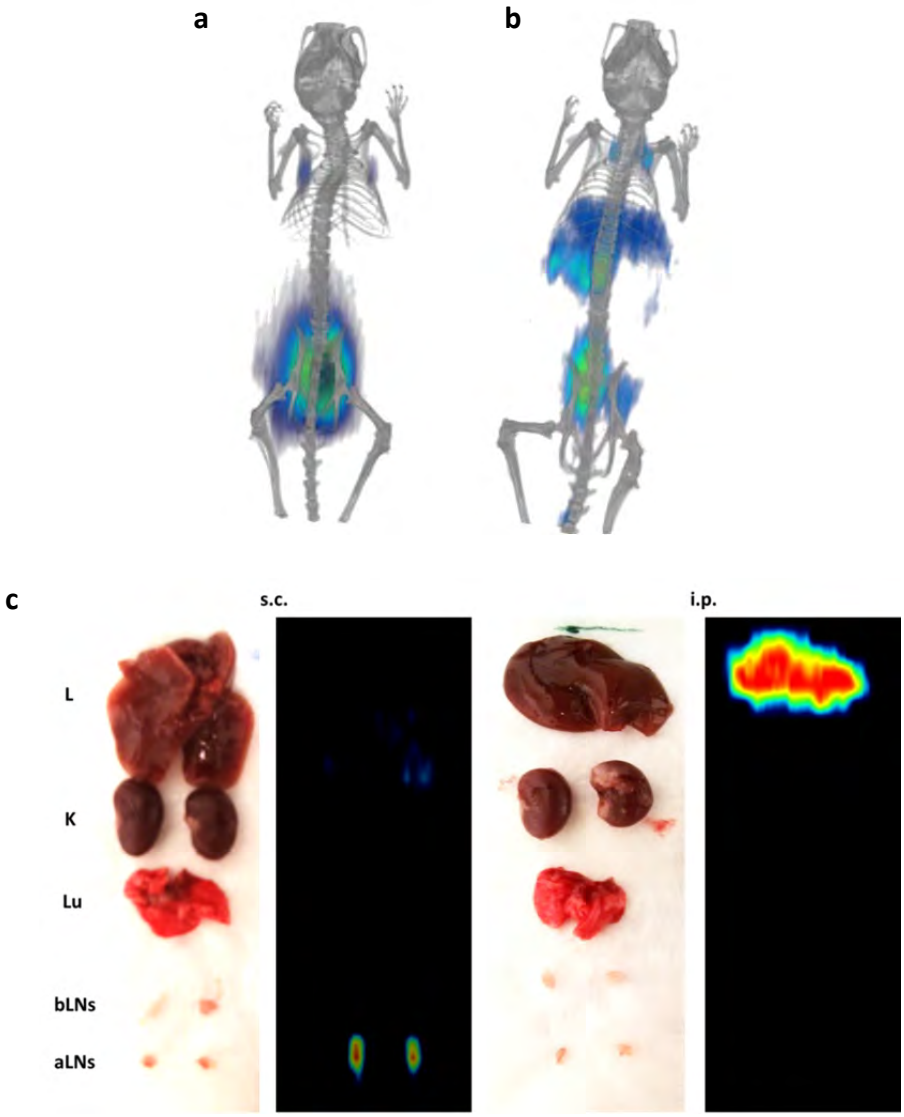

Fig. 3.19. SPECT images of mice 24 h after **(a)** subcutaneous and **(b)** intraperitoneal administration of ^{99m}Tc tricarbonyl-poly (I:C)-IONP@PL-PEG methoxy micelles in the abdominal region. **(c)** Photograph and SPECT images of selected harvested organs and LNs after s.c. administration in the abdominal region and i.p. injection. (L: liver; K: kidney; Lu: lungs; bLNs: brachial LNs and aLNs: axillary LNs).

When the mice are inoculated via s.c. injection in the abdominal region, the micelles are also able to migrate to lymph nodes distant from the site of injection, up to the axillary LNs. This is consistent with the pattern of lymphatic drainage,[102] because the

inguinal LNs which are directly connected with the axillary LNs are proximal to the site of injection.

In contrast, injection of poly (I:C)-IONP@PL-PEG methoxy micelles via the i.p. route results in accumulation in the liver, and detectable amounts also in the mediastinal lymph nodes located in the thoracic cavity, also in concordance with the known lymphatic drainage pattern from this injection area.[103–105] The peritoneal space drains to celiac, superior mesenteric, and periportal lymph node groups first and then, lymph continues via the thoracic duct to mediastinal lymph nodes.

In order to confirm the migration to lymph nodes, one mouse of each injection group was sacrificed after 24 h and the organs were harvested and imaged using *ex vivo* SPECT analysis. In the case of the s.c. injection, the axillary LNs present a strong radioactive signal, whereas the adjacent brachial LNs do not present radioactive signal. In the i.p. administration neither of these LNs are radioactive, thus show the different pattern drainage depending on the area the administration selected.[102] Unfortunately we were not able to collect the mediastinal lymph nodes to measure *ex vivo* activity due its proximity to the heart and thymus.

b) MRI imaging of poly (I:C)-IONP@PL-PEG methoxy micelles

The ability to detect poly (I:C)-IONP@PL-PEG methoxy micelles *in vivo* by high field MRI (7T) was also studied following their administration by s.c. and i.p. injection. Compared to SPECT, MRI offers much better spatial resolution and excellent soft tissue contrast. Balb/c mice were injected with 100 µL of poly (I:C)-IONP micelles ([Fe]= 6 mM) via the s.c. (into the flank) and i.p. routes. Mice are imaged before injection and at various time points after injection: 2, 24 and 72 h.

In the case of s.c. administration **(Fig. 3.20a)** no clear contrast is observed in any of the organs chosen for screening (inguinal LNs, spleen and liver) during the three days of acquisition. Although the proximity of iLNs to the site of injection would suggest some accumulation and therefore some darkening would occur at these LNs, it seems like there is no detectable accumulation of NPs at any time point. It is worth noting that the

sensitivity of MRI is considerably lower than for SPECT. The lack or relatively small presence of poly (I:C)-IONP@PL-PEG methoxy micelles in the liver could suggest that a depot effect is taking place in the site of injection as shown by SPECT/CT.

Thus, the following experiment was conducted in order to confirm the depot effect seen in the SPECT images. After 24 h of s.c. injection in the flank with poly (I:C)-IONP@PL-PEG methoxy micelles, the inoculated mice were sacrified and skin samples from the site of injection were harvested in three of them. One mouse was injected with 10 mM PBS as a negative control and the other two were injected with the sample of interest. The samples were treated following a protocol described previously in the literature.[107] Briefly, the tissues were submerged in 4 % formaldehyde solution and were kept at 4 °C until the day the images were taken. That day, the tissue was submerged into a Falcon tube containing Fomblin solution and was kept for 1h to exchange completely the formaldehyde. Then, the tissue was kept in the container (tubes of 2 mL) where images were recorded in the final solution (10 mM PBS).

As **Fig. 3.21** shows, T_2 relaxation times decrease significatively in the mice injected with poly (I:C)-IONP@PL-PEG methoxy micelles compared to the control. This result is in agreement with MRI and SPECT images described above and it demonstrates that s.c. injection in the flank results in a depot of poly (I:C)-IONP@PL-PEG methoxy micelles at the injection site and that extensive migration through the lymphatic system is not occuring.

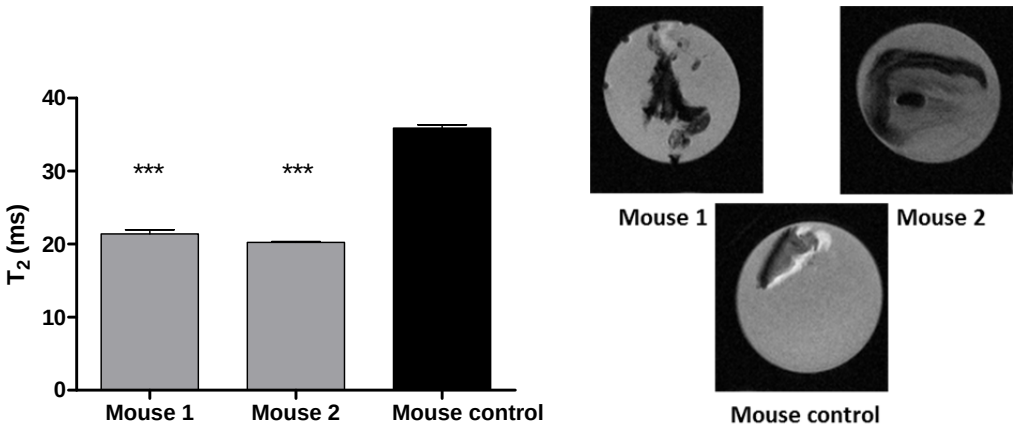

Fig. 3.21. T_2 relaxation times of skin samples harvested from the site of injection (s.c. in the flank). Mouse 1 and 2 were injected with poly (I:C)-IONP@PL-PEG methoxy micelles ([Fe]= 6 mM) whilst mouse 3 was injected with PBS 10 mM as a control. $^{***}P < 0.001$ compared to control mouse (one-way ANOVA followed by Turkey´s test).

In the case of i.p. administration **(Fig. 3.20b)**, the loss of signal intensity in the liver is evident at 2 h post injection. It is important to highlight that even after 72 h there is still a loss of signal intensity in the liver, thus, the poly (I:C)-IONP@PL-PEG methoxy micelles have not been cleared out completely.

Colorized-T_2 maps of the organs chosen (liver, spleen and local draining lymph nodes) for screening were generated and overlaped onto the proton-density weighted images to better visualize the nanoparticle accumulation.

Gradient echo axial MR images, color coded T_2 maps and the plot in **Fig. 3.20b** displaying the decrease in T_2 relaxation times, demonstrate the presence of poly (I:C)-IONP@PL-PEG methoxy micelles in the liver. Pre-injection values in the liver around 18 ms are compared with a significant variation to 12-14 ms during the acquisition times. However again, there is no presence or it is not possible to distinguish accumulation in iLNs and spleen.

a

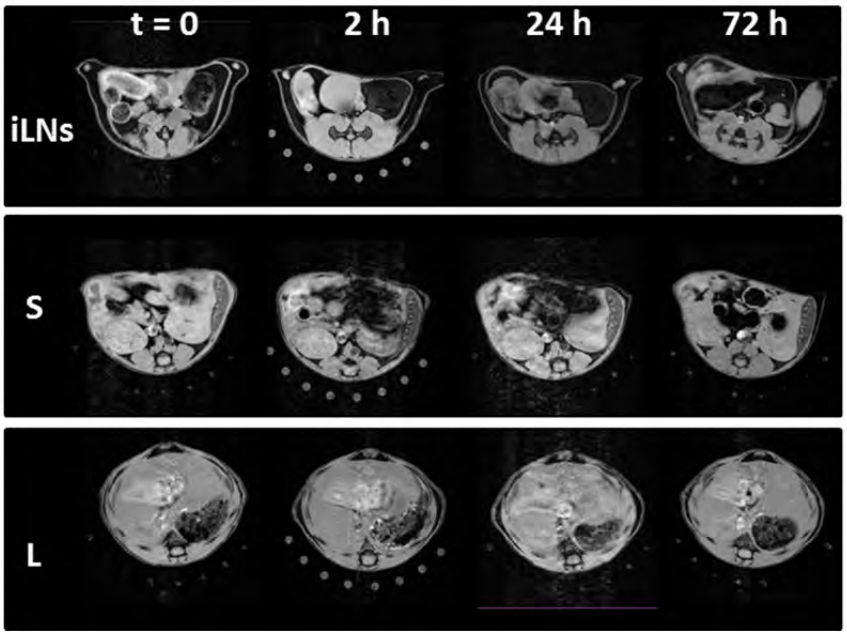

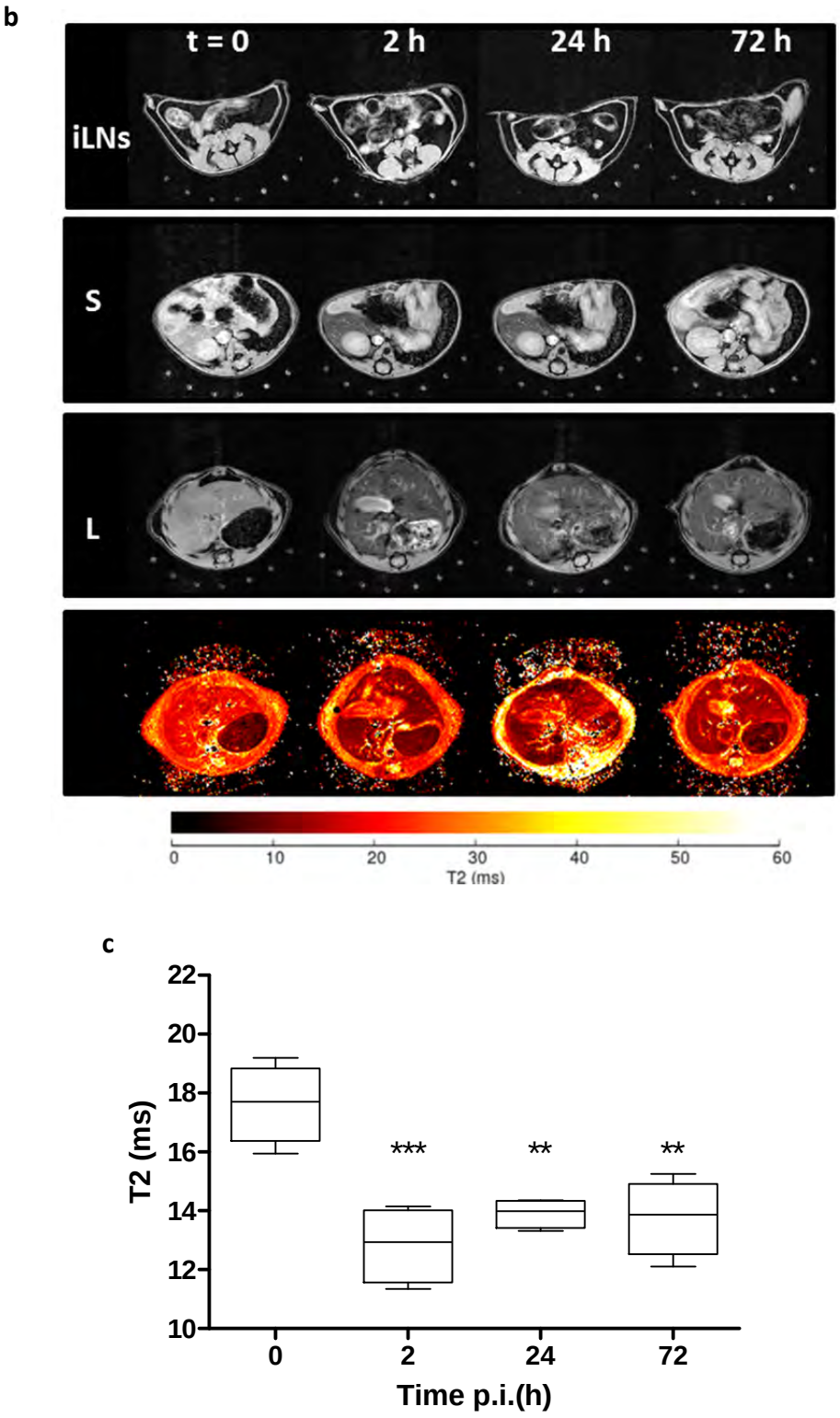

Fig. 3.20. Gradient echo axial MR images at different time points of mice **(a)** s.c. and **(b)** i.p. injected in the flank with poly (I:C)-IONP@PL-PEG methoxy micelles and colour coded T_2 maps of the liver at different time points of mice i.p. injected. **(c)** Distribution of quantitative T_2 values over time measured in the liver of 4 mice. $^{**}P < 0.01$, $^{***}P < 0.001$ compared to t=0 (one-way ANOVA followed by Turkey´s test).

The different behavior observed during the s.c. MRI and SPECT/CT images depending on the site of injection can be explained by previously studies reported in the literature with similar results.[108,109] These studies show that the differences in the structural organization of the s.c. tissue at different anatomical sites are the main reason to observe variability in the lymphatic drainage process and the dispersion of the fluid injected is regulated by the interstitial pressure, which is affected by a variable layer of adipose tissue at different anatomical regions.

c) Identifying lymph nodes using MRI

After SPECT/CT studies have shown the migration of poly (I:C)-IONP micelles to lymph nodes when the s.c. injection is made in the abdominal region, the lymph nodes present in the axilla were imaged in high resolution by high field (7 T) MRI **(Fig. 3.22)**. The magnified images clearly show the presence of poly (I:C)-IONP@PL-PEG methoxy micelles in the LNs. As expected, the poly (I:C)-IONP@PL-PEG methoxy micelles can be clearly detected 2 h post injection in the axillary LNs without any dark signal in the brachial LNs. This specific result is consistent with the pattern of lymphatic drainage identified for the cutaneous area of injection selected.[102] Several studies have shown that the axillary LNs are directly connected with the inguinal LNs, which are proximal to the site of injection.[110–112]

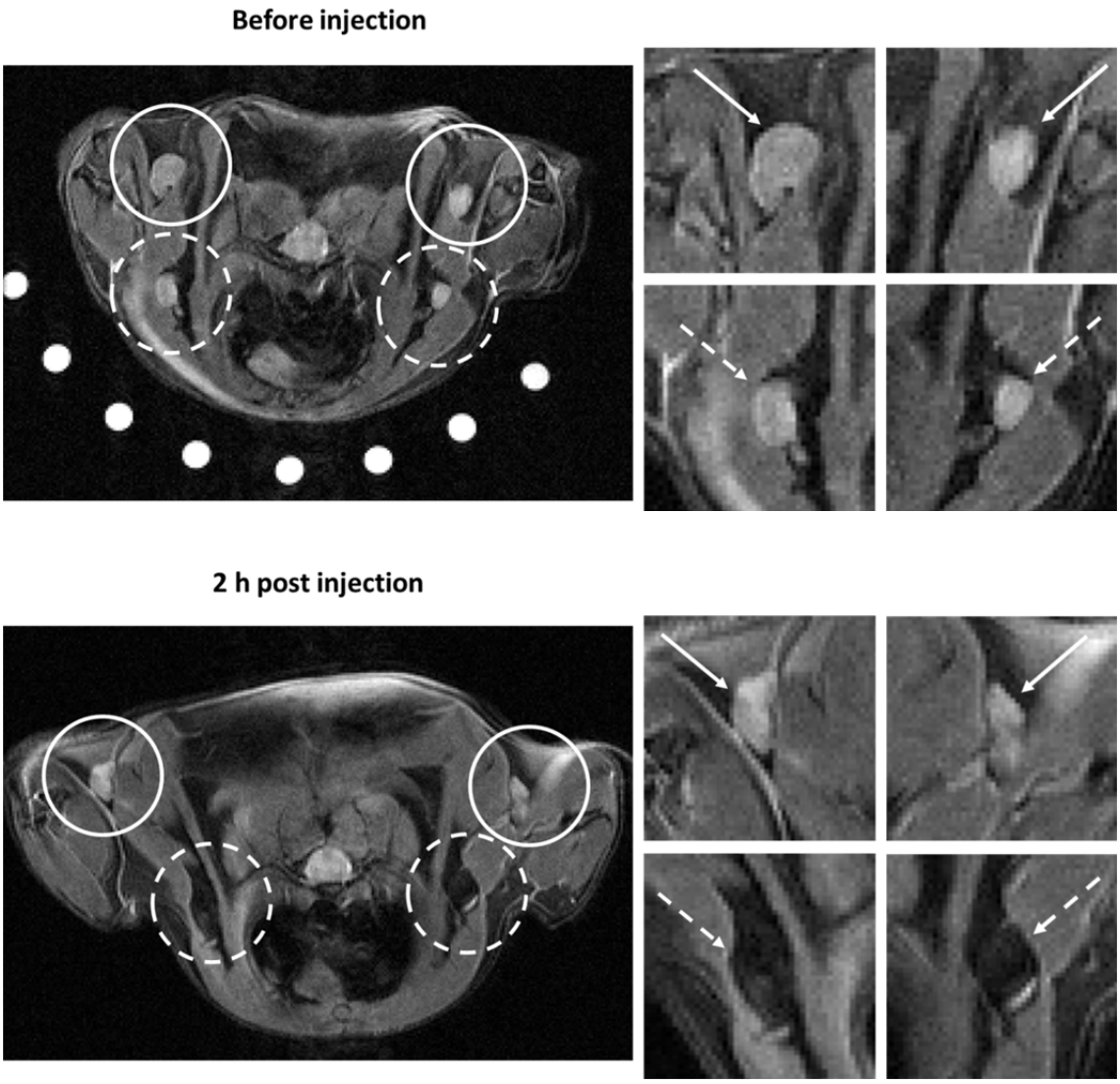

Fig. 3.22. MRI images (7T) of the migration of poly (I:C)-IONP@PL-PEG methoxy micelles to lymph nodes in the axilla following s.c. injection in the abdominal region. Axillary LNs and brachial LNs are represented by dashed and solid circles and arrows respectively.

3.2.2.6 Studying the innate immune response

Encouraged by the good results obtained *in vitro* with the delivery of poly (I:C) by the IONP@PL-PEG methoxy micelles and the *in vivo* biodistribution results obtained by MRI and SPECT/CT studies, the innate immune response was analyzed *in vivo* in BALB/c mice. Poly (I:C)-IONP@PL-PEG methoxy micelles, IONP@PL-PEG methoxy micelles and poly (I:C) alone, were administered by s.c. in the flank and via i.p. injection. Formulations were injected into the left flank of the mice (100 µL/dose). The amount of poly (I:C)

administered was 28 μg for the s.c. injection and 14 μg for the i.p. injection. In the periods indicated in **Fig. 3.23** blood samples (25 μL) were taken via the tail vein, then serum was separated from the extracted blood of immunized mice and analyzed for the presence of various cytokines using enzyme-linked immunosorbent assay (ELISA).

IL-6 and IL-12 are two of the most important cytokines involved in the regulation of the immune response and inflammation. IL-6 is secreted by macrophages or T cells in response to infection[113] (for instance promoted by a specific PAMP as poly (I:C)). IL-6 is a key cytokine in the development of Th17 T cell response,[114] whose main role is to provide anti-microbial immunity after tissue injury.[115] Meanwhile, the main role of IL-12 is to bridge innate and adaptive immunity.[116] IL-12 is produced by macrophages, DCs or B cells in response to pathogens during infection, but unlike IL-6 it is involved in the differentiation of naïve T cells into Th1 cells.[117] It is also reported that IL-12 elicits potent anti-tumor activity based on its ability to determine Th1 and cytotoxic T lymphocyte responses.[118]

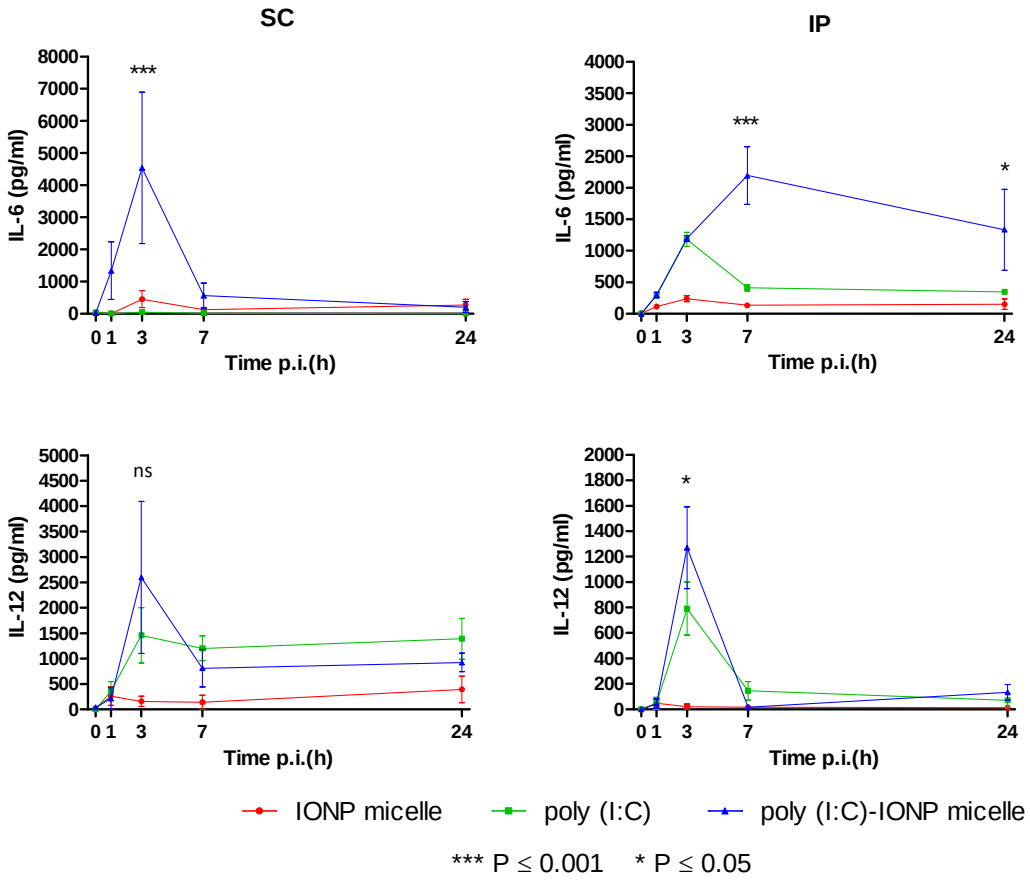

Fig. 3.23. Innate immune responses to poly (I:C)-IONP@PL-PEG methoxy micelles, IONP@PL-PEG methoxy micelles and poly (I:C) alone. The amount of poly (I:C) administered was 28 µg for the s.c. injection and 14 µg for the i.p. injection. Data are presented as mean ± SEM (n=3). The statistical significance of the differences between stimulation with poly (I:C) vs poly (I:C)-IONP micelles was analysed by two-way ANOVA (*= P < 0.05, ***= P < 0.001, ns = not significant).

Fig. 3.23 shows that the immunization with poly (I:C)-IONP@PL-PEG methoxy micelles induces higher production of cytokines than the same immunization using the IONP@PL-PEG methoxy micelles or the poly (I:C) alone in both of the administration routes tested. The IL-6 levels are significantly enhanced in mice treated with poly (I:C)-IONP@PL-PEG methoxy micelles compared to IONP@PL-PEG methoxy micelles and poly (I:C) alone. There is also a higher IL-12 cytokine production in mice injected with poly (I:C)-IONP@PL-PEG methoxy micelles compared to IONP@PL-PEG methoxy micelles and poly (I:C) alone, although the difference is not considered statistically significant due to the high sample-to-sample deviation.

The cytokine pattern produced after injection via the i.p. or s.c. is similar and comparable with other experiments reported in the literature.[119] After injection of poly (I:C)-IONP@PL-PEG methoxy micelles, systemic cytokine production increases rapidly, peaking at 3 h post injection (p.i.) and in most cases decrease almost to background by 24 h p.i.. This behavior is in agreement with what can be expected for an innate immune response.

3.3 Conclusions

In this chapter it has been shown that the selected IONP micelles can be considered a good, versatile and efficient drug delivery vehicle for poly (I:C).

It was demonstrated by spectroscopic techniques that poly (I:C) can be incorporated into the IONP@PL-PEG amino micelles covalently and non-covalently without modification or degradation for its dsRNA structure, and non-covalentely to IONP@PL-PEG methoxy micelles.

The ability of IONP@PL-PEG micelles decorated with poly (I:C) to activate the immune system was investigated *in vitro* in the immortalized murine macrophage cell line J774.1 and in bone marrow-derived dendritic cells as primary cell culture. It was demonstrated that the immunostimulatory properties of the poly (I:C) are enhanced several orders of magnitude after the attachment of poly (I:C) onto these IONP-filled micelles as shown by the significantly increased production of IL-6.

The multifunctional system developed in this work was visualized by different complementary imaging techniques such as optical, magnetic resonance and nuclear imaging demonstrating that the system is an effective delivery system both *in vitro* and *in vivo*. Specifically, fluorescence imaging studies demonstrated that the poly (I:C)-IONP@PL-PEG micelles are able to reach the target endosomal compartments *in* vitro (and specifically the endosomal TLR3 target) in cells of the immune system, a requirement to initiate the signaling cascade that activate cytokine production and the subsequent immune response.Then, MRI and SPECT/CT imaging techniques showed that this system inoculated by two routes of administration (s.c. in the flank and abdominal region and i.p. injection) is effectively transported via the lymphatics to reach secondary lymphoid organs such the lymph nodes and spleen.

The innate immune response of the system was also evaluated *in vivo* by these two different routes of injection. It was demonstrated that the system is sufficiently stable *in vivo* as it is capable of triggering potent innate immune responses.

References

1. Basset, C., Holton, J., O'Mahony, R. & Roitt, I. Innate immunity and pathogen–host interaction. *Vaccine* **21,** S12–S23 (2003).

2. Beutler, B. Innate immunity: an overview. *Mol. Immunol.* **40,** 845–859 (2004).

3. Janeway, C. A. & Medzhitov, R. Innate immune recognition. *Annu. Rev. Immunol.* **20,** 197–216 (2002).

4. Steinman, L. A brief history of T(H)17, the first major revision in the T(H)1/T(H)2 hypothesis of T cell-mediated tissue damage. *Nat. Med.* **13,** 139–45 (2007).

5. Stockinger, B. & Veldhoen, M. Differentiation and function of Th17 T cells. *Curr. Opin. Immunol.* **19,** 281–286 (2007).

6. Agrawal, S., Gupta, S. & Agrawal, A. Vaccinia virus proteins activate human dendritic cells to induce T cell responses in vitro. *Vaccine* **27,** 88–92 (2009).

7. Mittelbrunn, M. *et al.* Imaging of plasmacytoid dendritic cell interactions with T cells. *Blood* **113,** 75–84 (2009).

8. Banchereau, J. & Steinman, R. M. Dendritic cells and the control of immunity. *Nature* **392,** 245–52 (1998).

9. MartIn-Fontecha, A. *et al.* Regulation of dendritic cell migration to the draining lymph node: impact on T lymphocyte traffic and priming. *J. Exp. Med.* **198,** 615–21 (2003).

10. Kurts, C., Cannarile, M., Klebba, I. & Brocker, T. Cutting Edge: Dendritic Cells Are Sufficient to Cross-Present Self-Antigens to CD8 T Cells In Vivo. *J. Immunol.* **166,** 1439–1442 (2001).

11. Cella, M. Ligation of CD40 on dendritic cells triggers production of high levels of interleukin-12 and enhances T cell stimulatory capacity: T-T help via APC activation. *J. Exp. Med.* **184,** 747–752 (1996).

12. Gautier, G. *et al.* A type I interferon autocrine-paracrine loop is involved in Toll-like receptor-induced interleukin-12p70 secretion by dendritic cells. *J. Exp. Med.* **201,** 1435–46 (2005).

13. Iwasaki, A. & Medzhitov, R. Toll-like receptor control of the adaptive immune responses. *Nat. Immunol.* **5,** 987–95 (2004).

14. Bendelac, A. Adjuvants of immunity: harnessing innate immunity to promote adaptive immunity. *J. Exp. Med.* **195,** 19F–23 (2002).

15. Schnare, M. *et al.* Toll-like receptors control activation of adaptive immune responses. *Nat. Immunol.* **2,** 947–50 (2001).

16. Mogensen, T. H. Pathogen recognition and inflammatory signaling in innate immune defenses. *Clin. Microbiol. Rev.* **22,** 240–73, Table of Contents (2009).

17. Yoneyama, M. & Fujita, T. Function of RIG-I-like receptors in antiviral innate immunity. *J. Biol. Chem.* **282,** 15315–8 (2007).

18. Kanneganti, T.-D., Lamkanfi, M. & Núñez, G. Intracellular NOD-like receptors in host defense and disease. *Immunity* **27,** 549–59 (2007).

19. Mancini, R. J., Stutts, L., Ryu, K. A., Tom, J. K. & Esser-Kahn, A. P. Directing the immune system with chemical compounds. *ACS Chem. Biol.* **9,** 1075–85 (2014).

20. Takeda, K., Kaisho, T. & Akira, S. Toll-like receptors. *Annu. Rev. Immunol.* **21,** 335–76 (2003).

21. Lotze, M. T. *et al.* The grateful dead: damage-associated molecular pattern molecules and reduction/oxidation regulate immunity. *Immunol. Rev.* **220,** 60–81 (2007).

22. Hennessy, E. J., Parker, A. E. & O'Neill, L. A. J. Targeting Toll-like receptors: emerging therapeutics? *Nat. Rev. Drug Discov.* **9,** 293–307 (2010).

23. Alexopoulou, L., Holt, A. C., Medzhitov, R. & Flavell, R. A. Recognition of double-stranded RNA and activation of NF-κB by Toll-like receptor 3. *Nature* **413,** 732–8 (2001).

24. Akira, S., Uematsu, S. & Takeuchi, O. Pathogen recognition and innate immunity. *Cell* **124,** 783–801 (2006).

25. Funami, K. *et al.* The cytoplasmic "linker region" in Toll-like receptor 3 controls receptor localization and signaling. *Int. Immunol.* **16,** 1143–54 (2004).

26. Kumar, H., Kawai, T. & Akira, S., Pathogen recognition in the innate immune response. *Biochem. J.* ***420,*** *1-16* (2009).

27. Bell, J. K. *et al.* The molecular structure of the Toll-like receptor 3 ligand-binding domain. *Proc. Natl. Acad. Sci. U. S. A.* **102,** 10976–80 (2005).

28. Choe, J., Kelker, M. S. & Wilson, I. A. Crystal structure of human toll-like receptor 3 (TLR3) ectodomain. *Science* **309,** 581–5 (2005).

29. Liu, L. *et al.* Structural basis of toll-like receptor 3 signaling with double-stranded RNA. *Science* **320,** 379–81 (2008).

30. Botos, I., Liu, L., Wang, Y., Segal, D. M. & Davies, D. R. The toll-like receptor 3:dsRNA signaling complex. *Biochim. Biophys. Acta* **1789,** 667–74 (2009).

31. Coffman, R. L., Sher, A. & Seder, R. A. Vaccine adjuvants: putting innate immunity to work. *Immunity* **33,** 492–503 (2010).

32. Schijns, V. E. Immunological concepts of vaccine adjuvant activity. *Curr. Opin. Immunol.* **12,** 456–463 (2000).

33. Petrovsky, N. & Aguilar, J. C. Vaccine adjuvants: current state and future trends. *Immunol. Cell Biol.* **82,** 488–96 (2004).

34. Okada, H. *et al.* Induction of CD8+ T-cell responses against novel glioma-associated antigen peptides and clinical activity by vaccinations with {alpha}-type 1 polarized dendritic cells and polyinosinic-polycytidylic acid stabilized by lysine and carboxymethylcellulose in . *J. Clin. Oncol.* **29,** 330–6 (2011).

35. Butowski, N. *et al.* A phase II clinical trial of poly-ICLC with radiation for adult patients with newly diagnosed supratentorial glioblastoma: a North American Brain Tumor Consortium (NABTC01-05). *J. Neurooncol.* **91,** 175–82 (2009).

36. Hemispherx Biopharma Files New Drug Application for Ampligen®
as Treatment of Chronic Fatigue Syndrome

NDA of investigational drug includes four well-controlled trials,
more than 1,200 trial subjects and 90,000 doses
. at <http://www.hemispherx.net/content/investor/default.asp?goto=315>

37. Jacobs, B. L. & Langland, J. O. When two strands are better than one: the mediators and modulators of the cellular responses to double-stranded RNA. *Virology* **219,** 339–49 (1996).

38. Cui, Z. & Qiu, F. Synthetic double-stranded RNA poly(I:C) as a potent peptide vaccine adjuvant: therapeutic activity against human cervical cancer in a rodent model. *Cancer Immunol. Immunother.* **55,** 1267–79 (2006).

39. Salaun, B., Lebecque, S., Matikainen, S., Rimoldi, D. & Romero, P. Toll-like receptor 3 expressed by melanoma cells as a target for therapy? *Clin. Cancer Res.* **13,** 4565–74 (2007).

40. Salaun, B., Coste, I., Rissoan, M.-C., Lebecque, S. J. & Renno, T. TLR3 Can Directly Trigger Apoptosis in Human Cancer Cells. *J. Immunol.* **176,** 4894–4901 (2006).

41. Galli, R. *et al.* TLR stimulation of prostate tumor cells induces chemokine-mediated recruitment of specific immune cell types. *J. Immunol.* **184,** 6658–69 (2010).

42. Miyake, T. *et al.* Poly I:C-induced activation of NK cells by CD8 alpha+ dendritic cells via the IPS-1 and TRIF-dependent pathways. *J. Immunol.* **183,** 2522–8 (2009).

43. Gitlin, L. *et al.* Essential role of mda-5 in type I IFN responses to polyriboinosinic:polyribocytidylic acid and encephalomyocarditis picornavirus. *Proc. Natl. Acad. Sci. U. S. A.* **103,** 8459–64 (2006).

44. Kato, H. *et al.* Cell type-specific involvement of RIG-I in antiviral response. *Immunity* **23,** 19–28 (2005).

45. Le Goffic, R. *et al.* Cutting Edge: Influenza A virus activates TLR3-dependent inflammatory and RIG-I-dependent antiviral responses in human lung epithelial cells. *J. Immunol.* **178,** 3368–72 (2007).

46. Kato, H. *et al.* Length-dependent recognition of double-stranded ribonucleic acids by retinoic acid-inducible gene-I and melanoma differentiation-associated gene 5. *J. Exp. Med.* **205,** 1601–10 (2008).

47. Gamucci, O., Bertero, A., Gagliardi, M. & Bardi, G. Biomedical Nanoparticles: Overview of Their Surface Immune-Compatibility. *Coatings* **4,** 139–159 (2014).

48. Zolnik, B. S., González-Fernández, A., Sadrieh, N. & Dobrovolskaia, M. A. Nanoparticles and the immune system. *Endocrinology* **151,** 458–65 (2010).

49. Moghimi, S. . Chemical camouflage of nanospheres with a poorly reactive surface: towards development of stealth and target-specific nanocarriers. *Biochim. Biophys. Acta - Mol. Cell Res.* **1590,** 131–139 (2002).

50. Kalkanidis, M. *et al.* Methods for nano-particle based vaccine formulation and evaluation of their immunogenicity. *Methods* **40,** 20–9 (2006).

51. Dobrovolskaia, M. A., Aggarwal, P., Hall, J. B. & McNeil, S. E. Preclinical studies to understand nanoparticle interaction with the immune system and its potential effects on nanoparticle biodistribution. *Mol. Pharm.* **5,** 487–95 (2008).

52. Silva, J. M., Videira, M., Gaspar, R., Préat, V. & Florindo, H. F. Immune system targeting by biodegradable nanoparticles for cancer vaccines. *J. Control. Release* **168,** 179–99 (2013).

53. Fang, C. *et al.* In vivo tumor targeting of tumor necrosis factor-alpha-loaded stealth nanoparticles: effect of MePEG molecular weight and particle size. *Eur. J. Pharm. Sci.* **27,** 27–36 (2006).

54. Reddy, L. H., Arias, J. L., Nicolas, J. & Couvreur, P. Magnetic nanoparticles: design and characterization, toxicity and biocompatibility, pharmaceutical and biomedical applications. *Chem. Rev.* **112,** 5818–78 (2012).

55. Aggarwal, P., Hall, J. B., McLeland, C. B., Dobrovolskaia, M. A. & McNeil, S. E. Nanoparticle interaction with plasma proteins as it relates to particle biodistribution, biocompatibility and therapeutic efficacy. *Adv. Drug Deliv. Rev.* **61,** 428–37 (2009).

56. Hubbell, J. A., Thomas, S. N. & Swartz, M. A. Materials engineering for immunomodulation. *Nature* **462,** 449–60 (2009).

57. Fröhlich, E. The role of surface charge in cellular uptake and cytotoxicity of medical nanoparticles. *Int. J. Nanomedicine* **7,** 5577–91 (2012).

58. McNerny, D. Q., Leroueil, P. R. & Baker, J. R. Understanding specific and nonspecific toxicities: a requirement for the development of dendrimer-based pharmaceuticals. *Wiley Interdiscip. Rev. Nanomedicine Nanobiotechnology* **2,** 249–259 (2010).

59. Foged, C., Brodin, B., Frokjaer, S. & Sundblad, A. Particle size and surface charge affect particle uptake by human dendritic cells in an in vitro model. *Int. J. Pharm.* **298,** 315–22 (2005).

60. Yue, H. *et al.* Particle size affects the cellular response in macrophages. *Eur. J. Pharm. Sci.* **41,** 650–7 (2010).

61. Manolova, V. *et al.* Nanoparticles target distinct dendritic cell populations according to their size. *Eur. J. Immunol.* **38,** 1404–13 (2008).

62. Bachmann, M. F. & Jennings, G. T. Vaccine delivery: a matter of size, geometry, kinetics and molecular patterns. *Nat. Rev. Immunol.* **10,** 787–96 (2010).

63. Blasius, A. L. & Beutler, B. Intracellular toll-like receptors. *Immunity* **32,** 305–15 (2010).

64. Sahay, G., Alakhova, D. Y. & Kabanov, A. V. Endocytosis of nanomedicines. *J. Control. Release* **145,** 182–95 (2010).

65. Jovic, M., Sharma, M., Rahajeng, J. & Caplan, S. The early endosome: a busy sorting station for proteins at the crossroads. *Histol. Histopathol.* **25,** 99–112 (2010).

66. Stoorvogel, W., Strous, G. J., Geuze, H. J., Oorschot, V. & Schwartzt, A. L. Late endosomes derive from early endosomes by maturation. *Cell* **65,** 417–427 (1991).

67. Luzio, J. P., Pryor, P. R. & Bright, N. A. Lysosomes: fusion and function. *Nat. Rev. Mol. Cell Biol.* **8,** 622–32 (2007).

68. Mohanan, D. *et al.* Administration routes affect the quality of immune responses: A cross-sectional evaluation of particulate antigen-delivery systems. *J. Control. Release* **147,** 342–9 (2010).

69. Yildirimer, L., Thanh, N. T. K., Loizidou, M. & Seifalian, A. M. Toxicology and clinical potential of nanoparticles. *Nano Today* **6,** 585–607 (2011).

70. Zhang, X.-D. *et al.* Toxicologic effects of gold nanoparticles in vivo by different administration routes. *Int. J. Nanomedicine* **5,** 771–81 (2010).

71. Lu, Z., Wang, J., Wientjes, M. G. & Au, J. L.-S. Intraperitoneal therapy for peritoneal cancer. *Future Oncol.* **6,** 1625–41 (2010).

72. Gelperina, S., Kisich, K., Iseman, M. D. & Heifets, L. The potential advantages of nanoparticle drug delivery systems in chemotherapy of tuberculosis. *Am. J. Respir. Crit. Care Med.* **172,** 1487–90 (2005).

73. McLennan, D. N., Porter, C. J. H. & Charman, S. A. Subcutaneous drug delivery and the role of the lymphatics. *Drug Discov. Today. Technol.* **2,** 89–96 (2005).

74. Cubas, R. *et al.* Virus-like particle (VLP) lymphatic trafficking and immune response generation after immunization by different routes. *J. Immunother.* **32,** 118–28 (2009).

75. Reddy, S. T. *et al.* Exploiting lymphatic transport and complement activation in nanoparticle vaccines. *Nat. Biotechnol.* **25,** 1159–64 (2007).

76. Jewell, C. M., López, S. C. B. & Irvine, D. J. In situ engineering of the lymph node microenvironment via intranodal injection of adjuvant-releasing polymer particles. *Proc. Natl. Acad. Sci. U. S. A.* **108,** 15745–50 (2011).

77. De Titta, A. *et al.* Nanoparticle conjugation of CpG enhances adjuvancy for cellular immunity and memory recall at low dose. *Proc. Natl. Acad. Sci. U. S. A.* **110,** 19902–7 (2013).

78. Lund, V., Schmid, R., Rickwood, D., Homes, E. & S, A. L. A. Nucleic Acids Research. **16,** 10861–10880 (1988).

79. Chu, B. C. F., Wahl, G. M. & Orgel, L. E. Derivatization of unprotected polynudeotides. *Nucleic Acids Res.* (1983).

80. Shukoor, M. I. *et al.* Double-stranded RNA polyinosinic-polycytidylic acid immobilized onto gamma-Fe_2O_3 nanoparticles by using a multifunctional polymeric linker. *Small* **3,** 1374–8 (2007).

81. Shukoor, M. I. *et al.* dsRNA-functionalized multifunctional gamma-Fe_2O_3 nanocrystals: a tool for targeting cell surface receptors. *Angew. Chem. Int. Ed. Engl.* **47,** 4748–4752 (2008).

82. Parker-Esquivel, B. *et al.* Association of poly I:C RNA and plasmid DNA onto MnO nanorods mediated by PAMAM. *Langmuir* **28,** 3860–70 (2012).

83. Delong, R. K. *et al.* Functionalized gold nanoparticles for the binding, stabilization, and delivery of therapeutic DNA, RNA, and other biological macromolecules. *Nanotechnol. Sci. Appl.* **3,** 53–63 (2010).

84. Tros de Ilarduya, C., Sun, Y. & Düzgüneş, N. Gene delivery by lipoplexes and polyplexes. *Eur. J. Pharm. Sci.* **40,** 159–70 (2010).

85. Niemeyer, C. M. Nanoparticles, Proteins, and Nucleic Acids: Biotechnology Meets Materials Science. *Angew. Chemie Int. Ed.* **40,** 4128–4158 (2001).

86. Conde, J. *et al.* Design of Multifunctional Gold Nanoparticles for In Vitro and In Vivo Gene Silencing. *ACS Nano* **6,** 8316–8324 (2012).

87. Singh, N., Agrawal, A., Leung, A. K. L., Sharp, P. A. & Bhatia, S. N. Effect of Nanoparticle Conjugation on Gene Silencing by RNA Interference. *J. Am. Chem. Soc.* **132,** 8241–8243 (2010).

88. Froehlich, E., Mandeville, J. S., Arnold, D., Kreplak, L. & Tajmir-Riahi, H. A. Effect of PEG and mPEG-anthracene on tRNA aggregation and particle formation. *Biomacromolecules* **13,** 282–7 (2012).

89. Mahtab, R., Rogers, J. P., Singleton, C. P. & Murphy, C. J. Preferential adsorption of a “kinked” DNA to a neutral curved surface: comparisons to and implications for nonspecific DNA−protein interactions. *J. Am. Chem. Soc.* **118,** 7028–7032 (1996).

90. Mahtab, R., Harden, H. H. & Murphy, C. J. Temperature- and salt-dependent binding of long DNA to protein-sized Quantum Dots: thermodynamics of “inorganic protein”−DNA interactions. *J. Am. Chem. Soc.* **122,** 14–17 (2000).

91. Hernández-Gil, J. *et al.* Two novel ternary dicopper(II) μ-guanazole complexes with aromatic amines strongly activated by quantum dots for DNA cleavage. *Inorg. Chem.* **53,** 578–93 (2014).

92. Moghimi, S. M., Hamad, I., Andresen, T. L., Jørgensen, K. & Szebeni, J. Methylation of the phosphate oxygen moiety of phospholipid-methoxy(polyethylene glycol) conjugate prevents PEGylated liposome-mediated complement activation and anaphylatoxin production. *FASEB J.* **20,** 2591–3 (2006).

93. Watson, J. D. & Crick, F. H. Molecular structure of nucleic acids; a structure for deoxyribose nucleic acid. *Nature* **171,** 737–8 (1953).

94. Mandelkern, M., Elias, J. G., Eden, D. & Crothers, D. M. The dimensions of DNA in solution. *J. Mol. Biol.* **152,** 153–61 (1981).

95. Ipe, B. I. *et al.* Dynamic light-scattering analysis of the electrostatic interaction of hexahistidine-tagged cytochrome P450 enzyme with semiconductor quantum dots. *Chemphyschem* **7,** 1112–8 (2006).

96. Henriksen-Lacey, M. *et al.* Comparison of the depot effect and immunogenicity of liposomes based on dimethyldioctadecylammonium (DDA), 3β-[N-(N’,N'-Dimethylaminoethane)carbomyl] cholesterol (DC-Chol), and 1,2-Dioleoyl-3-trimethylammonium propane (DOTAP): prolonged liposome retention. *Mol. Pharm.* **8,** 153–61 (2011).

97. Hasan, M., Ruksznis, C., Wang, Y. & Leifer, C. A. Antimicrobial peptides inhibit polyinosinic-polycytidylic acid-induced immune responses. *J. Immunol.* **187,** 5653–9 (2011).

98. Wang, C. *et al.* Toll-like receptor 3 agonist complexed with cationic liposome augments vaccine-elicited antitumor immunity by enhancing TLR3-IRF3 signaling and type I interferons in dendritic cells. *Vaccine* **30,** 4790–9 (2012).

99. Smole, A., Krajnik, A. K., Oblak, A., Pirher, N. & Jerala, R. Innate Immunity. (2013). doi:10.1177/1753425912450346

100. Dunn, W. A., Hubbard, A. L. & Aronson, N. N. Low temperature selectively inhibits fusion between pinocytic vesicles and lysosomes during heterophagy of 125I-asialofetuin by the perfused rat liver. *J. Biol. Chem.* **255,** 5971–8 (1980).

101. Howe, C. L. *et al.* Derived protein sequence, oligosaccharides, and membrane insertion of the 120-kDa lysosomal membrane glycoprotein (lgp120): identification of a highly conserved family of lysosomal membrane glycoproteins. *Proc. Natl. Acad. Sci.* **85,** 7577–7581 (1988).

102. Tilney, N. L. Patterns of lymphatic drainage in the adult laboratory rat. *J. Anat.* **109,** 369–83 (1971).

103. Marco, A. J. *et al.* Lymphatic drainage of Listeria monocytogenes and Indian ink inoculated in the peritoneal cavity of the mouse. *Lab. Anim.* **26,** 200–5 (1992).

104. Shibata, S. *et al.* The time course of lymphatic routes emanating from the peritoneal cavity in rats. *Anat. Histol. Embryol.* **36,** 78–82 (2007).

105. Parungo, C. P. *et al.* Lymphatic drainage of the peritoneal space: a pattern dependent on bowel lymphatics. *Ann. Surg. Oncol.* **14,** 286–98 (2007).

106. Wang, Y. X., Hussain, S. M. & Krestin, G. P. Superparamagnetic iron oxide contrast agents: physicochemical characteristics and applications in MR imaging. *Eur. Radiol.* **11,** 2319–31 (2001).

107. Korteweg, M. A. *et al.* Characterization of ex vivo healthy human axillary lymph nodes with high resolution 7 Tesla MRI. *Eur. Radiol.* **21,** 310–7 (2011).

108. Oussoren, C. & Storm, G. Liposomes to target the lymphatics by subcutaneous administration. *Adv. Drug Deliv. Rev.* **50,** 143–56 (2001).

109. Christien Oussoren, Jan Zuidema, D. J. A. C. and G. S. Lymphatic uptake and biodistribution of liposomes after sybcutaneous injection I. Influence of the anatomycal site of injection. *J. Liposome Res.* **7,** 85–99 (1997).

110. Harrell, M. I., Iritani, B. M. & Ruddell, A. Lymph node mapping in the mouse. *J. Immunol. Methods* **332,** 170–4 (2008).

111. Tomura, M. *et al.* Monitoring cellular movement in vivo with photoconvertible fluorescence protein “Kaede” transgenic mice. *Proc. Natl. Acad. Sci. U. S. A.* **105,** 10871–6 (2008).

112. Nham, T., Filali, S., Danne, C., Derbise, A. & Carniel, E. Imaging of bubonic plague dynamics by in vivo tracking of bioluminescent Yersinia pestis. *PLoS One* **7,** e34714 (2012).

113. Deakin, A. M., Payne, A. N., Whittle, B. J. & Moncada, S. The modulation of IL-6 and TNF-alpha release by nitric oxide following stimulation of J774 cells with LPS and IFN-gamma. *Cytokine* **7,** 408–16 (1995).

114. McGeough, M. D. *et al.* Cutting edge: IL-6 is a marker of inflammation with no direct role in inflammasome-mediated mouse models. *J. Immunol.* **189,** 2707–11 (2012).

115. Bettelli, E. *et al.* Reciprocal developmental pathways for the generation of pathogenic effector TH17 and regulatory T cells. *Nature* **441,** 235–8 (2006).

116. Trinchieri, G. Interleukin-12 and the regulation of innate resistance and adaptive immunity. *Nat. Rev. Immunol.* **3,** 133–46 (2003).

117. Hsieh, C. S. *et al.* Development of TH1 CD4+ T cells through IL-12 produced by Listeria-induced macrophages. *Science* **260,** 547–9 (1993).

118. Smyth, M. J., Taniguchi, M. & Street, S. E. A. The anti-tumor activity of IL-12: mechanisms of innate immunity that are model and dose dependent. *J. Immunol.* **165,** 2665–2670 (2000).

119. Kato, H. *et al.* Differential roles of MDA5 and RIG-I helicases in the recognition of RNA viruses. *Nature* **441,** 101–5 (2006).

4

Development of IONP-filled PL-PEG micelles for harnessing a platinum-based chemotherapy with an immune system attack on cancer cells

The aim of this chapter is to harness the immunological activity of the previously described poly (I:C)-IONP@PL-PEG micelles with the co-delivery of a cisplatin Pt(IV) prodrug for combining targeted chemotherapy with immunotherapy. The chemotherapeutic agent is coupled by covalent attachment of the Pt(IV) prodrug to amine-modified PEGylated PL at the IONP-filled micelles. The cancer cell killing properties of the new construct are studied in different human cancer cell lines whilst the ability to activate an innate immune response are evaluated in different antigen presenting cells (APCs).

4.1 Introduction

4.1.1 Cancer therapies

Based on the most recent data published by World Health Organization (WHO) about incidence, prevalence and cancer mortality from the major types of cancer, it was estimated that there were 14.1 million cases around the world in 2012 and that number is expected to increase to 24 million by 2035.[1] Of that total estimated, 7.4 million cancer cases were in men and 6.7 million in women. Lung cancer was the most common cancer worldwide in men (nearly of 17 % of total) closely followed by prostate cancer with 15 %, whilst breast cancer represents more than 25 % of the total number of the diagnosed cancers in women.[2]

The incidence and mortality patterns between developed and developing countries for a given cancer are very different due to the prevalence of major risk factors, detection practices or the availability of treatments services. Even so, cancer is one of the leading causes of death worldwide (the leading cause of death in developed countries and the second leading cause of death in developing countries). The WHO highlights in its last report that 8.2 million people died from cancer in 2012.[1]

Cancer treatment may consist on the use of a single therapy or a combination of therapies, such as surgery, radiotherapy and chemotherapy. Surgery and radiation therapies are commonly used for diseases limited to a local region (locoregional), whereas systemic therapies are used to treat metastatic cancers. Standard chemotherapy uses drugs to kill cancer cells and usually, multiple drugs are combined for avoiding drug resistance and for achieving additive or synergistic antitumor efficiency.[3] However, one of the main limitations in combining different drugs in cancer treatments is that each drug has different biodistribution and pharmacokinetics, which generates a problem in developing more effective therapies.

Each therapy option alone is typically not enough to eradicate cancer and better cure rates come from combining different therapy modalities. Moreover, normal organs, tissues and cells are severely damaged during current cancer treatments and the development of new therapies which minimize the toxicity to healthy tissues is still one of the main goals of therapy against cancer.

Compared to chemotherapy, therapies that harness the body´s own immune system to recognize and destroy cancer cells are among the most promising cancer therapies developed in the last years. Although the immune system is able to recognize and eliminate abnormal cells (cancerous and/or precancerous cells) before they can cause harm, some cancers develop the capability to avoid detection and destruction by the immune system. There are different ways to obtain this capability, such as producing signals that reduce the ability to kill cancer cells or maybe the differences between normal and cancer cells are so small that the immune system is not able to detect them. Thereby immunotherapy is focused on stimulating the immune system to restore or enhance its ability to fight against cancer. The interest in immunotherapy as cancer treatment has grown rapidly after the approvals in 2010 and 2011 of immune-based therapies for the treatment of prostate and melanoma cancer patients respectively.[4]

The combination of immunotherapy with other cancer treatments could potentially lead to enhance the efficacy of conventional therapies. Some chemotherapeutics effectively used to treat cancer have shown in recent studies that can induce a form of tumor cell death that is immunologically active, thereby resulting in a potent antitumor immune response. [4–7] The combination of chemotherapy and immunotherapy to improve the efficacy of both therapies by a synergystic effect can therefore be a promising new strategy to combat cancer.

4.1.2 Anti-tumor immune response

Certain cells of the immune system, including natural killers cells (NK), dendritic cells (DCs) and effector T cells are capable of driving potent anti-tumor responses. Dendritic cells are professional antigen presenting cells which capture and present antigens (provided by dead or dying tumor cells) to T-cells for their priming.[8] To accomplish this task, DCs need to reach a mature status characterized by up-regulation of molecules involved in antigen presentation (MHC I, MHC II...), T-cell co-stimulation (CD80, CD86, CD40...) and release of cytokines (IL-12, TNF-α, IL-6...), which usually occurs after recognition of endogenous inflammatory signals, so-called damage associated molecular patterns (DAMPs). During the maturation process DCs migrate to the lymphoid organs, and once there, the antigen specific

immune response is activated and consists in the activation of antigen specific T $CD8^+$ (cytotoxic) and T $CD4^+$ (helper) cell responses, as well as B cell responses. Finally, antigen specific T and B cells have to reach the tumor to kill cancer cells **(Fig. 4.1)**.[9,10]

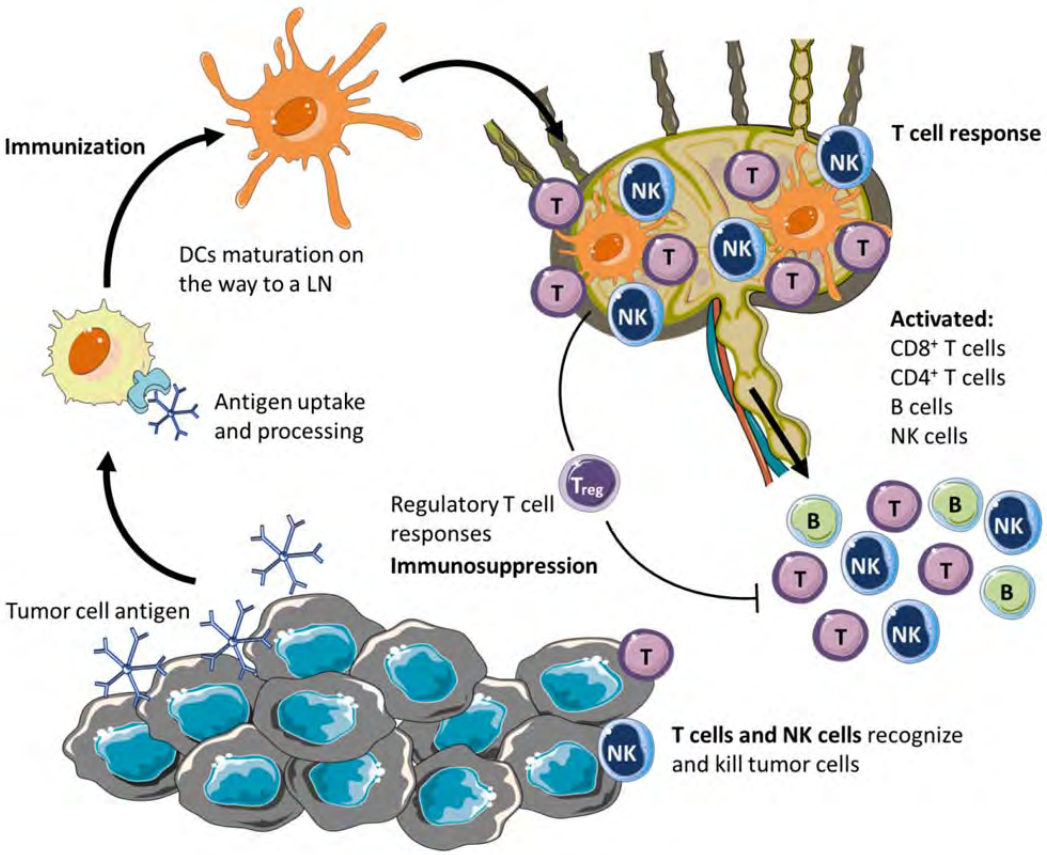

Fig. 4.1. Generation and regulation of anti-tumor immune response.

The tumour microenvironment is characterized for its ability to induce peripheral immune tolerance, so in normal conditions, even in the presence of tumour antigens, the organism is not able to orchestrate an immune response with the capacity to beat the disease. However, this immunological tolerance can be broken and generate effector T-cell responses specific for tumours. There are already some therapeutic strategies based on the administration of immunostimulatory agents, such as TLR ligands able to overcome the immunosuppressive condition of the *tumor* environment.[11,12] Administration of TLR agonists can help to break tolerance to self-antigens and promote immune responses to tumour

antigens. TLR ligands can be used as direct tumor immunotherapeutics or can be co-administered with anti-tumor agents acting as adjuvants for developing cancer vaccines.[13] The anti-tumor effect is related with their ability to stimulate APCs, which in turn, activate tumor-specific T cell responses. Currently various TLR agonists are under investigation in clinical trials for their ability to orchestrate antitumor immunity and in fact, Imiquimod (TLR7 agonist) has been approved by FDA for use in cancer patients and MPLA (TLR4) has been approved as a vaccine component. Poly (I:C) (TLR3) is a promising adjuvant in cancer vaccines due to the ability of inducing the maturation of DCs. A recent study showed that using poly (I:C) tumor growth inhibition has been achieved via this DCs stimulatory activity, which results in activation and maturation of T cells and NK cells to kill cancer cells.[14–16]

4.1.3 Cancer nanotechnology: targeting strategies

The growing interest to solve the aforementioned issues associated with conventional treatments and therapeutic agents includes the development and application of nanotechnology in both diagnosis and therapy of cancer.

Nanoparticles have been used as a platform to develop more efficient and selective anticancer drugs. The use of NPs offers the possibility to control the biodistribution and pharmacokinetics of the administered drug and exploiting the potential synergy between drugs through a single vehicle.[17] Furthermore, one of the main goals of nanomedicine is to develop safer therapeutic and diagnostic agents, eliminating or minimizing the systemic toxicity and side effects of the current therapies. These side effects are commonly associated with their action on normal cells, because the current therapies have little or no selectivity in the process of killing tumor cells and healthy cells are also damaged. The effectiveness of drug delivery to the tumor site using NPs can be achieved by either passively and/or actively targeting drugs strategies.

Whilst the passive targeting system does not require a special targeting moiety, the strategy of an active targeting is based on the incorporation of a specific ligand that binds specifically to a receptor of the cancer tissue.[18] These ligands are commonly antibodies, peptides, nucleic acids or other molecules such as vitamins or carbohydrates.

Passive targeting provides the possibility to enhance the accumulation of the therapeutic drug inside the tumor due to the physiology of the tumor vasculature.[19,20] The first step in tumor generation consists in the formation of a cluster of cells, whose growth is regulated by the availability of oxygen and nutrients. When this accumulation of cells (which can be already considered a tumor) reaches a maximum size of 1-2 mm, the inner cells are unable to grow and proliferate due to a lack of nutrients.[21] This forms the typical structure of a tumour with a core of dead cells surrounded by quiescent and proliferating cells. At this step the tumor can evolve in two ways, the tumour can remain in a latent state where cell proliferation is balanced by cell death, or alternatively, it can initiate the growth through formation of new blood vessels (angiogenesis). The term angiogenesis refers to the growth of new blood vessels from existing ones,[22] thereby, supplying the tumor oxygen and nutrients to allow rapid growth. The most malignant tumors have the greatest angiogenic potential because cancer cells are mixed with normal cells, extending and colonizing the surrounding tissue. However, apart from promoting the growth and subsequent metastasis of the tumor,[23] angiogenesis can be exploited to efficiently deliver anti-cancer drugs to all regions of the tumor.

The blood vessels in many tumor types are irregular in shape and present greater permeability compared with normal vessels. Due to these abnormalities NPs can diffuse easily inside the tissue and be retained due to poor lymphatic drainage which increases the retention of the NPs inside the tumor. This phenomenon is called enhanced permeability and retention (EPR) effect, and it was described twenty years ago by Matsumura and Maeda.[24,25] Through this passive targeting, the EPR effect provides a great opportunity for anti-cancer drug nanoparticles to access the tumor selectivity. However, this strategy has some disadvantages because EPR effect depends on tumor tissue environment and tumor type, which can modulate the accumulation of NPs governed among others, by the interstitial pressure gradient, the matrix around the tumor or the presence of immune cells around the tumor environment.[20,26,27] Furthermore, passive targeting is dependent on the size, shape and charge of the NP. NPs larger than 100 nm with high surface charges (positively or negatively high zeta potential values) are usually rapidly cleared by the liver and spleen before accumulating at the tumor.[28,29] It is also problematic that the EPR effect is much more prominent in xenograft models in mice that in actual tumors in humans.[30,31]

Other important process to take into account in the progress of metastasis is related with the morphology of the lymphatic system. Lymphatic vessels have been considered passive participants in tumor metastasis due to the aforementioned capacity of lymphatics to facilitate the entry and transport of tumor cells. However. recent studies show that tumors can actively induce the growth of lymphatic vessels and this growth promotes metastasis to lymph nodes which facilitates the spread to distant organs.[32,33]

Active targeting is very useful in the treatment of tumour regions poorly vascularized and thus, where the EPR effect is not very efficient yet.[18,34] Moreover, targeting ligands enable NPs to bind cell surface receptors on cancer cells and enter by receptor-mediated endocytosis mechanisms, thereby improving the cell uptake into cancer cells.[29] However, active targeting is often considered more expensive than the use of non-targeted nanoparticles, which could be the reason why so few formulations based on active targeting have reached clinical trials for use in cancer therapy.[18] Small-molecules are very attractive for use as targeting ligands due to their better stability, less immunogenicity and simple preparation. Probably, the best studied small-molecule is folic acid or folate (FA). FA is an essential water-soluble B vitamin involved in a myriad of body functions,[35] but it is especially important for rapid cell division and growth.[36] Because FA is essential for cell proliferation, it is normal that several cancer cells overexpress FA receptors. [37] These FA-targeted therapeutic drugs are a promising cancer therapy in which several research groups have focused their attention using cationic polymers, dendrimers, micelles and nanoparticles as scaffolds.

4.1.4 Development of cancer nanomedicine combining imaging and therapy

The early diagnosis and the continuous development of new therapies have improved notably cancer survival rates. Developing strategies which enable cancer diagnosis and therapy to take place together (a concept that has been recently coined as theranostics) using nanomaterials is one of the main new topics of nanomedicine research worldwide.[38–40]

The trend toward combining therapeutic and diagnostic functions in a single nanoformulation has been developed by taking advantage of the large surface provided by

the nanoparticle, which allows accommodating different types of drugs or imaging agents, as well as the intrinsic properties associated with some nanoparticles themselves (e.g. magnetic and gold nanoparticles possess properties which can be used for therapy and diagnosis purposes). Theranostic agents can simultaneously deliver therapeutic drugs and imaging agents to specific sites, organs or tissues. Several types of theranostic nanoparticles have been developed so far for treating cancer but none has yet satisfied all the main requirements of an effective agent: rapid and selective accumulation in targets of interest, efficient delivery of the therapeutic dose of drug without damaging healthy organs/tissues, rapid clearance from the body and the ability to report on the status of the disease.[28]

A widely used chemotherapeutic agent is the *cis*-dichlorodiamminoplatinum (II) complex (known as cisplatin) and its derivates, such as carboplatin and oxaliplatin. Cisplatin was approved by FDA in 1978 and so far has been used in the treatment against several solid tumors, such as bladder, cervical, ovarian or testicular cancer. Despite its clinical success, its application is limited due to the development of tumor resistant, the development of side effects and because it is not equally effective against all cancer types.[41]

A number of drug delivery systems have been investigated for the delivery of platinum-based drugs and prodrugs to overcome the disadvantages and limitations associated with cisplatin.[42–45] Several studies have focused on the controlled delivery of platinum anticancer drugs using inert Pt(IV) prodrugs which can intracellularly be reduced to cytotoxic Pt(II) drugs.[46] Octahedral Pt(IV) complexes are chemically inert and are capable of losing the two axial ligands of the platinum centre **(Fig. 4.2)** in the more reducing environment present in tumors and/or after uptake by the cancer cell.[47,48] The redox properties allow them to be reduced to Pt(II) complexes and convert the complexes into active therapeutic agents. The possibility to bind these axial ligands to other biomolecules or delivery systems has opened up an attractive range of possibilities, especially because the inertness of Pt(IV) complexes could result in fewer side effects than current Pt(II) drugs.

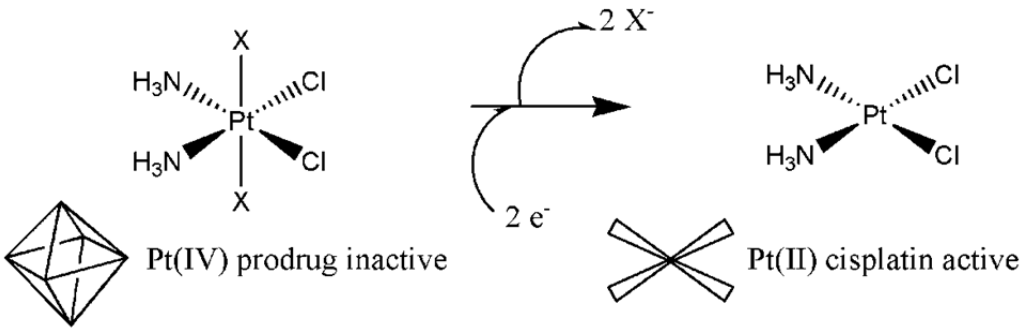

Fig. 4.2. Mechanism of cisplatin release from a Pt(IV)-based prodrug. The two electron reduction to the square-planar Pt(II) complex cisplatin with loss of the axial ligands (represented by X).

Probably one of the most relevant studies in this field in the last ten years is the work led by Stephen J. Lippard. Lippard and coworkers[42], who developed one of the first Pt(IV)-based nanoparticles systems using AuNPs as a scaffold, thereby achieving higher cytotoxicity in several cancer cell lines when the cells are incubated with Pt(IV)-AuNP than with free cisplatin. Encouraged by the good results, many other research groups have focused on Pt(IV)-based systems. Min *et al*.[49] have attached a Pt(IV) complex to PEGylated Au nanorods following a similar strategy demonstrating that the delivery system improves the cytotoxicity compared to free cisplatin in different types of cancer cells. Jian Li *et al.*[50] have reported recently the internalization of Pt(IV) prodrug in carbon nanotubes and the efficient delivery of Pt into cancer cells compared with the non-encapsulated prodrug.

However, all of the chemotherapy modalities mentioned above have focused their attention on the optimization of platinum cytotoxicity in cancer cells without assessing the possible influence of interactions with the immune system.

In this work, firstly a non toxic iron oxide micelle is functionalized with a Pt(IV) prodrug and with the immunostimulatory agent poly (I:C). Then, the potential effect of the drugs in several cancer cell lines and the activation of cells of the immune system is analyzed. Thereby, it is studied if it is possible to achieve an efficient construct for combining chemotherapy and immunotherapy in a single system. The ability of the system to activate DCs is studied by the expression of cytokines and co-stimulatory molecules involved in the anti-tumor immune response. And finally, the system is monitored *in vivo* to demonstrate

the ability of the nanoparticulate system to reach lymph nodes, which is important considering that lymph nodes are considered the command centres of the immune system and because lymph nodes close to the primary tumor are often the first site of metastases.

4.2 Results and discussion

4.2.1 Synthesis and Characterization of poly (I:C)-IONP@PL-PEG-Pt(IV) micelles

4.2.1.1 Synthesis and characterization of DSPE-PEG(2000)-Pt(IV)

The succinic acid-derivatized Pt(IV) complex *cis*,*cis*,*trans*-$[Pt(NH_3)_2Cl_2(O_2CCH_2CH_2CO_2H)_2]$ (**1, Scheme 4.1**) was synthesized following the procedure described by W. J. Rieter *et al.*[51] in 2008. This complex (inert prodrug) was attached to the amine end group of a commercially available phospholipid DSPE-PEG (2000)-NH_2 (previously used in chapter 2 to form amine decorated IONP-filled micelles) via dicyclohexylcarbodiimide (DCC) mediated traditional coupling reaction.[52] This strategy allows us to develop the all-in-one system which possesses imaging and combo drug delivery capabilities.

In a typical reaction *cis*,*cis*,*trans*-$[Pt(NH_3)_2Cl_2(O_2CCH_2CH_2CO_2H)_2]$ (9.6 mg, 18.0 µmol), DCC (3.7 mg, 18.0 µmol) and 4-(dimethylamino)pyridine (DMAP, 1.0 mg, 7.2 µmol) were dissolved in DMSO (130 µL). After 10 minutes, the solution containing the activated platinum(IV) complex was added to a DMSO solution of DSPE-PEG(2000)-NH_2 (10 mg, 3.6 µmol, 170 µL). The resulting mixture was allowed to react at room temperature for 72 h under continuous stirring. Then, water was added to the reaction mixture. The solution was centrifuged and the supernatant was passed through a 0.45 µm filter to remove insoluble traces. Then, the supernatant was dialyzed in a Slide-A-Lyzer Dialysis Cassete (Thermo Scientific) (MW cutoff of 2,000) against water (3 x 500 mL). The dialysate, containing the final product DSPE-PEG-Pt(IV) (**2, Scheme 4.1**) was lyophilized and the residue dried in vacuo over P_2O_5 (10.86 mg, 90%). The reaction yield was 65 %.

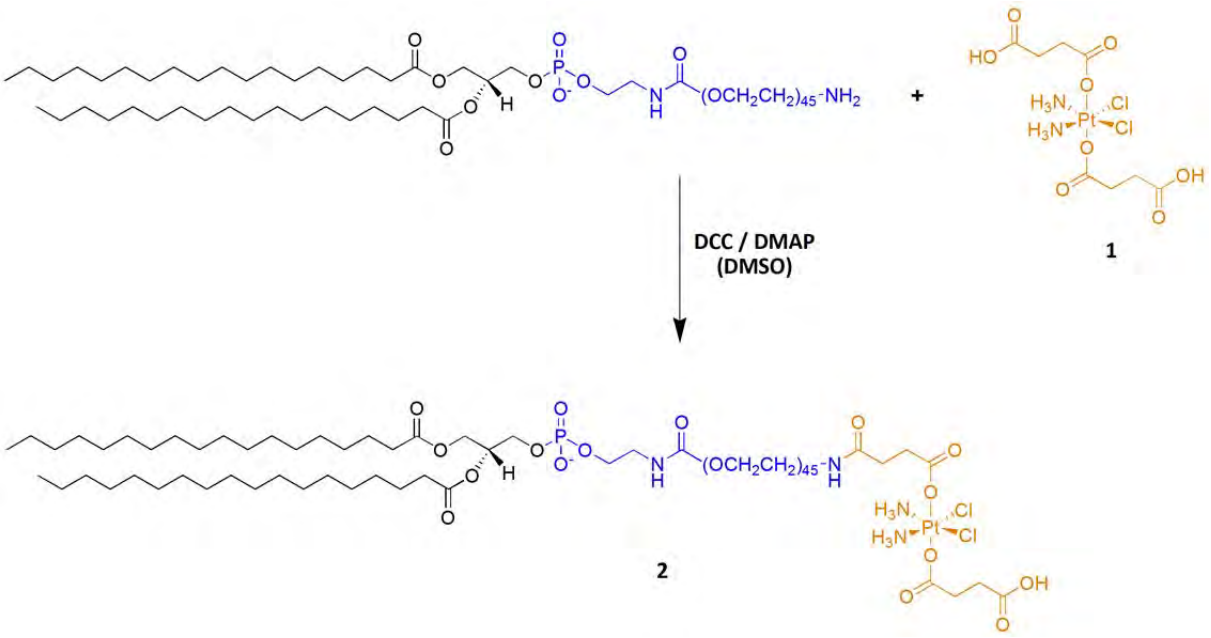

Scheme 4.1. Coupling reaction between DSPE-PEG(2000)-NH_2 and succinic acid-derivatized Pt (IV) prodrug **(1)**.

The structure of **2** is supported by different analytical and spectroscopy techniques, such as: liquid chromatography-electrospray ionization- tandem mass spectrometry (LC-ESI-MS), UV, XPS, NMR and DLS, which are represented in **Fig. 4.4-4.10,** confirming the successful coupling between Pt(IV)-based prodrug and DSPE-PEG(2000)-NH_2 phospholipid.

Fig. 4.4 shows the ESI time-of-flight (TOF) chromatograms of DSPE-PEG(2000)-NH_2 before and after the addition of Pt(IV) prodrug complex 1. The experimental results reflect a change in retention time before and after the coupling with **1**, indicating that the starting phospholipid has changed its polarity and consequently its structure. The time of flight of compound **2** has been reduced, resulting in less affinity for the stationary phase (reversed phase column or apolar), which reflects that **2** is more polar than the starting amine phospholipid. The experiment suggests that the terminal amine group of the phospholipid has been functionalized with the Pt(IV) prodrug. The analysis of both LC-ESI-MS chromatograms was required to verify this assumption **(Fig. 4.5).**

In the LC-ESI-MS spectrum represented in **Fig. 4.5a** the highest mass peak at *m/z* = 936.51 corresponds to [DSPE-PEG(2000)-NH_2+$2H^+$+$2NH_4^+$]$^{3+}$, matches very closely the

expected value (936.61 for $C_{132}H_{272}N_4O_{54}P$). In **Fig. 4.5b** the positive ESI ionization resulted in a spectrum with an ion at 1114.17 belonging to [DSPE-PEG(2000)-Pt(IV)+H^++3NH_4^+]$^{3+}$ also very close to the expected value of 1114.28 ($C_{140}H_{289}N_7O_{61}PPtCl_2$), showing the correct isotopic pattern for this formulation and in concordance with the distribution of a PEG-like polymer.[53]

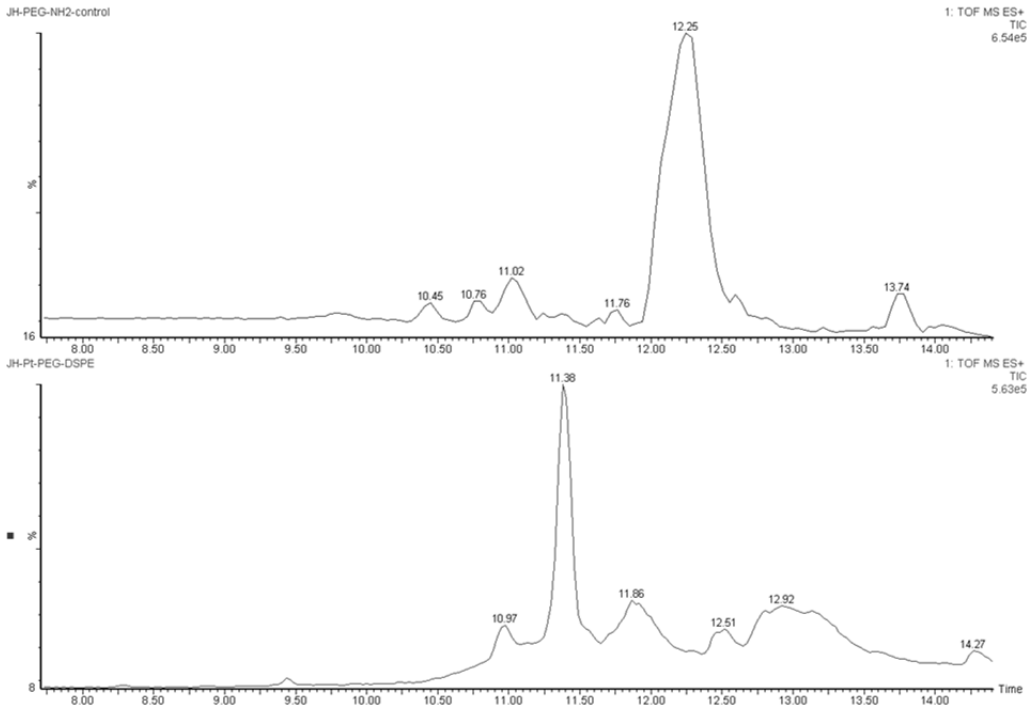

Fig. 4.4. Typical total ion chromatograms obtained for initial DSPE-PEG(2000)-NH_2 used as a control (*top*) and DSPE-PEG(2000)-Pt(IV) after dialysis purification (*bottom*).

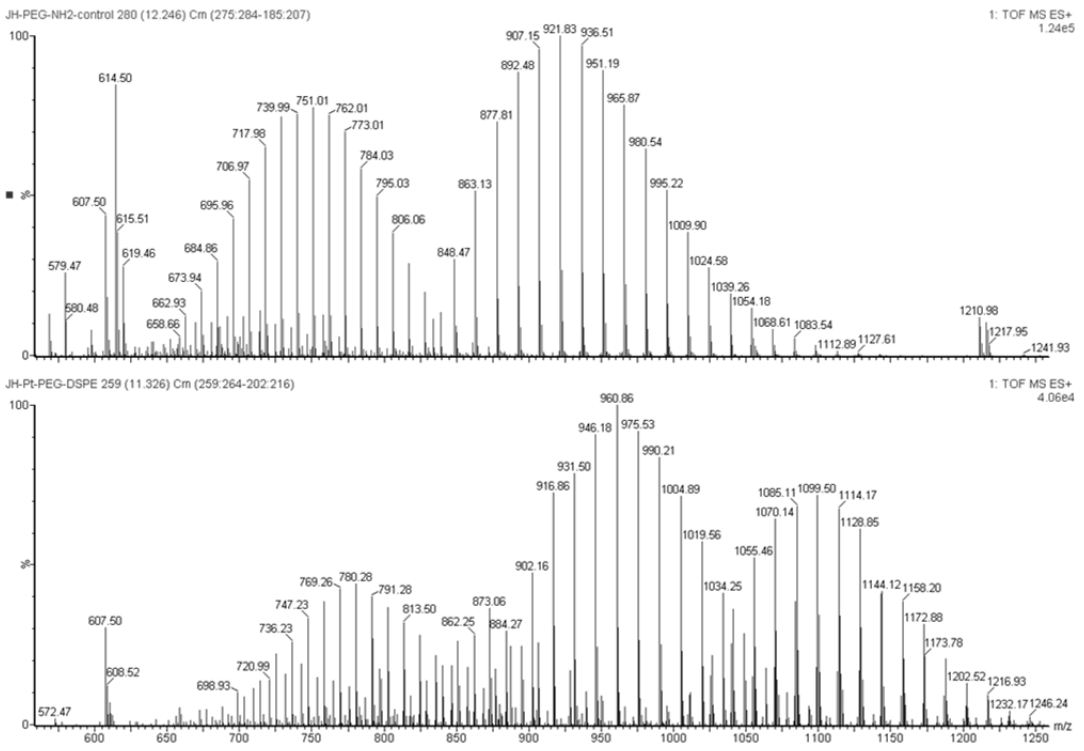

Fig. 4.5. Positive ESI-MS m/z spectra of the parent DSPE-PEG(2000)-NH_2 (*top*, control) and DSPE-PEG(2000)-Pt(IV) product (*bottom*): m/z for $[DSPE\text{-}PEG(2000)\text{-}NH_2+2H^+ +2NH_4^+]^{3+}$ ($C_{132}H_{272}N_4O_{54}P$) expected = 936.61, found = 936.51; m/z for $[DSPE\text{-}PEG(2000)\text{-}Pt(IV)+H^+ +3NH_4^+]^{3+}$ ($C_{140}H_{289}N_7O_{61}PPtCl_2$) expected = 1114.28, found = 1114.17

Following with the characterization of DSPE-PEG-Pt(IV), the ^{1}H NMR spectrum and two dimensional COSY (correlation spectroscopy) spectrum (500 MHz, $CDCl_3$) of **2** are displayed in **Fig. 4.6a**, showing the agreement with the structure proposed in **Scheme 4.1**. All resonances have been assigned with the aid of the COSY experiment by fitting the cross peak multiplets in the COSY spectrum. The presence of the characteristic chemical shift at 2.60 ppm in the ^{1}H NMR spectrum is assigned to the methylene protons of axial succinate ligands. The resonances corresponding to the phospholipid structure at 0.88 ppm (t, CH_3), 1.25 (s, CH_2), 1.61 (m, $\mathbf{CH_2}CH_2CO$) and 2.32 (m, $CH_2\mathbf{CH_2}CO$) and the characteristic chemical shift of PEG at 3.64 ppm (s, integrating to 180H) are present in the spectrum. The broad singlet at 6.25 ppm which integrates to 6H, corresponds to the square-planar amine ligands of of the Pt(IV) centre, represented in **Fig. 4.6a.**

The presence of two cross-peaks in 2D COSY spectrum helps to characterize the product **2** unequivocally. The cross-peak between signal at 6.68 ppm with 3.64 ppm

correspond to amide formed between succinic axial ligand of Pt(IV) complex and DSPE-PEG(2000)-NH_2, represented by green color as NH-amide-2 in **Fig. 4.6a**. The cross-peak between 6.82 and 3.44 ppm allows the characterisation of the amine forming part of the phospholipid structure, which is represented by blue color as NH-amide-1 in **Fig. 4.6a.**

Diffusion ordered spectroscopy (DOSY) determines the diffusion coefficient of each chemical species present in the sample.[54,55] The 2D-DOSY NMR spectrum shown in **Fig. 4.6b,** confirms the formation of **2.** In fact**,** proton signals due to the axial succinate ligands of **1** (2.50-2.80 ppm) display diffusion coefficients extremely similar to those corresponding to the phospholipid structure (e.g. 0.8, 1.25 and 3.64 ppm), consistent with the covalent attachment of the two fragments.

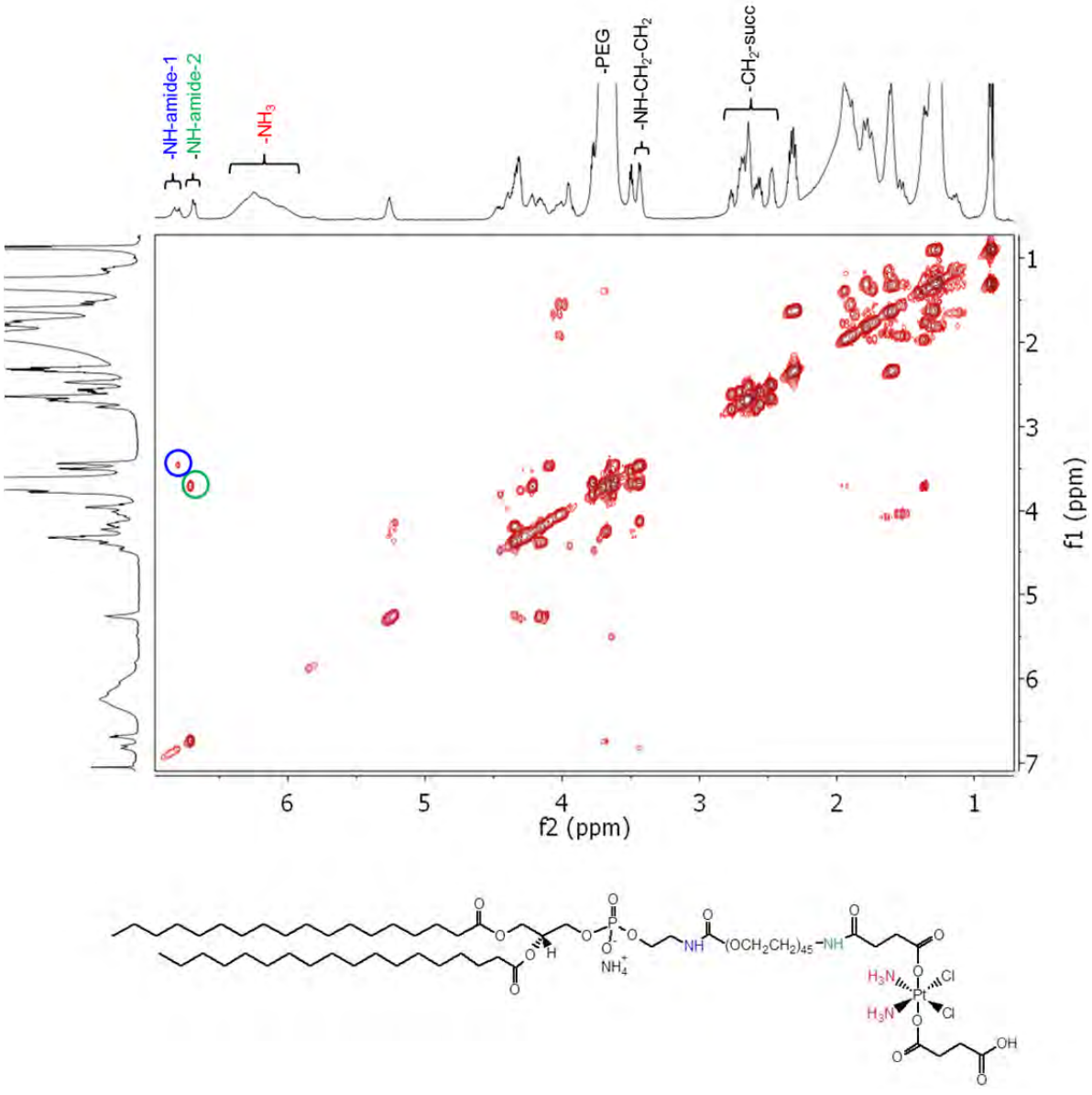

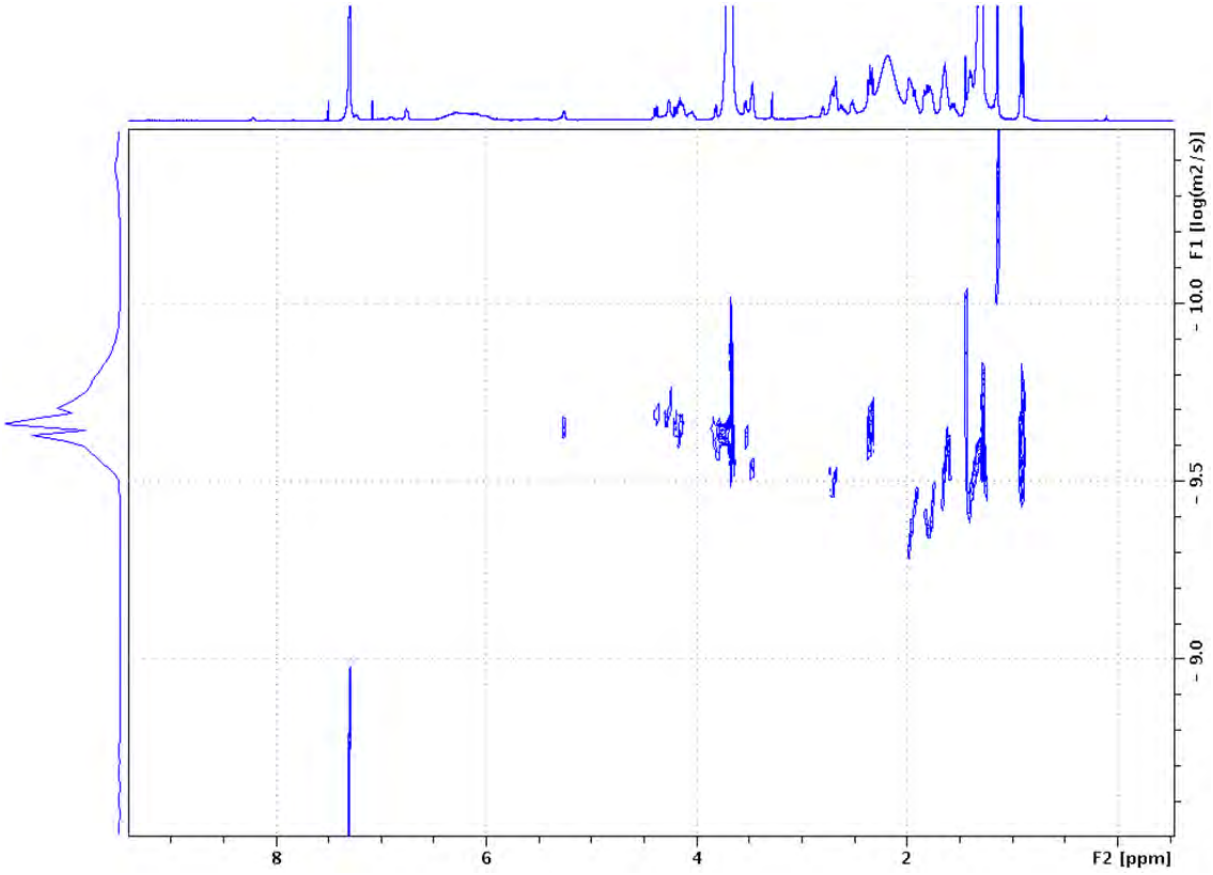

Fig. 4.6. a) ^{1}H-^{1}H COSY spectrum and **b)** 2D DOSY NMR spectrum of DSPE-PEG(2000)-Pt(IV) in $CDCl_3$.

XPS studies at the Pt 4f region unequivocally confirm that the oxidation state of the prodrug remained Pt(IV) after the phospholipid conjugation showing the characteristics Pt($4f_{7/2}$) and Pt($4f_{5/2}$) peaks at 75.5 eV and 78.8 eV respectively (represented by the blue dotted line in **Fig. 4.7)** and the absence of peaks at 72.7 eV and 76.1 eV corresponding to binding energies Pt($4f_{7/2}$) and Pt($4f_{5/2}$) of cisplatin (represented by green dotted line). The peaks obtained are in agreement with previous results published in the literature.[56,57]

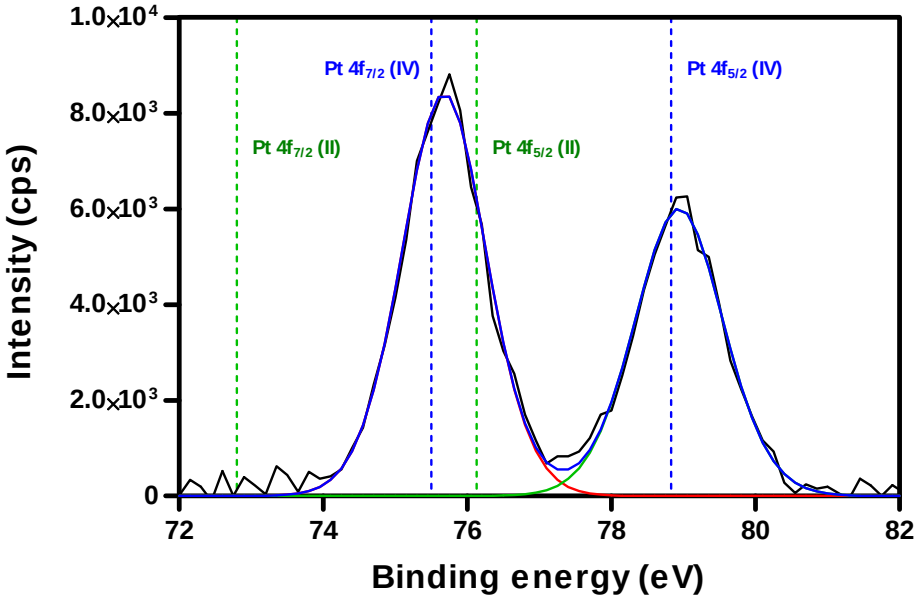

Fig. 4.7. X-ray photoelectron spectrum of DSPE-PEG(2000)-Pt(IV) showing the Pt 4f region.

4.2.1.2 Formation of poly (I:C)-IONP@PL-PEG-Pt(IV) micelles

The protocol followed for the formation of IONP@PL-PEG-Pt(IV) micelles and the addition of the immunostimulatory double stranded RNA poly (I:C) to the micelles is the same as in **Chapter 3.** The only difference was in the ratio between hydrophobic IONP and phospholipid added, because the solubility of the micelle was improved by slightly increasing the amount of PL. The Pt(IV) conjugated PL **2** (2.5 mg) and hydrophobic IONP (1 mg) are dissolved in chloroform (500 µL). The solvent is allowed to evaporate overnight, eliminating any remaining trace of solvent the next day under vacuum for 1 h. After 30 s in a water bath at 80 °C, 1 mL of nanopure water is added. The solution is transferred to an Eppendorf tube and centrifuged at 9500 g for 5 min. The supernatant is passed through a 0.45 µm filter and finally, the solution is centrifuged at 369 000 g for 45 min, 3 cycles to remove the empty micelles. In the final spin the pellet is dissolved in 600 µL of water or PBS (10 mM).

In order to provide optical imaging properties to the system, the rhodamine B-modified PL (Rhod) was incorporated during the evaporation step as in **Chapter 3** (25 µL of a 2mg/mL in $CHCl_3$ solution).

The attachment of poly (I:C) onto IONP@PL-PEG-Pt(IV) micelles is performed by a non-covalent approach following the same procedure that in **Chapter 3** with the only difference of carrying out all the protocol in the darkness to avoid the photoreduction of Pt (IV) complex. The general strategy for the assembly of poly (I:C)-IONP@PL-PEG-Pt(IV) micelles is represented in **Scheme 4.2.**

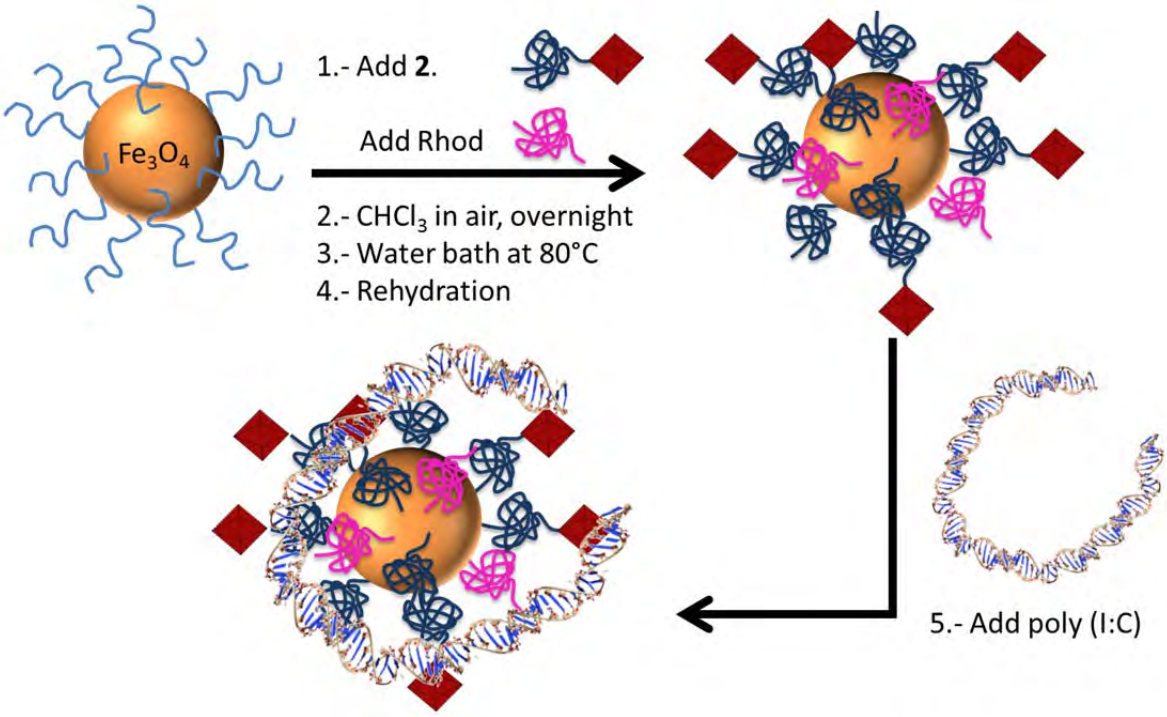

Scheme 4.2. Strategy for the construction of poly (I:C)-IONP@PL-PEG-Pt(IV) micelles.

TEM images **(Fig. 4.8)** and DLS measurements **(Fig. 4.10b)** were used to determine the size of the poly (I:C)-IONP@PL-PEG-Pt(IV) micelles . Both techniques are in concordance with an average hydrodynamic diameter of ca. 40 nm. The size of the micelles after the addition of poly (I:C) did not change significantly, since the high Fe/poly (I:C) ratio is preserved in the preparation of these poly (I:C)-IONP@PL-PEG-Pt(IV) micelles as in **Chapter 3**.

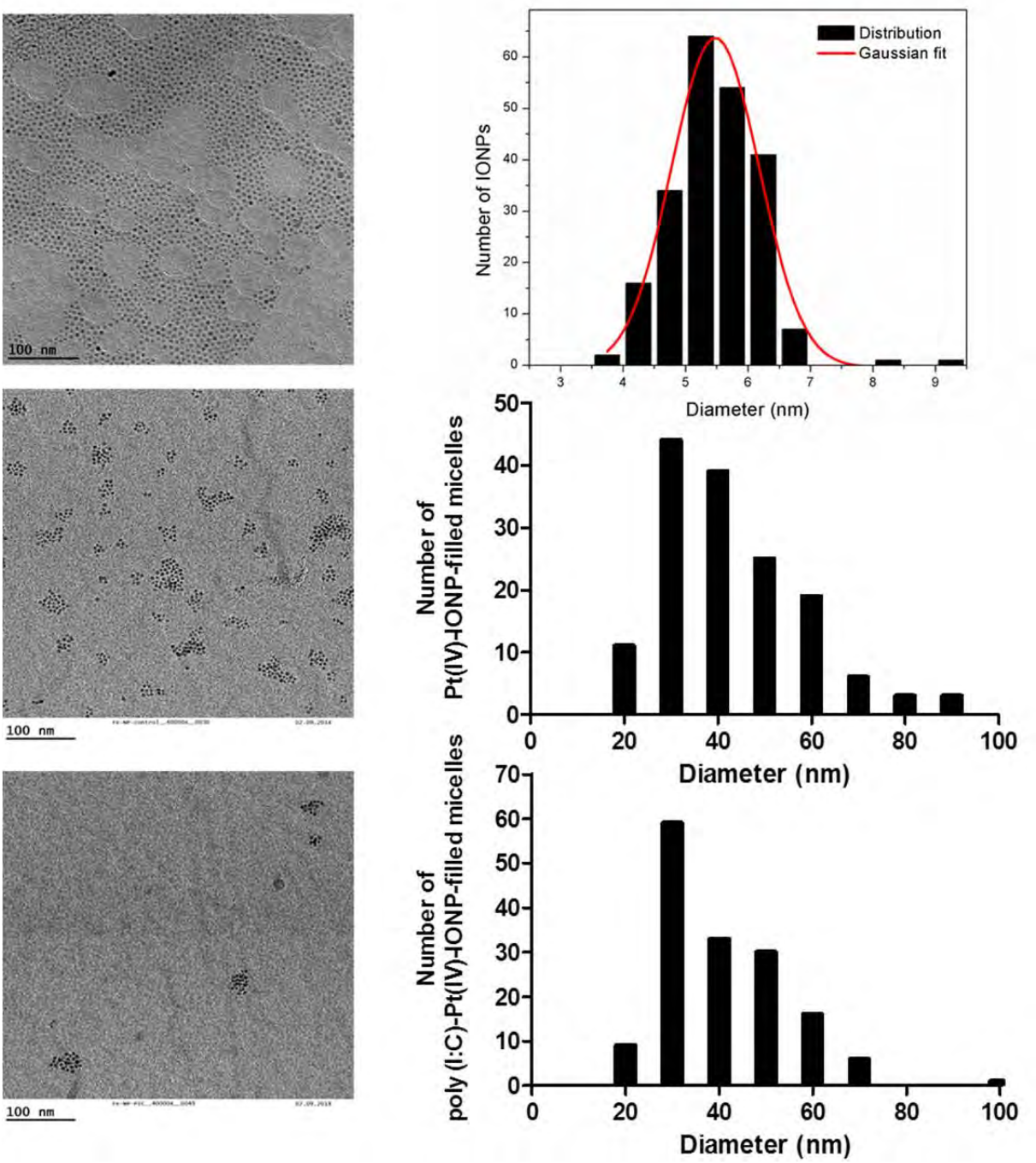

Fig. 4.8. Representative TEM images and size-histogram of hydrophobic IONPs (top), IONP@PL-PEG-Pt(IV) micelles (middle) and poly (I:C)-IONP@PL-PEG-Pt(IV) micelles (bottom).

The ICP-MS studies were essential to determine not only the amount of Fe and Pt present in the micelles but also for the calculations of the amount of Pt(IV) prodrug molecules present in each micelle. In **Table 4.1** four representative constructions with the corresponding concentration of Fe and Pt measured in each one are shown, as well as the calculated ratio of Pt per micelle, resulting than each IONP@PL-PEG micelle is able to carry

an average of 75 Pt(IV) prodrug molecules each. Analyzing the values of **Table 4.1** is noteworthy that the Fe/Pt ratio in each preparation is quite stable (approximately 1 mM Fe/20 μM Pt), being therefore, a very reproducible synthesis.

The number of molecules of **1** per IONP micelle was calculated as follows, based on the use of spherical hydrophobic IONPs (magnetite, Fe_3O_4) with an average diameter of = 5.47 ± 0.69 nm **(Fig. 4.8):**

$V(IONP)= 4/3 \cdot \pi \cdot r^3 = 4/3 \cdot \pi \cdot (2.75 \times 10^{-7})^3 = 0.8711 \times 10^{-19}$ cm^3

ρ (magnetite) = 5.17 g·cm^{-3}/ m = ρ (magnetite) · V(IONP) = 4.5038×10^{-19} g

moles of Fe_3O_4= m / MW (Fe_3O_4) = 4.5038×10^{-19} g/ 231.4 = 1.9463×10^{-21}

moles of Fe = 3 · moles of Fe_3O_4 = 3 · 1.9463×10^{-21}= 5.8389×10^{-21}

atoms of Fe per IONP = moles Fe in IONP · N_A = $5.8389 \times 10^{-21} \cdot 6.022 \times 10^{23}$ = 3516

If each IONP contains 4296 atoms of Fe, the [IONP] = [Fe] / atoms of Fe

IONP@PL-PEG-Pt(IV) micelles	ICP analysis		Calculations	
	[Fe] (mM)	**[Pt] (μM)**	**[IONPs](nM)**	**[Pt]/[IONPs]**
1	5.15	89.32	1465.73	60.94
2	2.95	63.69	839.02	75.91
3	4.43	110.5	1259.95	87.70

Table 4.1. Representative ICP-MS studies of three different batches of IONP@PL-PEG-Pt(IV) micelles prepared and measured at different time. It is reflected the amount of Fe and Pt obtained in each preparation.

Although the preparation of the poly (I:C)-IONP@PL-PEG-Pt(IV) micelles was always carried out in the dark, XPS studies are performed to corroborate that the oxidation state of the prodrug Pt(IV) remained in the final product as is represented in **Fig. 4.9**. As it was expected, the peaks at Pt 4f region at 75.5 eV and 78.8 eV corresponding to Pt($4f_{7/2}$) and Pt($4f_{5/2}$) respectively, confirm the Pt(IV) oxidation state even after the micelle formation. The XPS Fe 2p spectrum is also represented for the same sample in **Fig. 4.9** showing the characteristic spinel peak of Fe $2p_{3/2}$ narrower and stronger than the Fe $2p_{1/2}$ ca. 712 eV and 726 eV respectively. The difference between these peaks fits on the difference in energy between the doublet peaks for iron oxides of 13.6 eV.[58]

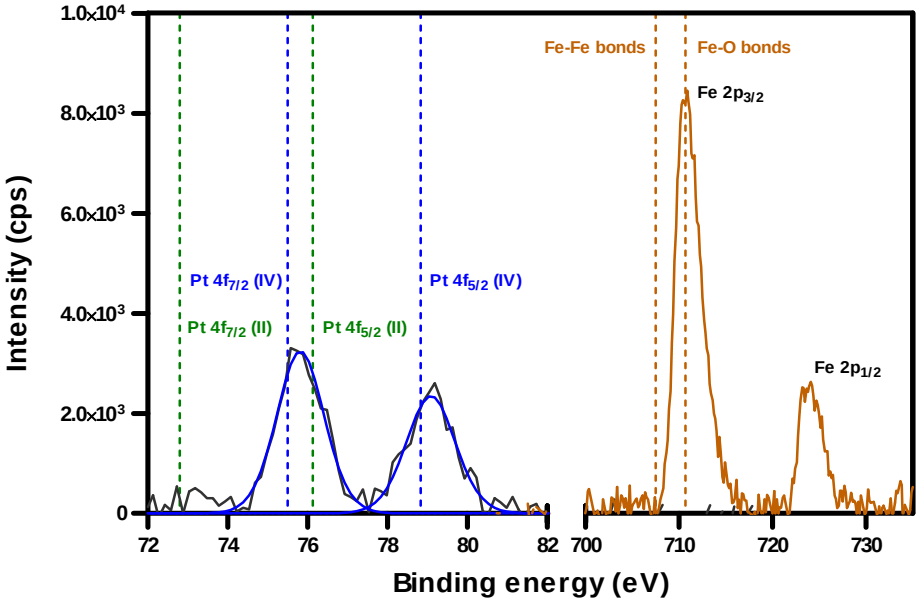

Fig. 4.9. XPS spectrum of the poly (I:C)-IONP@PL-PEG-Pt(IV) micelles showing the Pt 4f and Fe 2p peaks.

After the addition of poly (I:C) to IONP@PL-PEG-Pt(IV) micelles it is necessary to verify if the molecule retains the dsRNA structure as in the case of the micelles without Pt(IV) prodrug conjugated. In the UV spectra **(Fig. 4.10)** when the contribution of the micelle is removed from the poly (I:C)-IONP micelles absorbance, the characteristic peaks at 245 nm and 267 nm corresponding to each poly (I:C) chain are clearly visualized. The amount of poly (I:C) interacting with IONP@PL-PEG-Pt(IV) micelles was quantified by UV absorbance after hydrolyzing overnight and by comparison to a standard curve of hydrolyzed poly (I:C). As expected, there were not notable differences from previous studies.

The size and the surface properties can modify the circulation time of the nanoparticle inside the tumor, thus it is important to continue monitoring these two features of the NPs. The system has a negative charge before and after addition of poly (I:C), ranging from -6 to -9 mV as it is shown in **Fig. 4.10c**. The little change in the zeta potential value is in concordance with the value obtained in **Fig. 3.9** of Chapter 3, due to the small amount of nucleic acid added.

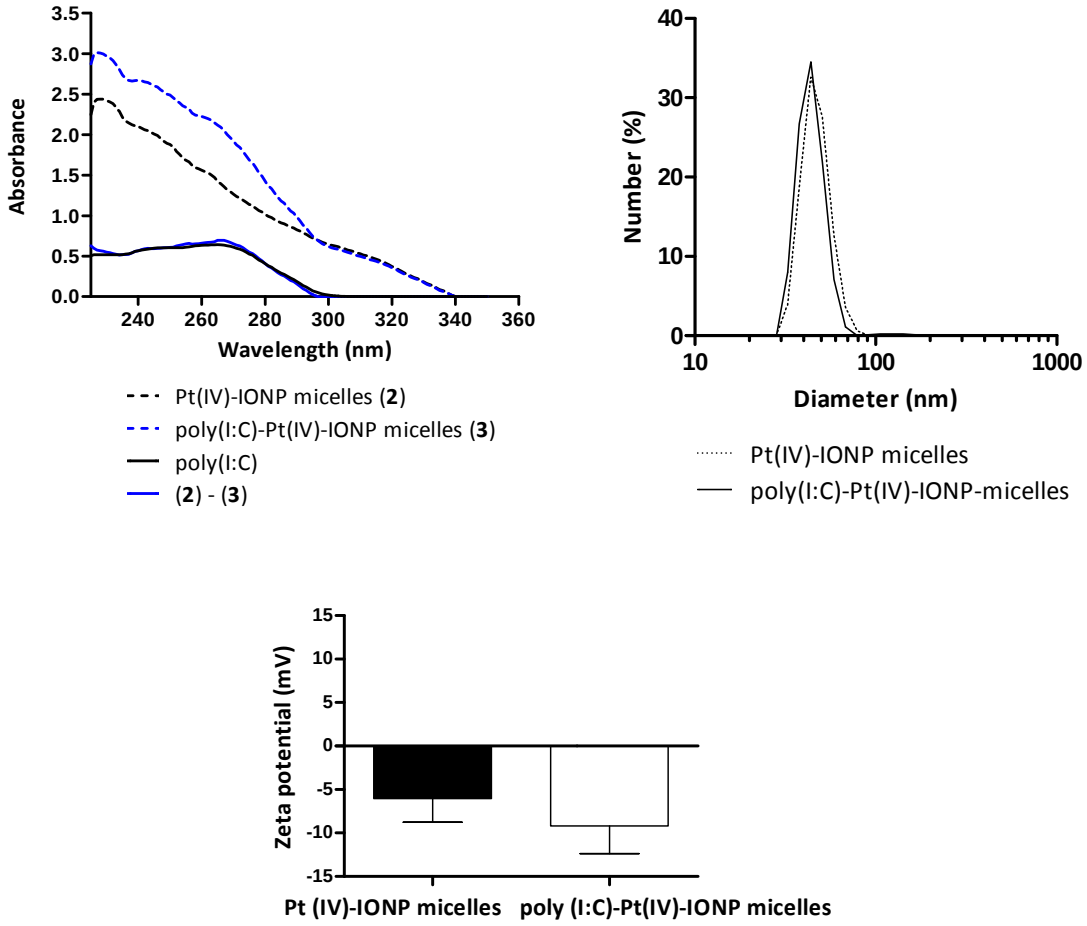

Fig. 4.10. Characterization of poly (I:C)-IONP@PL-PEG-Pt(IV) micelles by UV and DLS. **a)** UV absorbance spectra of IONP@PL-PEG-Pt(IV) micelles, poly (I:C) and poly (I:C)-IONP@PL-PEG-Pt(IV) micelles before and after subtracting the contribution of the IONP@PL-PEG-Pt(IV) component. **b)** Size distribution by DLS of IONP@PL-PEG-Pt(IV) micelles and poly (I:C)-IONP@PL-PEG-Pt(IV) micelles. **c)** Zeta potential of IONP@PL-PEG-Pt(IV) micelles and poly (I:C)-IONP@PL-PEG-Pt(IV) micelles.

4.2.2 *In vitro* and *in vivo* behavior of poly (I:C)-IONP@PL-PEG-Pt(IV) micelles

4.2.2.1 Cytotoxic activity of poly (I:C)-IONP@PL-PEG-Pt(IV) micelles in human cancer cell lines

The ability of poly (I:C)-IONP@PL-PEG-Pt(IV) micelles to kill different human cancer cells is evaluated in three cell lines representative of three cancer types with high

percentage in cancer incidence and mortality and in which cisplatin is frequently used as therapeutic drug. A prostate cancer cell line: PC3, a breast cancer cell line: MDA-MB 231 and a pancreatic cancer cell line: PANC-1.

Firstly the range of concentrations in which the vehicle itself (IONP@PL-PEG methoxy micelles) is not cytotoxic is analyzed. The cells are incubated with IONP@PL-PEG methoxy micelles in a range of iron concentration of 50-400 μM Fe (2.8-22.2 μg/mL Fe) for 72 h. Then, the supernatants are removed and the Sulforhodamine B colorimetric (SRB) assay (procedure described in the experimental part) is used to evaluate the cytotoxicity of the samples. In the cancer cells studied, the viability of IONP@PL-PEG methoxy micelles is higher than 90 % up to an iron concentration of 250 μM Fe (13.8 μg/mL Fe) and never below to 80 % in the full range **(Fig. 4.11a).**

Fig. 4.11b shows the cytotoxicity values of free poly (I:C) found after 72 h of incubation with the three cancer cell lines mentioned. As shown in the figure, only PC3 cell line is sensitive to poly (I:C) treatment, with an IC_{50} value of 15 μg/mL poly (I:C). In the studies performed for MDA-MB 231 and PANC-1 cells even at the highest concentration tested of 200 μg/mL poly (I:C) the dsRNA has negligible cytotoxicity. Our measurements in PC3, MDA-MB 231 and PANC-1 cell lines, together with the study of Van *et al.*[59] (48 h incubation, OVCAR-3 cell line) are the only examples where is possible to determine the IC_{50} value for poly (I:C) reported so far in the literature.

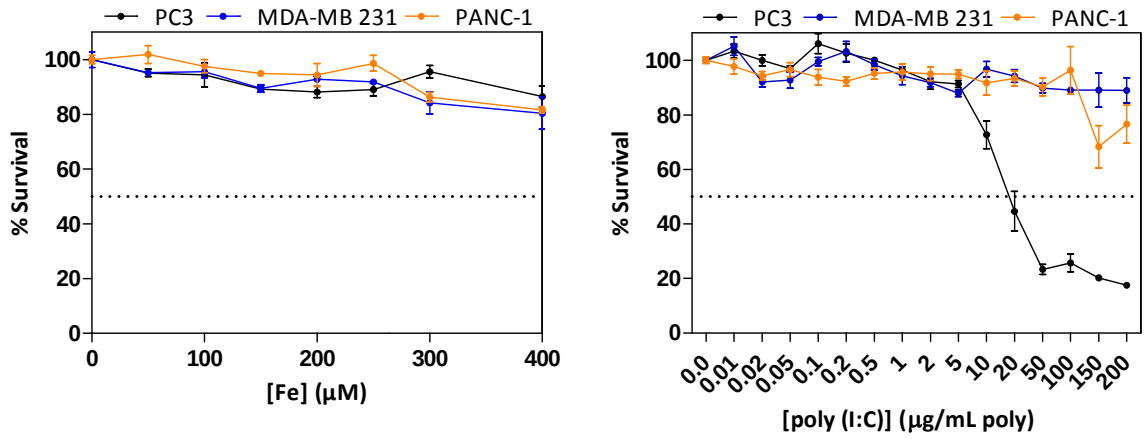

Fig. 4.11. Cytotoxicity profiles of the **a)** drug delivery vehicle (IONP@PL-PEG methoxy micelles) and **b)** poly (I:C) in PC3, MDA-MB 231 and PANC-1 cells.

Then, the capability of the IONP@PL-PEG-Pt(IV) micelles and poly (I:C)-IONP@PL-PEG-Pt(IV) micelles to release the Pt(II) cytotoxic payload upon intracellular reduction of Pt(IV) prodrug was evaluated. As **Fig. 4.12** shows the cells are incubated with Pt(IV) prodrug **(1),** cisplatin, IONP@PL-PEG-Pt(IV) micelles and poly (I:C)-IONP@PL-PEG-Pt(IV) micelles for 72 h. In the range of platinum concentrations studied (up to 15 µM), the cytotoxicity of the two different drug-loaded IONP micelles against each of the cell lines is compared to free cisplatin and Pt(IV) prodrug **(1).** The IC_{50} values achieved for IONP@PL-PEG-Pt(IV) micelles and poly (I:C)-IONP@PL-PEG-Pt(IV) micelles are comparable to each other and similar to those of cisplatin control as it is summarized on **Table 4.2.** The IC_{50} values of IONP@PL-PEG-Pt(IV) micelles and poly (I:C)-IONP@PL-PEG-Pt(IV) micelles in PC3, MDA-MB 231 and PANC-1 cell lines were 8.0 ± 0.9, 6.2 ± 0.2, 5.2 ± 1.5 µM Pt and 7.5 ± 0.3, 7.3 ± 0.3, 8.2 ± 2.5 µM Pt, respectively. The cytotoxic effect of IONP@PL-PEG-Pt(IV) micelles and poly (I:C)-IONP@PL-PEG-Pt(IV) micelles is attributed to the acidic intracellular environment in cancer cells which facilitates the reduction of Pt(IV) compound and the intracellular release of cisplatin.[60] These IC_{50} values are approximately from 60 to 100-fold lower than those of Pt(IV) prodrug **(1)** (above 500 µM Pt in the three cell lines), finding that the cell-killing ability of the prodrug was improved probably due to the high cellular uptake of the micelles compared to free prodrug, as has been found in other Pt(IV)-NP systems.[42,44,61] Thus, it was decided to determine the platinum content in PC3 cells by ICP-MS after the cells were incubated with **(1)** or the Pt-containing micelles ([Pt] = 10×10^{-6} M) for 6 h. Whilst no detectable levels of

Pt could be found in cells treated with **(1)**, the platinum uptake derived from the Pt-containing micelles was 50–60 ng Pt/10^6 cells, demonstrating the effect of the systems promoting Pt(IV) prodrug uptake.

	IC_{50} (μM)		
	PC3	**MDA-MB 231**	**PANC-1**
Pt (IV) prodrug (1)	> 500	> 500	> 500
Cisplatin	5.0 ± 0.7	10.0 ± 0.5	7.6 ± 0.5
IONP@PL-PEG-Pt(IV) micelles	8.0 ± 0.9	6.2 ± 0.2	5.2 ± 1.5
Poly(I:C)-IONP@PL-PEG-Pt(IV) micelles	7.5 ± 0.3	7.3 ± 0.3	8.2 ± 2.5

Table 4.2. Comparison of IC_{50} values based on the Pt concentration of Pt(IV) prodrug **(1)**, cisplatin, IONP@PL-PEG-Pt(IV) micelles and poly (I:C)-IONP@PL-PEG-Pt(IV) micelles against PC3, MDA-MB 231 and PANC-1 cancer cells after 72h of incubation.

The presence of poly (I:C) does not increase the cytotoxic activity of IONP@PL-PEG-Pt(IV) micelles, but its capability to kill cancer cells has not been reduced or inhibited for its presence. This result is an important and encouraging finding of this work. Firstly, because the presence of poly (I:C) is required for the stimulation of cells of the immune system and thereby achieve the combination of targeted chemotherapeutic and immunotherapeutic proposal. And secondly, because both systems are able to retain the chemotherapeutic efficacy *in vitro* with presumably fewer systemic side effects than cisplatin, as it was found so far in other Pt(IV)-NP constructs.[62]

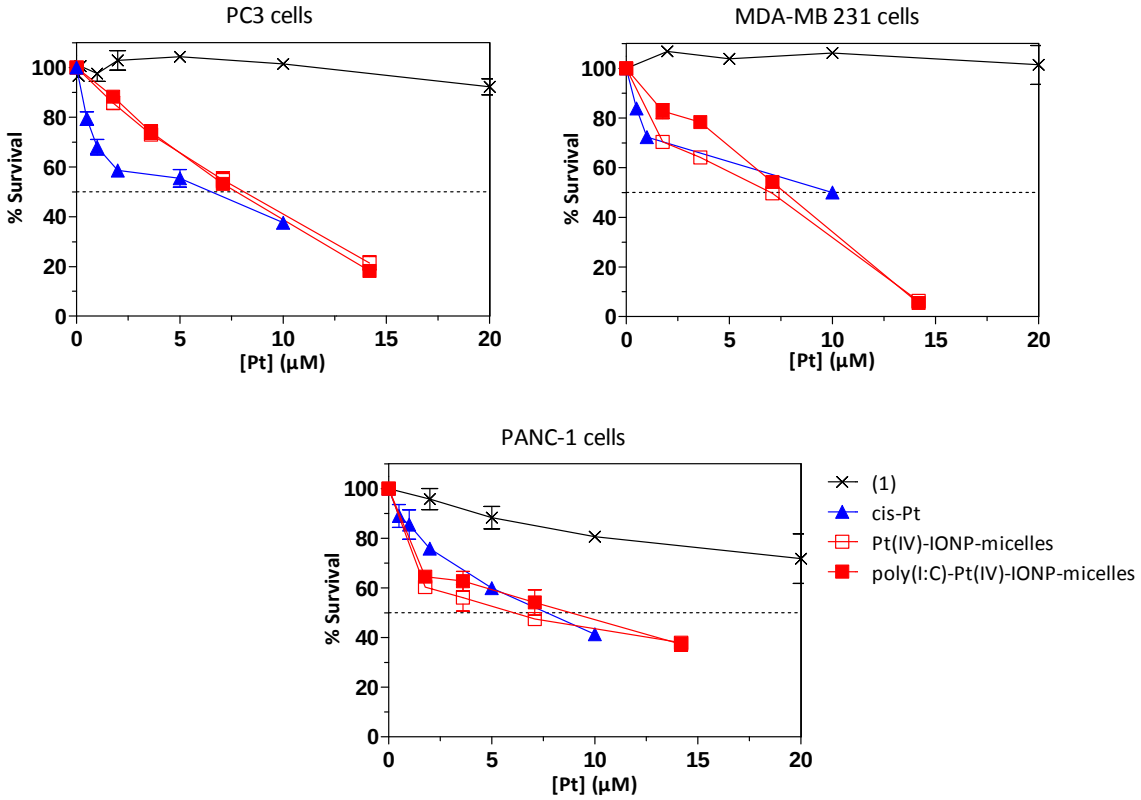

Fig. 4.12. Cytotoxicity profiles of Pt(IV) prodrug, cisplatin, IONP@PL-PEG-Pt(IV) micelles and poly (I:C)-IONP@PL-PEG-Pt(IV) micelles in **a)** PC3, **b)** MDA-MB 231 and **c)** PANC-1 cells.

4.2.2.2 Immunostimulatory activity of poly (I:C)-IONP@PL-PEG-Pt(IV) micelles in cells of the immune system

Dendritic cells (DCs) (as the most potent APCs) were selected to study the capability of poly (I:C)-IONP@PL-PEG-Pt(IV) micelles to activate the immune system and thus to analyze if the prepared nanoconstruct provides the adequate signals to activate innate immune responses. As it was previously explained the maturation of DCs leads to the generation of an antigen specific T cell response. The effective function of DCs depends on the ability to present sufficient amount of antigen, express costimulatory molecules and secrete proinflammatory cytokines, such as interleukin (IL)-12.[63] The IL-12 production and DCs maturation are analyzed after 24 h of incubation of BMDCs with the different nanoconstructs and free compounds as they are represented in **Fig. 4.13** and **Fig. 4.15**, respectively.

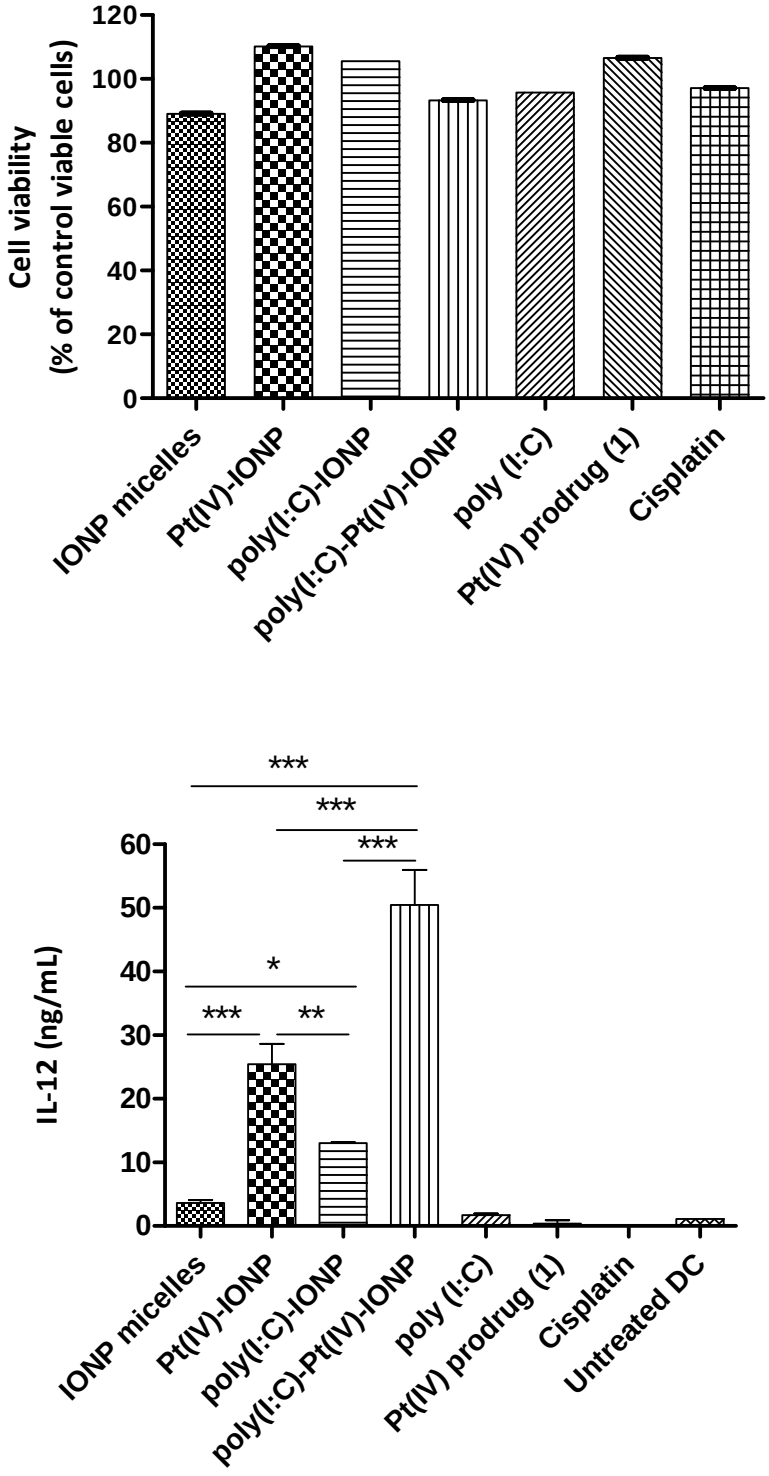

Fig. 4.13. Cell viability and IL-12 production mediated by BMDCs after stimulation for 24h with the different nanoconstructs and free compounds. [Fe]= 100 µM, [Pt]= 3.3 µM, [poly (I:C)]= 10 µg/mL. Data are represented as mean ± SD. The statistical significance of the differences between stimulation with the nanoconstructs was analyzed by one-way ANOVA followed by Tukey´s test (* = $P < 0.05$, ** = $P < 0.01$, *** = $P < 0.001$).

The cell viability results show that at the concentrations studied of [Fe]= 100 µM (5.6 µg/mL Fe), [Pt]= 3.3 µM, [poly (I:C)]= 10 µg/mL the viability of the BMDCs is always higher than 90%. The addition of Pt(IV) prodrug **(1)** and/or poly (I:C) to IONP micelles does not affect the survival of the cells of the immune system, which is one of the prerequisites to consider poly (I:C)-IONP@PL-PEG-Pt(IV) micelles as an effective immunotherapeutic drug.

Fig. 4.13b shows that stimulation with poly (I:C)-IONP@PL-PEG methoxy micelles induces IL-12 production with values of 13 ng/mL. Notably, IONP@PL-PEG-Pt(IV) micelles also increase the secretion of cytokines compared to cisplatin and the inert Pt(IV) prodrug **(1),** for which cytokine values are practically negligible**.** However, it is worthy to be highlighted that the amount of cytokines secreted by IONP@PL-PEG-Pt(IV) micelles compared to poly (I:C)-IONP@PL-PEG-Pt(IV) micelles is more than 2-fold higher, obtaining 28 ng/mL of IL-12 and compared with free poly (I:C), the production of cytokine is 10-fold higher with a value ca. 2 ng/mL. The control of IONP micelles suggests that the production of IL-12 by IONP@PL-PEG-Pt(IV) micelles is due to the Pt(IV) cargo. Although other research groups have published the chemotherapeutic effect of NP-Pt(IV) systems, the effect of the platinum drugs on immune cells has not been studied in detail.[64] These studies have focused mainly in the increase of the Pt uptake and the enhanced cytotoxicity helped by the delivery system in cancer cells, but not in the potential immune effect of the Pt(IV)-IONP micelles over the free platinum drug.

To study the uptake and fate of poly (I:C)-IONP@PL-PEG-Pt(IV) micelles in BMDCs two microscopy assays using micelles labeled with rhodamine B were performed. By live cell microscopy, it was possible to colocalize the system poly (I:C)-IONP@PL-PEG-Pt(IV) micelles with the endosomal compartments stained with Lysotracker. In the second assay, to ensure that the system can reach the TLR3 receptors inside the endosomes, an anti-TLR3 primary antibody and Alexa 488-labeled secondary antibody were used. Using fixed cells the colocalization of the poly (I:C)-IONP@PL-PEG-Pt(IV) micelles with the TLR3 receptors was achieved as it is shown in **Fig. 4.14**.

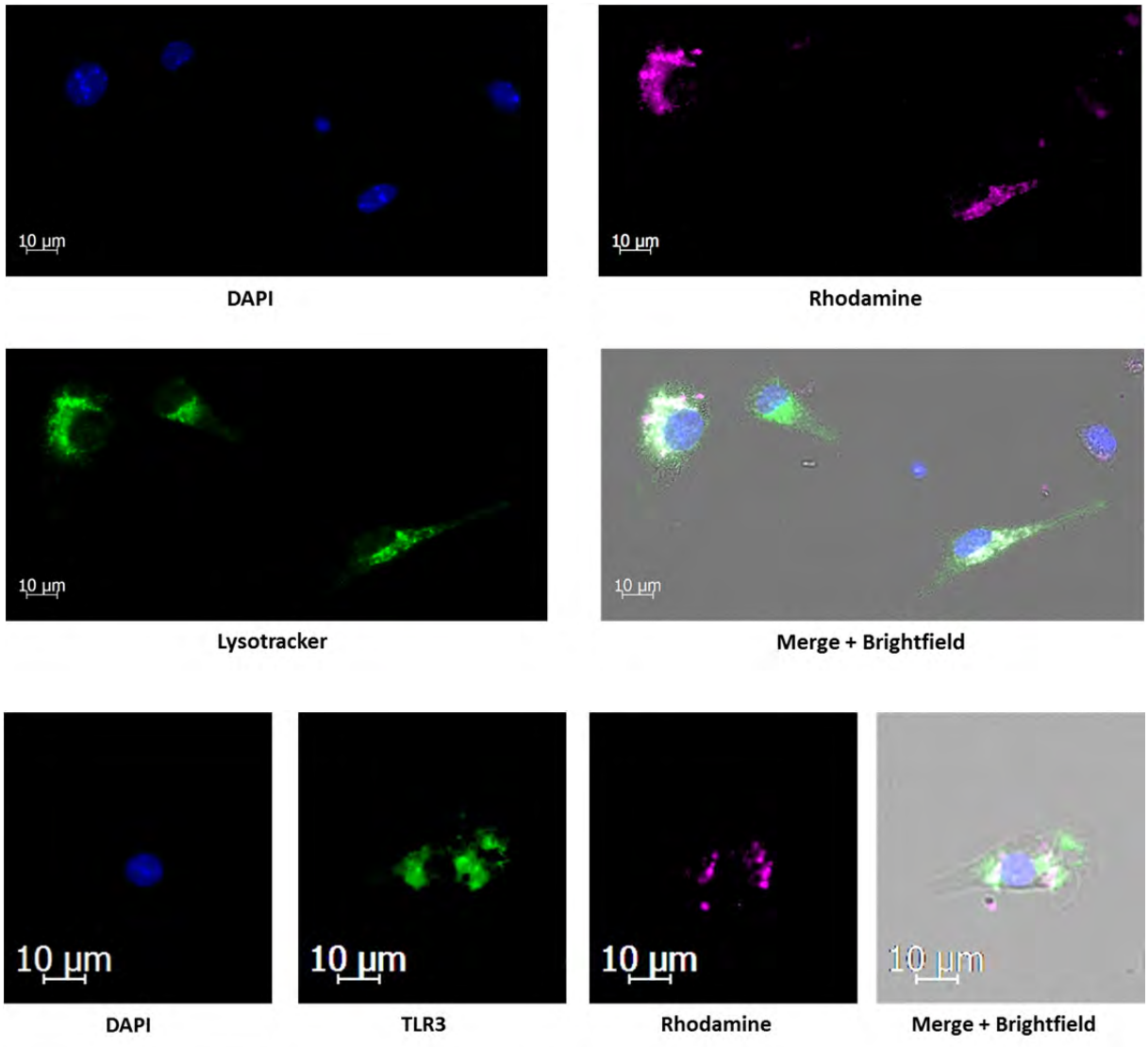

Fig. 4.14. Trafficking of poly (I:C)-IONP@PL-PEG-Pt(IV) micelles labeled with rhodamine B in BMDCs after 1 h of incubation.

Among several signals involved in T cell mediated immune responses against tumors, in this work it was decided to analyze the expression of the following specific markers: CD80, CD86 (costimulatory molecules), IA/IE (MHC class II) and CCR7 (chemokine receptor favoring the migration of DC to lymphoid organ) by flow cytometry.

The costimulatory molecules CD80 and CD86 are expressed on APCs, including DCs and macrophages.[65] When CD80 or CD86 bind to a specific receptor on T cell (CD28), the signal produced results in T cell proliferation.

CCR7 controls lymphocyte migration to secondary lymphoid organs. CCR7 is activated by two chemokines expressed by matured DCs (CCL19 and CCL21). These chemokines are important for the coordination of the adaptive immune responses between DCs, B cells and T cells and they function as mediators of the inflammatory response. CCR7 is also expressed by tumor cells, and recent studies have shown that CCR7 promotes the migration of tumor cells to draining lymph nodes, favoring the appearance of metastasis. [66] So, CCR7 may contribute to tumor cell lymph node localization.[67]

During the maturation process, DCs upregulate on their surface a major histocompatibility complex (MHC) class II molecules. MHC class II molecules present antigens to $CD4^+$ T-helper cells, which are involved in the differentiation of B cells in antibody producing B-cells and in the activation of $CD8^+$ T cytotoxic cells. Thus, they play an essential function in the activation of adaptive immune responses and induction of memory responses.[68]

To determine the capacity of the nanoconstructs to activate DCs, *in vitro* assays were carried out in BMDCs with the delivery systems and their corresponding controls to analyze the expression of these relevant molecules in the process of antigen presentation.

After the incubation of the nanoconstructs with BMDCs for 24 h, there were noticeable differences in the maturation induced by different NPs constructs compared to the maturation observed in untreated DCs **(Fig. 4.15)**. It is necessary to consider that the mechanical stimulation during the manipulation of BMDCs provides a background signal in the costimulatory molecules tested. The presence of poly (I:C) and platinum drug induces an increase in the expression of CD80 and CD86 compared with IONP micelles. The expression level of CD80 and CD86 are clearly enhanced in the presence of poly (I:C)-IONP@PL-PEG micelles and IONP@PL-PEG-Pt(IV) micelles and especially in the presence of poly (I:C)-IONP@PL-PEG-Pt(IV) micelles. This result suggests that poly (I:C) and platinum drug, and particularly the combination of both in one only system could stimulate DCs to activate more efficiently $CD4^+$ and $CD8^+$ T-cell-mediated immune responses.

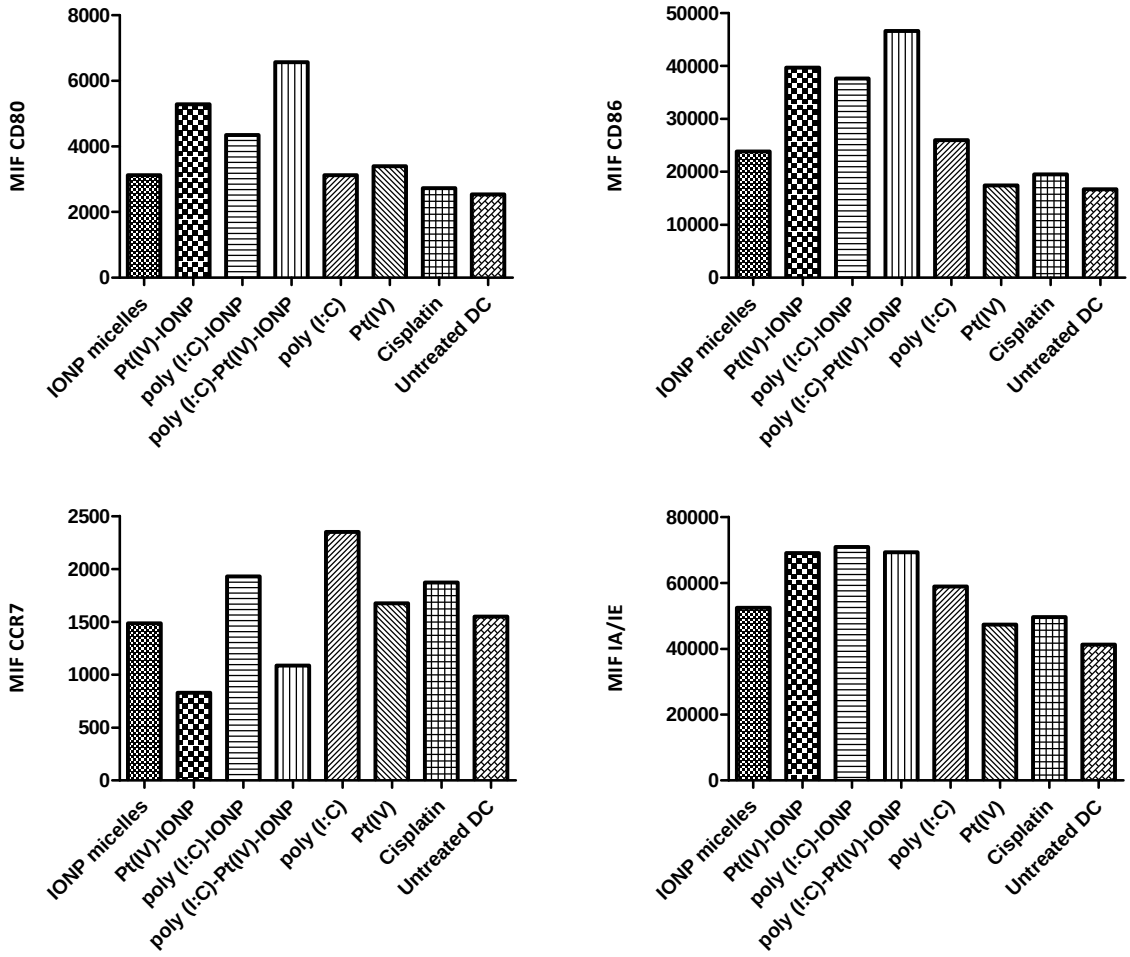

Fig. 4.15. Analysis of the markers expression in the antigen presentation process after 24 h of incubation with all the nanoconstructs at [Fe]= 100 μM, [Pt]= 3.3 μM, [poly (I:C)]= 10 μg/mL in BMDCs.

As shown in **Fig. 4.15,** the highest increase in the expression levels of CCR7 was induced after stimulation with free poly (I:C) followed by poly (I:C)-IONP@PL-PEG micelles. However, the stimulation of DCs with IONP@PL-PEG-Pt(IV) micelles and poly (I:C)-IONP@PL-PEG-Pt(IV) micelles reduces the expression of CCR7 compared to those constructs without platinum attached. Although it may seem a negative effect on the cells of the immune system, the inhibition of CCR7 expression on tumor cell could be beneficial as tumor cells with lower expression levels of CCR7 would have less capacity to migrate to lymph nodes (i.e. to metastasize).

In general, all the treatments induced a slight increase in the expression of MHC class II molecules compared to untreated cells. The NPs functionalized with poly (I:C) and /or Pt(IV) prodrug **(1)** induce the greatest increase in the expression of this molecule, although the combination of both drugs does not promote higher expression of MHC class II molecules than the singly functionalization. However, the increase in the expression of the conjugated nanoconstructs compared to IONP micelles suggests the possibility to generate a T-cell activation with the micelles functionalized.

4.2.2.3 Immunostimulatory activity of poly (I:C)-IONP@PL-PEG-Pt(IV) micelles *in vivo*

The ability of poly (I:C)-IONP@PL-PEG methoxy micelles and poly (I:C)-IONP@PL-PEG-Pt(IV) micelles and their corresponding controls to activate an immune response was also assessed *in vivo* in mice models by studying the efficacy of activation of NK cells and DCs. The activation of NK cells and the DCs was analyzed by flow cytometry. In the case of NK cells, the expression of CD69 (an early activation marker) was determined and in the case of DCs, the expression of CD80, CD86, IA/IE and CCR7 were explored.

To investigate and analyze the activation of innate immune response, naïve BALB/c mice were immunized with PBS, free poly (I:C) and the two nanoparticles formulation containing poly (I:C) (poly (I:C)-IONP@PL-PEG methoxy micelles and poly (I:C)-IONP@PL-PEG-Pt(IV) micelles) by s.c. administration in the hind limbs (specifically at the hock, 20 µL/ limb). After 24 h mice were sacrificed and inguinal LNs (iLNs, lymph nodes draining the site of injection) and spleens were isolated, dissociated into single cell suspensions (explained in detail in the experimental section) and analyzed by flow cytometry.

As **Fig. 4.16** shows, mice injected with poly (I:C)-IONP@PL-PEG methoxy micelles or poly (I:C)-IONP@PL-PEG-Pt(IV) micelles had a higher activation of the innate response compared with the activation induced by free poly (I:C) in draining LNs. Particularly, in the expression of CD86 and CCR7 both nanoconstructs have shown significant differences compared with free poly (I:C). Thus suggests that targeting an adjuvant as poly (I:C) to the

lymph nodes (see Section 4.2.2.6) via iron oxide nanoparticles (with or without Pt(IV) prodrug conjugated) may be responsible for the enhanced adjuvant efficacy.

There are several immune responses regulated by NK cells, including responses to viral-infected cells and tumours.[69] Although NK cells exhibit natural cytotoxcity against tumor cells, they are involved in several antitumor mechanisms where innate and adaptive immune cells are actively present (cancer immunosurveillance). Tumor cells can be eliminated when NK cells are activated and additionally, NK cells are involved in the maturation process of DCs, which ultimately promote T cell activation and cytotoxic T-cell responses.[70] It has been shown in preclinical models that when potent T-cell responses are induced against a tumor antigen, the rejection of the tumor usually takes place.[71] In **Fig. 4.16** the activation of NK cells is analyzed by the expression of CD69 activation marker. The administration of poly (I:C)-IONP@PL-PEG methoxy micelles or poly (I:C)-IONP@PL-PEG-Pt(IV) micelles produces significant differences in the expression of CD69 compared with control mice, which can be involved in a higher maturation of DCs as it has been discussed above.

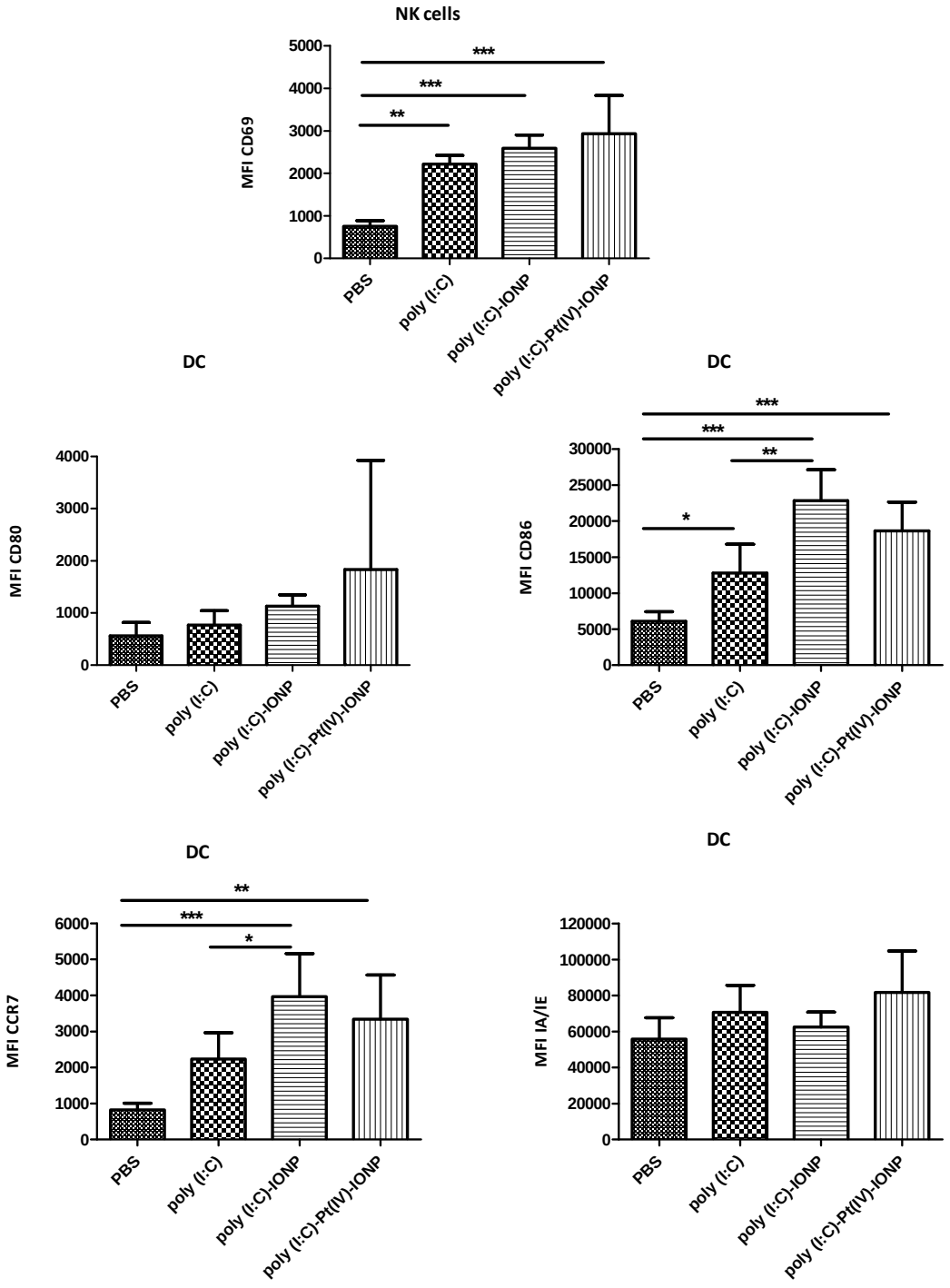

Fig. 4.16. Representative flow cytometry *ex vivo* analysis of CD69 expression on NK cells and CD80, CD86, CCR7 and MHC class II expression on DCs. Mice were immunized s.c. in the lower limbs with 14 µg Fe, 11 µg of poly (I:C) and 0.48 µg of Pt. After 24 h iLNs were harvested and treated as a single cell suspension. Data are presented as mean ± SEM (n=5). The statistical significance was analyzed by one-way ANOVA (*= P < 0.05, **= P < 0.001, ***= P < 0.0001).

The maturation of spleen DCs is assessed as described before and the results are represented in **Fig. 4.17.** As expected, the magnitude of the immune response induced in the LNs was higher than the one induced in the spleens, which confirms the preferential migration from the injection site to the draining LNs through the lymphatic system. Although the difference between the maturation induced by poly (I:C)-IONP micelles and the free adjuvant is not as marked as the observed for the lymph nodes DCs, an increase is observed in the expression of CD86 and CCR7 when mice are immunized with poly (I:C)-IONP@PL-PEG methoxy micelles and poly (I:C)-IONP@PL-PEG-Pt(IV) micelles compared to the maturation induced by free poly (I:C). No differences between the presence or absence of Pt(IV) prodrug **(1)** in the nanoparticle were observed in the markers analyzed.

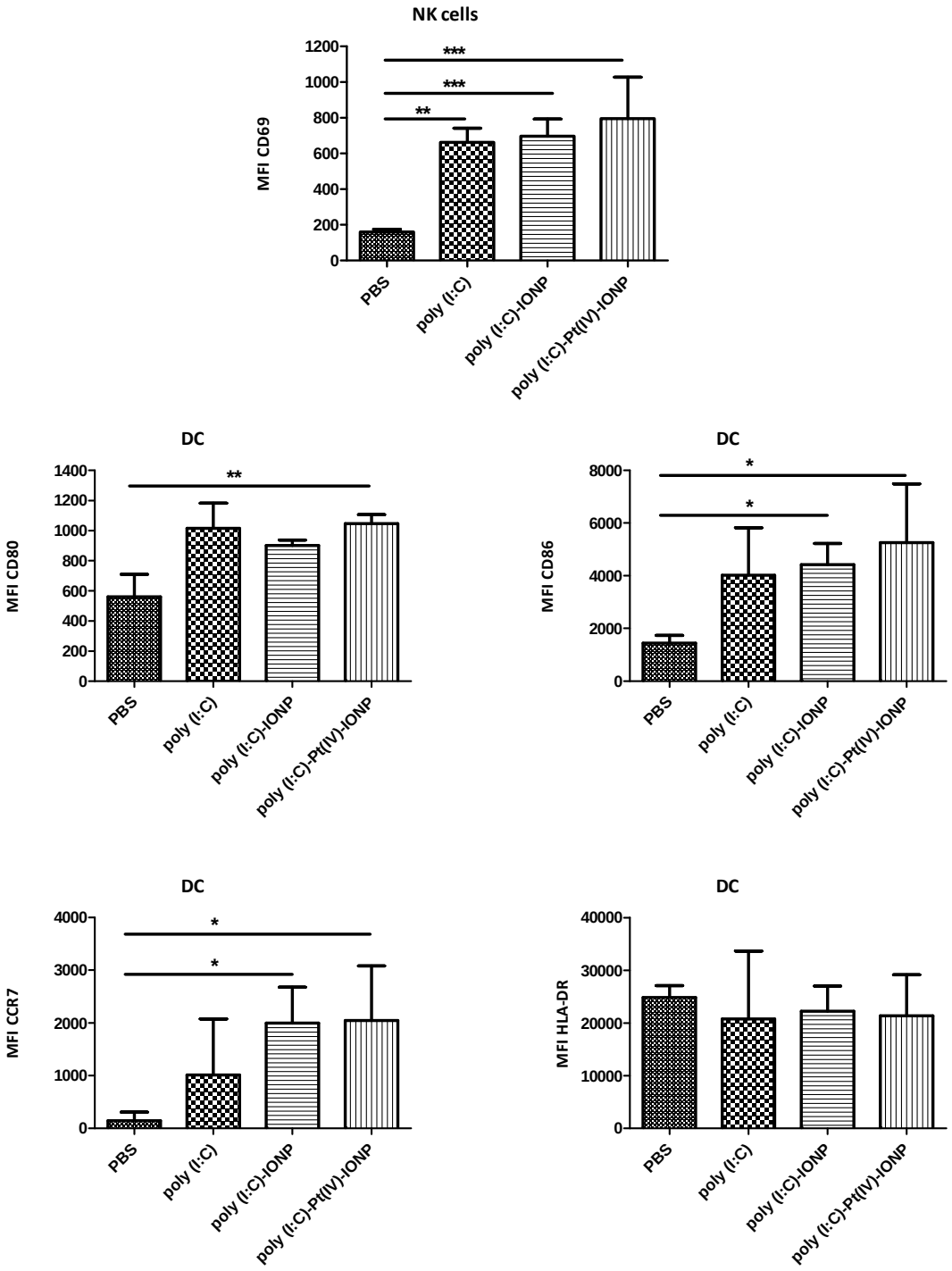

Fig. 4.17. Representative flow cytometry *ex vivo* analysis of CD69 expression on NK cells and CD80, CD86, CCR7 and MHC class II expression on DCs. Mice were immunized s.c. in the lower limbs with 14 µg Fe, 11 µg of poly (I:C) and 0.48 µg of Pt. After 24 h spleens were harvested and treated as a single cell suspension. Data are presented as mean ± SEM (n=5). The statistical significance was analyzed by one-way ANOVA (*= P < 0.05, **= P < 0.001, ***= P < 0.0001).

4.2.2.4 *In vivo* trafficking of poly (I:C)-IONP@PL-PEG-Pt(IV) micelles

The possibility of targeting locoregional and non-regional LNs by subcutaneous (s.c.) administrations in different anatomical regions of mice was investigated by nuclear imaging. poly (I:C)-IONP@PL-PEG-Pt(IV) micelles labeled with ^{99m}Tc tricarbonyl were administrated subcutaneously (s.c.) in the forearm or the hind hock and by intraperiotoneal (i.p). and intratumoral (i.t.) injection.

SPECT/CT studies at 22 h after injection of the drug-loaded micelles are summarized in **Fig. 4.18** showing the migration from the injection site to the draining LNs through the lymphatic system**.** After s.c. administration in the forearms, IONP@PL-PEG-Pt(IV)-poly (I:C) micelles reached the axillary LNs, which are the SLNs in breast cancer. After s.c. injection in the hind hock, poly (I:C)-IONP@PL-PEG-Pt(IV) micelles are able to migrate to inguinal and popliteal LNs. The ability of poly (I:C)-IONP@PL-PEG-Pt(IV) micelles to migrate distant from the site of injection is demonstrated because a clear signal is also detected in the axillary and iliac LNs, according with the pattern of lymphatic drainage from this site.[72]

In the case of i.p. administration of poly (I:C)-IONP@PL-PEG-Pt(IV) micelles a clear accumulation in mediastinal LNs located in the thoracic cavity as well as liver and spleen was observed, also in agreement with the lymphatic drainage routes from the peritoneal cavity and the studies discussed in Chapter 3.[73] This is an important result since many cancers originate from organs in the peritoneal cavity (e.g., ovarian, pancreatic, colorectal, gastric and liver) and their metastasis are difficult to treat.[74]

When PANC-1 cells were s.c. implanted in nude mice for tumor induction, the SPECT/CT studies showed that i.t. administered poly (I:C)-IONP@PL-PEG-Pt(IV) micelles were predominantly retained within the tumor area. Importantly, the poly (I:C)-IONP@PL-PEG-Pt(IV) micelles could also quickly reach the cervical LNs, which are communicated via the lymphatics with the site where the tumor was implanted as is shown in **Fig. 4.18d.** Although this administration route has failed to become an conventional route of administration in routine clinical practice, it offers interesting possibilities for: **i)** enhancing tumor exposure to the drugs to reduce or reject tumors, **ii)** reversing the immunosuppresor tumor environment or **iii)** a direct cytotoxic effect on the tumor cell, which can results in an anti-tumor immune response.[75]

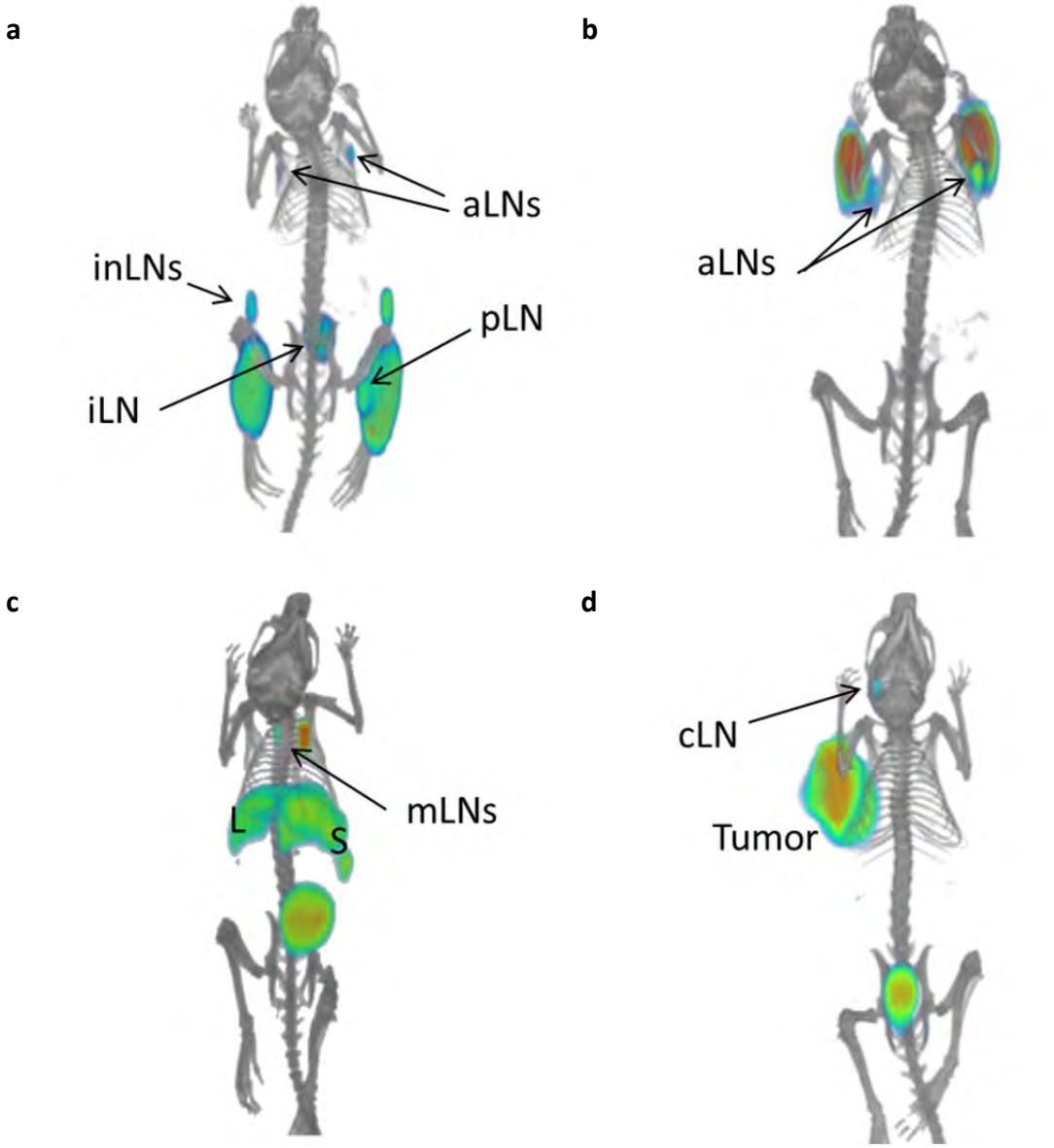

Fig. 4.18. SPECT/CT images of mice injected by different routes with the ^{99m}Tc tricarbonyl-labeled IONP@PL-PEG-Pt(IV)-poly (I:C) micelles 22 h post injection. **(a)** s.c. administration in the forearm, **(b)** s.c. administration in the hind hock, **(c)** i.p. administration and **(d)** i.t. administration at 3 h. aLN, axillar LN; inLN, inguinal LN; iLN, iliac LN; pLN, popliteal LN; mLN, mediastinal LN; cLN, cervical LN, L, liver; S, spleen and Tumor.

4.3 Conclusions

Recent developments in oncology treatments involve the combination of novel immunotherapies with conventional chemotherapeutic drugs. In the work discussed in this chapter a nanocarrier delivers simultaneously chemotherapy and immunostimulatory drugs. A non toxic iron oxide micellar system could be functionalized with a Pt(IV) prodrug and then with an immunostimulatory molecule as a strong vaccine adjuvant (poly (I:C)).

It was demonstrated that the inert Pt(IV) prodrug conjugated with the IONPs becomes a drug as active as cisplatin against several human cancer cell lines and promotes the stimulation of cells of the immune system. Furthermore, after the addition of poly (I:C), the system retains its cancer cell killing properties but remarkably enhances activation of DCs.

The combination of both drugs induces greater activation of the innate immune response than either agent administered singly. The administration of poly (I:C)-IONP@PL-PEG-Pt(IV) micelles induces greater NK cells activation than free adjuvant and it is able to induce higher IL-12 cytokine production mediated by DCs. These constructs also induce higher expression of CD80 and CD86 co-stimulatory molecules in these immune cells.

Imaging studies show that following i.t. admistration the poly (I:C)-IONP@PL-PEG-Pt(IV) micelles are either retained in the tumor site (to enable direct attack on the cancer cells) or escape to the lymph nodes (LNs) draining the tumor site (to potentially orchestrate a tumor specific immune response with the capacity to act on cancer cells at primary tumor and metastatic nodules).

Additional studies are required to further understand the immune effector mechanisms involved and characterize the tumor specific immune response due to the administration of poly (I:C)-IONP@PL-PEG-Pt(IV) micelles *in vitro* and *in vivo*. However, this study highlights that these nanoscaffolds may be promising novel systems to effectively deliver chemotherapeutic and immunologically active components to target sites and promote direct cancer cell killing and activation of specific signaling pathways in immune cells to generate an antitumor T-cell responses.

References

1. Ferlay, J. *et al.* Cancer incidence and mortality worldwide: sources, methods and major patterns in GLOBOCAN 2012. *Int. J. Cancer* **136,** E359–86 (2014).

2. Jemal, A. *et al.* Global cancer statistics. *CA. Cancer J. Clin.* **61,** 69–90 (2011).

3. Blackwell, K. L. *et al.* Overall survival benefit with lapatinib in combination with trastuzumab for patients with human epidermal growth factor receptor 2-positive metastatic breast cancer: final results from the EGF104900 Study. *J. Clin. Oncol.* **30,** 2585–92 (2012).

4. Chen, G. & Emens, L. A. Chemoimmunotherapy: reengineering tumor immunity. *Cancer Immunol. Immunother.* **62,** 203–16 (2013).

5. Emens, L. A. Chemoimmunotherapy. *Cancer J.* **16,** 295–303 (2010).

6. De Biasi, A. R., Villena-Vargas, J. & Adusumilli, P. S. Cisplatin-induced antitumor immunomodulation: a review of preclinical and clinical evidence. *Clin. Cancer Res.* **20,** 5384–91 (2014).

7. Hato, S. V, Khong, A., de Vries, I. J. M. & Lesterhuis, W. J. Molecular pathways: the immunogenic effects of platinum-based chemotherapeutics. *Clin. Cancer Res.* **20,** 2831–7 (2014).

8. Banchereau, J. *et al.* Immunobiology of dendritic cells. *Annu. Rev. Immunol.* **18,** 767–811 (2000).

9. Mellman, I., Coukos, G. & Dranoff, G. Cancer immunotherapy comes of age. *Nature* **480,** 480–9 (2011).

10. Hanke, N., Alizadeh, D., Katsanis, E. & Larmonier, N. Dendritic cell tumor killing activity and its potential applications in cancer immunotherapy. *Crit. Rev. Immunol.* **33,** 1–21 (2013).

11. Adams, S. Toll-like receptor agonists in cancer therapy. *Immunotherapy* **1,** 949–64 (2009).

12. Kaczanowska, S., Joseph, A. M. & Davila, E. TLR agonists: our best frenemy in cancer immunotherapy. *J. Leukoc. Biol.* **93,** 847–63 (2013).

13. Conroy, H., Marshall, N. A. & Mills, K. H. G. TLR ligand suppression or enhancement of Treg cells? A double-edged sword in immunity to tumours. *Oncogene* **27,** 168–80 (2008).

14. Kanzler, H., Barrat, F. J., Hessel, E. M. & Coffman, R. L. Therapeutic targeting of innate immunity with Toll-like receptor agonists and antagonists. *Nat. Med.* **13,** 552–9 (2007).

15. Salaun, B., Lebecque, S., Matikainen, S., Rimoldi, D. & Romero, P. Toll-like receptor 3 expressed by melanoma cells as a target for therapy? *Clin. Cancer Res.* **13,** 4565–74 (2007).

16. McCartney, S. *et al.* Distinct and complementary functions of MDA5 and TLR3 in poly(I:C)-mediated activation of mouse NK cells. *J. Exp. Med.* **206,** 2967–76 (2009).

17. Poon, C., He, C., Liu, D., Lu, K. & Lin, W. Self-assembled nanoscale coordination polymers carrying oxaliplatin and gemcitabine for synergistic combination therapy of pancreatic cancer. *J. Control. Release* **201,** 90–9 (2015).

18. Cheng, Z., Al Zaki, A., Hui, J. Z., Muzykantov, V. R. & Tsourkas, A. Multifunctional nanoparticles: cost versus benefit of adding targeting and imaging capabilities. *Science* **338,** 903–10 (2012).

19. Dreher, M. R. *et al.* Tumor vascular permeability, accumulation, and penetration of macromolecular drug carriers. *J. Natl. Cancer Inst.* **98,** 335–44 (2006).

20. Bertrand, N., Wu, J., Xu, X., Kamaly, N. & Farokhzad, O. C. Cancer nanotechnology: the impact of passive and active targeting in the era of modern cancer biology. *Adv. Drug Deliv. Rev.* **66,** 2–25 (2014).

21. Kerbel, R. S. Tumor angiogenesis: past, present and the near future. *Carcinogenesis* **21,** 505–515 (2000).

22. Carmeliet, P. & Jain, R. K. Angiogenesis in cancer and other diseases. *Nature* **407,** 249–57 (2000).

23. Zetter, B. R. Angiogenesis and tumor metastasis. *Annu. Rev. Med.* **49,** 407–24 (1998).

24. Matsumura, Y. & Maeda, H. A new concept for macromolecular therapeutics in cancer chemotherapy: mechanism of tumoritropic accumulation of proteins and the antitumor agent smancs. *Cancer Res.* **46,** 6387–92 (1986).

25. Maeda, H. & Matsumura, Y. Tumoritropic and lymphotropic principles of macromolecular drugs. *Crit. Rev. Ther. Drug Carrier Syst.* **6,** 193–210 (1989).

26. Hobbs, S. K. *et al.* Regulation of transport pathways in tumor vessels: role of tumor type and microenvironment. *Proc. Natl. Acad. Sci. U. S. A.* **95,** 4607–12 (1998).

27. Bae, Y. H. Drug targeting and tumor heterogeneity. *J. Control. Release* **133,** 2–3 (2009).

28. Jokerst, J. V & Gambhir, S. S. Molecular imaging with theranostic nanoparticles. *Acc. Chem. Res.* **44,** 1050–60 (2011).

29. Davis, M. E., Chen, Z. G. & Shin, D. M. Nanoparticle therapeutics: an emerging treatment modality for cancer. *Nat. Rev. Drug Discov.* **7,** 771–82 (2008).

30. Prabhakar, U. *et al.* Challenges and key considerations of the enhanced permeability and retention effect for nanomedicine drug delivery in oncology. *Cancer Res.* **73,** 2412–7 (2013).

31. Lammers, T., Kiessling, F., Hennink, W. E. & Storm, G. Drug targeting to tumors: principles, pitfalls and (pre-) clinical progress. *J. Control. Release* **161,** 175–87 (2012).

32. Stacker, S. A. *et al.* Lymphangiogenesis and lymphatic vessel remodelling in cancer. *Nat. Rev. Cancer* **14,** 159–72 (2014).

33. Christiansen, A. & Detmar, M. Lymphangiogenesis and cancer. *Genes Cancer* **2,** 1146–58 (2011).

34. Schroeder, A. *et al.* Treating metastatic cancer with nanotechnology. *Nat. Rev. Cancer* **12,** 39–50 (2012).

35. Weinstein, S. J. *et al.* Null association between prostate cancer and serum folate, vitamin B(6), vitamin B(12), and homocysteine. *Cancer Epidemiol. Biomarkers Prev.* **12,** 1271–2 (2003).

36. Kamen, B. Folate and antifolate pharmacology. *Semin. Oncol.* **24,** S18–30–S18–39 (1997).

37. Xia, W. & Low, P. S. Folate-targeted therapies for cancer. *J. Med. Chem.* **53,** 6811–24 (2010).

38. Bardhan, R., Lal, S., Joshi, A. & Halas, N. J. Theranostic nanoshells: from probe design to imaging and treatment of cancer. *Acc. Chem. Res.* **44,** 936–46 (2011).

39. Melancon, M. P., Zhou, M. & Li, C. Cancer theranostics with near-infrared light-activatable multimodal nanoparticles. *Acc. Chem. Res.* **44,** 947–56 (2011).

40. Yoo, D., Lee, J.-H., Shin, T.-H. & Cheon, J. Theranostic magnetic nanoparticles. *Acc. Chem. Res.* **44,** 863–74 (2011).

41. Johnstone, T. C., Park, G. Y. & Lippard, S. J. Understanding and improving platinum anticancer drugs--phenanthriplatin. *Anticancer Res.* **34,** 471–6 (2014).

42. Dhar, S., Daniel, W. L., Giljohann, D. A., Mirkin, C. A. & Lippard, S. J. Polyvalent oligonucleotide gold nanoparticle conjugates as delivery vehicles for platinum(IV) warheads. *J. Am. Chem. Soc.* **131,** 14652–3 (2009).

43. Brown, S. D. *et al.* Gold nanoparticles for the improved anticancer drug delivery of the active component of oxaliplatin. *J. Am. Chem. Soc.* **132,** 4678–84 (2010).

44. He, C., Lu, K., Liu, D. & Lin, W. Nanoscale metal-organic frameworks for the co-delivery of cisplatin and pooled siRNAs to enhance therapeutic efficacy in drug-resistant ovarian cancer cells. *J. Am. Chem. Soc.* **136,** 5181–4 (2014).

45. Liang, X.-J. *et al.* Metallofullerene nanoparticles circumvent tumor resistance to cisplatin by reactivating endocytosis. *Proc. Natl. Acad. Sci. U. S. A.* **107,** 7449–54 (2010).

46. Maldonado, C. R., Salassa, L., Gomez-Blanco, N. & Mareque-Rivas, J. C. Nano-functionalization of metal complexes for molecular imaging and anticancer therapy. *Coord. Chem. Rev.* **257,** 2668–2688 (2013).

47. Hall, M. D. & Hambley, T. W. Platinum(IV) antitumour compounds: their bioinorganic chemistry. *Coord. Chem. Rev.* **232,** 49–67 (2002).

48. Graf, N. & Lippard, S. J. Redox activation of metal-based prodrugs as a strategy for drug delivery. *Adv. Drug Deliv. Rev.* **64,** 993–1004 (2012).

49. Min, Y., Mao, C., Xu, D., Wang, J. & Liu, Y. Gold nanorods for platinum based prodrug delivery. *Chem. Commun.* **46,** 8424–6 (2010).

50. Li, J. *et al.* Platinum(iv) prodrugs entrapped within multiwalled carbon nanotubes: Selective release by chemical reduction and hydrophobicity reversal. *Chem. Sci.* **3,** 2083 (2012).

51. Rieter, W. J., Pott, K. M., Taylor, K. M. L. & Lin, W. Nanoscale coordination polymers for platinum-based anticancer drug delivery. *J. Am. Chem. Soc.* **130,** 11584–5 (2008).

52. Gabizon, A. *et al.* Targeting folate receptor with folate linked to extremities of poly(ethylene glycol)-grafted liposomes: in vitro studies. *Bioconjug. Chem.* **10,** 289–98 (1999).

53. Bagal, D., Zhang, H. & Schnier, P. D. Gas-phase proton-transfer chemistry coupled with TOF mass spectrometry and ion mobility-MS for the facile analysis of poly(ethylene glycols) and PEGylated polypeptide conjugates. *Anal. Chem.* **80,** 2408–18 (2008).

54. Cohen, Y., Avram, L. & Frish, L. Diffusion NMR spectroscopy in supramolecular and combinatorial chemistry: an old parameter--new insights. *Angew. Chem. Int. Ed. Engl.* **44,** 520–54 (2005).

55. Toft, D. J. *et al.* Coassembled cytotoxic and pegylated peptide amphiphiles form filamentous nanostructures with potent antitumor activity in models of breast cancer. *ACS Nano* **6,** 7956–65 (2012).

56. Maldonado, C. R. *et al.* QD-filled micelles which combine SPECT and optical imaging with light-induced activation of a platinum(IV) prodrug for anticancer applications. *Chem. Commun.* **49,** 3985–7 (2013).

57. Ruggiero, E., Hernández-Gil, J., Mareque-Rivas, J. C. & Salassa, L. Near infrared activation of an anticancer Pt(IV) complex by Tm-doped upconversion nanoparticles. *Chem. Commun.* **51,** 2091–4 (2015).

58. Bukhtiyarova, M. V. *et al.* Selective catalytic reduction of nitrogen oxide by ammonia on substituted strontium ferrites. *Appl. Catal. A Gen.* **384,** 230–240 (2010).

59. Van, D. N. *et al.* Innate immune agonist, dsRNA, induces apoptosis in ovarian cancer cells and enhances the potency of cytotoxic chemotherapeutics. *FASEB J.* **26,** 3188–98 (2012).

60. Wexselblatt, E. & Gibson, D. What do we know about the reduction of Pt(IV) pro-drugs? *J. Inorg. Biochem.* **117,** 220–9 (2012).

61. Zheng, Y.-R., Suntharalingam, K., Johnstone, T. C. & Lippard, S. J. Encapsulation of Pt(IV) prodrugs within a Pt(II) cage for drug delivery. *Chem. Sci.* **6,** 1189–1193 (2014).

62. Moon, J. J., Huang, B. & Irvine, D. J. Engineering nano- and microparticles to tune immunity. *Adv. Mater.* **24,** 3724–46 (2012).

63. Kaka, A. S., Foster, A. E., Weiss, H. L., Rooney, C. M. & Leen, A. M. Using dendritic cell maturation and IL-12 producing capacity as markers of function: a cautionary tale. *J. Immunother.* **31,** 359–69 (2008).

64. Hato, S. V, de Vries, I. J. M. & Lesterhuis, W. J. STATing the importance of immune modulation by platinum chemotherapeutics. *Oncoimmunology* **1,** 234–236 (2012).

65. Melichar, B., Nash, M. A., Lenzi, R., Platsoucas, C. D. & Freedman, R. S. Expression of costimulatory molecules CD80 and CD86 and their receptors CD28, CTLA-4 on malignant ascites CD3+ tumour-infiltrating lymphocytes (TIL) from patients with ovarian and other types of peritoneal carcinomatosis. *Clin. Exp. Immunol.* **119,** 19–27 (2000).

66. Legler, D. F., Uetz-von Allmen, E. & Hauser, M. A. CCR7: roles in cancer cell dissemination, migration and metastasis formation. *Int. J. Biochem. Cell Biol.* **54,** 78–82 (2014).

67. Cunningham, H. D. *et al.* Expression of the C-C chemokine receptor 7 mediates metastasis of breast cancer to the lymph nodes in mice. *Transl. Oncol.* **3,** 354–61 (2010).

68. Rocha, N. & Neefjes, J. MHC class II molecules on the move for successful antigen presentation. *EMBO J.* **27,** 1–5 (2008).

69. Vivier, E., Tomasello, E., Baratin, M., Walzer, T. & Ugolini, S. Functions of natural killer cells. *Nat. Immunol.* **9,** 503–10 (2008).

70. Cheng, M., Chen, Y., Xiao, W., Sun, R. & Tian, Z. NK cell-based immunotherapy for malignant diseases. *Cell. Mol. Immunol.* **10,** 230–52 (2013).

71. Llopiz, D. *et al.* Combined immunization with adjuvant molecules poly(I:C) and anti-CD40 plus a tumor antigen has potent prophylactic and therapeutic antitumor effects. *Cancer Immunol. Immunother.* **57,** 19–29 (2008).

72. Tilney, N. L. Patterns of lymphatic drainage in the adult laboratory rat. *J. Anat.* **109,** 369–83 (1971).

73. Shibata, S. *et al.* The time course of lymphatic routes emanating from the peritoneal cavity in rats. *Anat. Histol. Embryol.* **36,** 78–82 (2007).

74. Lu, Z., Wang, J., Wientjes, M. G. & Au, J. L.-S. Intraperitoneal therapy for peritoneal cancer. *Future Oncol.* **6,** 1625–41 (2010).

75. Lammers, T. *et al.* Effect of intratumoral injection on the biodistribution and the therapeutic potential of HPMA copolymer-based drug delivery systems. *Neoplasia* **8,** 788–95 (2006).

Summary of results

- ✓ Hydrophobic IONPs (Fe_3O_4 and $Zn_xFe_{1-x})Fe_2O_4$) have been encapsulated inside PEGylated phospholipid (PL-PEG) micelles achieving control over their hydrodynamic diameter by changing the mass ratio of IONP to PEGylated phospholipids during the synthesis.

- ✓ The attachment of a gamma emitting radionuclide ^{99m}Tc in the form of $[^{99m}Tc(CO)_3]^+$ to the IONP-filled micelles was achieved without use of chelates or covalent attachment, conferring multimodality imaging (MR/SPECT) features to the system.

- ✓ By the incorporation of a commercially available rhodamine B-modified phospholipid, the IONP-filled micelles were also imaged by fluorescence microscopy, leading to a MR/SPECT/optical triple modality contrast agent.

- ✓ Using a self-assembling protocol the immunostimulatory dsRNA (poly (I:C)) was incorporated onto the IONP-filled micelles. Poly (I:C)-IONP@PL-PEG micelles triggered a more potent innate immune response than free poly (I:C) *in vitro* and *in vivo*.

- ✓ The optical imaging capabilities incorporated into the nanoconstruct have allowed us to visualize poly (I:C)-IONP@PL-PEG micelles *in vitro*. The system is able to reach the target endosomal compartments and TLR3 receptor in cells of the immune system, which is an essential requirement for effective activation of immune responses against viral infections mediated by TLR3.

- ✓ The multimodal imaging capabilities (MRI and SPECT) have allowed us to visualize that poly (I:C)-IONP@PL-PEG micelles are able to migrate from the site of injection to local and distant lymph nodes (LNs) through the lymphatic system by different routes of administration *in vivo* and *ex vivo*.

- ✓ The covalent attachment of a Pt(IV) prodrug to the DPPE-PEG(2000)-NH_2 and its incorporation in the IONP-filled micelles has led to the development of a new delivery system for cisplatin (IONP@PL-PEG-Pt(IV) micelles) with potent cancer cell killing and immunomodulatory activity which was lacking in the prodrug alone.

- ✓ Decorating with poly (I:C) the IONP@PL-PEG-Pt(IV) micelles keeps or enhances the immunostimulatory capabilities *in vitro* and *in vivo* without losing its ability to kill cancer cells. This system (poly (I:C)-IONP@PL-PEG-Pt(IV) micelles) is the first example of double functionalization of a nanocarrier with chemotherapy and immunostimulatory drugs.

- ✓ Imaging studies of poly (I:C)-IONP@PL-PEG-Pt(IV) micelles micelles have demonstrated that following intratumoral administration they can migrate to LNs. Taken together these preliminary imaging and functional studies suggest that this system could potentially act over the cancer cells in the primary tumor to directly destroy cancer cells and also exert its anticancer function at metastatic nodules whilst potentiating an immune response against the tumor cells.

Experimental section

Materials

All the syntheses were carried out with the following commercially available reagents used without further purification. Hexane (99%; LABSCAN), chloroform (water 0.005%; LABSCAN), chloroform-d (99.5%; Euriso-top), diphenyl ether (99%; Sigma Aldrich), dibenzyl ether (>98%; Alfa Aesar), ethanol (≥98%; Sigma Aldrich), (3-aminopropyl)triethoxysilane (>98%; Sigma Aldrich), 1,2-hexadecanediol (>98%; Tokyo Chemical Industry Co. Ltd), oleic acid (90%; Alfa Aesar), oleylamine (70%; Sigma Aldrich), iron(III) acetylacetonate (99%; Strem Chemicals), diethylzinc solution (1.0 M in hexanes), *meso*-2,3-dimercaptosuccinic acid (98 %, sigma aldrich), potassium tetrachloroplatinate (II) (99.9%; Alfa Aesar), potassium iodide (≥99%; Sigma Aldrich), ammonia (≥99.9%; Fluka), silver nitrate (≥99%; Sigma Aldrich), sodium phosphate dibasic (≥ 99%; Panreac), sodium phosphate monobasic monohydrate (98.00-102%; Sigma Aldrich), sodium chloride (>99.5%, Panreac), potassium chloride (≥99.5%; Panreac), succinic anhydride (99%; Sigma Aldrich), hydrogen peroxide solution (30 wt. % in H_2O; Sigma Aldrich), *N*,*N*'-dicyclohexylcarbodiimide (99%; Sigma Aldrich), Bromopentacarbonylrhenium(I) (98 %, Sigma Aldrich), polyinosinic-polycytidylic acid (poly (I:C) (high molecular weight) 1.5 - 8 kb; InvivoGen), 1-ethyl-3-[-3-dimethylaminopropyl]carbodiimide hydrochloride (EDC) (Thermo scientific). 1,2-dipalmitoyl-sn-glycero-3-phosphoethanolamine-N-[methoxy(polyethylene glycol)-2000] (ammonium salt) (DPPE-PEG(2000)-OMe), 1,2-distearoyl-sn-glycero-3-phosphoethanolamine-N-[amino(polyethylene glycol)-2000] (ammonium salt) (DSPE-PEG(2000)-NH_2), 1,2-distearoyl-*sn*-glycero-3-phosphoethanolamine-N-[carboxy(polyethylene glycol)-2000] (ammonium salt) (DSPE-PEG(2000)-COOH), 1,2-dipalmitoyl-3-trimethylammonium-propane (chloride salt) (DOTAP), 1-palmitoyl-2-oleoyl-*sn*-glycero-3-phosphocholine (PC) and 1,2-dipalmitoyl-sn-glycero-3-phosphoethanolamine-N-(lissamine rhodamine B sulfonyl) (DPPE-Rho) were purchased from Avanti Polar Lipids.

Instrumentation

Transmission electron microscopy (TEM)

TEM studies were conducted on a JEOL JEM-2011 electron microscope operating at 200 kV. The samples were prepared by depositing a drop of a solution of IONPs onto a copper specimen grid coated with a holey carbon film and allowing it to dry. For IONP size determination using TEM, a minimum of 200 particles were measured using the *Image J* software.

Fourier Transform Infrared (FTIR)

Fourier spectra of hydrophobic IONP, IONP micelles and Re labelled IONP micelles were recorded on Nicolet FTIR 6700 spectrometer as KBr pellet.

Dynamic Light Scattering (DLS)

Particle size analysis was measured with a NanoSizer (Malvern Nano-Zs, UK) with 173 ° scattering angle at 25 °C. For each sample, the correlation function was measured four times and the average value was used for data fitting.

Zeta potential measurements were performed with the mentioned NanoSizer instrument at 25 °C and with a cell drive voltage of 25 V using a Smoluchowski model.

UV/Vis spectrophotometer

UV/Vis absorption spectra were recorded on a NanoDrop ND 1000 Spectrophotometer (NanoDrop Technologies) and on a V-630Bio Spectrophotometer (JASCO analytical Instruments).

The measurement of the absorbance in 96-well plates was performed on a TECAN Genios Pro 96/384 multifunction microplate reader.

ICP-AES and ICP-MS analysis.

ICP-AES studies were performed on a Perkin Elmer Optima 5300 DV (Perkin Elmer, Santa Clara, USA) at the SGIker analytical facility of the Universidad del País Vasco (UPV/EHU; Leioa, Spain), employing an RF forward power of 1400 W, with argon gas flows of

15, 0.2 and 0.75 L/min for plasma, auxiliary, and nebuliser flows, respectively. Using a peristaltic pump, sample solutions were taken up into a Gem Tip cross-Flow nebuliser and Scotts spray chamber at a rate of 1.50 mL/min. The instrument was operated in axial mode. To measure the iron content in the samples, three wavelengths (238.024, 239.562, 259.939 nm) were selected analysed in a fully quant mode (three points per unit wavelength). A range of calibration standards were prepared using single element 1000 mg/l stock solutions (Fisher Scientific UKLTD) and a Merk multi element standard (ICP Multi element standard solution, VICertiPUR®) was employed as a reference standard. ICP-MS studies were performed on an Agilent 7700x ICP-MS (Agilent Technologies, Palo Alto, USA) with a MicroMist micro-uptake glass concentric nebulizer (Glass Expansion, West Melbourne, Victoria, Australia) and, employing an RF power of 1550 W, with gas flows of 15 and 1.05 L/min for plasma and carrier, respectively. To measure the platinum content in the samples, three isotopic masses (194, 195 and 196 m/z) were selected and analysed in spectrum mode (three points per unit point/mass and 200 ms of integration time). In order to reduce MO^+ formation in the plasma, the spray chamber was peltier cooled at 2 °C. A standard quartz torch with 2.5 mm internal diameter injector was used. Finally, standard nickel cones (sample and skimmer) were used. The optimization of the ICP-MS conditions was achieved by adjusting the torch position and tuning for reducing oxide and doubly charged ion formation with a standard tuning solution containing 1.0 µg/L of ^{7}Li, ^{24}Mg, ^{59}Co, ^{89}Y, ^{140}Ce and ^{205}Tl in 1.0% HNO_3. This equipment includes a collision cell (He gas, ORS3 system, Agilent Technologies) for discriminate spectral interferences with high performance.

Relaxivities measurements.

Relaxivities are measured at 37 °C on a Bruker Minispec mq60 instrument operating at 1.47 T. T1 and T2 values were measured for each sample at different Fe concentrations using inversion-recovery and CPMG methods respectively. The relaxivity values, r_1 and r_2, are calculated through linear least squares fitting of 1/relaxation time (s^{-1}) *versus* the iron concentration ([Fe] mM).

The MRI phantom experiments were carried out on a Bruker Biospec 11.7 T with a 9 cm gradient capable of delivering 740 mT/m using a 40 mm volume coil. T2 maps were acquired by using Bruker's MSME (Multi slice Spin echo) sequence. The echo time (TE) values

were varied in 128 steps ranging from 10 ms to 1280 ms and a repetition time (TR) of 15 s. T1 maps were obtained by using a spin echo sequence. Images were acquired at ten different TR values 150, 500, 1000, 1500, 2200, 3000, 4000, 5200, 7.600, 17500 ms). All data were acquired with: 256 x 256 points and a Field of View of 3 cm x 3 cm, slice thickness of 1.5 mm, no gap between slices and one average. T2 weighted images correspond to TE = 36 ms and TR = 15 s. The T1 and T2 map images were calculated using the Bruker's Paravision 5.1 software via the Levenberg-Margardt method. The relaxivity values, r_1 and r_2, were calculated through linear least squares fitting of 1/relaxation time (s^{-1}) versus the iron concentration ([Fe] mM).

Magnetic measurements

Magnetic measurements were done using the Vibrating Sample Magnetometry (VSM) technique at SGIker of the Universidad del País Vasco (UPV/EHU; Leioa, Spain)). The hysteresis loops at RT, with very good low field accuracy (better than 1 x 10^{-5} T) were performed in a home-made VSM equipped with an electromagnet up to a maximum field of 1.8 T. Another VSM fitted to a Cryogenic Free 14 T magnet system (Cryogenic Ltd) was used for the measurements below RT from -8 T to +8 T.

Termogravimetric analysis (TGA)

The thermogravimetric analysis (TGA) were performed on a TGA/SDTA 851 Mettler Toledo thermogravimetric analyzer under nitrogen atmosphere at a heating rate of 10 K/min at SGIker of the Universidad del País Vasco (UPV/EHU; San Sebastián, Spain)).

Atomic force microscopy (AFM)

The morphology of the INOP-filled micelles, poly (I:C), as well as poly (I:C)-decorated IONP micelles were characterized using intermittent contact atomic force microscopy (AFM). To this end the samples are added to (3-aminopropyl)triethoxysilane-functionalised mica substrates, incubated and rinsed, never letting them dry. The measurements were carried out in water with a JPK Nanowizard II AFM and Nanoworld FM cantilevers. These studies were carried out by Dr. Anja Bernecker (CIC biomaGUNE).

X-Ray Photoelectron Spectroscopy (XPS)

XPS experiments are performed in a SPECS Sage HR 100 spectrometer with a non-monochromatic X-ray source Magnesium Kα line of 1253.6 eV energy and a power applied of 250 W and calibrated using the $3d_{5/2}$ line of Ar with a full width at half maximum (FWHM) of 1.1 eV. The selected resolution for the spectra was 15 eV of Pass Energy and 0.15 eV/step. An electron flood gun was used to compensate for charging during XPS data acquisition. All measurements are made in an ultra high vacuum (UHV) chamber at a pressure below $8x10^{-8}$ mbar. Samples were measured on silica surfaces. In the fittings Gaussian-Lorentzian functions were used, where the FWHM of all the peaks were constrained while the peak positions and areas were set free. These studies were carried out by the surface analysis and fabrication platform of CIC biomaGUNE (Dr. Luis Yate).

Nuclear Magnetic Resonance (NMR).

One-dimensional (1D) ^{1}H, two-dimensional (2D) ^{1}H-^{1}H COSY and diffusion ordered spectroscopy (DOSY) NMR spectra were measured on a **Bruker Ultrashield™ Plus 500** spectrometer at 500 MHz at room temperature using standard pulse programs. Chemical shifts are reported in parts-per-million (ppm) and referenced to the residual solvent signal ($CDCl_3$-d: δ 7.26 ppm).

These studies were carried out by Dr. Luca Salassa and Dr. Javier Hernández Gil in collaboration with the NMR service of CIC biomaGUNE.

Liquid chromatography-electrospray ionization-tandem mass spectrometry (LC-ESI-MS)

Liquid chromatography was performed on an ACQUITY UPLC system (Waters, Milford, MA, USA) with a conditioned autosampler at room temperature. The separation was carried out on an ACQUITY UPLC BEH C18 column (100 mm × 2.1 mm i.d., 1.7 µm). The column temperature was maintained at 40 °C. The analysis was achieved using 0.1 % formic acid in water/MeOH as the mobile phase with a flow rate of 0.3 $mL{\cdot}min^{-1}$. The injection volume was 5 µL. A Waters LCT-ToF premier Spectrometer (Waters, Milford, MA, USA) was connected to the UPLC system via an electrospray ionization (ESI) interface. The ESI source was operated in W-optics positive ionization scan mode with the capillary voltage at 2.5 kV.

The temperature of the source and desolvation was set at 120 °C. The cone and desolvation gas flows were 50 L/h and 600 L/h, respectively. The instrument was calibrated over the range m/z 50-4000 before each measurement using a standard NaI solution (1 μM). All data collected in centroid mode were acquired using Masslynx software (Waters, Milford, MA, USA). These studies were carried out by Dr. Javier Hernández Gil in collaboration with the mass spectrometry platform (CIC biomaGUNE).

Synthesis of hydrophobic iron oxide nanoparticles

IONPs Synthesis. IONPs were prepared using methods previously described in the literature.[1]

Synthesis of 4.21 nm IONPs. In a typical reaction $Fe(acac)_3$ (2 mmol, 0.7064 g), 1,2-hexadecanediol (10 mmol, 2.6371 g), oleic acid (6 mmol, 2.123 mL), oleylamine (6 mmol, 2.82 mL), and phenyl ether (20 mL) are mixed and magnetically stirred under a flow of nitrogen. The mixture is heated to 200 °C for 30 min and then heated to reflux (260 °C) for another 30 min. The black-brown mixture is cooled to room temperature by removing the heat source. Under ambient conditions, ethanol (40 mL) is added, and a black material is precipitated and separated via centrifugation (30 min., 3000 x g). The black product is dissolved in hexane (10 ml) in the presence of oleic acid (0.05 mL) and oleylamine (0.05 mL). Centrifugation (10 min., 3803 x g) is applied to remove any undispersed residue. Ethanol (20 ml) is added and then centrifuged (10 min., 3803 x g). The product, 4 nm Fe_3O_4 nanoparticles, is obtained.

Synthesis of 6.92 nm IONPs. In a typical reaction $Fe(acac)_3$ (2 mmol), 1,2-hexadecanediol (10 mmol), oleic acid (6 mmol), oleylamine (6 mmol), and benzyl ether (20 mL) are mixed and magnetically stirred under a flow of nitrogen. The mixture is heated to 210 °C for 2 h and then heated to reflux (300 °C) for 1 h. The black-colored mixture is cooled to room temperature by removing the heat source. Following the workup procedures described in the synthesis of 4 nm particles, the product, 6 nm Fe_3O_4 nanoparticles, is obtained. To synthesize larger nanoparticles, this product is used as a seeds following a similar protocol.

Synthesis of 9.23 IONPs. In a typical reaction $Fe(acac)_3$ (2 mmol), 1,2-hexadecanediol (10 mmol), oleic acid (2mmol), oleylamine (2 mmol), and benzyl ether (20 mL) are mixed and magnetically stirred under a flow of nitrogen. A 84 mg sample of 6 nm Fe_3O_4 nanoparticles dispersed in 4 mL hexane is added. The mixture is heated to 100 °C for 30 min to remove hexane and then to 200 °C for 1 h. The mixture is then heated to reflux (300 °C) for 30 min. The black-colored mixture is cooled to room temperature by removing the heat source. Following the workup procedures described in the previous synthesis, 10 nm Fe_3O_4 nanoparticles are produced.

In all cases, the dried powder is redispersed in hexane or chloroform for TEM characterisation or micelle formation.

Synthesis of ZnSPIONs. ZnSPIONs were prepared following a protocol described previously on the literature.[2] We have to take special care with this protocol due to the presence of the pyrophoric reagent $ZnEt_2$, keeping the reaction under inert atmosphere and avoiding as much as possible any contact with water.

Synthesis of 3.55 nm ZnSPIONs. In a typical synthesis $Fe(acac)_3$ (4 mmol), 1,2-hexadecanediol (25 mmol), oleic acid (15 mmol), hexadecylamine (15 mmol), and octyl ether (25 mL) are mixed and magnetically stirred under a flow of nitrogen in a three-neck round bottom flask. The mixture is heated at 150 °C for 30 min. $ZnEt_2$ (0.85 mmol) is then injected and temperature is raised to 275 °C and held for 30 min. The mixture is cooled to room temperature by removing the heat source. Then, ethanol (40 mL) is added to precipitate the nanoparticles and after centrifugation (10 min, 3803 x g), the supernatant is discarded and the nanoparticles on the pellet are left on air until complete evaporation.

Synthesis of 5.65 nm ZnSPIONs. In a typical synthesis $Fe(acac)_3$ (4 mmol), 1,2-hexadecanediol (25 mmol), oleic acid (15 mmol), hexadecylamine (15 mmol), and octyl ether (25 mL) are mixed and magnetically stirred under a flow of nitrogen in a three-neck round bottom flask. The mixture is heated at 200 °C for 1 h. $ZnEt_2$ (0.85 mmol) is then injected and temperature was raised to 300 °C and held for 1h. Following the workup procedures described in the synthesis of 3.5 nm particles, the product, 5.5 nm ZnSPIO, is obtained.

Synthesis of 9.02 nm ZnSPIONs. In a typical synthesis $Fe(acac)_3$ (2 mmol), 1,2-hexadecanediol (12.5 mmol), oleic acid (7.5 mmol), hexadecylamine (7.5 mmol), and benzylether (25 mL) are mixed and magnetically stirred under a flow of nitrogen in a three-neck round bottom flask. A 84 mg sample of 5.5 nm ZnSPIO nanoparticles dispersed in 4 mL hexane are added. The mixture is heated to 100 °C for 30 min to remove hexane and then to 200 °C for 1 h. Then, $ZnEt_2$ (0.42 mmol) is added and the mixture is heated at 300 °C for 1 h. After the mixture is cooled until room temperature, 40 mL of ethanol are added to precipitate the nanoparticles and then a centrifugation step is carried out (30 min, 3803 x g). The supernatant is discarded and the pellet is resuspended in 4 mL of hexane. Another 40 mL of ethanol are added to purify the nanoparticles and another spin is done. Finally, the product is dried on air.

Preparation and characterization of water soluble MFe_2O_4

1. IONP@DMSA systems

The ligand exchange reaction is performed following a procedure described previously in the literature.[3] Firstly, 1 mg of IONPs is dissolved in 500 µL of toluene. Then 1.8 mg of DMSA are dissolved in 100 µL DMSO and added into the vial containing the nanoparticle solution. The mixture is transferred to facilitate the stirring into a 10 mL round bottom flask and is kept stirring overnight. A thin film appears on the wall of the flask and 1 mL toluene is added to eliminate the free organic ligand. Then, 3 mL of a mixture of EtOH:Acetone (4:2) are added to dissolve the solid. The solution is centrifuged 10 min at 2800 g. The supernatant is discarded and the pellet is resuspended again in the same media. The final pellet is resuspended in 200 µL of an alkaline solution (NaOH 0.01M). After that, 50 µL of HCl (0.01M) are added to adjust the solution at pH 7. Finally, the solution is filtered through 0.2 µm pore size filter.

2. IONP@PEI systems

The ligand exchange reaction was performed following a protocol previously described in the literature for QDs coated with PEI.[4] In a 25 µL round bottom flask, 0.4 mg of IONP (0.5 nmols of NP) are firstly redispersed in chloroform (200 µL). 40 mg of PEI (1.6 µmols of M_n=25 kDa) dissolved in 300 µL of chloroform are added into the flask, and the mixture is kept under magnetic stirring for 2 h at room temperature. Afterward, the solvent is evaporated under argon flow (approximately 30 min) and the dried film formed is dissolved in 400 µL of water. The sample is centrifuged at 6000 x g for 10 min, the pellet is discarded and the supernatant is dialyzed in a Dispo-Biodialyzer dialysis device (Sigma Aldrich, M_w cutoff of 50 kDa) for 24 h against water (3 x 500 mL) to remove free unbounded PEI molecules.

3. IONP@PL-PEG micelles

The preparation of PEGylated micelles is based on the self-assembly of phospholipids around hydrophobic nanoparticles.[5] PEG-phospholipid(s) (2 mg) and IONPs (1 mg) are dissolved in chloroform (500 µL final volume). In the specific case of amine micelles or carboxylic micelles, they are prepared mixing 1 mg of DPPE-PEG(2000)-OMe phospholipid and the corresponding phospholipid (DSPE-PEG(2000)-NH_2 or DSPE-PEG(2000)-COOH)) taking into account that the final amount of 2 mg of phospholids should be kept. The solvent is allowed to evaporate overnight in a 3 mL vial at room temperature. Any remaining solvent is removed under vacuum for 1 h. The flask is placed in a water bath at 80 °C for 30 s, after which 1 mL of nanopure water is added. The solution is transferred to an Eppendorf tube and centrifuged at 9700 x g for 5 min. The pellet is discarded and the supernatant is passed through a 0.45 µm filter. This solution is ultracentrifuged (369,000 x g, 1 h, 3 cycles) to remove the empty micelles. Finally, the pellet is dissolved in 400 µL of nanopure water or Phosphate Buffered Saline, PBS (10 mM), specifically in the case of *in vivo* assays. The IONP-filled micelles are stored at room temperature.

Fluorescent micelles are prepared as above with the modification that, DPPE-Rho is added at the 1-5% of the total amounts of phospholipids mols (4.5-25 µL of a 2 mg/mL

solution in chloroform) to the chloroform solutions of PEGphospholipid(s) and IONPs and that the remaining steps are conducted in darkness.

The concentration of the stock solution is always measured by ICP-AES technique for keeping adjusted the iron concentration in each sample. The concentration range may oscillate between 18 and 20 mM of iron.

4. ZnSPION@PL-PEG micelles

The micelles were prepared adopting a protocol described in the literature with some differences.[2] The amount of PEG-phospholipid(s) was reduced four times (5 mg instead of 20 mg of PEG-phospholipid per 1 mg of nanoparticle).

PEG-phospholipid(s) (5 mg) and ZnSPIONs (1 mg) are dissolved in chloroform (500 µL final volume). The solvent is evaporated using an argon flow in a 10 mL round-bottom flask at room temperature. After 20 min., a final evaporation with 30 s in a water bath at 70 °C was carried out. The thin film, placed on the wall of the round bottom flask after solvent evaporation, is resuspended with 1mL of HEPES at pH=7.4. The solution is transferred to a centrifugal device (Eppendorf tube) and heated at 70 °C for 3 h. Then, the samples are filtered with 0.2 µm and are kept at room temperature.

The concentration of the stock solution is always measured by ICP-AES technique for keeping adjusted the iron and zinc concentrations in each sample The concentration range may oscillate between 8 and 10 mM of iron, and between 1 and 2 mM of zinc.

5. Synthesis and Characterization of IONP@PL-PEG-Pt(IV)-micelles

All the synthesis and experiments containing Pt(IV) compounds are performed under dark conditions. These studies were carried out by Dr. Javier Hernández Gil (CIC biomaGUNE).

Pt (IV) prodrug (1) *cis*,*cis*,*trans*-[$Pt^{IV}(NH_3)_2Cl_2(O_2CCH_2CH_2CO_2H)_2$]. The platinum (IV) complex was synthesized as previously described.[6]

Synthesis of DSPE-PEG-Pt(IV). In a typical reaction *cis*,*cis*,*trans*-$[Pt(NH_3)_2Cl_2(O_2CCH_2CH_2CO_2H)_2]$ (9.6 mg, 18.0 μmol), DCC (3.7 mg, 18.0 μmol) and 4-(dimethylamino)pyridine (DMAP, 1.0 mg, 7.2 μmol) are dissolved in DMSO (130 μL). After 10 minutes, the solution containing the activated platinum(IV) complex is added to a DMSO solution of DSPE-PEG(2000)-NH_2 (10 mg, 3.6 μmol, 170 μL). The resulting mixture is allowed to react at room temperature for 72 h *under continuous stirring*. Water is then added to the reaction mixture. The solution is centrifuged and the supernatant is passed through a 0.45 μm filter to remove insoluble traces. Then, the supernatant is dialyzed in a Slide-A-Lyzer Dialysis Cassete (Thermo Scientific) (MW cutoff of 2,000) against water (3 x 500 mL). The dialysate, containing the final product DSPE-PEG-Pt(IV) (**2, Scheme 4.1**) is lyophilized and the residue dried in vacuo over P_2O_5 (10.86 mg, 90%). Reaction yield obtained of 65 %. UPLC/MS Tr =11.38 min; m/z for $[C_{140}H_{289}N_7O_{61}PPtCl_2]^{3+}$ expected = 1114.28, found = 1114.17 (ESI^+).

^{1}H NMR (500 MHz, $CDCl_3$) for **(2):** δ 0.88 (t, CH_3, 6H), 1.25 (s, CH_2, 56H), 1.61 (m, **CH_2**CH_2CO, 4H), 2.32 (m, CH_2**CH_2**CO, 4H), 2.60 (m, CH_2-succinic, 8H), 3.44 (m, **CH_2**CH_2N, 2H). 3.64 (s, PEG ~ 180H), 3.96 (m, CH_2**CH_2**NH, 2H), 4.22 (m, trans-PO_4**CH_2**CH, 1H), 4.32 (m, COO**CH_2**CH(OCO), 2H), 4.40 (m, cis-PO_4**CH_2**CH, 1H), 5.26 (m, PO_4CH_2**CH**, 1H), 6.25 (bs, NH_3, 6H), 6.68 (bs, $NHCOCH_2$), 6.82 (bs, $NHCOOCH_2$)

Formation of IONP@PL-PEG-Pt(IV) micelles. The Pt(IV) conjugated phospholipid DSPE-PEG-Pt(IV) (2.5 mg) and hydrophobic IONP (1 mg) are dissolved in chloroform (500 μL). The solvent is allowed to evaporate overnight, eliminating any remaining trace of solvent the next day under vacuum for 1h. After 30s in a water bath at 80 °C, 1 mL of nanopure water is added. The solution is transferred to an Eppendorf tube and centrifuged at 9500 g for 5 min. The supernatant is passed through a 0.45 μm filter and finally, the solution is centrifuged at 369 000 g for 45 min, 3 cycles to remove the empty micelles. In the final spin the pellet is dissolved in 600 μL of water or PBS (10 mM).

Cationic liposome formation

DOTAP-containing liposomes were prepared using a method previously described.[7] In brief, DOTAP and PC, dissolved in $CHCl_3$, are mixed at a 1:3 molar ratio (total lipid 1.5mM) in

a small 25 mL round-bottomed flask. The solvent is evaporated using a rotary evaporator for 30 min at 60 °C, and then the film is flushed with N_2. The film is rehydrated using 1 mL of Tris buffer (10 mM, pH = 7.4) and vortexed with occasional heat to encourage liposome formation. In some samples PC was omitted from the starting lipid mixture. Liposomes are stored at 4 °C.

Attachment of poly (I:C) onto IONPs-filled micelles

Poly (I:C) is resuspended in sterile endotoxin-free physiological water (NaCl 0.9 %) to a final concentration of 1 mg/mL. It is stored in aliquots in DNA/RNAase free centrifugation tubes, to avoid repeated freeze/thaw cycles. All the experiments containing poly (I:C) are carried out using RNAse free materials.

1. Covalent method

IONP@PL-PEG micelles decorated with DSPE-PEG(2000)-NH_2 were prepared following the procedure described above. The reaction mechanism between primary amine and a phosphate group using 1-ethyl-3-[3-dimethylamino propyl]carbodiimide (EDC) in the presence of methyl imidazole buffer (MeIm, 0.1M, pH = 7.5) was described more than two decades ago.[8,9] The conjugation of poly (I:C) to the IONP-filled micelles by covalent approach was adapted to a previous described method.[10] Through the 5' phosphate group using the amine-to-phosphate crosslinking carbodiimide EDC in the presence of methyl imidazole poly (I:C) is conjugated to the IONP-filled micelles. 100 µL of poly (I:C) solution (1mg/mL) is mixed with EDC (1.25mg, 6.5 µmol) in MeIm buffer (0.1M, pH = 7.5). The activated poly (I:C) is then added to 20 µL of IONP@PL-PEG micelles decorated with DSPE-PEG(2000)-NH_2. The volume is adjusted to 200 µL with MeIm (0.1 M, pH= 7.5) buffer and the mixtures were stirred overnight at room temperature. Then, the sample is purified first by passing through a NanoSep 100k (MWCO 100kDa) ultrafiltration centrifugal device (Pall Life Sciences) at 1475 x g for 10 min (3 cycles) and then by ultracentrifugation (369,000 x g, 30 min, 1 cycle) to remove to the excess of EDC and free poly (I:C). In the final ultracentrifuge step, the poly

(I:C)-IONP@PL-PEG micelle conjugates are resuspended in PBS (1mM). The samples are kept at room temperature.

2. Non-covalent method

IONP@PL-PEG micelles decorated with DPPE-PEG(2000)-OMe, DSPE-PEG(2000)-NH_2 or DSPE-PEG-Pt(IV) are used to study the non-covalent approach of poly (I:C). In a typical conjugation, 20 µL of stock micelle (approximately 17 mM Fe) are mixed with different amounts of poly (I:C), covering a wide range of concentrations from 62.5 to 900 µg/mL, in a final volume of 200 µL PBS (1 mM). The mixture is stirred overnight at room temperature and purified first by passing through a NanoSep at 1475 x g for 10 min (3 cycles) and then by ultracentrifugation (369,000 x g, 30 min, 1 cycle) to remove free poly (I:C). The samples are kept at room temperature.

Labeling of IONP@PL-PEG micelles with *fac*-$[Re(OH_2)_3(CO)_3]^+$

Synthesis of *fac*-$[Re(OH_2)_3(CO)_3]^+$ complex. The inorganic complex is synthesized following a procedure described previously on the literature.[11] Briefly, a suspension of commercially available $[Re(CO)_5]Br$ (16.6 mg, 0.041 mmoles) in deuterated water (15 ml, previously degassed) is heated and brought to reflux under argon flow for 24 h. Upon boiling, the mixture became a clear solution. The heat source is removed and the mixture is cooled down to room temperature. The solution is lyophilized and $Re(OH_2)_3(CO)_3$is isolated as a light green powder. The product is analyzed by FTIR and by HPLC.

Binding of *fac*-$[Re(OH_2)_3(CO)_3]^+$ to IONP@PL-PEG micelles. A solution of IONP@PL-PEG micelles in water at concentrations ranging from 6 mM to 16 mM Fe (250 µL) is added to aqueous solutions of *fac*-$[Re(OH_2)_3(CO)_3]^+$ (400 µL, 2.8 mM). The mixture is vortexed for 30 s and then heated at 90 °C for 20 min. The reaction mixture is allowed to cool down to RT and then centrifuged at 1000 x g for 3 min. The supernatant is transferred to a NanoSep 100k centrifugal device and centrifuged at 8200 x g for 10 min. The retentate is washed with water twice and after the final centrifugation, the IONP micelles are recovered from the

membrane surface by adding and rinsing with a pipette tip (final volume of 500 µL). This purification process is repeated using a new NanoSep 100k centrifugal device. Retentates and filtrates are lyophilized and analyzed by FT-IR.

These studies were carried out by Dr. Nina Gómez Blanco (CIC biomaGUNE).

Labeling of IONP@PL-PEG micelles with *fac*-$[^{99m}Tc(OH_2)_3(CO)_3]^+$

Synthesis of *fac*-$[^{99m}Tc(OH_2)_3(CO)_3]^+$ complex. ^{99m}Tc pertechnetate ($Na[^{99m}TcO_4]$) was eluted with saline from a Drytec generator (GE Healthcare, Amersham, UK) at the Radiopharmacy at Guy's and St Thomas' Hospital NHS Trust (London, UK) (or obtained from Molypharma S. A. (Madrid, Spain)) and converted to *fac*-$[^{99m}Tc(OH_2)_3(CO)_3]^+$ using the lyophilized kit "Isolink" (Covidien, Petten, The Netherlands). The synthesis and quality control of tricarbonyltechnetium (^{99m}Tc-TC) were carried out following the manufacturer's instructions. Briefly, 1 mL of $Na[^{99m}TcO_4]$ (1.0-1.7 GBq) was injected into the kit and the mixture was heated at 100 °C for 30 min. The vial was allowed to cool to room temperature, and its content was neutralised with 1 M HCl. The reaction was monitored by either thin layer chromatography (TLC) using silica gel TLC strips (Merck) with methanol/HCl 99/1 as mobile phase or by out by high performance liquid chromatography (HPLC). In the case of TLC, ^{99m}Tc-TC has a Rf of about 0.3-0.4, while $[^{99m}TcO_4]^-$ moves with the solvent front. TLC strips were scanned using a Mini-scan radio TLC scanner with a FC3600 FlowCount detector of γ photons (LabLogic, Sheffield, UK). When the radiochemical conversion was monitored by HPLC, an Agilent 1200 series HPLC equipped with a quaternary pump and a radiometric detector (Gabi, Raytest) was used. A Mediterranea^{TM} Sea18 column (4.6 x 250 mm, 5 µm) was used as stationary phase. The elution solutions were A (triethylammonium phosphate, pH = 2.25) and B (MeOH). The column was eluted with a linear gradient: t = 0-5 min, 100% A; t = 5-6 min, 100-75% A; t = 6-9 min, 75-66% A; t = 9-20min, 66-0% A; t = 20-30 min, 0% A; t = 30-31 min, 0-100% A; t = 31-35 min, 100% A, at a flow rate of 1 mL/min (retention times = 11.1 min and 4.9 min for $^{99m}TcO_4^-$ and ^{99m}Tc-TC, respectively).

Binding of *fac*-$[^{99m}Tc(OH_2)_3(CO)_3]^+$ to IONP@PL-PEG micelles. A fixed volume (400 µL) of *fac*-$[^{99m}Tc(OH_2)_3(CO)_3]^+$ was added to an aqueous solution of the IONP@PL-PEG micelles, poly

(I:C)-IONP@PL-PEG micelles and poly (I:C)-IONP@PL-PEG-Pt(IV) micelles (at concentrations ranging from 0.3 to 250 nM) in an eppendorf tube or glass vial and the mixture was heated at 70-90°C for 25-60 min. The eppendorf tube or vial was then allowed to cool down to room temperature and the contents were transferred to a Nanosep 30k (MWCO 30kDa) ultrafiltration centrifugal device (Pall Life Sciences), which was centrifuged at 7500 rpm for 10 min. This allowed separation of the radiolabeled micelles, which remained in the retentate, from the unbound ^{99m}Tc-TC, which was in the filtrate. The filtrate was discarded, and deionized water (500 μL) was added to the retentate. The radiolabeled IONP@PL-PEG micelles were washed by centrifugal filtration and this process was repeated twice. The total radioactivity in the filtrates and retentates was measured in a CRC-25R dose calibrator (Capintec, USA) in order to determine the radiolabeling yield. The radiolabeled micelles were recovered from the filter by the addition of water or phosphate buffer solution (PBS) (200-300 μL) to the retentate.

NanoSPECT/CT phantoms images. Eppendorf tubes with different concentrations of the radiolabeled poly (I:C)-IONP@PL-PEG micelles were placed in the scanner. SPECT scans were acquired using a NanoSPECT/CT scanner (Bioscan, Paris, France) with SPECT acquisition time 3300 s, obtained in 55 projections using a 4-head scanner with 4 x 9 (1 mm) pinhole collimators in helical scanning mode, acquiring a transaxial field of view of 206.6 mm and an axial field of view of 24 mm. Images were reconstructed using the HiSPECT (Scivis GmbH) reconstruction software package, and fused using proprietary Bioscan InVivoScope (IVS) software.

These studies were carried out by Dr. Maite Jauregui Osoro (Division of imaging sciences and biomedical engineering King´s College London, St. Thomas´ Hospital, London) and by the radiochemistry platform of CIC biomaGUNE.

In vitro procedures and studies

Cytotoxicity studies on cells of the immune system

1. **Macrophages.**

J774A.1 cells are obtained from the ATCC and cultured in Dulbecco's Modified Eagle Medium (DMEM) supplemented with 5 % fetal bovine serum (FBS) and 1 % penicillium streptomycin (PS) (Invitrogen™, Madrid) and maintained in a humid atmosphere at 37 °C, 5 % CO_2. Cells are passaged at ~70 % confluence and a low passage number is maintained using cryopreserved stocks stored in FBS supplemented with 10 % DMSO (Sigma Aldrich).

Cells are seeded at 3.5 x 10^5 cells/mL in 96-well plates (100 µL/well) and allowed to adhere overnight. Phenol red-free media is used when conducting experiments. Media is removed from each well prior to adding 100 µL of nanoparticle formulations, diluted accordingly in media, per well in triplicate or quintuple. Cells are incubated for various time-points at 37 °C following which the cell supernatant is removed and frozen for subsequent cytokine analysis.

In the specific case where the role of endocytosis is assessed, the incubation of cells with formulations was conducted at 4 °C. The experiment was conducted in the same way except that for after adding formulations, cells are placed in the fridge for the relevant time period.

In all cases cell viability is assessed at 24 h, therefore if the incubation time between cells and formulations is less than 24 h, supernatants are removed at the relevant time-point and fresh media added.

2. **Bone marrow-derived dendritic cells (BMDCs) differentiation and preparation.**

Bone marrow derived dendritic cells (BMDC) were generated from 6-12 weeks old BALB/c mice. Femurs and tibiae of hind limbs are removed and the marrows were flushed with PBS using a syringe as described.[12] Clusters within the marrow are disgregated to get a homogeneous cell suspension and after the erythrocytes were lysed, the cells are washed

and resuspended in RPMI-1640 supplemented with penicillin (100 µg/ml), Streptomycin (100 µg/ml), L-glutamin (2 mM) and heat inactivated FBS (10%). At day zero cells are seeded at a concentration of 2 x 10^6 cells per 100 mm bacteriological petri dish (Falcon) in 10 mL of medium supplemented with 20 ng/ml of murine GM-CSF (Peprotech). At day 3 another 10 mL supplemented with 20 ng/ml of GM-CSF are added per dish. At day 6 half of the supernatant is collected, centrifuged and cell pellet resuspended in 10 mL fresh medium containing 10 ng/mL of GM-CSF. At day 8-9 cells are harvested and used to test the cell viability and the immunostimulatory capacity of different formulations. These studies were performed in collaboration with Dr. Aintzane Zabaleta Azpiroz (CIC biomaGUNE).

Cytotoxicity studies

Cells are counted and resuspended in media (in cRPMI containing 20 ng/mL GMCSF) at a final concentration of 2 x 10^5 cells/well (100 µL/well) in 96-well plates.

The cell viability was measured using the MTT assay.[13] After relevant incubation times, supernatants are collected from the wells and 100 µL of MTT reagent (Roche) diluted in phenol-free media (final concentration of 0.25 mg/mL) is added/well. Cells are incubated at 37 °C for 1 h, after which the liquid is removed and 200 µL DMSO/well are added to lyse cells. The absorbance of samples is measured using a microplate reader at 550 nm and data represented as the cell viability compared to control wells.

Maturation assays

BMDCs maturation was analyzed after incubating 2 × 10^5 cells/well (96 well plate) during 24 h at 37 °C in culture medium, in the presence of different nanoparticle formulations and their respective controls, including a group of BMDCs untreated. Cells are then incubated in the presence of Fc Block™ for 10 min at 4 °C in phosphate buffered saline (PBS) containing 2% FBS. CCR7-BV421 and the isotype control staining are performed next for 15 min at 37 °C. Finally, cells are stained with the phenotype markers CD11c-APC and I-A/I-E-PerCp-Cy5.5 and the maturation markers CD80-FITC and CD86-PE and the

corresponding isotype controls FITC Armenian Hamster IgG and PE Rat IgG2a at 4 °C for 15 min. Samples were analyzed using FACS Canto flow cytometer (BD-Biosciences) and the data were analyzed with FlowJo software. All antibodies and reagents were from Biolegend unless otherwise stated. These studies were performed in collaboration with Dr. Aintzane Zabaleta Azpiroz (CIC biomaGUNE).

Quantification of cytokines by ELISA (Enzyme-Linked ImmunoSorbent Assay)

IL-6 and IL-12 cytokines are measured in cell supernatants and blood serum using sandwich ELISA (IL-6 kit, R&D Systems; IL-12 kit, PeproTech). A 4-parameter sigmoidal (logistic) standard curve is used to quantify the cytokine present (GraphPad Prism software). Results are expressed as mean ± SEM in pg/mL.

ELISA sandwich. The plate is coated with a known quantity of capture antibody and let it overnight at room temperature. Non-specific binding sites are blocked with the addition of a BSA solution (Bovine Serum Albumin) as a reagent diluent. Standards and diluted samples (antigen-containing sample) are added and captured by antibody. A specific biotin-labeled detection antibody is added and binds to antigen. Enzyme-linked secondary antibody is added for detecting the antibody (Streptavidin-Horseradish Peroxidase, Strep-HRP). A TMB (tetramethylbenzidine) substrate is added and is converted by enzyme to detectable form. To stop the color reaction an acid solution (2N H_2SO_4) is added to the substrate. The color developed is proportional to the amount of cytokine in the samples or standards.

Cell Imaging

To investigate the cellular fate of the nanoconstructs, microscope co-localization imaging studies are performed using specific markers of lysosomes (Lysotracker Green, Molecular Probes) and intracellular TLR3 (anti-TLR3 antibody, abcam).

1. Reach endosomes and lysosomes

J774 and BMDCs are seeded in a Ibidi µ-Slide VI 0.4 at 30,000 and 90,000 cells/channel respectively and allowed to adhere overnight in a humidified incubator with 37 °C and 5% CO2 in their corresponding media. Nuclei were stained with DAPI (5 µg/mL in medium) for 15 min. The medium was changed and the cells are incubated with the solution containing poly (I:C)-IONP@PL-PEG micelles or poly (I:C)-IONP@PL-PEG-Pt(IV) micelles labeled with rhodamine B-modified phospholipid for 1 h (360 µM Fe). The medium is removed and fresh medium containing Lysotracker (1 µM) is added. After 45 min, the medium is removed, the cells are washed twice with sterile 10 mM PBS and fresh medium is added to preserve the cells.

2. Target TLR3 receptor

To investigate if the micelles target TLR3, the cells are seeded as above and the micelles are incubated at the same concentration and incubation time.

In J774 macrophages cell line, then the medium was removed and the adherent cells were fixed for 20 min with 4% formaldehyde in sterile 10 mM PBS at room temperature. After being washed twice with sterile 10 mM PBS, the cells were treated with permeabilizing solution (0.1% Triton X-100 in 10 mM PBS) for 5 min. After washing, the blocking buffer (1% BSA in 10 mM PBS) was then added for 20 min at room temperature.

In BMDCs the medium is removed and the adherent cells are treated with the fixation and permeabilization commercial solution BD Cytofix/CytopermTM for 20 min at room temperature. The cells are washed twice with BD Perm/Wash^{TM} buffer. The blocking buffer (1% BSA in 10 mM PBS) is then added for 20 min at room temperature.

In both cases, after blocking buffer step the cells are incubated overnight at 4 °C with the primary antibody (anti-TLR3 abcam, 10 µg/mL in blocking buffer). Then at room temperature, the cells are washed twice with sterile 10 mM PBS. The labeled secondary antibody (Alexa 488-labeled, 10 µg/mL in blocking buffer) is used to visualize staining of the

primary TLR3 antibody. The cells are washed twice with sterile 10 mM PBS. Nuclei are staining with DAPI (5 µg/mL) for 5 min.

Cells are visualized using a Zeiss Axio Observer wide field fluorescence microscope (Carl Zeiss, Germany). Brightfield and fluorescence images are collected and processed using AxioVision software.

Cytotoxicity studies on Human Cancer Cells

PC3 cells were obtained from the American Type Tissue Collection (LGC Promochem) and cultured in Ham's F-12K (Kaighn's) medium (Gibco®) supplemented with 10% FBS and 1 % PS (Invitrogen™). ***MDA-MB 231*** cells were obtained from the ATCC and cultured in RPMI 1640 (Lonza) supplemented with 10 % fetal bovine serum (FBS), 1 % PS and 1% L-Glutamine (Invitrogen™). ***PANC-1*** cells were obtained from the Sigma Aldrich (ECACC) and cultured in RPMI 1640 (Lonza) supplemented with 10 % fetal bovine serum (FBS), 1 % PS and 1% L-Glutamine (Invitrogen™). Cells are maintained in a humid atmosphere at 37 °C, 5 % CO_2. Cells are passaged at ~70 % confluence and a low passage number is maintained using cryopreserved stocks stored in FBS supplemented with 10 % DMSO (Sigma Aldrich).

PANC-1, PC3 and MDA-MB 231 cells are seeded in 96-well plates at 2000, 3500 and 5000 cells/well respectively. Cells are allowed to adhere overnight. Media is removed from each well prior to adding 200 µL of pre-drug, drug or nanoparticle formulations. The different concentrations and the corresponding controls are diluted accordingly in media and incubated with cells for 72 h at 37°C.

The cell viability of drug formulations on cancer cells is measured using the Sulforhodamine B assay.[14] Briefly, after the corresponding incubation time, cells are fixed by addition of 25% trichloroacetic acid (TCA) cold solution. Plates are washed with tap water and dried prior to staining with Sulforhodamine B (SRB) dye solution. Plates are washed with 1% glacial acetic acid, dried and resuspended in 10 mM Tris buffer, pH 10.5 before reading absorbance at 550 nm.

Curve fitting and generation of IC_{50} values are carried out using GraphPad Prism 4 software.

Quantification of intracellular platinum accumulation in PC3

PC3 cells were seeded at 29 000 cells/well in 24-well plates and allowed to adhere overnight. These cells were then treated either with (**1**) or IONP@PL-PEG-Pt(IV) micelles/poly(I:C)–IONP@PL-PEG-Pt(IV) micelles (in all cases [Pt] = 10×10^{-6} M) and subsequently incubated for 6 h at 37 °C. Cells were washed with ice-cold PBS (10×10^{-3} M) three times, incubated with 1.5 mL of sodium chloride (0.15 M, pH 3.0 was adjusted by acetic acid) for 3 min at 4 °C, then rinsed with 2 mL of ice-cold PBS, harvested by scraping in ice-cold PBS, centrifuged, and cell numbers were counted.[15] The cell pellet was digested in 160 µL of nitric acid (65% v/v) at 75 °C for 2 h. The Pt content was analyzed by ICP-MS.

Animal procedures and studies

Animals were cared for and handled in compliance with the Guidelines for Accommodation and Care of Animals (European Convention for the Protection of Vertebrate Animals Used for Experimental and Other Scientific Purposes) and internal guidelines. The animal procedures were approved by the appropriate local authorities and were performed in accordance with protocols approved by the Spanish regulations governing animal welfare and protection and following the criteria outlined in the Guide of the Care and Use of Laboratoy Animals by the National Academy of Sciences.

Likewise the animal studies conducted in UK were in accordance with UK Research Councils' and Medical Research Charities' guidelines on Responsibility in the Use of Animals in Bioscience Research, under a UK Home Office license, and all the experimental procedures were approved by the appropriate local authorities.

Tumor induction

For the imaging studies in tumor-bearing mice, seven to eight week old male athymic-nude Foxn1 nu/nu mice (Charles River) are inoculated subcutaneously with a suspension in Dulbecco's Phosphate-Buffered Saline/Matrigel (1:1) of PANC-1 cells (2×10^6 cells, 200-μL). Animal weight and tumor volume are determined three times a week. Tumor growth is measured with a calliper. The tumors are measured using two orthogonal measurements L and W (perpendicular to L) and the volumes are calculated using the formula $V = LW^2/2$ and recorded. These studies were carried out by Dr. María Jiménez González and Maria Puigivila Viñeta (CICbiomaGUNE).

MRI studies

Balb/c mice (n = 5), aged 6-12 weeks of age, are injected with the poly (I:C)-IONP micelle formulations of interest (100 μL/dose) via subcutaneous (s.c.) into the flank and abdominal region and intraperitoneal (i.p.) route. Images obtained at t prior and at t = 2 h, 24 h and 72 h post injection (p.i) to detect the presence of NPs in various organs of interest (spleen, liver and inguinal lymph nodes). Animals are anesthetised prior to imaging using 3.5 % isofluorane and maintained at 1.5 – 2.5 % in 100 % O_2 during the whole acquisition. Animals are placed in a mouse holder compatible with the MRI equipment and kept at a constant body temperature of 37°C throughout the study using a heated water blanket. Temperature and respiration rate are monitored with an MRI compatible animal monitoring system (SA Instruments Inc., New York, USA) with animals maintained at a respiration rate of 60 - 80 breaths per minute. Experiments are performed on a 70/30 Bruker Biospec system (Bruker Biospin GmbH, Ettlingen, Germany) using the BGA12-S mini imaging gradient and 40 mm inner diameter transmit/receive mouse body volumetric coil. Axial gradient echo experiments were performed with the following parameters: A respiration synchronized (TR = one respiration cycle) FLASH sequence, TE = 3 ms, FOV = 28 mm x 28 mm , Matrix = 256 x 256, Slice Thickness = 0.75 mm , N Slices= 32 and 2 averages. Axial T2 maps were acquired using the following parameters: A respiration synchronized (TR = 6 respiration cycles) Multi Slice Multi Echo (MSME) sequence, TE = 8, 16, 24, 32, 40, 48, 56, 64 ms; FOV = 28 mm x 28

mm , Matrix = 128 x 128, Slice Thickness = 0.75 mm , N Slices= 9 and 2 averages. The images are fitted into Levenberg-Margardt method to calculate T2 values using Bruker's Paravision 5.1 software. These studies were carried out by the NMR service of CICbiomaGUNE.

SPECT/CT studies

These studies were carried out by the division of imaging sciences and biomedical engineering King´s College London, St. Thomas´ Hospital, London and by the radiochemistry platform of CIC biomaGUNE.

1. Poly (I:C)-IONP@PL-PEG micelles studies

Mice received a s.c. in the abdomen region or i.p. injection of 70±10 MBq of ^{99m}Tc-radiolabeled micelles in 150 µL PBS. With the mouse under isoflurane anaesthesia (1.5-2% in oxygen), whole-body SPECT/CT scans were acquired at 3h and 24 h post-injection (p.i.). With the full ring detector, 360° of data were acquired by rotating the collimator 45° (45 steps, 1°/step). Data were collected in an energy window of 125-150 keV and the duration of the scans was 60 min (80sec/step). During image acquisition, mice were kept normothermic using a heating blanket (Homeothermic Blanket Control Unit; Bruker BioSpin GmbH, Karlsruhe, Germany).

After each SPECT scan, CT acquisitions are performed to provide anatomical information of each animal. The CT acquisition consisted of 220 views were acquired in 0.88° increments around the animal with 16 ms exposure per view. The X-ray tube settings were 70 kV and 32 mA. SPECT/CT images are acquired using the eXplore speCZT CT preclinical imaging system (GE Healthcare, USA). The system combines SPECT and CT on one gantry, allowing coregistration of the SPECT and CT datasets without additional post-processing. The SPECT scanner uses a stationary, full ring of CZT detectors and interchangeable rotating cylindrical collimators. An 8-slit collimator was used with a field of view of 32 and 78 mm in the transaxial and axial directions, respectively. The SPECT images are reconstructed using the OSEM iterative algorithm (5 iterations, 15 subsets) into 128 x 128 x 32 array with a voxel

size of 0.4 x 0.4 x 2.46 mm, and are not corrected for scatter and attenuation. The CT images are reconstructed using a cone beam filtered back-projection Feldkamp algorithm into 437 x 437 x 523 array with a voxel size of 0.2 x 0.2 x 0.2 mm.

In the case of s.c. into the flank region a mouse received 16 MBq poly(I:C)-IONP-$^{99m}Tc(CO)_3$ micelles in 100 µL micelles in saline (FreseniusKabi). With the mouse under isoflurane anaesthesia (1.5-2% in oxygen) in a Minerve imaging chamber, whole-body SPECT/CT scans were acquired at 10 min, 3 h and 24 h post-injection (p.i.), using a NanoSPECT/CT Plus scanner (Mediso, Budapest, Hungary). SPECT images are obtained at 45 sec/frame (10 min and 3 h p.i., ca. 30 min per whole-body scan) and 150 sec/frame (24 h p.i., ca. 90 min per whole-body scan) using a 4-head scanner equipped with four 9 (1 mm) pinhole collimators in helical scanning mode and CT images with a 45 kVP X-ray source, 500 ms exposure time in 180 projections over 9 min. Images were reconstructed in a 256 × 256 matrix using the HiSPECT (Scivis GmbH) reconstruction software package, and fused using proprietary VivoQuant (Invicro) software. At the end of the scanning procedure, the mouse was culled by cervical dislocation.

2. Poly (I:C)-IONP@PL-PEG-Pt(IV) micelles studies

Mice received injections of ^{99m}Tc-radiolabeled poly (I:C)-IONP@PL-PEG-Pt(IV) micelles dissolved in 10 mM PBS via different administration routes: s.c. on the inner side of the front forearms (20 µL, 13.1 MBq per side) or into the hocks (the lateral tarsal region just above the ankle) (20 µL, 12.0 MBq per side) or i.p. (100 µL, 74.8 MBq). In the case of tumor bearing mice, mice received a single intratumoral injection of the ^{99m}Tc-radiolabeled micelles (50 µL, 33.7 MBq). In each case, with the mouse under isoflurane anaesthesia (1.5-2% in oxygen), whole-body SPECT/CT scans are acquired at 3 h and 24 h post-injection (p.i.). With the full ring detector, 360° of data are acquired by rotating the collimator 45° (45 steps, 1 °/step). Data are collected in an energy window of 125-150 keV and the duration of the scans was 60 min (80 sec/step). During image acquisition, mice are kept normothermic using a heating blanket (Homeothermic Blanket Control Unit; Bruker BioSpin GmbH, Karlsruhe, Germany). After each SPECT scan, CT acquisitions are performed to provide anatomical information of

each animal as above in s.c. in the abdominal region and i.p. injections of ^{99m}Tc-radiolabeled poly (I:C)-IONP micelles.

Assessing innate immune responses

These studies were performed in collaboration with Dr. Malou Henriksen Lacey, Dr. Aintzane Zabaleta Azpiroz and Ane Ruiz de Angulo Dorronsoro (CIC biomaGUNE).

1. **Poly (I:C)-IONP@PL-PEG micelles (innate immune response)**

Balb/c mice, aged 6-10 weeks, were housed in ventilated cages and fed on a standard diet ad libitum. Formulations (100 μL/dose) were either i.p. or s.c. injected into the left flank of the mice (n=3). Both pre-injection, and at various time-points thereafter, blood was taken (25 μL) via the tail vein using capillary tube dipped in heparin solution (Chiesi, 1000UI/ml). Immediately, blood samples are placed into centrifugal devices containing 225 μL of sterile PBS 10 mM. The blood samples are centrifuged at 13000 x g for 5 min. The supernatant (serum) is collected and frozen for subsequent cytokine analysis. After the final blood collection mice are sacrificed by cervical dislocation.

2. **Poly (I:C)-IONP@PL-PEG-Pt(IV) micelles (BMDCs maturation assay)**

Balb/c mice, aged 6-10 weeks, were housed in ventilated cages and fed on a standard diet ad libitum. Formulations are injected into hind limb (20 μL/hind) of the mice (n=5). After 24 h mice are sacrificed and their inguinal lymph nodes (iLNs) and spleens are harvested. To analyse BMDCs activation the procedure as above was followed. To analyse NK cell activation, cells from the lymph nodes and spleen were incubated in the presence of Fc Block™ at 4 °C for 10 min. Finally, cells were stained with Nkp46-PE, CD3-BV421 and CD69-APC and corresponding isotype control at 4 °C for 15 min.

References

1. Sun, S. *et al.* Monodisperse MFe_2O_4 (M = Fe, Co, Mn) nanoparticles. *J. Am. Chem. Soc.* **126,** 273–9 (2004).

2. Bárcena, C. *et al.* Zinc ferrite nanoparticles as MRI contrast agents. *Chem. Commun.* 2224–6 (2008). doi:10.1039/b801041b

3. Roca, A. G. *et al.* Effect of nanoparticle and aggregate size on the relaxometric properties of MR contrast agents based on high quality magnetite nanoparticles. *J. Phys. Chem. B* **113,** 7033–9 (2009).

4. Duan, H. & Nie, S. Cell-penetrating quantum dots based on multivalent and endosome-disrupting surface coatings. *J. Am. Chem. Soc.* **129,** 3333–8 (2007).

5. Dubertret, B. *et al.* In vivo imaging of quantum dots encapsulated in phospholipid micelles. *Science* **298,** 1759–62 (2002).

6. Rieter, W. J., Pott, K. M., Taylor, K. M. L. & Lin, W. Nanoscale coordination polymers for platinum-based anticancer drug delivery. *J. Am. Chem. Soc.* **130,** 11584–5 (2008).

7. Henriksen-Lacey, M. *et al.* Comparison of the depot effect and immunogenicity of liposomes based on dimethyldioctadecylammonium (DDA), 3β-[N-(N',N'-Dimethylaminoethane)carbomyl] cholesterol (DC-Chol), and 1,2-Dioleoyl-3-trimethylammonium propane (DOTAP): prolonged liposome retention. *Mol. Pharm.* **8,** 153–61 (2011).

8. Lund, V., Schmid, R., Rickwood, D., Homes, E. & S, A. L. A. Nucleic Acids Research. **16,** 10861–10880 (1988).

9. Chu, B. C. F., Wahl, G. M. & Orgel, L. E. Derivatization of unprotected polynudeotides. *Nucleic Acids Res.* (1983).

10. Shukoor, M. I. *et al.* Double-stranded RNA polyinosinic-polycytidylic acid immobilized onto gamma-Fe_2O_3 nanoparticles by using a multifunctional polymeric linker. *Small* **3,** 1374–8 (2007).

11. Lazarova, N., James, S., Babich, J. & Zubieta, J. A convenient synthesis, chemical characterization and reactivity of $[Re(CO)_3(H_2O)_3]Br$: the crystal and molecular structure of $[Re(CO)_3(CH_3CN)_2Br]$. *Inorg. Chem. Commun.* **7,** 1023–1026 (2004).

12. Lutz, M. B. *et al.* An advanced culture method for generating large quantities of highly pure dendritic cells from mouse bone marrow. *J. Immunol. Methods* **223,** 77–92 (1999).

13. Vistica, D. T. *et al.* Tetrazolium-based assays for cellular viability: a critical examination of selected parameters affecting formazan production. *Cancer Res.* **51,** 2515–20 (1991).

14. Vichai, V. & Kirtikara, K. Sulforhodamine B colorimetric assay for cytotoxicity screening. *Nat. Protoc.* **1,** 1112–6 (2006).

15. Peng, X.-H. *et al.* Targeted delivery of cisplatin to lung cancer using ScFvEGFR-heparin-cisplatin nanoparticles. *ACS Nano* **5,** 9480–93 (2011).

Appendix

Publications

- N. Gómez Blanco, M. Jauregui-Osoro, **M. Cobaleda-Siles**, C. R. Maldonado, M. Henriksen-Lacey, D. Padro, S. Clark and J. C. Mareque-Rivas. Iron oxide-filled micelles as ligands for *fac*-$[M(CO)_3]^+$ ($M=^{99m}Tc$, Re). *Chem. Comm.*, **2012,** 48**,** 4211-4213.

- **M. Cobaleda-Siles,** M. Henriksen-Lacey, A. Ruiz de Angulo, A. Bernecker, V. Gómez Vallejo, B. Szczupak, J. Llop, G. Pastor, S. Plaza-García, M. Jauregui-Osoro, L. K. Meszaros and Juan C. Mareque-Rivas. An Iron Oxide Nanocarrier for dsRNA to Target Lymph Nodes and Strongly Activate Cells of the Immune System. *Small*, **2014**, 10, 5054-5067. (Frontispiece).

- J. Hernández-Gil, **M. Cobaleda-Siles**, A. Zabaleta Azpiroz, L. Salassa, J. Calvo and Juan C. Mareque-Rivas. An Iron Oxide Nanocarrier Loaded with a Pt(IV) Prodrug and Immunostimulatory dsRNA for Combining Complementary Cancer Killing Effects. *Adv. Healthcare Mater.*, **2015,** 4, 1034-1042. (Back cover).

Conference proceedings

- **11th European Biological Inorganic Chemistry Conference, Granada (2012)**

Nanoparticles-filled micelles as ligands for fac-$[M(CO)_3]^+$($M=^{99m}Tc$, Re) for multimodal imaging

N. Gómez Blanco, M. Jauregui-Osoro, **M. Cobaleda-Siles**, C. R. Maldonado, M. Henriksen-Lacey, D. Padro, S. Clark and J. C. Mareque-Rivas.

- **9th Elsinore Meeting on Infection Immunity. Translating Breakthroughs in Immunology into Vaccines of Global Importance, Denmark (2013)**

Iron oxide nanoparticles functionalized to activate immune responses

A. Ruiz de Angulo, **M. Cobaleda-Siles**, M. Henriksen-Lacey and J.C. Mareque-Rivas.

- **GRC Cancer Nanotechnology, Boston (2013)**

Iron oxide nanoparticles as multimodal contrast agents with immunostimulatory activity

M. Cobaleda-Siles, M. Henriksen-Lacey and J. C. Mareque-Rivas.

- **RSEQ Reunión Bienal, Santander (2013)**

Nanopartículas de Fe_3O_4 como agentes de contraste multimodal con actividad inmunoestimuladora

M. Cobaleda-Siles, M. Henriksen-Lacey and J. C. Mareque-Rivas.

- **ESSR´14-17th European Symposium of Radiopharmacy and Radiopharmaceuticals, Pamplona (2014)**

Intrinsically labelled magnetite-and quantum dot-filled micelles: improving specific activity of labelled Nanoparticles

M. Cobaleda-Siles, N. Gómez Blanco, M. González, V. Gómez-Vallejo, J. Llop and J. C. Mareque-Rivas.

- ***4th Early Stage Researchers Workshop, IMDEA Nanociencia, Madrid (2014)***
  - *Iron Oxide Nanoparticles Carrying dsRNA and Targeting Lymph Nodes for Immunotherapy.* ***Oral Presentation.***
  - *Superparamagnetic iron oxide nanoparticles for the delivery of a Toll-like receptor 7 agonist*.

    Ana. I. Bocanegra Gondan, **M. Cobaleda-Siles** and J. C. Mareque-Rivas.

CIC biomaGUNE